QUANTITATIVE ANALYSIS OF ANOMALOUS SEISMIC AMPLITUDES CAUSED BY FLUID MIGRATION

ABDULKAREEM, LAMEES,NAZAR

Department of Earth Sciences, Durham University

QUANTITATIVE ANALYSIS OF ANOMALOUS SEISMIC AMPLITUDES CAUSED BY FLUID MIGRATION

A thesis submitted to the Department of Earth Sciences at Durham University in partial fulfilment of the requirements for the Degree of Doctor of Philosophy

Abdulkareem, Lamees

September 2018

Abstract

Two- (2D) and three- (3D) dimensional pre-stack and post-stack seismic reflection data are used to investigate the processes which have led to the development of amplitude anomalies on reflections in the faulted, Cenozoic overburden on the Laminaria High, Northwest Shelf of Australia.

The integration of amplitude and seismic attribute maps for four key horizons (the seabed, Horizon H9, Horizon H10 and Horizon H13) with the corresponding two-way time (TWT) structure maps has identified the structural controls on the distribution of seismic anomalies. On the seabed, the main anomaly is located on the up-dip side of the fault trace, and is elongated parallel to the local time structure contours. These observations are consistent with the anomalies having developed in response to structurally-controlled fluid seepage along, and up-dip migration away from the fault trace. Amplitude anomalies associated with the deeper H9 reflector are also located adjacent to fault traces but are discordant to the local time structure contours. This observation suggests that the anomalies may be due to cemented hardgrounds that formed due to seepage when the faults intersected the palaeo-seafloor but were subsequently buried and deformed during ongoing sedimentation and fault growth/linkage.

Reprocessing of the 2D and 3D seismic pre-stack data supports the seismic interpretation of amplitude anomalies at the seabed. It is concluded that these anomalies are robust – that is, they are likely to reflect geological processes and are not simply a function of the chosen seismic processing workflow – and are caused by localised changes in acoustic impedence in the subsurface. More important is that using processed data without the knowledge of the background processing sequence for the data could be an issue in any 2D or 3D seismic interpretation. For this reason

the veracity of processing of any seismic data needs to be questioned, and should not be taken for granted especially if different surveys produce conflicting interpretations.

2D hydrocarbon migration modelling combined with fault slip- and dilation-tendency analyses were undertaken in order to investigate the impact of faults and host-rock lithologies on hydrocarbon seepage at the present-day sea floor. Results show that some active faults associated with amplitude anomalies (e.g. Fault F10) are critically stressed, assuming a static, and spatially homogeneous regional stress field. However, other faults associated with amplitude anomalies (e.g. Fault F11) appear not to be critically stressed. These results suggests that the "regional" stress field could, in fact, vary spatially and temporally allowing faults in different parts of the study area to become critically stressed – hence act as fluid migration pathways – at different times. The migration models show that hydrocarbon migration pathways are strongly influenced by fault-zone properties, specifically the capillary entry pressure (CEP) along faults. The dip of the sediment layers also influences hydrocarbon leakage from the subsurface to the seabed. In general, the migration models show vertical hydrocarbon migration along faults coupled with lateral migration below the seal layers and between faults. Fluids migrate along faults with two patterns of flow based on the CEP values along the faults: 1) focused – fluids migrate as a linear pattern along faults when the capillary entry pressure along the fault is within the lower range of the "background" CEP values; 2) diffuse – fluids are guided by faults when the capillary entry pressure along the fault is within the higher range of the "background" CEP values.

Contents

List of figures

Appendices

List of tables

Declaration

No part of this thesis has previously been submitted for a degree at this or any other university. The work described in this thesis is entirely that of the author, except where reference is made to previously published or unpublished work.

Acknowledgements

Firstly, I would like to express my sincere gratitude to my supervisors, Jonny Imber, Richard Hobbs, and Andy Aplin for the continuous support of my Ph.D study and related research, for their patience, motivation, and immense knowledge.

I am deeply grateful to my supervisor Jonny Imber, his incredible support and guidance helped me in all the time of research and writing of this thesis. I could not have imagined having a better advisor for my PhD.

I would like to thank the higher committee for education development in Iraq (HCED) for their financial support of my PhD study. My sincere thanks to Jon Gluyas, who support and encouraged me in my PhD journey. I appreciate all the effort of Matthew Hepburn, Gary Wilkinson and Dave Stevenson on offering IT support whenever necessary.

Thanks for the software companies for providing Academic Licenses, Badley Geoscience Ltd (Trap Tester/T7), Schlumberger (Petrel), Halliburton (Permedia), and GNS Science (Claritas).

I am very grateful to Dimitrios Michelioudakis for his support in using Claritas software and his great advices in the seismic processing. Special thanks to Loraine Postoriza for her support and being with me in all the difficult time of my study. I'd like to thank all my friends, in particular, Nadia Narayan, Alex Lapadat, Chimaobi Nwachukwu for their great support, friendship and all the lovely time we spent together. I am so grateful to my special friends who I first met them in Durham; Liah, Kat, Dhoha, Esma, and Mint.

A big thank to my small lovely family, especially my two little kids (Yousif and Yaqoob), thanks for being sometimes patient with me and praying for me. Last, but not least, a special thanks to my mum, dad, and my brothers and sister, thanks for being supportive of everything, thanks for your prayers, and all the motivation you gave me to finish my PhD.

Chapter 1: Introduction

1.1 Research rationale

Investigating active seepage and detection of fluid migration, especially of hydrocarbons, is a potential tool in the assessment of hydrocarbon exploration risk (Newton et al., 1980; Judd and Hovland, 1992). Also, fluid seepage could be indicative of an active petroleum system (Hovland, 2002; Schroot et al., 2005, Benjamin and Huuse, 2017). Hydrocarbon migration and leakage at the seabed produce a range of characteristic seepage features such as pockmarks, authigenic carbonate cementation and mud volcanos (Hovland and Judd, 1988). In addition, seismic reflection profiles of the subsurface may present features that indicate fluid migration in general and hydrocarbon migration in particular, such as gas chimneys and bright spots (Hovland and Judd, 1988). Many sedimentary basins show evidence of hydrocarbon leakage due to overpressure that caused focused fluid flow from the subsurface to the seabed, or fault reactivation that caused trap breaching. Examples of hydrocarbon leakage are found worldwide, for example in the North Sea (Hovland et al., 1987 a; Hovland and Judd, 1988; Heggland, 1998; Heggland, 2005); Maldives, Indian Ocean (Betzler et al., 2011); Offshore Taranaki Basin, New Zealand (Chenrai and Huuse, 2017); Gulf of Cadiz (Rensebergan et al., 2005); Niger Delta (Loseth et al., 2009;Benjamin and Huuse, 2017); Mauritania (Davis et al., 2014); Gulf of Mexico (Robert and Carny, 1997); and Porcupine Basin, offshore Ireland (Bailey et al., 2003); offshore Namibia (Moss and Cartwright, 2010).

Petroleum migration from the source rock, to its possible entrapment in reservoir and its leakage to the surface is controlled by the interaction of the driving force (buoyancy force) and the resistive force (capillary entry pressure - CEP) (England et al., 1987;

Vavra et al., 1992). For migration to occur, the buoyancy force must overcome the capillary entry pressure of the seal lithology (Carruthers and Ringrose, 1998).

Many studies on petroleum migration (Schowalter, 1979; Carruthers, 2003; Corradi et al., 2009; Ukekwe et al., 2012; Luo et al., 2015) were conducted which are based upscaling the spatial distributions of the lithological components in that different lithologies have different CEPs in order to carry out both static and dynamic migration modelling (Carruthers and Neufeld, 2008). However, Aplin and Larter (2005) stated that estimation of threshold capillary entry pressure to define the migration pathways in petroleum system for both homogeneous and heterogeneous sequences remain uncertain.

Mapping of subsurface structures is an essential step to find where oil or gas may be trapped or may have leaked, to help reduce the risk of drilling an unsuccessful well. In particular, the mapping of faults that might be barriers or conduits for fluid migration (Meldhal et al., 2001; Bacon et al., 2003; Ligtenberg, 2003; Ligtenberg, 2005; Meldhal et al., 2001) can help to understand fault properties in the context of flow within hydrocarbon reservoirs and their impact on fluid flow behavior which may result in hydrocarbon leakage. The pore-throat size of the fault rocks within a fault zone controls the capillary entry pressure which in turn controls fluid migration. (Bretan et al., 2003; Bretan, 2016).

The impact of fault seal analysis and fault properties on fluid migration have been investigated in many studies (Knipe et al., 1993; Knipe et al., 1998, King et al, 1994; Aydin, 2000; Yielding et al., 2010). These studies integrate microstructural analysis and the assessment of the geometrical evolution of faults to help identify fluid migration pathways and the evaluation of fault zone properties.

Manzocchi et al. (2010) conducted a study on fault-related fluid flow in hydrocarbon basins based on capillary entry pressure theory to model hydrocarbon migration into traps through geological time, and to simulate the production of hydrocarbons from reservoirs.

In this thesis, the Laminaria High in the Bonaparte Basin on the north west shelf of Australia is chosen for further research to investigate the evidence of hydrocarbon leakage and to examine the role of faults on fluid migration by the integration of seismic interpretation, fault seal analysis and fluid migration modelling. The particular strength and novelty of this thesis is that I have carried out seismic reprocessing using two- (2D) and three-dimensional (3D) pre-stack seismic data alongside this geological analysis.

There is a major problem with seismic data processing. Even when dealing with the same raw data, the result of processing the data by one person show different results from that of another one (Yilmaz, 2001). Figure 1.1 demonstrates this problem, these data have been processed by six different companies.

The result show significant differences in the frequency content, signal to noise ratio, and the extent of structural continuity from one section to another. These differences often related to the differences in the choice of the parameters and the detail of the processing algorithms (Yilmaz, 2001). Hence, in this thesis, reprocessing the raw data of the 3D seismic volume helps to examine the veracity of the seismic interpretation using the 3D seismic data.

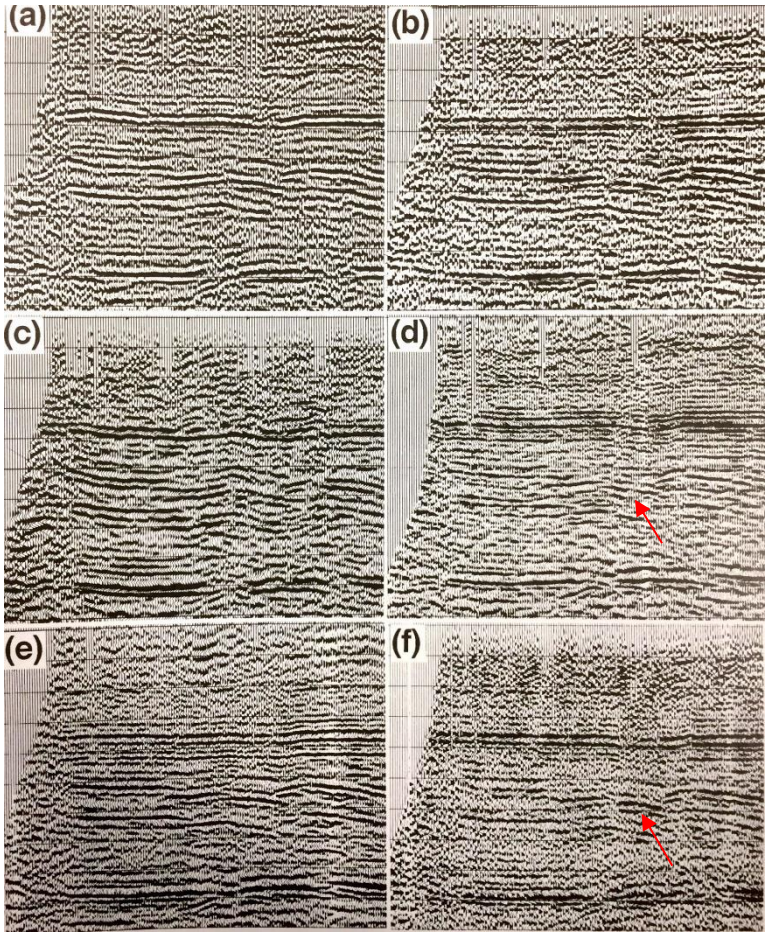

Figure 1.1. A seismic line processed by six different companies. (Data courtesy British Petroleum Development, Ltd., Carless Exploration Ltd.; Clyde Petroleum Plc.; Premier Consolidated Oilfields Plc.; and Tricentrol Oil Corporation Ltd.) Note that the arrow in Fig.1.1f show a strong or bright reflection, while in Fig.1.1d the same reflection is weak and less bright as shown by the arrow (from Yilmaz, 2001).

1.2 The study area: Laminaria High

The Laminaria High is located at the edge of the northern Bonaparte Basin and to the south edge of the Timor Trough (Figure 1.2a). It represents a small, remnant platform with an east-west orientation between the Flamingo and Sahul synclines and the larger Sahul and Ashmore platforms (Smith et al., 1996) (Figure 1.2a). Water depths range from 50 m on the nearby shelf to 300-400 m near the Laminaria High, and reach a maximum depth of 2000 m in the Timor Trough to the north (Smith et al., 1996). The

tectonic and the tectonostratigraphic setting of the Bonaparte Basin-Timor Sea is described in detail by Mory (1988) and Keep et al. (2002). The Bonaparte Basin is a Palaeozoic rift basin, mainly orientated NE-SW. This basin covers an area of approximately 250,000 km^2. It is bounded by the Vulcan Sub-basin and Browse Basin to the northwest and the Petrel Sub-basin to the southeast (Figure 1.2b).

The Timor Sea, which lies between the NW Shelf of Australia and the Indonesian Arc to the east of the Banda Arc (Charlton and Barkham, 1991) (Figures 1.2b and 1.1c), has been the focus for intensive hydrocarbon exploration since 1989 to 1999 (de Ruig et al., 2000), and there are several hydrocarbon discoveries in this area, including the Laminaria, Coralina, Buffalo, Elang and Kakatua fields (Figure 1.2a). The first oil field on the Laminaria High was discovered in 1994 in permit AC/P8 through the drilling of Laminaria-1 oil well (Figure 1.2a). Gas fields (e.g. the Bayu/Undan field/s) were also discovered and developed on the Flamingo High, south-east of the study area (Figure 1.2a) (de Ruig et al., 2010). However, the Timor Sea is considered to be a region with potentially high exploration risk (e.g. the Nancar Trough and the Laminaria High) (Whibley and Jacobson, 1990; Lisk et al., 1998; Castillo et al., 1998; de Ruig et al., 2000). It was noted after a few years, that this area had failed to deliver new oil discoveries (Powell, 2004) and exploration drilling had encountered dry or under-filled structures (de Ruig et al., 2000). In addition, the Timor Sea is considered as an active tectonic area at the Australian- Indonesian collision zone and has been affected by a series of significant earthquakes in the past time to the present day (Castillo et al., 2000)(Figure 1.3a and b).

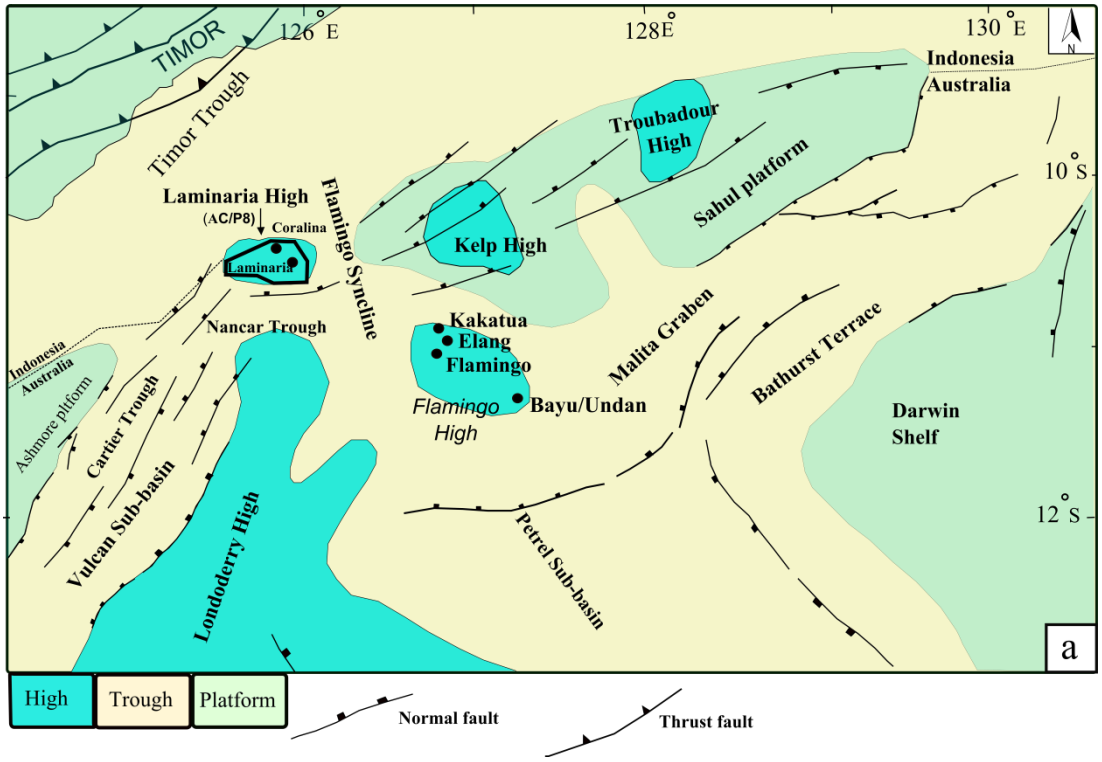
TIMOR
126° E
128° E
130° E
Indonesia
Australia
Timor Trough
Troubadour High
Sahul platform
10° S
Laminaria High
(AC/P8)
Coralina
Laminaria
Flamingo Syncline
Kelp High
Nancar Trough
Kakatua
Elang
Flamingo
Malita Graben
Bathurst Terrace
Indonesia
Australia
Ashmore pliform
Cartier Trough
Flamingo High
Bayu/Undan
Darwin Shelf
Vulcan Sub-basin
Londoderry High
Petrel Sub-basin
12° S
a
High
Trough
Platform
Normal fault
Thrust fault

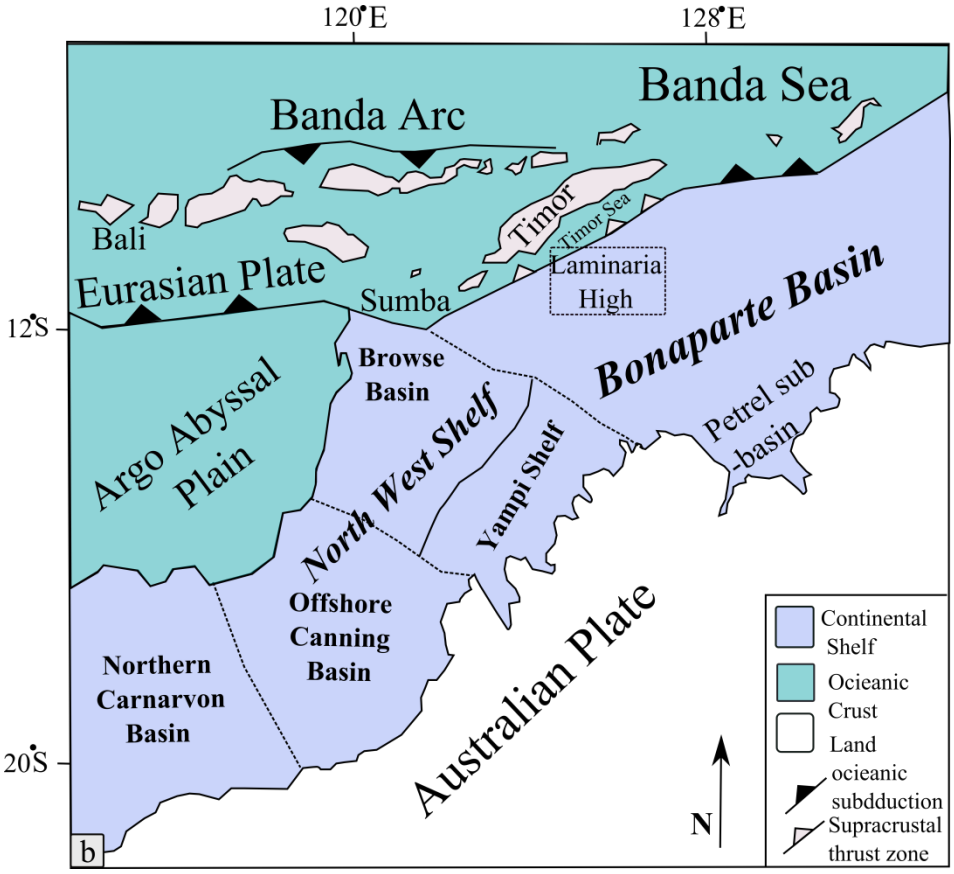
120°E
128°E
Banda Arc
Banda Sea
Bali
Timor
Timor Sea
Eurasian Plate
Sumba
Laminaria High
Bonaparte Basin
12°S
Browse Basin
Argo Abyssal Plain
North West Shelf
Yampi Shelf
Petrel sub -basin
Offshore Canning Basin
Northern Carnarvon Basin
Australian Plate
20°S
N
b
Continental Shelf
Ocieanic Crust
Land
ocieanic subdduction
Supracrustal thrust zone

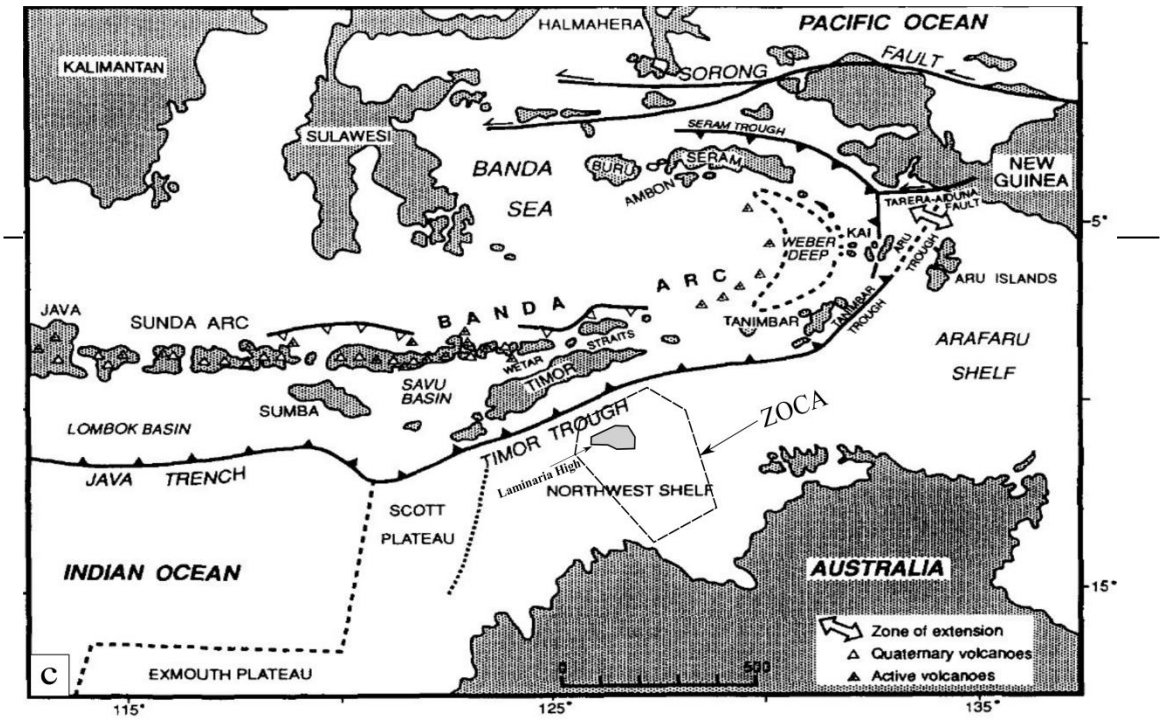

Figure 1.2. Location map of the study are. **(a)** Geological setting and Jurassic structure map of north western Bonaparte Basin, showing examples of oil and gas discoveries in the NW shelf of Australia (modified from Long and Imber, (2012); **(b)** Tectonic element map of the North West Shelf of Australia (modified from Gartrell et al., 2010; **(c)** General tectonic setting of the Timor Sea (After Charlton and Barkham, 1991).

The oblique collision between the Australian and Eurasian plates in the late Miocene-Pliocene (Figure 1.2c) resulted in reactivation of faults bounding Jurassic-age hydrocarbon reservoirs and traps, which breached the lateral seal of the faults, causing hydrocarbon leakage along faults (O'Brien et al., 1999; George et al., 2004; Gartrell et al., 2003; Gartrell et al., 2004; Gartrell and Lisk, 2005; Gartrell et al., 2006; Langhi et al., 2011).

De Ruig et al. (2000) suggested that fault reactivation had resulted in trap breaching, in particular for fault-bounded traps, and causes hydrocarbon leakage in the Laminaria and the Nancar Trough area. The link between active faulting and fluid flow is seen

elswhere in seismically active basins (e.g. the North Sea, Gulf of Mexico, Nigeria and Caspian sea) (Heggland, 2005; Ligtenberg, 2005).

Previous studies (Mildren et al., 1994; Castillo et al., 1998) argued that the orientation of the fault planes relative to the Late Miocene-Recent stress field in the Timor Sea in the Zone of Cooperation (ZOCA) (Figure 1.1c) is controlling the sealing potential of fault-bounded traps. Previous studies (O'Brien et al., 1999) on the Vulcan sub basin; (de Ruig et al., 2000; Dyt et al., 2012), the Laminaria High and the Nancar Trough suggested that hydrocarbon leakage is located at the intersection between the Jurassic and Mio-Pliocene faults, which are critically stressed. Evidence of hydrocarbon remigration and leakage in the Timor Sea is reported by the presence of hydrocarbon-related diagenetic zones (HRDZs) (Charlton et al., 1991; O'Brien and Woods, 1995), gas chimneys, pockmarks and large present-day carbonate mounds (Hovland et al., 1994; Lavering and Andrew, 2002).

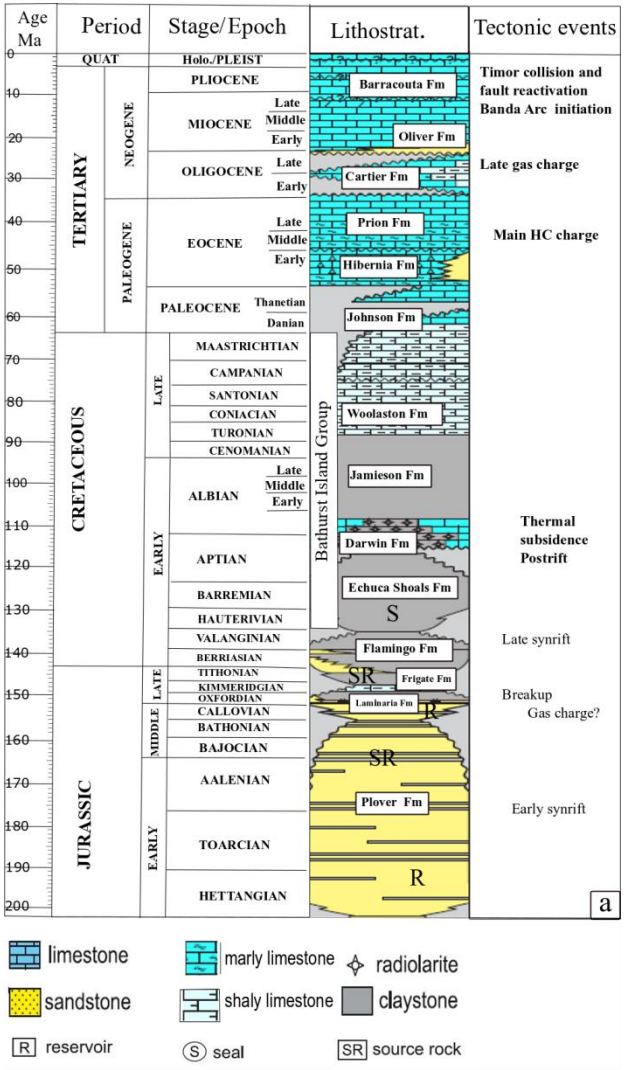

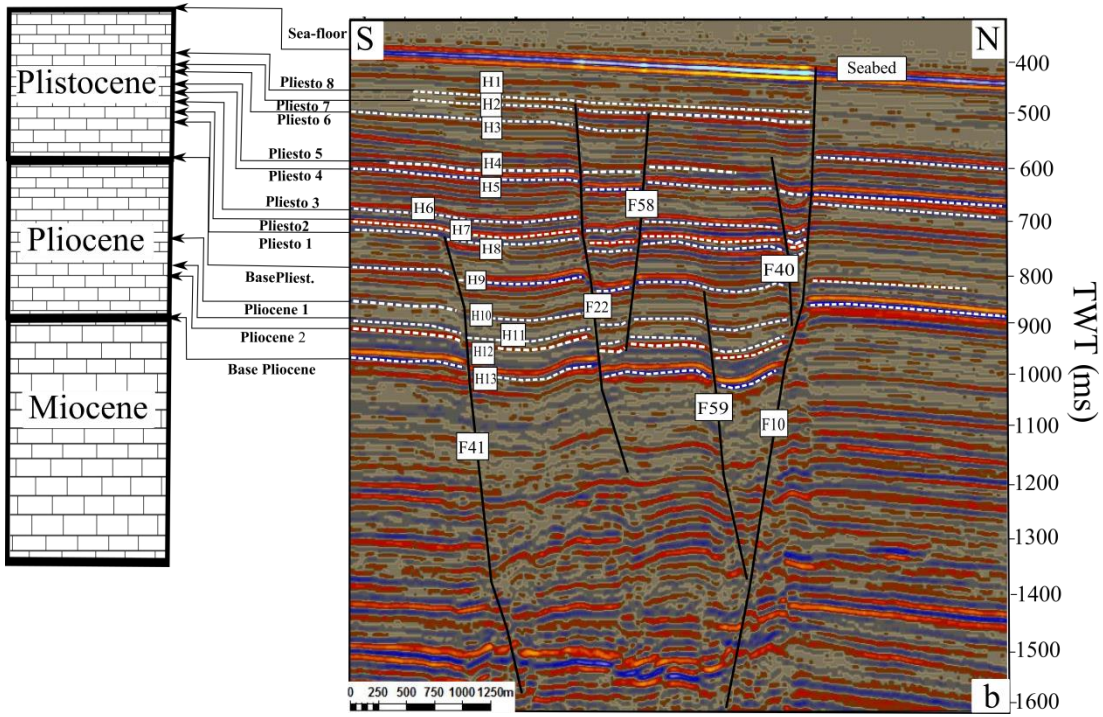

Figure 1.3. **a**. Generalized stratigraphic column for the Laminaria High (modified from De Ruig et al. 2000); **b**. Seismic section showing the interpreted horizons and their age used for the seismic and structural interpretation in Chapter 2.

The Laminaria High includes either underfilled or dry structural traps (de Ruig et al., 2002). Geophysical evidence of hydrocarbon seepage at the seabed in the Laminaria High includes high amplitude anomalies (bright spots) associated with active faults that cut and offset the seabed reflector (Langhi et al., 2010). These anomalies are correlated with the evidence of hydrocarbon remigration from the Jurassic reservoir along reactivated faults in the Vulcan sub-basin (O'Brien and Woods, 1995; O'Brien et al., 1999); Browse Basin (Howarth and Alves, 2016; Tuyl et al., 2018) and the Yampi Shelf – south-southwest of the Laminaria High (Rollet et al., 2006) – and these anomalies interpreted as being the result of hydrocarbon migration producing authigenic carbonates on the seabed (Hovland et al., 1987a; O'Brien and Woods, 1995). Gartell et al. (2006) suggested that the size and/or frequency of the earthquakes in the Laminaria High associated with high displacement fault could cause significant hydrocarbon leakage contrast to the low-displacement faults.

The Laminaria High is located at the edge of at the edge of Timor Sea, which is a tectonically active area and this area is seismically active. Hills et al. (2008) identify four significant zones of enhanced seismicity along the Australian continent ; one of them is the NW Seismic Zone located mainly on the NW Shelf, which is the passive margin bordering the Indian Ocean and Timor Sea. This areas of high seismic activity in the Neogene to Recent tectonic activity suggest that deformation is still active in the present day (Hills et al., 2008).

1.3 Thesis objectives

The main questions that will be addressed are:

1. What evidence is there to support the idea that the seismic anomalies at the seabed and the shallow subsurface are interpreted as authigenic carbonate cementation due to hydrocarbon seepage in the Laminaria High?
2. What is the influence of seismic processing and acquisition on the seismic amplitude anomalies associated with the seabed reflector?
3. What are the circumstances that cause faults to act as conduits or barriers for hydrocarbon migration and leakage?

These questions will be answered by a series of research objectives that:

1. investigate the spatial and temporal relationships between the amplitude anomalies and the present-day structure, and identify the structural control on fluid migration;
2. identify the base of the syn-faulting horizon, as this will help to distinguish which horizons were at the paleoseabed and which horizons were buried at the time of faulting;
3. correlate between the existence of amplitude anomalies and the subsurface structures for a better understanding of the structural control on fluid migration;
4. establish the confidence in the 3D interpreted data, by specifically investigating the influence of seismic processing on amplitude anomalies at the seabed;
5. undertake hydrocarbon migration modelling in order to investigate the impact of faults and host-rock lithologies on hydrocarbon seepage at the present-day sea floor.

1.4 Key concepts and terminology

1.4.1 Bright Spots

Direct evidence of hydrocarbon accumulation is recognised on seismic data as "bright spots" (Ligtenberg, 2005) (Figure 1.4) and appear as high amplitude, negative phase anomalies as a result of decreased impedance. This decrease is produced when the overlying rock has a higher velocity and/or density than the underlying reservoir that is filled with hydrocarbons, especially gas. The first characterisation of bright spots in seismic data exists in the Gulf of Oman, northwest of the Indian Ocean (Figure 1.4a) (White, 1977) and were identified along contiguous seismic sections and were interpreted as an indication of gas accumulations. However, bright spots are not always an indication of hydrocarbon accumulation as they could be related to the lithology. For example, when coal is interbedded within the formation layers, it will increase the impedance contrast between the different lithologies, which then will also produce a bright spot (Judd and Hovland, 1992). Other amplitude anomalies could be a result of the effect of thin layers; Widess (1973) showed that interference between the upper and lower boundaries of a thin layer can produce tuning effects with a maximum amplitude response that depends on the frequency of the seismic data. Bright spots adjacent to faults are indicative of leaking faults that may be within or above hydrocarbon reservoirs (Sheriff and Geldart, 1995; Ligtenberg, 2005). An example of bright spots associated with leaking faults in the Mediterranean Sea is shown in Figure 1.4b.

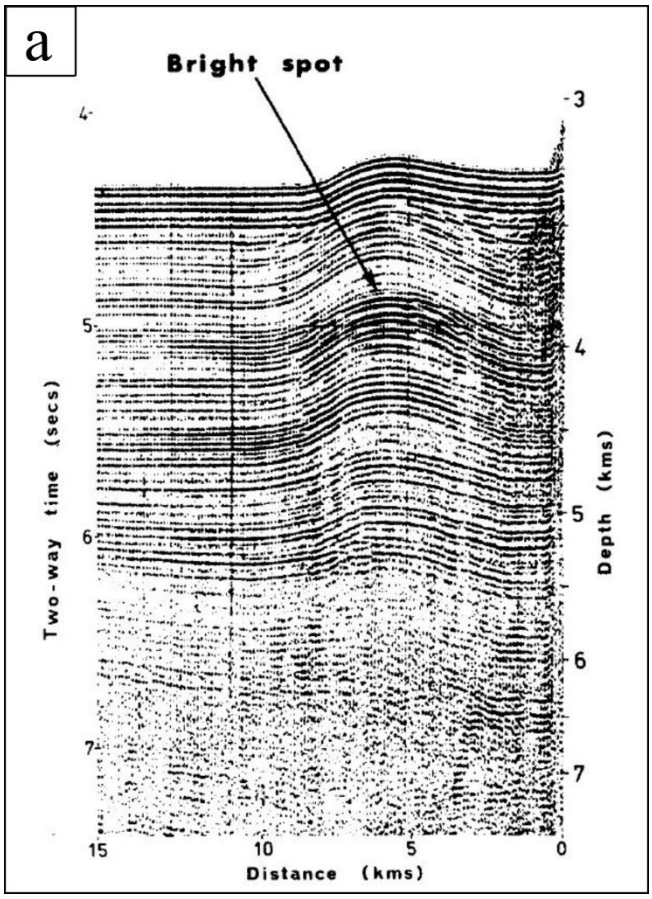

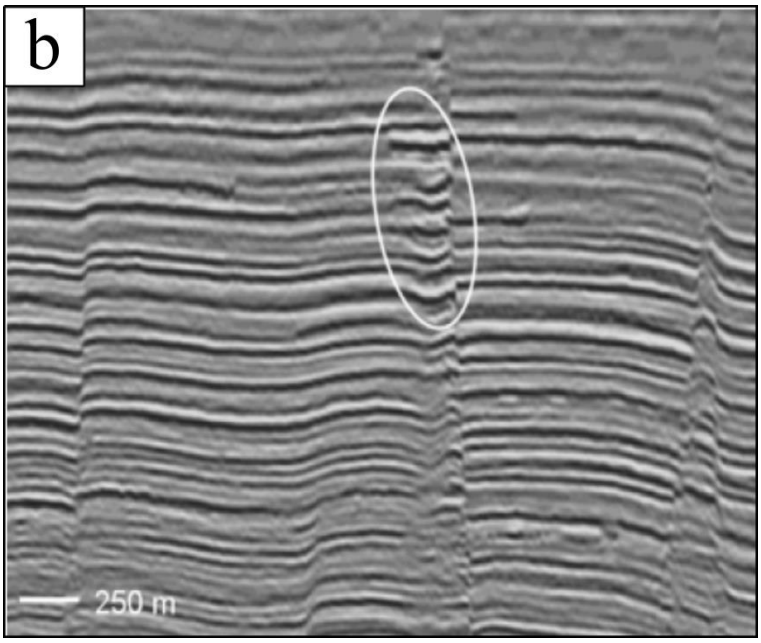

Figure 1.4. 2D seismic sections showing examples of bright spots. **(a)** Bright spot above a fold at the edge of the Makran continental margin of Pakistan and Iran in the Gulf of Oman (from White, 1977). **(b)** Bright spots due to hydrocarbon leakage along fault at the Mediterranean Sea (from Ligtenberg, 2005).

1.4.2 Authigenic carbonate hardground

Authigenic carbonates can form cemented carbonate surfaces at the seabed, often through the generation of bacterial mats and chemosynthetic fauna within limestone sequences (Barnes and Goldberg, 1976; Hovland, 1990; Rollet et al., 2006). Authigenic carbonate is a result of the aerobic oxidation of methane (AOM) which could be sourced from hydrocarbon accumulations (oil and gas) or local biogenic matter. This oxidation increases the water's alkalinity and creates a favorable ecosystem for the precipitation of carbonate hardgrounds (Barnes and Goldberg, 1976; Hovland, 1990; Blumenberg et al., 2015) (Figure 1.5).This carbonate cementation produces a significant increase in acoustic impedance (O'Brien, 2000; O'Brien et al., 2002). It is often associated with hydrocarbon leakage along faults and hence, has a linear expression (Figure 1.5). Oxidation of methane occurs based on the following equation (Barnes and Goldberg, 1976; O'Brien and Woods, 1995):

$$CH_4+2O_2 \longrightarrow CO_2+2H_2O \qquad (1.1)$$

The first hardgrounds and benthic communities were found in 1980 in the Gulf of Mexico at the base of the continental slope of Louisiana (Paull et al., 1984). Hydrocarbon seepage provides the carbon source and acts as a nutrient for the organic communities, where the formation of the precipitation of these features depends on the seeping compounds of the fluid, which includes CH_4, CO_2 and H_2S (Hovland, 1990). Hovland et al. (1994) proposed that many carbonate hardgrounds have developed in areas of active hydrocarbon leakage within the Timor Sea. Examples of hydrocarbon leakage-related carbonate hardgrounds had been found in the North West Shelf of Australia's basins (Bonaparte Basin and Browse Basin) and Gippsland Basin

(Cowley and O'Brien, 2000). Authigenic carbonates associated with hydrocarbon seeps exhibits a range of mineralogical as well as carbon and oxygen isotopic composition (Roberts and Feng, 2013). Brendt et al. (2014) conducted a study to derive the minimum age of the onset marine methane released from the seabed. This study applied U/Th isotope measurement to deduce the age of the seepage and showed that methane related precipitation had occurred at 3000 years before the present (Brendt et al., 2014). Hence, methane related authigenic process represents a good geologic archive as it provides both permanent and transient records of seepage and imply changes in the fluid flow system in the sedimentary basins (Roberts and Feng, 2013; Feng and Chen, 2009).

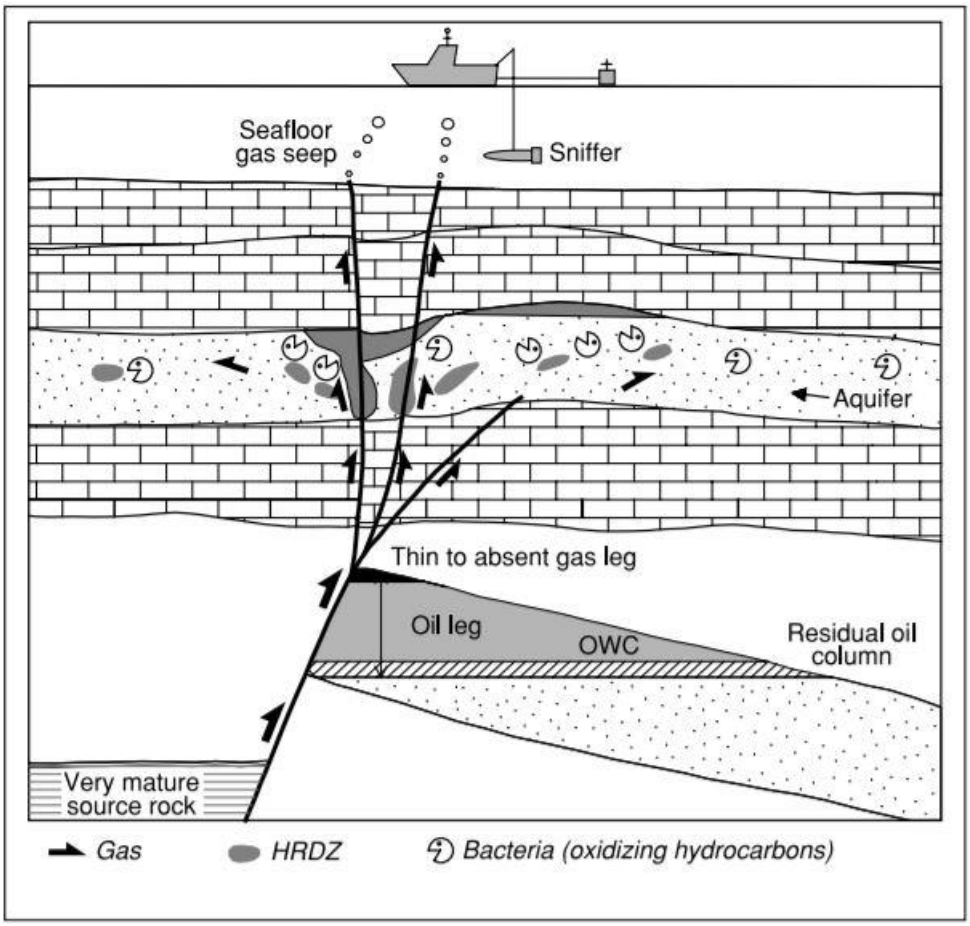

Figure 1.5. Schematic, showing the formation process of the authigenic carbonate in the Vulcan sub-basin. Hydrocarbons migrating up the faults and are oxidized by bacteria releasing CO_2 that is combined with carbonate cementation along the fault zone (from O'Brein et al., 2002). HRDZ= hydrocarbon related diagenetic zones.

1.4.3 Pockmarks

Hydrocarbon leakage at the seabed can be identified in unconsolidated sediment as sub-circular depressions or craters that are called "pockmarks" (Judd and Hovalnd, 2007) and are caused by gas leakage or groundwater overpressure venting from the shallow or deep subsurface (Hovland, 1984; Hovland, 1987b). Previous studies (Dimitrov and Woodside, 2003; Andresen et al., 2008) suggested that pockmarks formed under a variety of geological and biological conditions such as lithology, sedimentation rate, faults and fractures and seabed erosion and formed as a result of

gas leakage or groundwater overpressure venting from the shallow or deep subsurface (Hovland, 1984; Hovland, 1987b). Also, pockmarks occur in different characteristic patterns, and vary in size and are formed under different conditions (Hovland et al., 2002) (Figure 1.6). A "unit pockmark," which is a small crater, ranges from 1 m to 10 m in diameter and 0.5 m in deep and it represents a one-time expulsion event. It is usually formed around the "Normal Pockmarks" and are circular depressions, ranging from 10 to 700m in diameter and from 1 to 45m in depth (Figures 1.6a and 1.6b), which form by repeated expulsion events.

The "elongated pockmark" occurs on slopes and areas of the seabed that are influenced by strong bottom currents (Hovland et al., 2002) (Figure 1.6c). An "eyed pockmark" is formed as a result of either the precipitation of authigenic carbonates or an erosive process caused by biological activities that result in a higher acoustic reflectivity area at the seabed (Figure 1.5d) (Hovland and Judd, 1988; Hovland et al., 2002). Paleo-pockmarks also occur within the sediments and have been recognized in seismic data (Andresen and Huuse, 2011; Cartwright and Santamarina, 2015). Pockmarks are an indication of sub-surface hydrocarbon accumulation and are also considered as a geohazard for hydrocarbon exploration as they may be associated with shallow gas (Newton et al., 1980; Sills and Wheeler, 1992).

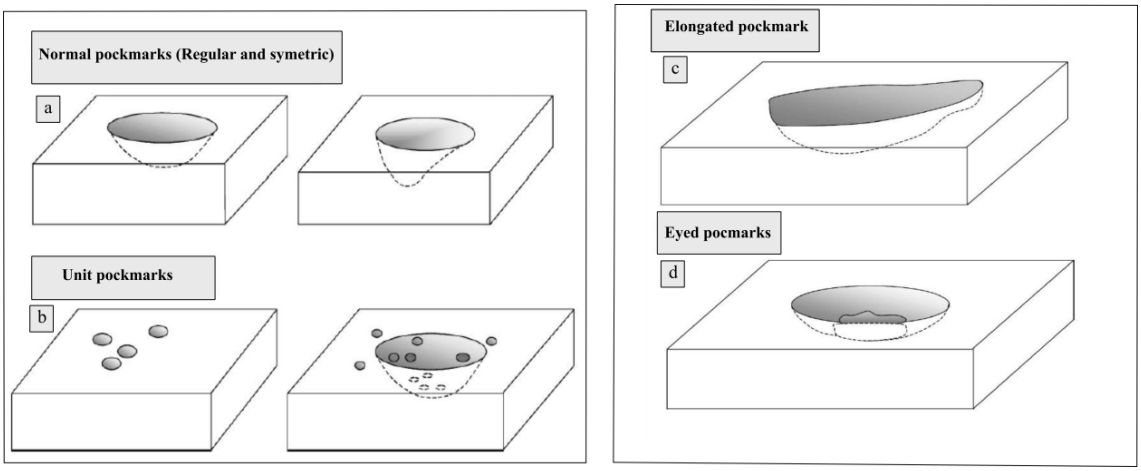

Figure 1.6. Examples of pockmark characteristics at the seabed. **(a)** Normal pockmarks (Regular and symmetric in shape); **(b)** Unit pockmarks with and without associated normal pockmarks ; **(c)** Elongated pockmarks; **(d)** Eyed pockmarks (from Hovland et al., 2002).

1.4.3 Gas chimneys

Gas chimneys are direct evidence of upward hydrocarbon migration and accumulations trapped in an anticline, and they indicate a deeper hydrocarbon reservoir (Løseth et al., 2009) (Figure 1.7). A gas chimney was first identified by Heggland (1970) from seismic data as a distorted region of the seismic amplitude and phase of the seismic reflectors. This disturbed seismic data is a result of reducing the acoustic velocities due to the presence of gas migration (Judd and Hovland, 1992; Arntsen et al., 2007). Gas chimneys can be identified along the seismic data as disturbance columns that have weaker reflection amplitude than the surrounding seismic reflections (Figure 1.7). Some gas chimneys are associated with faults when these faults are open and act as pathways for gas migration or other fluids (Heggland, 2005). Gas chimneys could be a result of released gas pressure from upward-moving water (Meldahl and Heggland, 2001). They could act as feeds for mud volcanos and

pockmarks at the seabed and they are considered as a drilling hazard, but also an indication of an active petroleum system (Heggland, 2005).

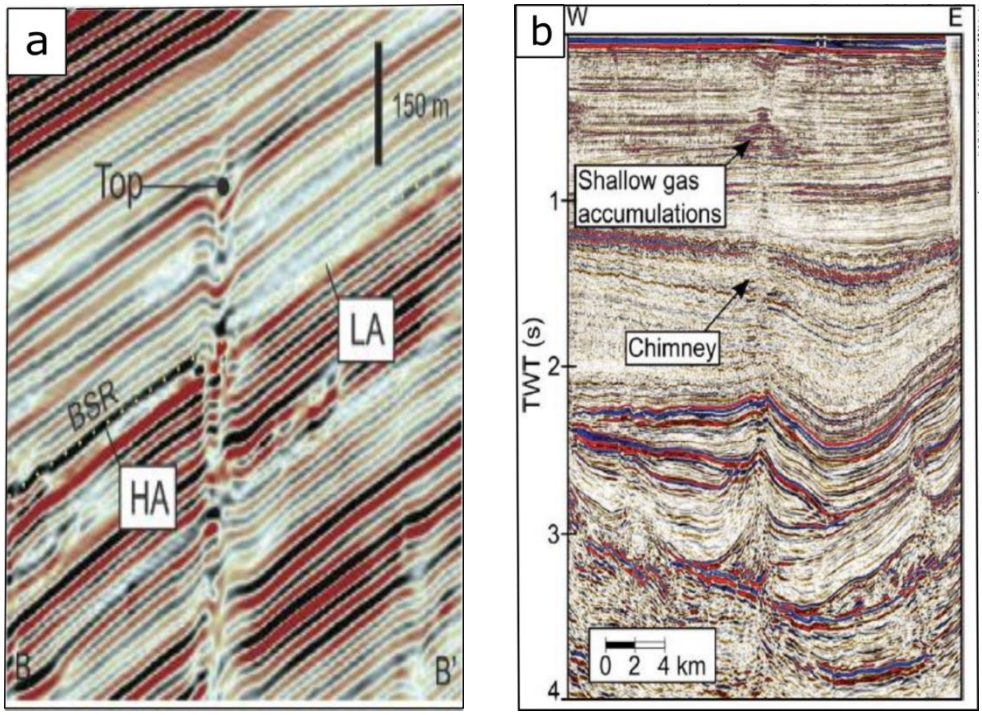

Figure 1.7. 2D seismic sections showing an example of gas chimneys **(a)** Vertical seismic chimney from offshore Mauritania. LA is low amplitude up dip of the chimney, HA is high amplitude downdip the chimney. (from Davis et al., 2014) ;**(b)** Gas chimney from the North Sea with shallow –gas accumulation. (from Arts and Vandeweijer, 2011).

1.4.5 Mud volcanoes

Mud volcanos are conical topographic structures that can be recognised on seismic data as a vertical wipe-out zone (Figure 1.8). They result from the expulsion of fluids, solids, and gases from the deep subsurface to the seabed and they contribute large volumes of fossil methane to the atmosphere (Judd, 2005; Stewart and Davis, 2006). Mud volcanoes occur in both onshore and offshore and are found globally with different sizes ranging from a few meters to several kilometers (Hovland & Judd,

1988; Milkov, 2000). Paleo-mud volcanoes are also recognised on seismic data buried under thick layers of sediments and indicate long-term focused fluid expulsion (Heggland, 1998; Benjamin and Huuse, 2017).

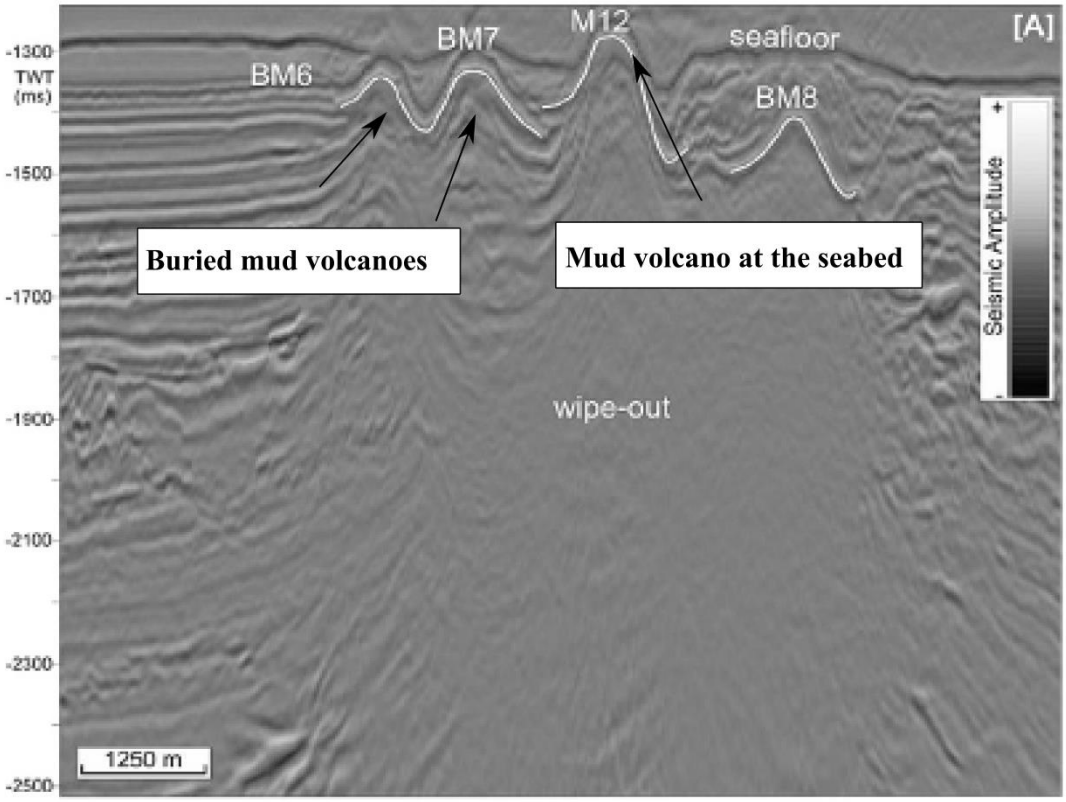

Figure 1.8. Seismic section showing examples of buried mud volcanoes and seabed mud volcano. Note the wipe-out zones on seismic data below each mud volcano (from Benjamin and Huuse, 2017)

1.5 Background and overview of the 2D and 3D seismic data

As this research is based on analyses of 2D and 3D seismic reflection data, therefore, for a successful interpretation, a proper understanding of the background and principles of the seismic reflection data and identification the differences between the 2D and 3D seismic data is essential in this study (Brown, 2011).

3D and 2D seismic data are essential tools in the oil and gas industry, primarily to reduce exploration drilling risk. It helps to understand the subsurface geological structures and provide structural images (Sheriff and Geldart, 1995; 2002; Bacon et al., 2003). The 2D seismic reflection method was developed in the 1920s and then improved in the 1950s. For regional surveys, data are acquired on parallel and orthogonal profiles with typical spacing of 100-1000 m, which provides primary seismic information for the subsurface.

The 3D seismic reflection method was developed in the 1970s (Sheriff and Geldart, 1995) and acquired by applying a grid of profiles spaced approximately 12.5-20 m apart, this produces a continuously sampled 3D cube that provided details and extensive seismic coverage for the subsurface in the study area (Bacon et al., 2003; Cartwright and Huuse, 2005; Cartwright, 2007) (Figure 1.9). The 3D seismic data added major improvement in data resolution and interpretation compared to the 2D seismic data, but the processing and interpretation processes remain essentially the same (Bacon et al., 2003; Brown, 2011) .

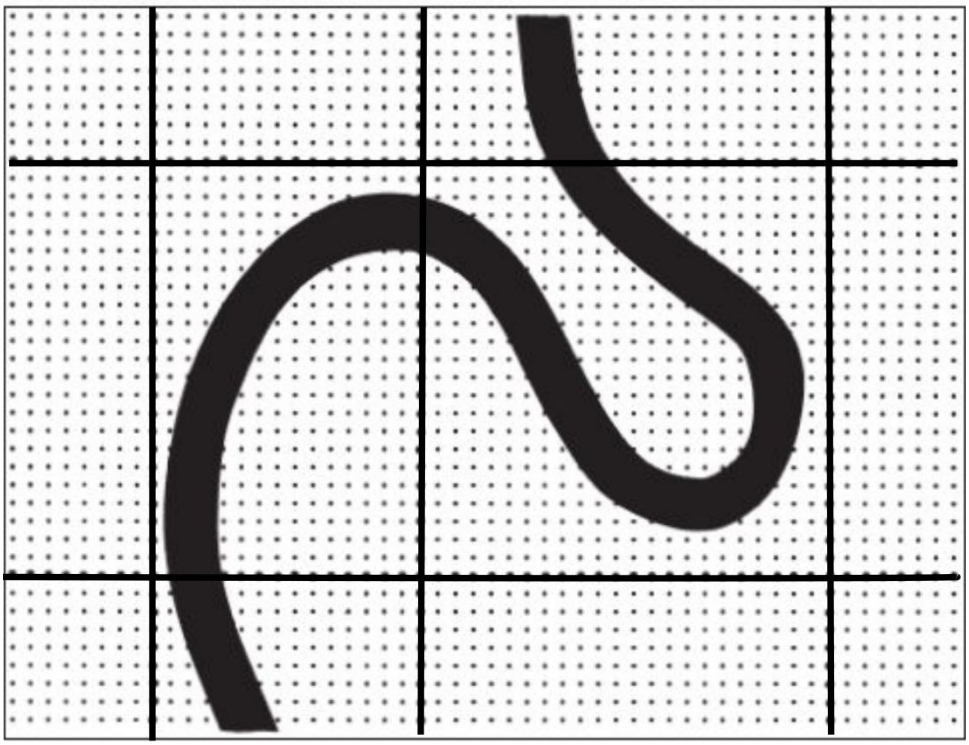

Figure 1.9. Schematic showing the 3D seismic coverage (dotted lines) over the 2D seismic coverage (solid lines). Note how the 2D coverage misses the meander loop (from Brown, 2011).

1.6 Acquisition of the seismic reflection data

The acquisition of marine seismic data is based on the energy source and receiver array being towed by a ship. The source produces an impulsive acoustic pulse and a receiver array records the reflected echoes from the impedance contrasts in the subsurface. The compressional acoustic seismic pulses (p-waves) are generated by an air gun array (Brown, 2011). This expulsion sends the seismic or sound waves through the water and into the rock below the seabed (Bacon et al., 2003).

In the 2D seismic acquisition, the data are acquired from a single source, and recorded on a receiver array, while the 3D seismic data is acquired using multiple sources and up to 12 receiver arrays of 4-8 km in length (Brown, 2011). Use of multiple sources

and receiver arrays significantly reduces the time and the cost of acquiring this type of data.

1.7 Principles of the seismic reflection methods

Seismic waves travel down through the subsurface and are reflected or refracted by different geological interfaces that have different rock properties based mainly on the lithology but also on the fluid content in the pores of the rock (Kearey et al., 2002 and Bacon et al., 2003).The P-wave reflections are the most important in marine seismic surveys because the S-waves do not transmit through fluids (Bacon et al., 2003). Also, P-wave reflection arrives before the corresponding S-wave, as the slower and later S-wave events can be confused with multiple reverberation of P-wave energy within the water layer. In addition, because the P waves have the highest velocities makes picking the velocity model used in processing easier. Though the seismic reflection method could be applied both offshore and onshore, this study is conducted to understand the offshore region.

A change in the rock properties and the bulk density produces changes in the velocity of the seismic P-wave of the rock, which in turn changes the acoustic impedance (Z) (Brown, 2011). Acoustic impedance is defined as:

$$Z=\rho V \qquad (1.2)$$

Z: acoustic impedance

ρ: density

V: P-wave velocity

1.8 Resolution of seismic reflection data

The resolution of the seismic data is affected by the thickness of the formation, the attenuation of the noise caused by scattering and inelastic absorption and the signal-to-noise ratio, which in turn will affect the ability to map the structural features within the seismic data (Simm and Bacon, 2014). In general, the resolution of the seismic data is based on the frequency of the waves that propagate through the subsurface (Brown, 2011). Most seismic reflection data has frequencies typically ranging from 5 to 150 Hertz. The highest frequencies of the seismic data have higher resolution in the shallow subsurface and decrease with depth as a result of the absorption and the attenuation of the seismic energy (Brown, 2011). The acoustic velocity increases due to compaction on the sediments which increases the wavelength of the seismic data with a consequential loss of resolution (Kearey et al., 2002). The resolution of the seismic data is based on calculating the wavelength (λ) of the wave, the frequency (f) and the velocity (V) of the wave that propagates through the subsurface.

$$\lambda = \frac{V}{f} \qquad (1.3)$$

The resolution is identified as the minimum distance between two features that are recognised within the seismic. It includes:

The vertical resolution $R_{(V)}$: this is how far the separation should be between two interfaces, either in time or in space, to be recognised as separate reflectors. A layer is recognised when its thickness is ≥ ¼ the wavelength. The vertical resolution is calculated by:

$$R_{(V)} = ¼ \lambda \qquad (1.4)$$

The vertical resolution of the seismic data is improved by applying deconvolution (Brown, 2011), which is a pre-stack processing that helps to suppress some of the lower frequencies in the seismic data. However, there could be a risk in degrading the data from the deeper subsurface (Sheriff and Geldart, 1995).

The horizontal resolution $R_{(H)}$: this is how far the separation should be between two features in a single layer, either in time or in space, to be recognised as separate features in the seismic data. Seismic wavelets that are returned to a detector within half a wavelength of the initial reflected arrival forms the Fresnel zone (Kearey et al., 2002) (Figure 1.10a) .The horizontal resolution is more complex in stacked data prior to migration imaging (Brown, 2011). On stacked data the horizontal resolution is defined by the first Fresnel zone, the diameter of which is dependent on both the frequency of the source and the reflector depth (Brown, 2011).

Post migration, the horizontal resolution of the seismic data is improved (Brown, 2011) as it: 1) relocates the dipping events back to their correct geological relationships 2) collapses diffraction hyperbola, and 3) focuses energy over the Fresnel zone to about half the dominant wavelength (Figure 1.10b) (Lindsey, 1989). Migration applied to the 2D seismic data collapses the Fresnel zone along the in-line direction only so may still include spurious events from out-of-plane of section in surveys over geologically complex areas. For the 3D seismic data, migration collapses the Fresnel zone along the in-line and the cross line direction (Kearey et al., 2002) and gives the same horizontal resolution irrespective of direction of:

$$R_{(H)} = \tfrac{1}{2}\lambda \qquad (1.5)$$

The use of half rather than a quarter of the wavelength (Rayleigh's criterion) recognises the limitations in the velocity model used for imaging.

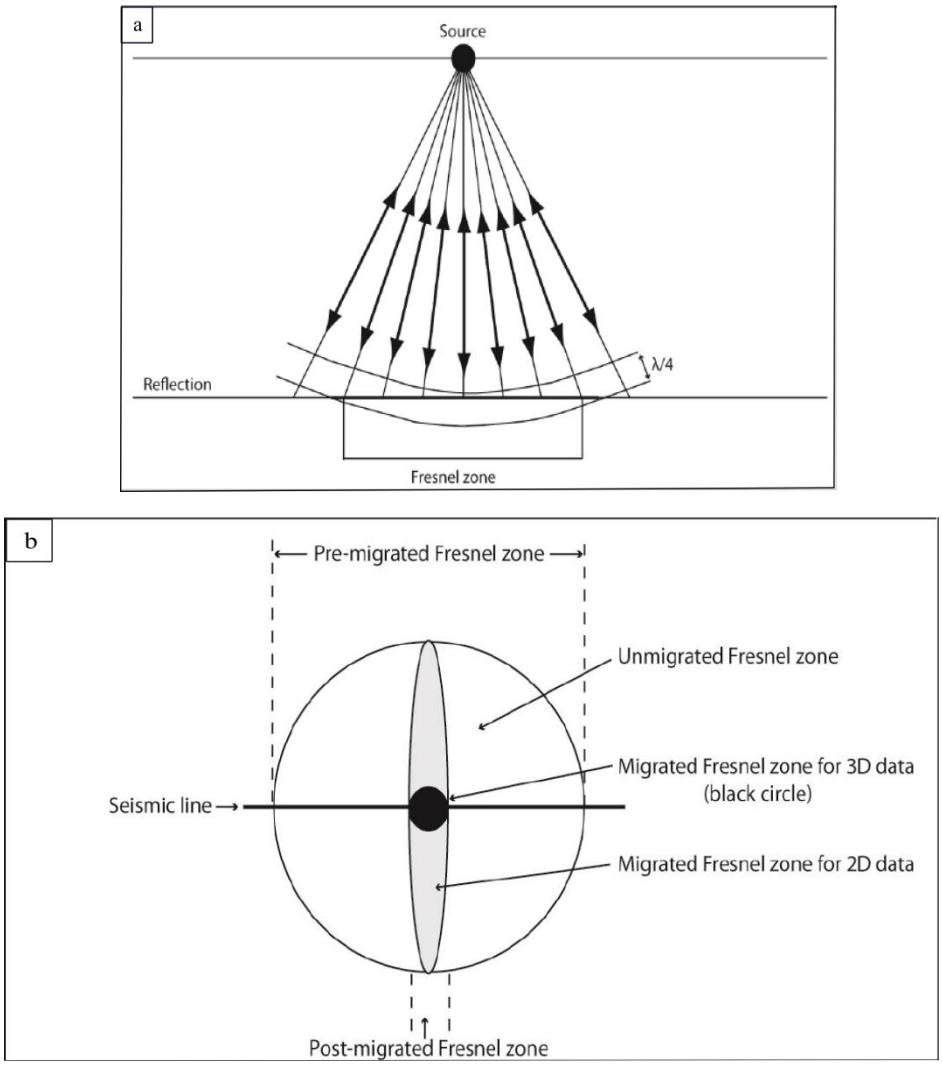

Figure1.10. (a) Seismic wavelets that are returned to a detector within half a wavelength of the initial reflected arrival forms the Fresnel zone (from Kearey et al., 2002). **(b**) The Fresnel zone before and after migration (from Brown, 2011).

1.9 Thesis outline

Following this introduction chapter, this thesis includes three main chapters which present and discuss my research; each contains its own introduction, data, methodology, and discussion. Each chapter also proposes and tests one key hypothesis. The thesis is concluded with a final summary.

The outline for each chapter is:

Chapter 2. *Geophysical evidence for structurally controlled, authigenic carbonate cementation on the Laminaria High, Bonaparte basin, North West Shelf of Australia*

This chapter tests the hypothesis that the seismic anomalies on the seabed reflector and in the shallow subsurface result from authigenic carbonate cementation. In the absence of suitable core samples on which to perform geochemical analyses (cf. O'Brien et al., 1999), the hypothesis is tested by investigating the spatial and temporal relationships between the amplitude anomalies, the present-day structure, and faults that intersected the paleo-seabed at different times during the deposition of the syn-faulting, Pliocene-Pleistocene succession. The studied 3D seismic reflection dataset was calibrated with well Alaria-1 from the AC/P8 permit area on the Laminaria High to carry out detailed structural mapping. The reflection data were then used to characterise the distributions of amplitude, RMS (root mean square), spectral decomposition and edge detection attribute maps in the shallow subsurface. My results are consistent with Langhi et al.'s (2010) findings, and demonstrate the importance of small-, in addition to large-, throw faults in controlling hydrocarbon (re-)migration and authigenic carbonate cementation within the Cenozoic overburden on the Laminaria High. However, due to the different distribution of the amplitude anomalies at the seabed in this research and in Langhi et al. 's (2010) study, the veracity of these amplitude anomalies at the seabed needs further investigation, as shown below in Chapter 3, to examine the validity of the seismic interpretation in this chapter.

This chapter is written in the style of a published manuscript and submitted as ***Geophysical evidence for structurally controlled, authigenic carbonate cementation in the Laminaria High, Bonaparte basin, North West Shelf of Australia*** to Marine and Petroleum Geology Journal. This paper is accepted and available online at Marine and Petroleum Geology Journal. Contribution by the Authors are as follows: Lamees

Abdulkareem (seismic interpretation, structural analysis, geological interpretation, figure preparation and writing), Jonathan Imber and Richard Hobbs – discussion of geological concepts and editorial guidance.

Chapter 3. *Quantitative analysis for amplitude anomalies at the seabed from the 2D and 3D pre-stack data*

To examine the findings of Chapter 2, this chapter establishes the confidence in the 3D interpreted data that is used in Chapter 2, by specifically investigating the influence of seismic processing on amplitude anomalies at the seabed due to the differences between the interpretations presented in Chapter 2 and that of Langhi et al. (2010). Therefore, this study will investigate whether these differences are attributed to acquisition/processing or do these anomalies represent actual changes in the hydrocarbon leakage with time?

This study processed data from two survey vintages, specifically the 2D 1992 Caulerpa and the 3D 1995 Laminaria pre-stack seismic data with different configurations using similar processing steps that were applied on the original 3D seismic data used in Chapter 2. The main reason for that is to investigate the implications of robustness in seismic processing on geophysical interpretation using 2D or 3D post-stack migrated data. Re-processing of the two pre-stack datasets confirmed the veracity of the 3D seismic interpretation in Chapter 2. It highlights the fact that amplitude anomalies at the seabed are frequency dependent. Also, the effect of the thin beds at or close to the seabed should be considered as these could affect the amplitude anomalies (Widess, 1973). The differences in the time of acquiring the two surveys (2D Caulerpa 1992 and 3D 1995 Laminaria) used in this study could suggest that the variation in the appearance of the amplitude anomalies in these data sets could be the response of the

leakage to regional tectonic activity in the wider study area. Hence, this could influence the stress in the study area. The interpretation is that a change the stress conditions along faults will moderate the leakage which in turn could change the amplitude anomalies at the seabed. Therefore, the following chapter investigates the role of faults on fluid migration and the effect that stress may have on the sealing or leaking properties of faults.

Chapter 4. *Petroleum migration modelling in the Laminaria High: influence of critically stressed faults on hydrocarbon migration and leakage*

In order to investigate the role of faults and stress field on hydrocarbon migration and leakage in the study area (Chapter 3), this chapter tests the hypothesis that hydrocarbon leakage at the present-day seabed is associated with critically stressed faults. This study performs migration modelling using a 2D depth-converted seismic sections to: **(a)** investigate the possible impact of the stress regime on fault flow properties; **(b)** constrain the circumstances of when faults act as conduits, compared to flows through the background stratigraphy; **(c)** assess how migration modelling and percolation can inform our understanding of seepage in the area of interest; and **(d)** correlate between the output models of fluid migration with the location of the high amplitude anomalies on the seabed and the subsurface structures in Chapter 2.

The results of this chapter suggest that the different distributions of the capillary entry pressure (CEPs) along the faults have a significant impact on fluid flow in that faults could act as 1) linear pathways for focussed migration, mainly when a low CEP is assigned along the fault line; 2) a general guide for migration when a high CEP is assigned along the fault; 3) a conduit at some point and barrier for hydrocarbon

migration at another point based on the distribution of the lithofacies within the fault zone.

Chapter 5. *Discussion and conclusion*

This chapter includes a summary of the results from this thesis and discusses the potential implications of my findings from the Laminaria High and other hydrocarbon basins. Also, the potential future work is discussed in this chapter.

1.10 Summary

This chapter has introduced the topic of this thesis and outlined the research objectives. It also provides an overview of the principal key concepts and terminology and review the background of the seismic reflection method.

Chapter 2: Geophysical evidence for structurally-controlled, authigenic carbonate cementation in the Laminaria High, Bonaparte basin, Northwest Shelf of Australia

2.1. Introduction

Hovland (1990) demonstrated a close association between carbonate build ups (reef formation) and active hydrocarbon seeps at the seafloor. The seeps provide sources of energy and carbon for bacterial communities. Specifically, authigenic carbonate is a result of the aerobic oxidation of methane, which creates a favorable ecosystem for the precipitation of carbonate hardgrounds (Barens and Goldberg, 1976; Blumenberg et al. 2015). Evidence for such authigenic carbonate cementation has been widely documented, for example, in the North Sea (e.g. Hovland et al., 1987; Hovland, 2002, Schroot et al .,2005), Porcupine Basin (e.g. Hovland et al. 1994) and on the Northwest Shelf of Australia (e.g. O'Brian and Woods, 1995; O'Brian et al., 1999; Cowley and O'Brien,2000; O'Brian et al.2002; Howarth and Alves, 2016; Van Tuyl et al., 2018). The present study uses 3D seismic reflection data to evaluate the spatial and temporal relationships between authigenic carbonate cementation and Pliocene-Recent fault activity on the Laminaria High, Northwest Shelf of Australia.

The Laminaria High lies within the Timor Sea and includes numerous oil and gas accumulations (Smith et al., 1996). These accumulations are typically found within Jurassic reservoirs in the footwalls of Mesozoic, rift-related normal faults (Whittam et al., 1996). However, several traps were found to be dry, or to contain only residual hydrocarbon columns (De Ruig et al., 2000; Abbassi et al., 2015). Complete or partial trap failure was caused by transtensional reactivation of these rift-related normal faults during late Miocene-Pliocene oblique collision between the Australian plate and the SE Asian plate (De Ruig et al., 2000). Gartrell et al. (2006) found that intact traps are

preserved where the fault closure (at the depth of the reservoir) is provided by a structure with < 60 m of post-rift, Miocene-Pliocene throw. Trap failure occurs where the bounding fault segment has a high post-rift throw (> 80 m). Gartrell et al. (2005, 2006) proposed a trap integrity model in which hydrocarbons from breached or partially breached traps migrate upwards towards the seabed along major faults that cut the Cenozoic overburden.

Previous authors working on seismic reflection profiles from the Yampi Shelf (ca. 300 km south-southwest of the Laminaria High) have identified a correlation between high amplitudes on the seabed reflector and features that relate to active hydrocarbon seepage, including carbonate hardgrounds (areas of enhanced cementation on the sea floor) (Rollet et al., 2006). O'Brien et al. (1999) described similar high amplitude anomalies associated with Eocene strata within the shallow subsurface of the Vulcan sub-basin, ca. 150 km southwest of the Laminaria High. These authors integrated interpretations of the seismic reflection profiles with geochemical analyses of samples obtained from boreholes. They proposed that co-migration of hydrocarbons and high-salinity brines through the Cenozoic fault network resulted in isotopically-light carbonate cementation that, in turn, produced high acoustic impedance contrasts with the surrounding, less well-cemented sediments (O'Brien et al., 1999).

Langhi et al. (2010) noted the presence of amplitude anomalies on the seabed reflection and other shallow horizons on the Laminaria High. Here, the distribution of amplitude anomalies is strongly controlled by the Cenozoic fault network and, in some cases, the anomalies are associated with hydrocarbon flags along some of the Cenozoic fault planes (Langhi et al., 2010). These observations, and the similarity with the seismic anomalies reported elsewhere on the Northwest Shelf (e.g. O'Brien et al., 1999; O'Brein and Woods, 2005; Rollet et al., 2006), led Langhi et al. (2010) to

propose that the amplitude anomalies associated with seismic reflectors on the Laminaria High are the result of hydrocarbon seeps and associated authigenic carbonate cementation along fault planes.

In our study, we will test Langhi et al.'s (2010) hypothesis that the seismic anomalies on the seabed reflector and in the shallow subsurface result from authigenic carbonate cementation. Specifically, this study investigates the relationships between the amplitude anomalies, the present-day structure, and active faults that intersected the palaeo-seabed at different times during the deposition of the syn-faulting, Pliocene-Pleistocene succession. We utilise 3D seismic reflection dataset calibrated with exploration wells from the AC/P8 permit area on the Laminaria High to carry out detailed structural mapping and to characterise the distributions of amplitude and RMS (root mean square) anomalies in the shallow subsurface. Our results are consistent with Langhi et al's (2010) hypothesis, and demonstrate the importance of small-, in addition to large-throw faults in controlling hydrocarbon (re-) migration and authigenic carbonate cementation within the Cenozoic overburden on the Laminaria High.

2.2. Background

2.2.1. Tectonic and structural setting:

The Laminaria High is located in the northern part of the Bonaparte Basin, near the southern edge of the Timor Trough (Figure 2.1a). It is bordered by the Nancar and Cartier troughs to the south and by the Flamingo Syncline to the east (Charlton et al.,1991 Smith et al., 1996) (Figure 1b). The Laminaria High appears to lie within a broad "hinge" zone, where the structural trend changes from NE-SW to the south, to ENE-WSW to the north (Figure 2.1b).

The structural history of the Bonaparte Basin is complex and is characterised by three rifting phases during the Palaeozoic–Mesozoic eras (Whittam et al., 1996). 1) A NW–SE rifting phase associated with faulting that initiated during the Late Cambrian, and subsequent reactivation during the Late Devonian to Early Carboniferous. 2) A Neotethys rifting phase, which is responsible for the thin crust of the Bonaparte Basin and took place during the Late Carboniferous to the Early Permian. 3) A Late Jurassic-Early Cretaceous rifting phase, caused by the breakup of Gondwana. During the Cenozoic, the geological evolution of the Laminaria High has been dominated by the ongoing collision between the Australian plate and the Southeast Asian plate, which happened in two stages. The first stage started ca. 8 Ma during the late Miocene. The second stage began during the Pliocene, about 3-4 Ma, with deformation accommodated by reactivation of pre-existing faults. Fault activity decreased during the Pleistocene (Whittam et al.,1996; Baillie et al., 1994; Keep et al., 2002).

The structural trend of the Laminaria High is oriented E-W to ENE-WSW. The direction of the present-day maximum horizontal stress (S_{Hmax}) is NNE-SSW, sub-perpendicular to the regional fault strike (de Ruig et al., 2000) (Figure 2.1a). For the purposes of this study, the key structures that accommodated Mesozoic to Neogene extension on the Laminaria High are: 1) a set of ENE-WSW striking, Jurassic-Cretaceous horst and graben structures; and 2) a set of mainly ENE-WSW striking, Neogene normal faults that initiated above the reactivated Mesozoic structures (Shuster et al., 1998; Gartell et al., 2006; Langhi et al., 2010) (Figure 2.2a). A deeper set of E-W striking, Permian horsts underlies the area (Langhi et al., 2008), but are too deep to be imaged within our 3D seismic volume, and are not considered further here.

2.2.2. Stratigraphy

The stratigraphy of the Laminaria High is described in detail by Smith et al. (1996). The hydrocarbon reservoir section is within the Laminaria Formation, which is Callovian to Oxfordian in age. The Laminaria Formation consists of massive sandstone with minor interbedded claystone. Open marine shales of the Frigate (Oxfordian–Kimmeridgian), Flamingo (Tithonian-Berriasian) and Echuca Shoals (Valanginian-Barremian) formations represent the seal through which any deep-sourced hydrocarbons must have migrated to reach the shallow subsurface. The Lower and Upper Cretaceous are represented by the Bathurst Island Group, above which the lithology changes from dominantly clastic sequences into the carbonate-dominated sequence represented by the Johnson, Hibernia, Prion and Cartier formations (Palaeocene to Oligocene). The Miocene to Pleistocene Oliver and Barracouta formations include calcarenites and calcilutites, which are the shallowest sedimentary rocks within the study area, and represent an extensive cover of prograding shelf carbonate deposits (Smith et al., 1996) (Figure 2.1c).

2.2.3. Hydrocarbon charge history

The main source rocks in the Laminaria High include shales of the Plover, Laminaria, Frigate and Flamingo formations (Smith et al., 1996; George et al., 2004). The initial charge of oil and gas occurred during the Late Jurassic to Early Cretaceous, followed by the main phase of oil charge during the Middle to Late Eocene. A later phase of oil and gas charge is suggested to have occurred from the Miocene onward (Wittham et al., 1996). Most of the drilled traps show evidence of residual oil, confirmed by geochemical and petrophysical analysis of core samples (Abbassi et al., 2015). This

observation is consistent with the traps having been breached, and the hydrocarbons having leaked.

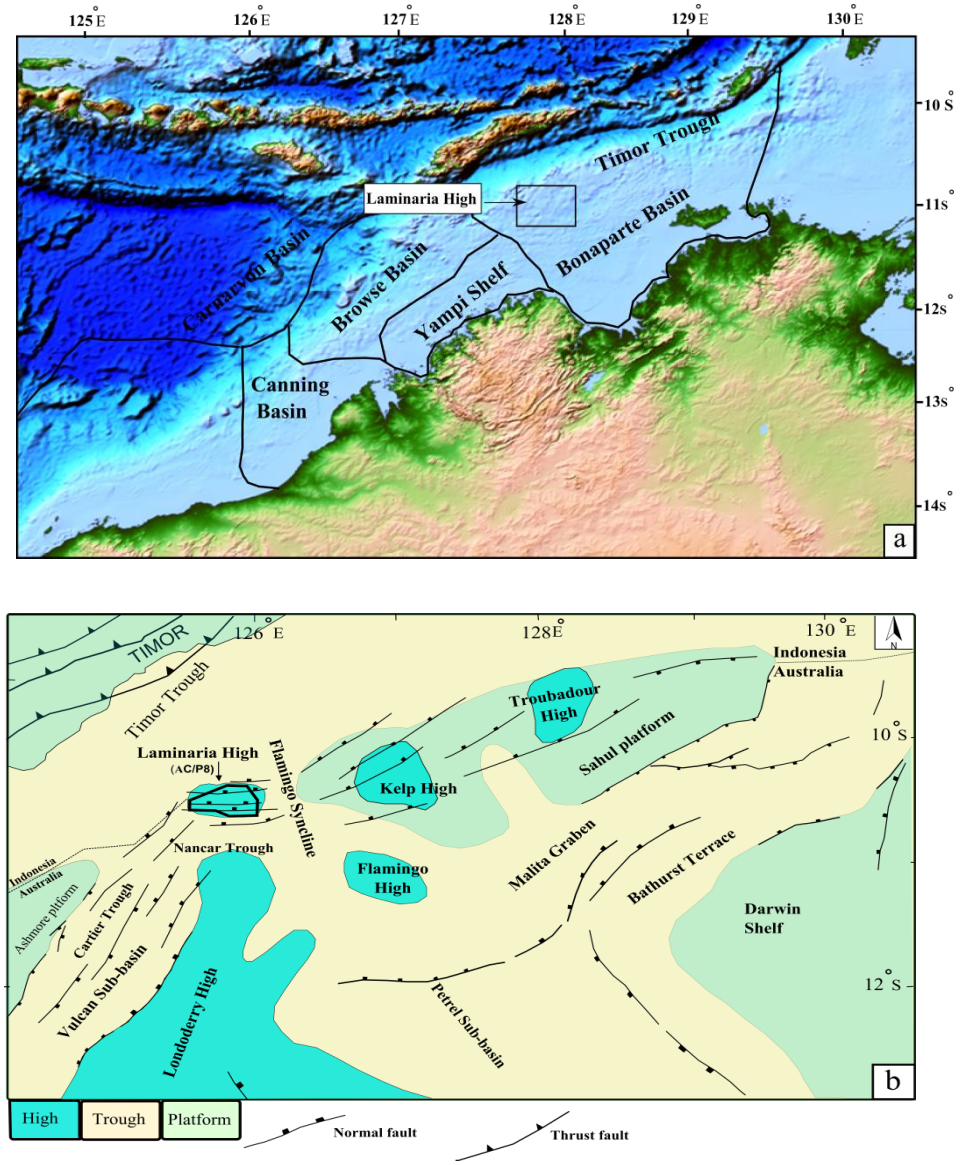

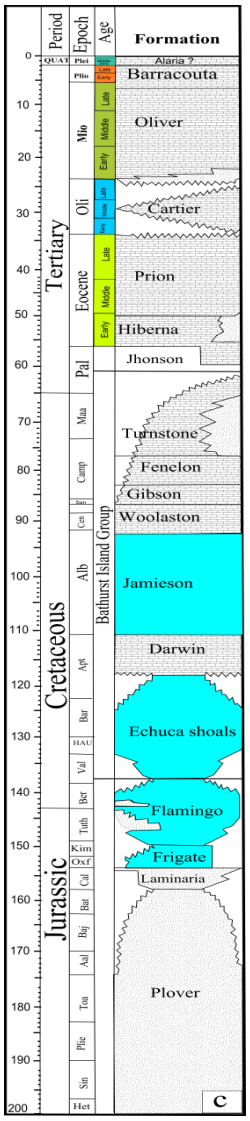

Figure 2.1. (a) Topographic and bathymetric map of the main basins on the Northwest Shelf of Australia. Elevation and depth data provided by Geoscience Australia (2018). **(b)** Geological setting and Jurassic structure map of northwestern Bonaparte Basin, modified from Long and Imber (2012). **(c)** Generalized stratigraphic column for the Laminaria High (modified from De Ruig et al. 2000).

2.3. Data and methodology

2.3.1. Data

The dataset used in this study is a three-dimensional (3D), time migrated seismic volume supplied by Geoscience Australia. These data were acquired in 1995 within the AC/P8 permit block over the Laminaria High, which has an area of approximately 760 km^2 (Figures 2.1a and 2.1b). The data were shot in E-W direction; the bin dimensions are 12.5 m (inline) × 12.33 m (crossline). A series of seismic processing steps were applied on this volume which includes: true amplitude recovery, FK filter, deconvolution and DMO (dip moveout) correction. Velocity analysis (NMO) was applied to the pre-stack data, which were then CDP stacked followed by the 3D post-stack time migration. An example of a north-south section extracted from the volume is shown in Figure 2.2. The data as provided by Geoscience Australia have a bias of about -6; the positive impedance seabed reflection shows a zero-phase wavelet with a larger negative central lobe that confirms the polarity of data is negative (Langhi et a.,2011). In our interpretation, we used this volume to map seismic reflectors (Horizons H1-H13) and faults, the regional dip of the seabed and sediment thickness (Brown, 2011). Depth conversion was not applied to the whole volume as a reliable velocity model was not available, but given the consistency of the stratigraphy across the volume, we believe that depth conversion would have minimal effect on fault and horizon geometries (Long and Imber, 2012). Check shots from well Alaria-1 (Figures 2.2a and b) are used to calibrate the seismic horizons to the geological formations of the study area.

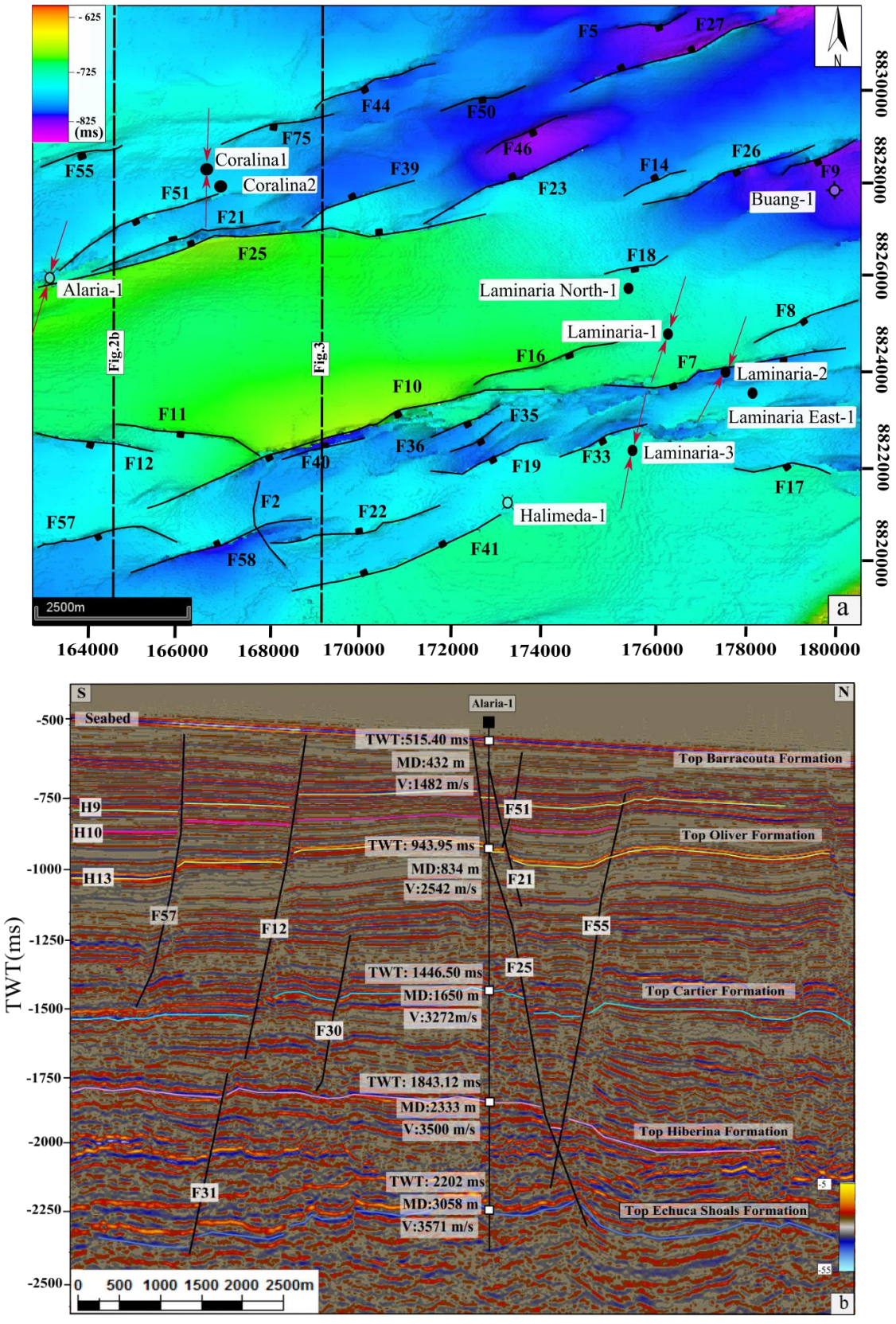

Figure 2.2 (a) Two-way time (TWT) structural map of horizon H9 showing the main structural elements and well locations. The locations of the seismic sections shown in Fig. 2 (a) and in Fig. 3 are indicated. Red arrows are the direction of the maximum horizontal stress (SHmax) and are taken from De Ruig et al. (2000). Note that the cartographic reference system is Universal Transverse Mercator (UTM) Zone 52S. **(b)** Seismic profile (cross line no. 2545) showing the interpreted horizons and faults. Note formation tops and check shots are from well Alaria-1. Note that horizons in 2.2b are drawn on top of the actual auto-tracked horizons

2.3.2. Methodology

2.3.2.1 Fault interpretation

Faults were manually picked in the 3D seismic volume on every 10th cross-line, and correlated on time slices to obtain an accurate fault framework model. The locations of faults were then compared with the locations of amplitude anomalies on the seabed and other interpreted horizons, in order to test for potential structural control on the spatial distribution and shape of the amplitude anomalies. Figure 2.3 shows the main geometry of the faults in the study area.

According to Childs et al. (2003), throw contours drawn on a strike projection of a growth fault will be approximately vertical within the pre-faulting sequence, and approximately horizontal within the syn-faulting sequence. This contour pattern arises because the down-dip throw gradients are high relative to the lateral gradients within the syn-faulting succession. Therefore, the boundary between the sub-vertical and the sub-horizontal contours separates the pre- and syn-faulting regions of a fault surface (Childs et al., 2003). Horizon surfaces and faults were exported from Petrel® to Trap Tester®. We combine each fault surface with the interpreted horizons to generate fault polygons defined by the hanging-wall and footwall cut-off lines along each fault surface. Then, we use functionality within Trap Tester® to compute the throw attribute for each fault and, finally, generate throw contour maps for each fault plane.

2.3.2.2. Horizon interpretation

In this study, we focus on four key horizons in the shallow subsurface: the seabed, horizon H9, horizon H10 and horizon H13 (Figure 2.2b), which are characterised by bright, sub-parallel and laterally continuous seismic reflectors. (Note: for the rest of

the paper we refer to all of the horizons using the letter "H" followed by a number (e.g. H9 for horizon H9), and the faults (see below) using the letter "F" followed by a number (e.g. F10 for fault F10). The horizons were interpreted manually every 10th to 15th cross-line and every 25th in-line. Manual interpretation was followed by 3D autotracking to infill the interpreted horizons. Additionally, a further 10 horizons were interpreted in the subsurface in order to constrain the throw distributions along active faults (section 2.3.2.2). We extract the amplitude (i.e. the absolute amplitude of the tracked seismic reflection event) along the seabed reflection and along subsurface horizons H9, H10 and H13 in order to investigate spatial variations in seismic amplitude. Such variations imply changes in the velocity and/or density of the sediments, and provide a qualitative indication of changes in lithology and fluid content.

2.3.2.3. Seismic attribute analysis

We extract the root mean square (RMS) amplitudes along the seabed reflector and along the key horizon surfaces (H9, H10 and H13) within a window that extends 20 ms above and below the key horizons. The RMS amplitude attribute is useful to highlight isolated amplitude anomalies and can be used to track changes in lithology and/or fluid content (e.g. Chen and Sidney, 1997). For example, Simm and Bacon (2014) showed the consistency between an RMS amplitude anomaly associated with a hydrocarbon flat spot, and the structure contours associated with a 4-way dip closure. We use a similar approach in our study. Specifically, the migration of buoyant fluids (e.g. hydrocarbons) is controlled by the local and regional subsurface structure: the flow direction is towards structural highs, i.e. up-dip, perpendicular to the time (or depth) structure contours. In addition, fluid contacts are controlled by local spill points, which are again determined by the structure contours. We therefore investigate the

relationship between the two-way time (TWT) structure contours and the amplitude and RMS anomalies on key horizons within the Cenozoic succession.

We also utilised the edge detection and spectral decomposition seismic attributes (e.g. Brown, 2011). These attributes were extracted along selected horizon surfaces to highlight subtle structural and stratigraphical features. The edge detection attribute is based on the calculation of the local dip for the seismic event (Luo et al., 1996). This attribute identifies discrete edges on a horizon surface, which might be related to the presence of minor (small-throw) faults and increases the confidence in our structural interpretation. The spectral decomposition (SD) attribute helps to delineate subtle features at a specific frequency (Partyka et al., 1999; Othman et al., 2016). For example, when hydrocarbons replace water in porous sediments it attenuates the frequency response of the seismic reflector. Langhi et al. (2010) used an SD map of the seabed reflector to support their interpretation of the seismic anomalies on the Laminaria High. Below, we compare the SD attribute extracted along the seabed within our seismic volume with Langhi et al's (2010) SD map.

2.4. Results

2.4.1. Seabed

2.4.1.1. Amplitude

The amplitude map is characterised by two distinct families of anomalies. The highest amplitude anomalies are elongated in an ENE-WSW direction and are developed adjacent to the ENE-WSW striking faults that intersect the seabed reflector (Figure 2.4). The second group of anomalies is somewhat dimmer. These anomalies are elongated in a NW-SE direction, approximately perpendicular to the TWT structure contours, and appear to be cross-cut by the fault traces (Figure 2.4 – arrow).

The highest amplitude anomaly on the seabed map (< 7 km in length) is associated with F10 and ranges from -27 to -33 (Figure 2.4). The anomaly is located on the hanging-wall side of F10 and is elongated parallel to the TWT structure contours of the seabed. In the vicinity of F10, the seabed reflector dips towards the northwest; thus the hanging-wall side of the fault lies up-dip of the footwall side (Figure 2.3).

Smaller seabed amplitude anomalies (< 2.5 km in length; Figure 4) also appear along F11 and F12, within the amplitude range of -25 to -30, all on the hanging-wall side of these faults. Fault F7 is associated with an amplitude anomaly ranging between -25 and -27, in the vicinity of the Laminaria-1, 2 and the Laminaria East wells (which discovered oil). Moderate seabed amplitude anomalies exist along a series of small, ENE-WSW striking faults F19, F33, F35 and F36. These faults intersect the seabed in the vicinity of the Halimeda-1 well (dry/ off structure) (Figure 2.4). The northern part of the seabed amplitude map shows no obvious seismic anomalies along faults F25,

F23 and F39 in the vicinity of the Alaria-1 well (which was dry/off-structure), or the Coralina-1 and 2 wells (which discovered oil) (Figure 2.4).

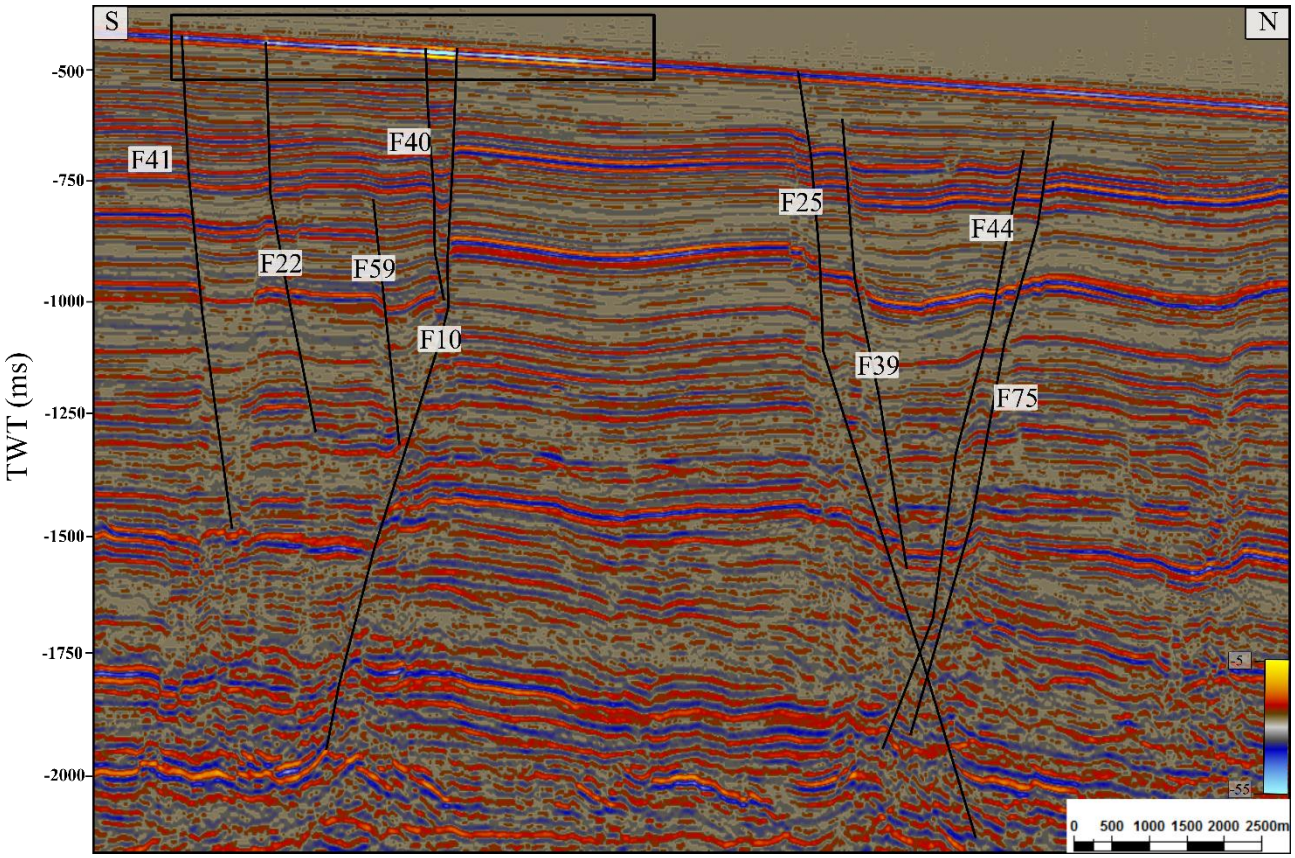

Figure 2.3. Seismic profile (cross line no. 2325) showing the geometry of the main faults in the study area. Note the amplitude anomaly at the seabed associated with fault F10 (box). Location of the seismic profile is shown in Figures 2.2a and 2.4.

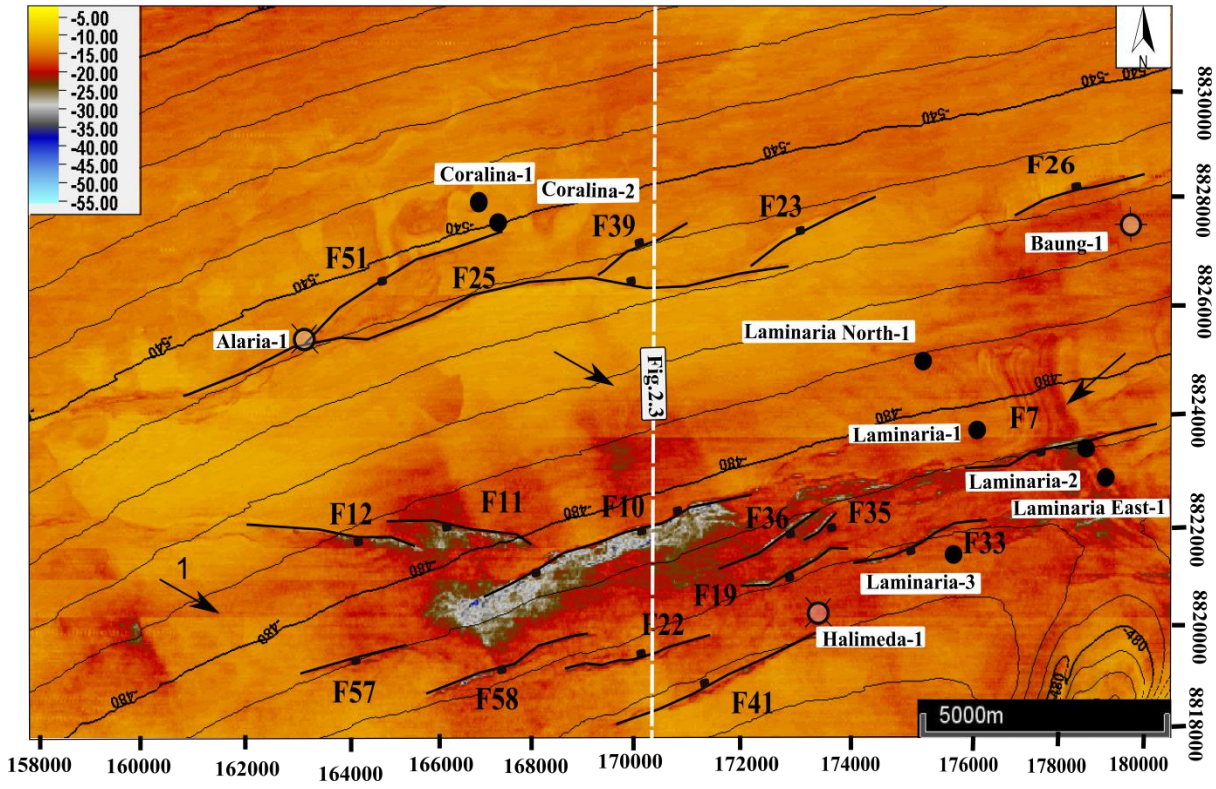

Figure 2.4. Amplitude map for the seabed. The two-way time structure contours are shown. The map shows high negative amplitude anomalies associated with sets of normal faults F7, F10, F11, F12, F19, F35 and F36 in the southern part of the study area. Note the lack of amplitude anomaly associated with fault F25 in the northern part of the area. Well locations are presented on this map (off structure/breached wells (dry) ☼ , oil discovery well ●,breached well/dry ☼). East-west striping in the amplitude map is a footprint of the original E-W acquisition geometry as shown by arrow1. The origin of the low amplitude anomalies to the north of F25 is unknown.

2.4.1.2. RMS amplitudes

The RMS amplitude map highlights similar features (Figure 2.5). Again, the brightest anomalies occur within the hanging-wall of F10, with smaller RMS anomalies being associated with F7, F11, F12, F19, F33, F35 and F36. The second family of anomalies identified on the amplitude map (section 2.4.1.1) is slightly less prominent on the RMS amplitude map (Figure 2.5).

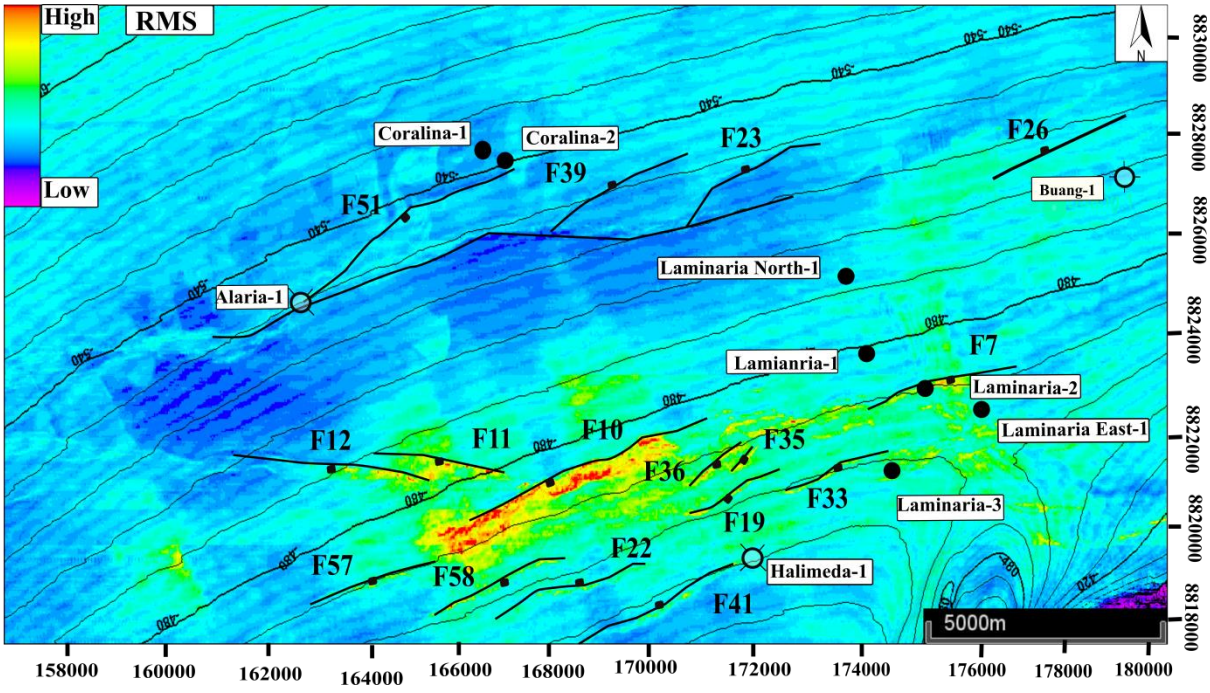

Figure 2.5. RMS amplitude map for the seabed showing a similar distribution of anomalies as shown in Figure 2.4. The two-way time structure contours for this horizon are shown. The principal RMS amplitude anomalies are associated with sets of normal faults F7, F10, F11, F12, F19, F35 and F36 in the southern part of the study area.

2.4.1.3. Spectral decomposition attribute

Three frequency volumes (30Hz, 45Hz, and 80Hz) were generated using the spectral decomposition (SD) attribute. SD maps for the seabed were extracted from each volume. The amplitude map obtained from the 30Hz SD volume (Figure 2.6a) shows very similar features to those observed in the amplitude and RMS amplitude maps (Figures 2.4 and 2.5), although the SD attribute enhances the appearance of the bright spots compared with the amplitude map (Figure 2.4). For example, the SD map shows the anomaly along F58 more clearly compared to the equivalent amplitude anomaly in Figure 2.4.

At the seabed, we note that our SD results are different from the previous study reported by Langhi et al. (2010). The SD map from our survey shows that the high

amplitude anomalies are only associated with the faults in the southern part of the survey (Figure 2.6a). In contrast, the Langhi et al. (2010) study shows high amplitude anomalies along their "F1" array (Langhi et al.'s fault numbers) (Figure 2.6b) near well Alaria-1. Furthermore, amplitude anomalies exist along F11 and F12 in our SD map (Figure 2.4a), but there are no corresponding anomalies along "F4" (Langhi et al's fault numbers) in Langhi's SD map (Figure 4b). We suggest a possible reason for these differences in results is that the Langhi et al. (2010) study used a merged seismic volume that is composed of five different seismic surveys. It is possibly that matching filters, necessary to equalise the amplitude and frequency content of the input surveys, may have created artefacts. In our work, we used only one seismic survey that covers our study area. Therefore, we have not applied any additional frequency manipulation other than that applied to the original seismic volume as supplied by Geoscience Australia.

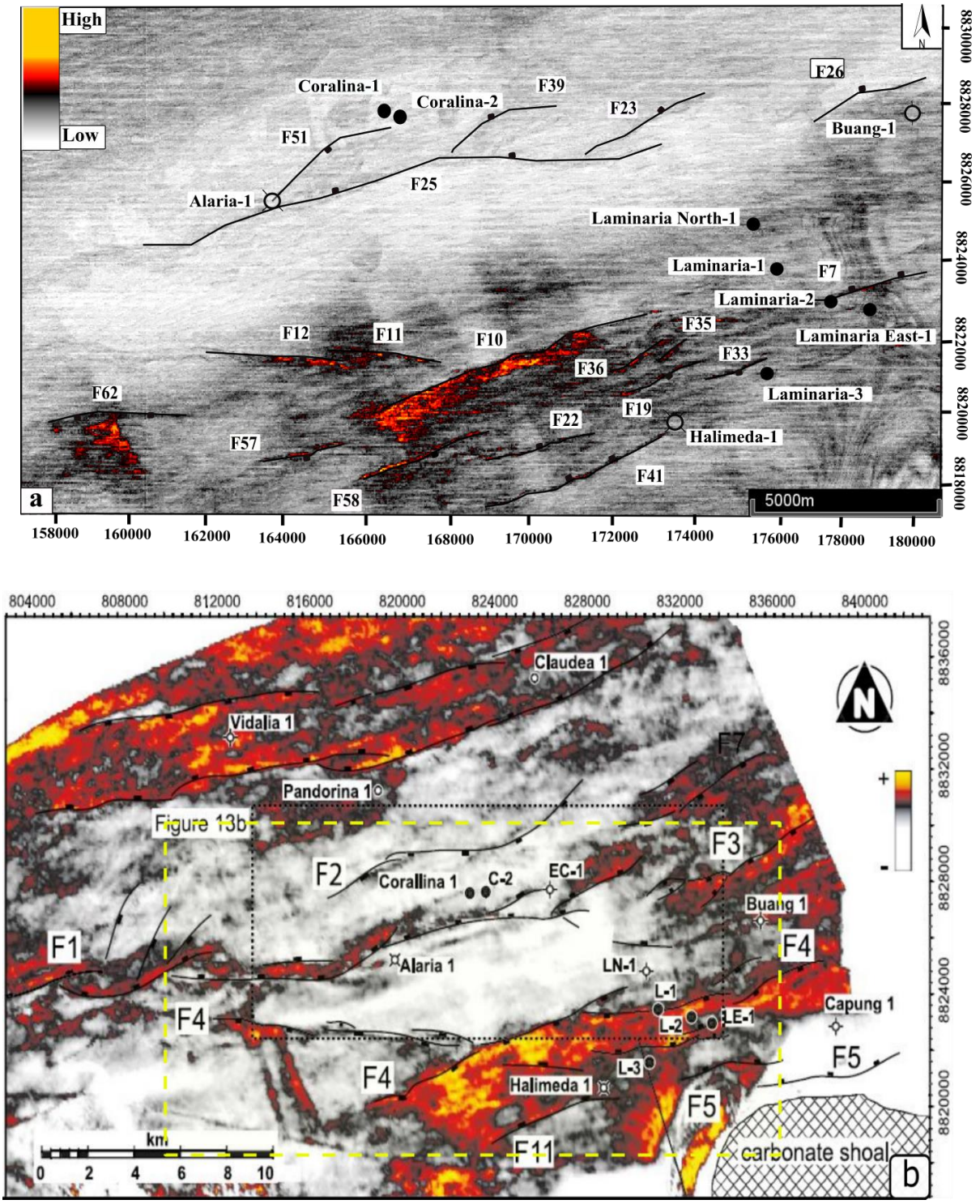

Figure 2.6. (a) Spectral decomposition map at 30 Hz frequency extracted from the seabed showing the fault traces and well locations. SD anomalies, indicated by the hot colours, are associated with the major faults in the southern part of the study area. **(b)** Spectral decomposition map at 30 Hz for the seabed (from Langhi et al. (2010) authorised by the AAPG Journal). This map shows a different distribution of SD anomalies compared to **(a)**. The yellow dashed box is the area covered by Figure 2.6a. Note the difference in x axis coordinates, Langhi et al. (2010) used a different Universal Transverse Mercator (UTM) projection, and in this study the 52 s UTM zone was used. Also note the fault numbering schemes are different between the two plots.

2.4.2. Horizon H9

2.4.2.1. Amplitude

Horizon H9 lies within the Barracouta Formation (Figure 2.1c). The amplitude map (Figure 2.7a) shows that amplitude anomalies exist in the footwalls of F7, F10, and F11 (in contrast to those on the seabed, which exist on the hanging-walls along the same faults). The amplitude anomaly associated with F10 (maximum throw of 106 ms on this horizon) ranges from -12 to -14 and is elongated in a NNW-SSE direction, discordant to the local TWT structure contours. Furthermore, the brightest parts of this anomaly do not coincide precisely with the footwall crest (Figures 2.7a and 2.1b-arrow).

The amplitude anomaly along F12 becomes dim and exists only at the eastern tip of the fault. Here, the amplitude anomaly ranges between -12 and -14. An amplitude anomaly exists along F11 and is connected with the anomaly that appears at the eastern tip of F12. F7 is also associated with an amplitude anomaly, which ranges from -12 to -13, and lies adjacent to the point of maximum throw (65 ms) in the hanging-wall of this fault (Figure 2.7a). This anomaly is elongated in an N-S direction and is again discordant to the local TWT structure contours.

Fault F25 has a maximum throw of 108 ms along H9, but the amplitude anomaly is much smaller in extent and less bright compared to the main anomaly along F10. In contrast to the seabed, there are significant anomalies along fault traces F44 and F75, which range from -12 to -14. The shape of these anomalies is complex; the brightest anomaly to the north of F44 is elongated in a NNE-SSW direction and is discordant to the local TWT structure contours (Figure 2.7a). In contrast, the slightly less distinct

anomaly in the footwall of F75, at least locally, follows the structure contours (Figure 2.7a).

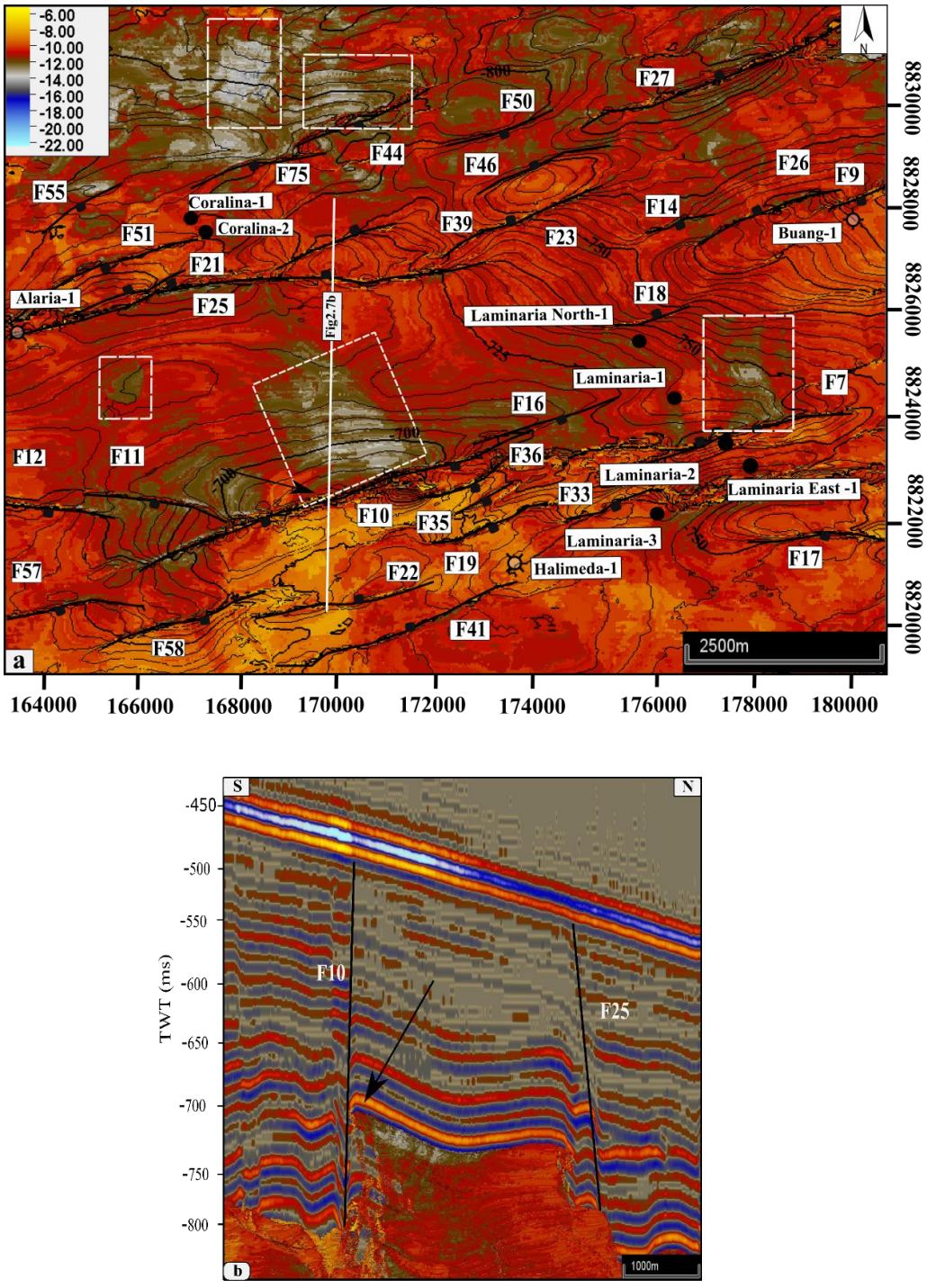

Figure 2.7. (a) Amplitude map for H9, overlain by the two-way time structural contours for this horizon. The map shows high negative amplitude anomalies along faults F10, F11, F12 and F7 in the southern part of the study area, and along faults F44 and F75 in the northern part. The white boxes indicate places were the strike of the TWT contour lines are discordant to the trends of the amplitude anomalies. **(b)** Seismic profile (cross line) orthogonal to F10 and H9. This section is displayed with 2 times vertical exaggeration. This anomaly becomes less bright near the highest point of the footwall of F10 (arrowed). Location of this section is shown in Figure2.7a.

2.4.2.2. RMS amplitudes

The RMS amplitude map highlights similar features (Figure 2.8). Two RMS amplitude anomalies corresponding to the NNW-SSE and N-S trending features observed in the amplitude map (section 2.4.2.1) can be seen. Again, these features are discordant to the local TWT structure contours. There is also a region characterised by low RMS amplitudes (blue colours) within the hanging-wall of F10 that continues towards the southern edge of the study area and appears to be cross-cut by faults F22 and F41.

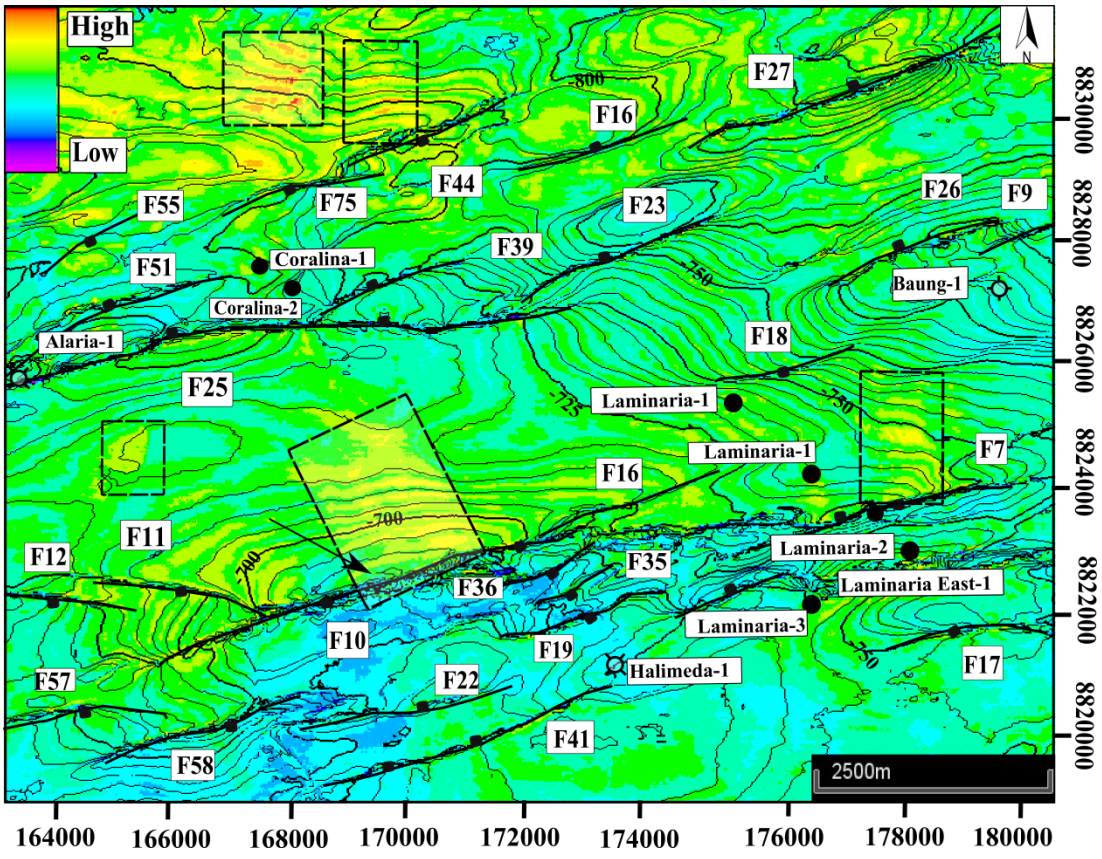

Figure 2.8. RMS amplitude map with two-way time structure contours for H9. The map shows high RMS amplitude anomalies associated with faults F7, F10 and F11 in the southern part of the study area and with faults F44 and F75 in the northern part of the study area.

2.4.3. Horizon H10

2.4.3.1. Amplitude and edge detection attribute

It was not possible to map H10 with confidence across the entire seismic survey area; we therefore focussed on the main region that shows the amplitude anomalies. Here, anomalies exist in both the footwall and hanging-wall of F10. In the footwall, the principal anomaly is elongated in a NW-SE direction and is discordant to the TWT structure contours.

The brightest anomaly occurs in the hanging-wall of F10 between two small-throw, minor faults F1 and F2 with maximum throws of approximately 15ms. These faults strike perpendicular to faults F10 (Figure 2.9a). A further anomaly occurs adjacent to the minor, NW-SE striking fault F3 (Figure 2.9a). F1, F2 and F3 are below the seismic resolution. Therefore, we use the edge detection filter on the seismic data. Along H10, this filter was able to highlight the major faults and structures and also many of the minor faults (Figure 2.9b), and shows the relationship between them. It is clear how the small throw faults (F1, F2 and F3) intersect the major faults (F22, F41,F57 and F58) at branch points (the points of intersection between two faults) on this horizon (Figure 2.9b).

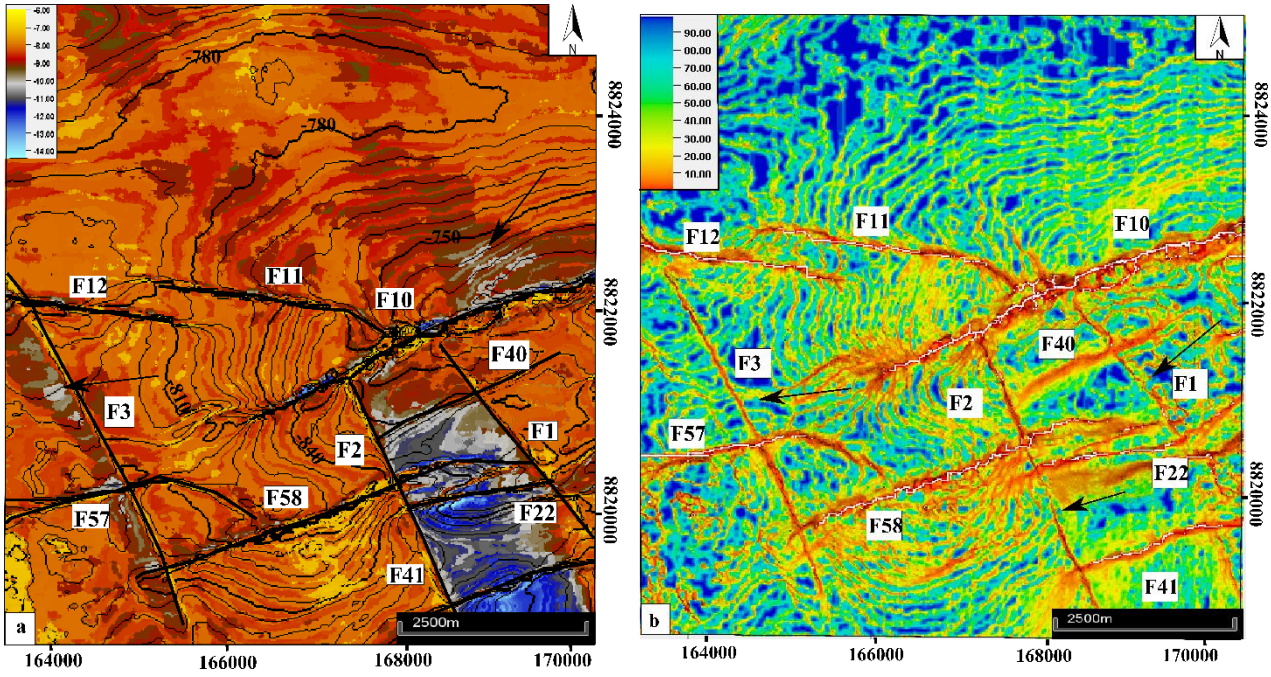

Figure 2.9. (a) Amplitude extraction map of H10, showing the two-way time structure contours. Note the high negative amplitude anomalies along F10, F22, F41 and F58 (blue and grey colours in the hanging walls of these faults). The distribution of these amplitude anomalies is controlled by three small-throw faults (F1, F2 and F3) that are perpendicular to F57, F58 and F22 respectively. **(b)** Edge detection map of H10 showing the three sets of minor faults, F1, F2 and F3, perpendicular to the major faults F10, F22, F41, F57 and F58 respectively. These minor faults are highlighted by black arrows.

2.4.3.2. RMS amplitudes

Anomalies shown on the RMS amplitude map (Figure 2.10) for H10 display similar trends and locations as the amplitude anomalies described above. The map shows the NW-SE elongation of the anomaly associated with F3, and the discordance between the anomaly and the local TWT structure contours (Figure 2.10-arrow). The RMS amplitude map again highlights the importance of the minor, small-throw faults in controlling the distribution of anomalies on H10.

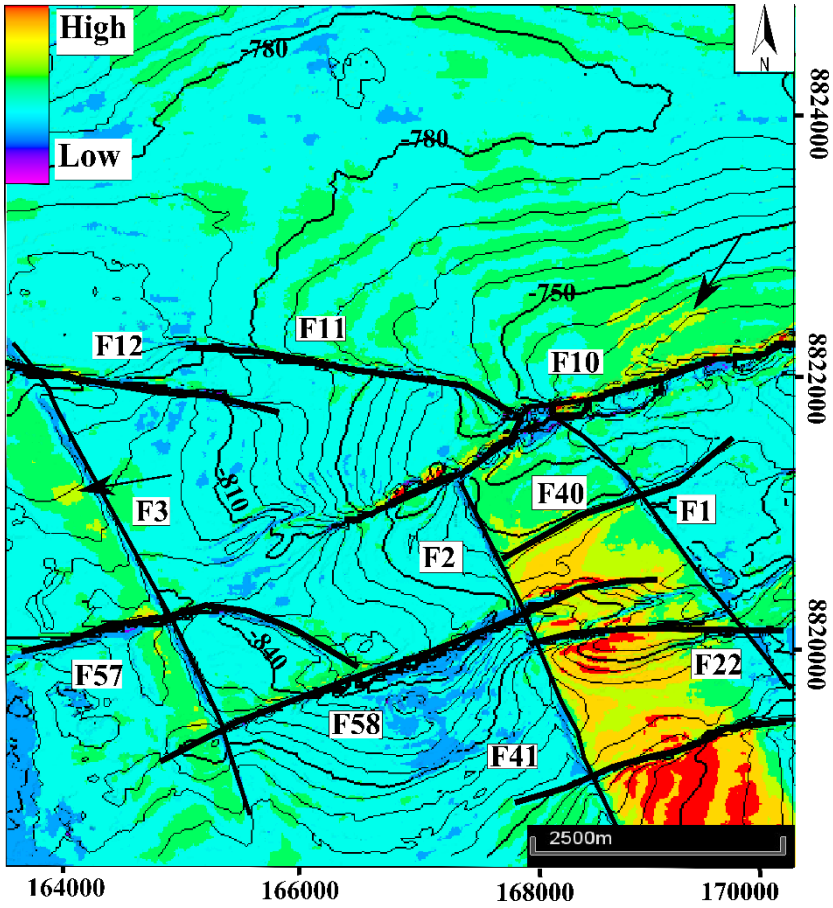

Figure 2.10. RMS amplitude map of H10 showing high RMS amplitude anomalies associated with faults F1, F2 and F3 in the NW-SE direction and with fault F10 in the E-W direction. Note the discordance between the anomalies along F3 and F10 and the local TWT structure contours as shown by arrows.

2.4.4. Horizon H13

2.4.4.1. Amplitude

The distribution of amplitude anomalies on along H13 is different to those observed on H9 and H10. For example, the anomaly associated with F10 is indistinct on this horizon (Figure 2.11). There is another set of anomalies that are elongated in N-S or NE-SW directions and appear to be cut by the fault traces. Overall, the amplitude map for H13 shows a change from predominantly orange colours in the west, to predominantly yellow colours in the east; however, the cause is unknown.

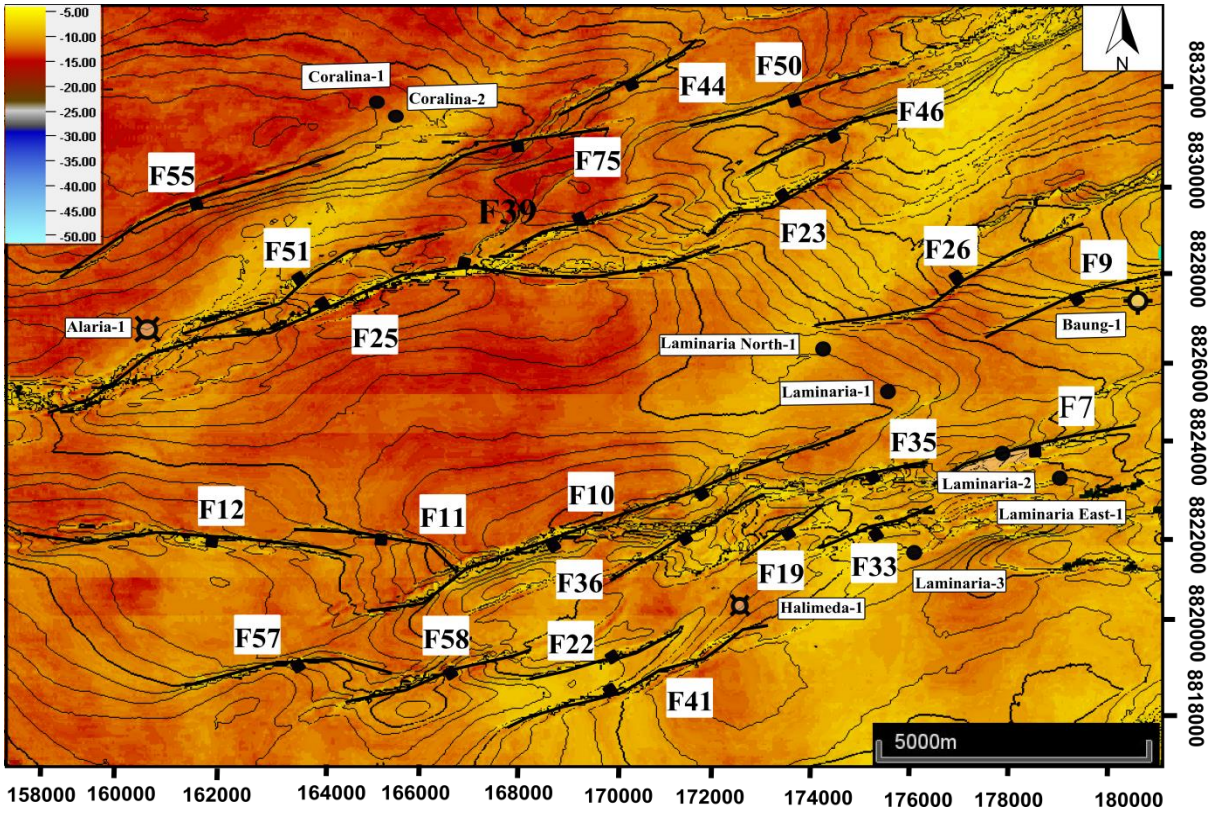

Figure 2.11. Amplitude extraction map for H13 showing the well locations and two-way time structure contours. The amplitude anomalies on this map have different distributions and are less distinctive compared to the amplitude anomalies on the shallower horizons.

2.4.4.2. RMS amplitudes

The RMS amplitude map highlights the N-S and NE-SW trending anomalies (Figure 2.12). These anomalies are oblique to the strike of the major faults and to the TWT structure contours, and appear to be cross-cut by the fault traces on H13.

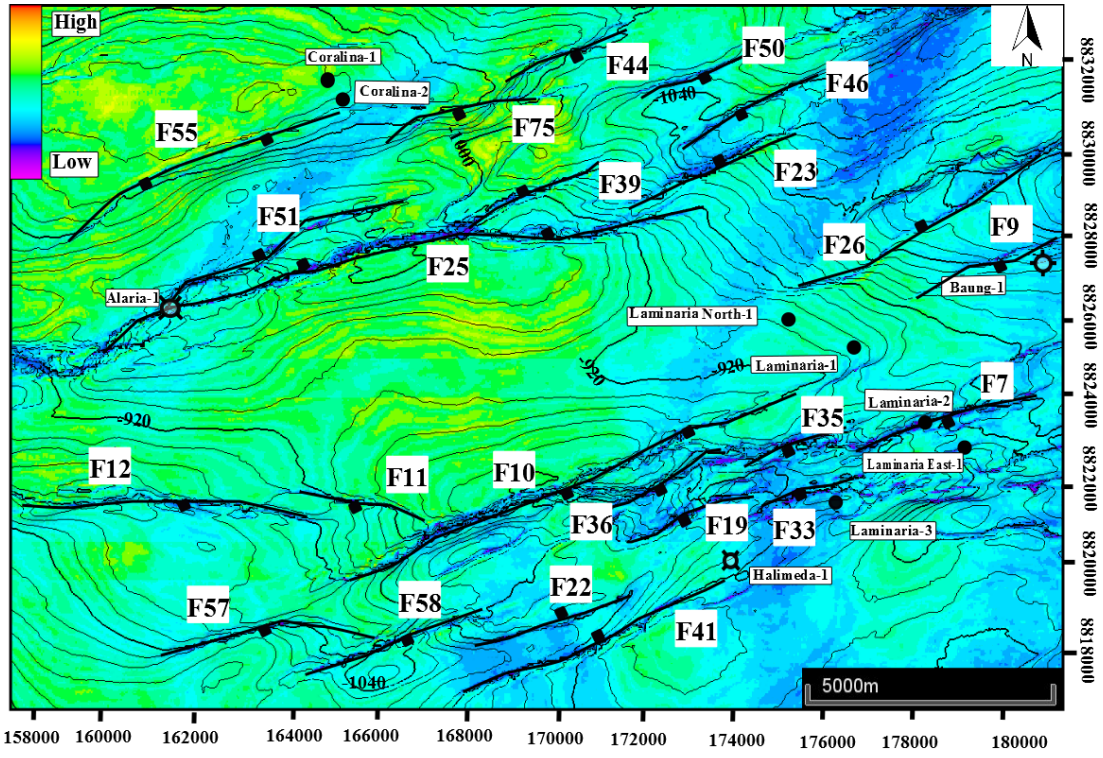

Figure 2.12. RMS amplitude map of H13 showing the two-way time structure contours; amplitude anomalies on this map have different distributions and are less distinctive to the amplitudes anomalies on the shallower horizons.

2.4.5. Timing and duration of fault activity

Gartrell et al. (2006) suggested that breached or partially-breached hydrocarbon traps at reservoir level (Laminaria Formation) develop where the reservoir is cut, or is bounded by vertically continuous, long-lived faults that link the reservoir with discharge sites at the seabed. Therefore, we might predict that amplitude anomalies are most likely to occur along faults that were active for the longest durations, and which cut the present-day seabed.

Figures 2.4 and 2.7 show that the majority of faults that cut H9 are also visible on the seabed amplitude and RMS anomaly maps. The exceptions are F44, F55 and F75 in Figure 2.7, which do not have a clear expression on the seabed (Figure 2.4). This

observation suggests that the majority of faults within our study area – including many of those that are associated with amplitude anomalies on the deeper horizons – are active at the present day.

We now constrain the *onset* of fault activity using the methodology described by Childs et al. (2003) (see section 2.3.2.2). For the purposes of this study, we need to identify the base of the syn-faulting sequence for different faults within the study area. The base of the syn-faulting sequence is defined as the oldest stratigraphic sediment that was deposited at the start of the period of activity (displacement) along an individual fault plane. The differences in fault throw measured on each successive syn-faulting horizon is a function of fault growth and sedimentation rate, provided sedimentation rates exceed fault throw rates (i.e. a growth fault; Childs et al. 1993, 2003). There is no evidence for erosion of footwall crests at the level of H9 or older horizons, nor is there evidence for significant channel development at shallower levels. We therefore assume that the condition that fault scarps were preserved by rapid burial has been met.

Figures 2.13 a, b and c show the throw-contoured strike projection maps of faults F11, F12 and F22, and the fault polygons along each intersecting horizon. These figures show that the boundary between the sub-vertical and sub-horizontal throw contours on each fault coincides approximately with horizon H9. Thus, H9 represents the base of the syn-faulting sequence. In other words, these faults became active at approximately the same time as the deposition of sediments associated with the H9 reflector which we infer formed the sea-floor at that time. All these faults are visible on the seabed amplitude map (Figure 2.4), which indicates that they remain active at the present day.

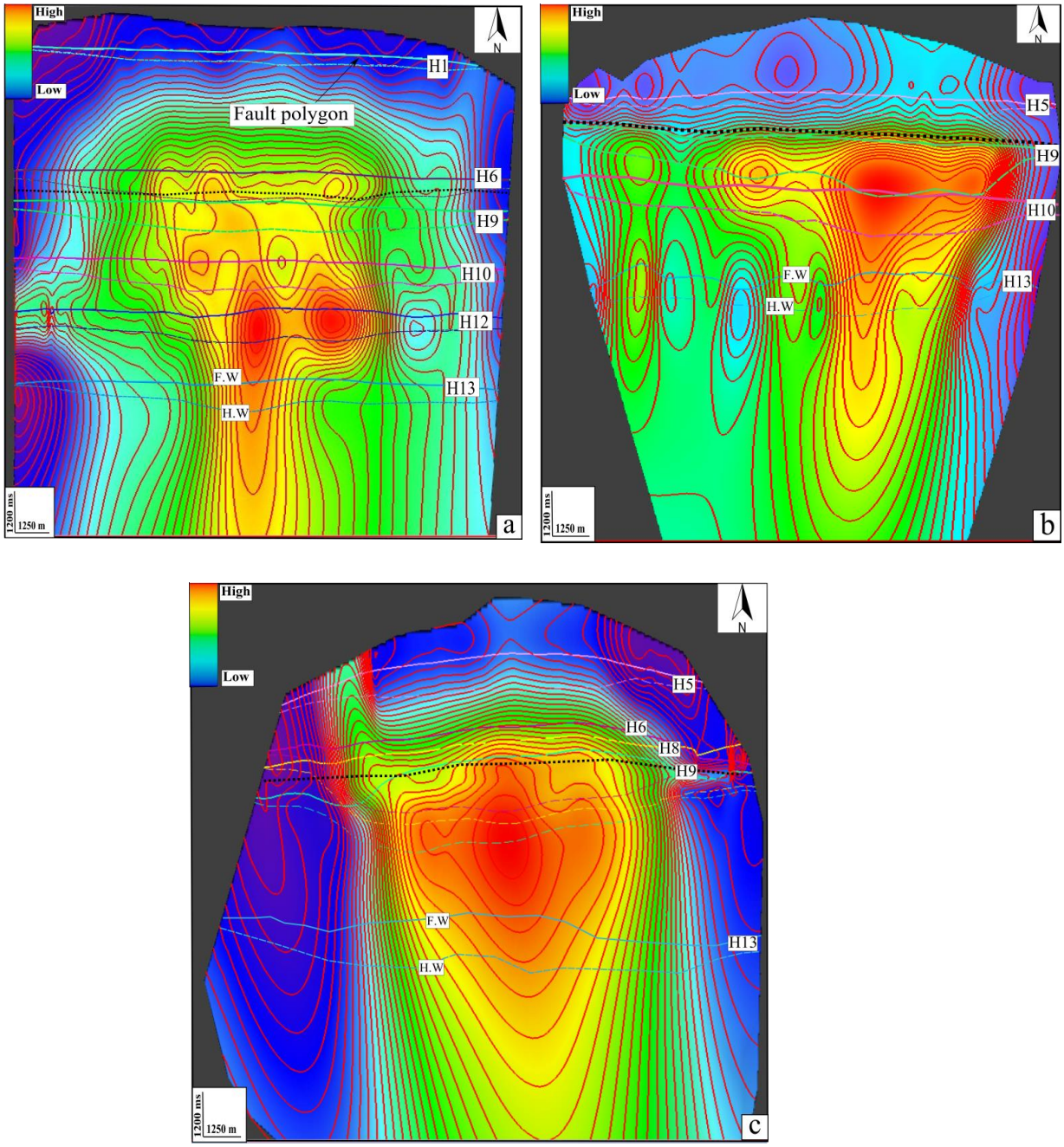

Figure 2.13 (a, b, and c). Throw-contoured strike projection maps of faults F11, F12 and F22, showing the intersections of each mapped horizon in the footwall and hanging wall of each fault. The black dotted line indicates the boundary between the pre- and syn-faulting sequences. Note that H9 is located approximately within this boundary were the contour lines change from sub-vertical to sub-horizontal.

2.5. Discussion

2.5.1 The distribution of amplitude and RMS anomalies on syn- and pre-faulting horizons

The results show that the seabed reflector and H9 – which represent the present-day seafloor and the palaeo-seafloor at the onset of Cenozoic faulting, respectively, are characterised by prominent amplitude and RMS amplitude anomalies that are associated with the mainly ENE-WSW striking faults. This observation is consistent with Langhi et al's (2010) finding (using a different seismic volume) that the reflectivity distribution of the near-seabed reflectors is controlled by the structural network.

In contrast, the amplitude and RMS amplitude anomalies on the oldest mapped pre-faulting horizon (H13) are oblique to the overall fault strike and appear to be cross-cut by the fault traces. These observations suggest that the anomalies on H13 are likely to be caused by features that pre-date faulting, and are not related to structural or tectonic processes. H10 is the shallowest horizon mapped within the pre-faulting succession and shows an association between the amplitude and RMS anomalies and the minor, NW-SE striking faults (F1, F2 and F3).

Overall, the results indicate that the distribution of amplitude anomalies on the two syn-faulting horizons (seabed and H9) is significantly different from that on the two pre-faulting horizons (H10 and H13). An important finding is that evidence for the structural control on the reflectivity distribution identified by Langhi et al. (2010) is most obvious on horizons that were deposited synchronous with activity on the ENE-WSW striking fault network.

2.5.2 Structurally-controlled seepage and cementation at the seabed and palaeo-seabed

The principal anomaly on the seabed reflector occurs on the hanging-wall side of F10 and is elongated parallel to the TWT structure contours (Figure 2.4). The trace of F10 can be observed on the seabed amplitude map; however, F10 has no significant bathymetric expression on the sea floor (Figure 2.3). As a result, the seabed reflector in the hanging-wall of F10 lies *up*-dip of the fault trace. Similar geometries are associated with the smaller anomalies observed along F11 and F12 (Figure 2.4). A possible explanation is that buoyant fluids migrate upward along F10 towards the seabed. The fault cuts permeable strata immediately at and below the seabed. Seepage, fluid migration and associated authigenic carbonate cementation on the seafloor (e.g. Langhi et al., 2010) and within these permeable strata is then controlled by the regional dip of the seabed. In this model, the trace of F10 along the seabed acts as a linear source for fluid seepage (Figure 2.14a).

The principal amplitude anomalies on H9 occur within the footwalls of F7, F10, F11 and F12, but are discordant to the local TWT structure contours. Their distribution cannot be explained by processes that involve ongoing (present-day) migration of buoyant fluids. Nevertheless, analysis of the throw contours demonstrates that H9 was at the (palaeo-) sea floor at the onset of fault activity. We suggest that the onset of faulting may have triggered upward (re)migration of buoyant fluids, along faults that cut the Laminaria Formation reservoirs as suggested by Gartrell et al. (2006). By analogy with the anomalies preserved on the present-day seabed reflector, the fluids encountered poorly compacted, permeable strata at, and immediately below, the (palaeo-) sea floor (i.e. H9). Lateral migration of the fluids into these strata and along the palaeo-seafloor would have been up-dip towards local structural highs, such as

(palaeo-) footwall crests (Figure 2.14b). The anomalies on H9 may result from the development of cemented hardgrounds that formed in response to hydrocarbon seepage at this time (Rollet et al., 2006; Figure2.14b). During subsequent burial, continued activity and possible growth/linkage along F10, F11, and F12 and nearby faults continued to modify the local subsurface structure. As a result, the hardgrounds were deformed and the associated anomalies are now discordant to the present-day TWT structure contours. Our interpretation is based on that the anomalies observed on H9 being related to early diagenetic features (i.e. cemented hardgrounds), which effectively preserve evidence for fluid seepage at the palaeo-seabed. Detailed structural restoration of the evolving fault geometries is required to further test our proposal, but is beyond the scope of the present study.

2.5.3. Fluid migration, fault throw and the duration of fault activity

Our results show that the most prominent amplitude anomalies are associated with F10, which has a throw on H9 of approximately 100 ms, and with F7, F11, F12, which have throws of approximately 30 to 65 ms. By contrast, F25, which has a maximum throw of 108 ms along H9 does not have any significant associated anomalies. The duration of activity along these faults – with and without anomalies – is similar. Observations of the youngest pre-faulting horizon, H10, show that sub-seismic scale, NW-SE striking faults locally control the distribution of amplitude anomalies and the inferred locus of fluid migration and cementation. Thus, there is no direct relationship between fault size, or longevity, and fluid migration in the shallowest subsurface. Gartrell et al's (2006) trap integrity model suggests that remigration and loss of hydrocarbons from the Laminaria Formation occurred along large faults with high post-rift (Cenozoic) throws. The present results suggest that local variations in permeability – in addition to the structural configuration – played a significant role in

controlling fluid migration and seepage in the shallowest subsurface, at or just below the seafloor/palaeo-seafloor.

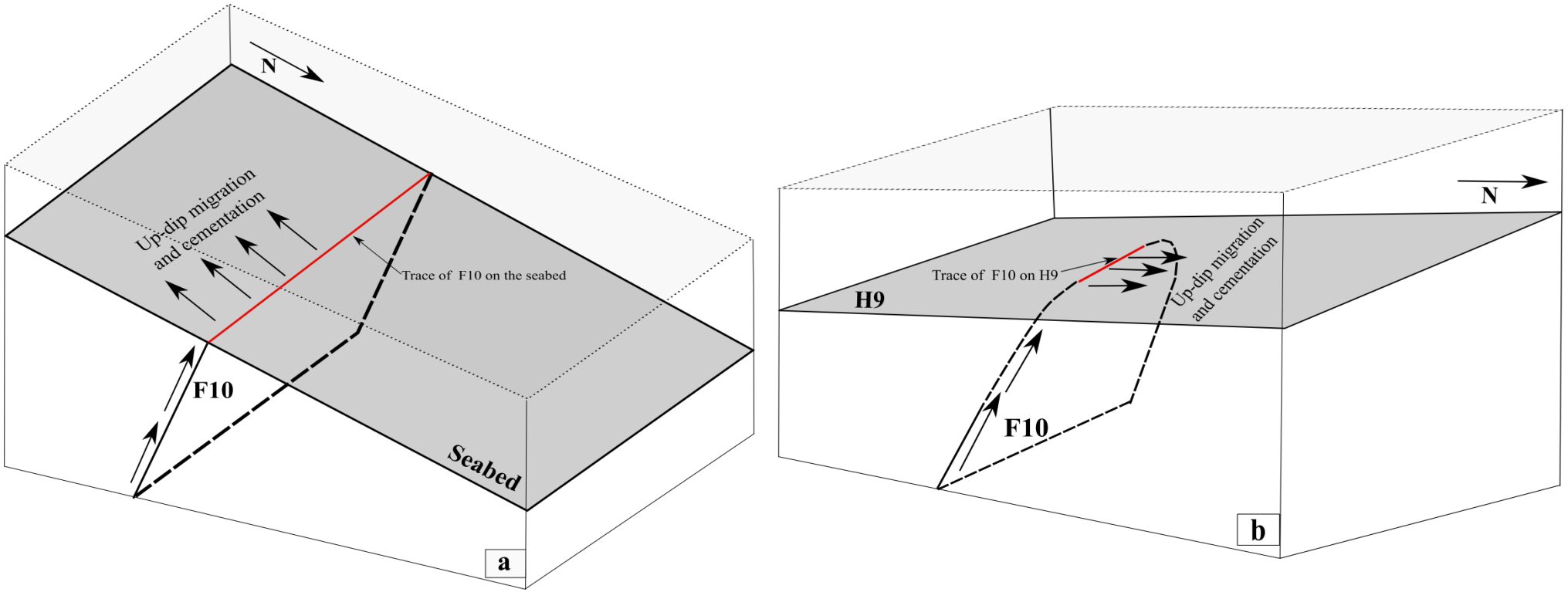

Figure 2.14. Schematic block diagrams showing the inferred migration of fluids upwards along F10, and seepage of fluids at the seafloor or palaeo-seafloor along the trace of F10 (red line). **(a)** Present day configuration of fault F10 and the seabed reflector, showing up-dip fluid migration and seepage and cementation on the seafloor; **(b)** Inferred configuration F10 and the palaeo-seabed (H9) at the time of fault initiation. Previous authors suggest that the Cenozoic faults, such as F10, propagated upwards from the underlying, Mesozoic rift system (Gartrell et al., 2006). As a result, we infer that the trace of F10 along the palaeo-seabed (H9) may have been shorter than the present-day fault length (cf. Long and Imber 2010).

2.6. Conclusion

In this study, interpretations of the amplitude and root mean square (RMS) anomalies and the three-dimensional structure are integrated in order to understand the structural controls on fluid migration on the Laminaria High. The key findings are that:

- prominent amplitude anomalies occur on horizons within the syn-faulting, Cenozoic succession. These anomalies are associated with mainly ENE-WSW striking faults, consistent with a structural control on their distribution;
- the most prominent amplitude anomaly on the present-day seabed reflector is elongated parallel to the trace of an ENE-WSW striking fault. The anomaly is located on the up-dip side of the fault trace, parallel to the two-way time (TWT) structural contours on the seabed. These observations are consistent with the anomalies having developed in response to structurally-controlled fluid seepage along, and up-dip migration away from the fault trace;
- the prominent amplitude anomalies on the oldest syn-faulting reflector, whilst located adjacent to fault traces, are discordant to the local TWT structural contours. These observations are consistent with structurally-controlled fluid seepage and cementation whilst the reflector was at the (palaeo-) seafloor; the resulting hardgrounds were subsequently buried and deformed during ongoing sedimentation and fault growth/linkage;
- the prominent amplitude anomalies on the youngest mapped pre-faulting reflector are located adjacent to sub-seismic scale, NW-SE striking faults. These observations are consistent with the small-scale faults having influenced fluid migration and cementation within the shallowest part of the pre-faulting succession;

- there is no clear relationship between the presence of structurally-controlled anomalies and the magnitude, or the duration, of movement along individual faults within the Cenozoic succession.

Chapter 3: Quantitative analysis for amplitude anomalies at the seabed from the 2D and 3D Pre-stack data

3.1. Introduction

Variation in seismic amplitudes provides different information from the subsurface such as evidence of hydrocarbon accumulation or changes in the lithologies (Brown, 2011). Furthermore, amplitude anomalies may also be created by thin layers. Widess, (1973) who showed that interference between the upper and lower boundaries of a thin layer can produce tuning effects with a maximum amplitude response with thickness being one quarter of the dominant seismic source wavelength. The ability of thin layers to respond is frequency dependent; the higher the frequency, the thinner the layer that can be resolved (Widess, 1973; Kallweit and Wood, 1982; Puryear and Castagna, 2008).

However, amplitude anomalies are affected by various factors that may not be caused by changes in the lithology or the existence of hydrocarbons such as those caused by acquisition or processing of the seismic data (Steeples and Miller, 1988; Marfurt and Alves, 2015). Hence, these effects need to be understood, eliminated or reduced to background noise levels (Sheriff, 1975). Seismic processing affects seismic amplitudes and needs to be carefully applied to the seismic data as it will influence the final seismic stack sections that will be used in the seismic and stratigraphic interpretation. Also, the appearance of amplitude anomalies depends on the quality of the original seismic data and the acquisition parameters (Simm and Bacon, 2014). Though many studies use the post-stack migrated data to address or investigate different topics; for example exploring new hydrocarbon sources directly from the seismic data, trap integrity and basin analysis studies (e.g. De Ruig et al., 2000;

Cartwright and Huuse, 2005; O'Brien et al., 1999), appreciation of the seismic processing and acquisition on these data is seldom discussed, or investigated, but is crucial as part of seismic interpretation.

Amplitude anomalies associated with active faults at the seabed are shown in the southern part of the seabed in the Laminaria High; these anomalies are interpreted as authigenic carbonate cementation due to hydrocarbon leakage along faults (O'Brien and Wood, 1995; Rollet et al., 2006; Langhi et al., 2010). However, in this study these anomalies appear to have different amplitude strengths, "brightness", (from the 3D seismic volume used in chapter 2) and different amplitude distributions from those in another published paper by Langhi et al. (2010). So can these differences be attributed to acquisition/processing or do these anomalies represent actual changes in the hydrocarbon leakage with time?

This chapter aims to establish the confidence in the 3D interpreted data that is used in Chapter 2, by specifically investigating the influence of seismic processing on amplitude anomalies at the seabed. This study processed data from two surveys shot at different times with different configurations using similar processing steps that were applied on the original 3D seismic data. This data includes the 2D 1992 Caulerpa and the 3D 1995 Laminaria pre-stack seismic data (Figure 3.1a). Given the differences between the interpretation presented here and that of Langhi et al. (2010), reprocessing of the raw seismic data is essential in this study to quantify the uncertainties in the perception of amplitude anomalies. Hence, this chapter will investigate the implication of trust in seismic processing on geophysical interpretation using 2D or 3D post-stack migrated data.

3.2 Data

3.2.1 2D pre-stack seismic data

3.2.1.1 Acquisition

The 1992 Caulerpa 2D pre-stack seismic data used in this study was acquired by Western Geophysical Company, on behalf of Woodside Offshore Petroleum Ltd. This survey consists of 27 lines covering about 675 km^2 within the AC/P8 (Figure 3.1) in the north-west of the Bonaparte Basin. The hydrophone streamer is about 4000 m in length and towed at 7 m depth with 240 channels. The near to middle offsets (1-180) have group intervals of 13.3 m and the far offsets (180-240) have group intervals of 26.6 m and the data is sampled at 2 ms with a 6 Hz low cut filter, and a 188 Hz high cut anti-alias filter (Table 3.1 and Figure 3.2). For the purposes of this study (Figure 3.1a), three dip lines (3328, 3329 and 3330) are selected from this survey and reprocessed.

3.2.1.2 Processing

A series of seismic processing steps were applied as part of the original processing as shown in Table 3.1. This resulted in good quality data from the seabed into the lower Cretaceous. The quality of the final image became poor below the Valanginian Unconformity as a result of the structure complexity at the lower Cretaceous, Jurassic, and Triassic sequences.

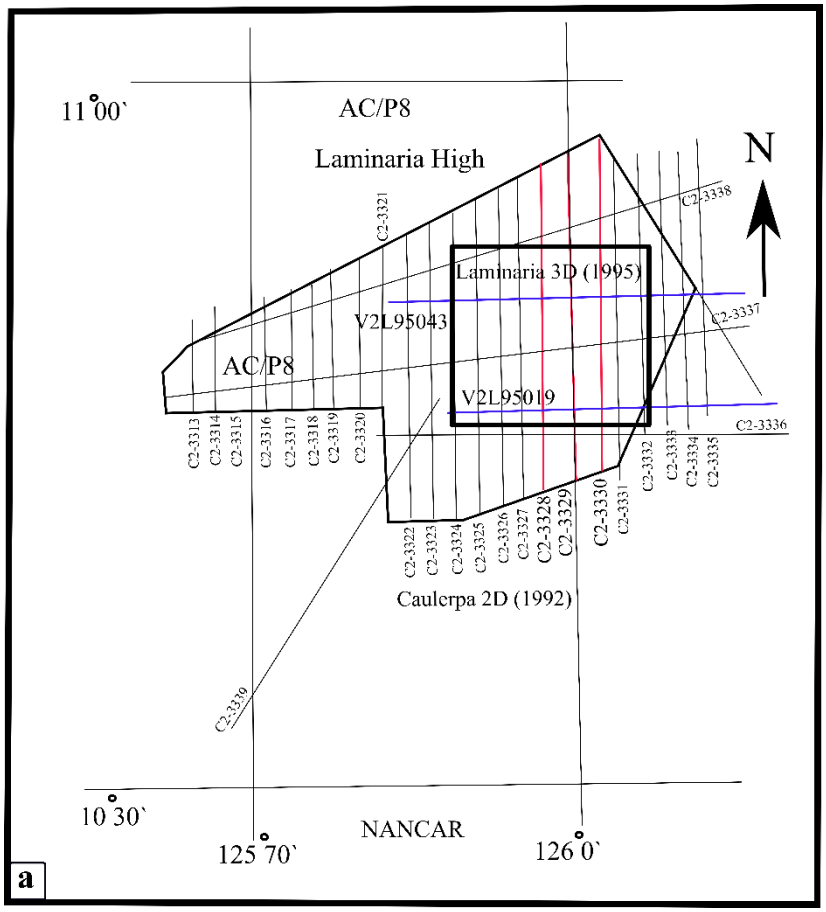

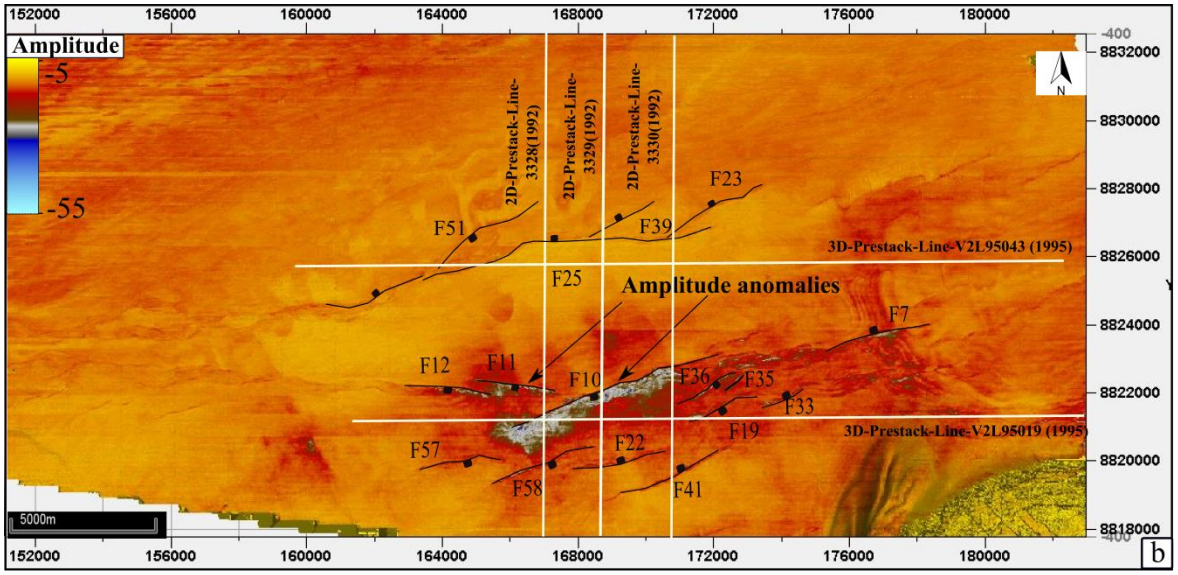

Figure 3.1. (a) Seismic base map showing the survey area within permit AC/P8 that covers the Laminaria High; this map shows the location of all the 2D and two of the 3D profiles provided by Geosciences Australia. Note that the blue and the red lines are the 2D and the 3D profiles that are used in this study. The black box show the extended area covered in Fig 3.1b **(b)** Amplitude map for the seabed showing the amplitude anomalies associated with faults in the southern part of the seabed overlain by the 2D and the 3D seismic profiles that are used in this study.

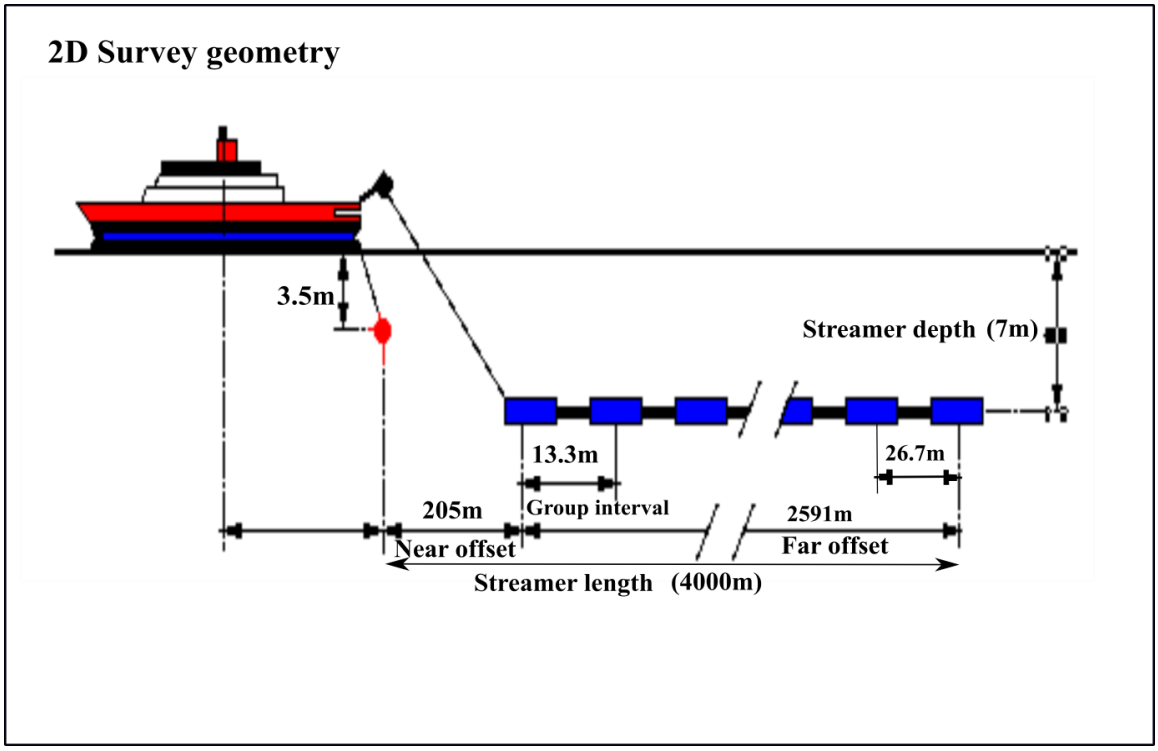

Figure 3.2. Seismic acquisition configuration of the 2D pre-stack data along lines 3328, 3329 and 3330 that are used in setting the geometry

---

3.2.2 3D pre-stack data

3.2.2.1 Acquisition

The 1995 Laminaria 3D pre-stack seismic data is also used in this study. This data was acquired by Western Geophysical Company, on behalf of Woodside Offshore Petroleum Ltd within the AC/P8 and covers an area of 728 km^2. This survey was equipped with two sources and four hydrophone streamers of 3800 m in length and towed at 8 m in depth. However, the data provided by Geoscience Australia only contained information from two of these streamers.

Each streamer has 304 m channels with group intervals of 12.5m; the data is sampled at 2ms with a 3 Hz low cut filter and a 125 Hz anti-alias high cut filter (Figure 3.3).

Table 3.2 shows the acquisition parameters that are used to set the geometry file for the 2D and the 3D seismic profiles.

Table 3.1. Summary of the seismic processing on the 1992 Caulepra 2D seismic data by a Western Geophysical seismic vessel

2D Processing sequences
Format conversion
Shot domain FK filtering
Adjacent trace sum
Instrument diphase
Amplitude recovery
Deconvolution before stack
Trace scaling
Common offset sort
First pass velocity
Dip moveout (DMO)
Gun and cable correction
Kirchhoff migration
Tau-P dip filter
Zero phase conversion
Time variant bandpass filtering
Scaling (500ms gate)

3.2.2.2 Processing

The Laminaria 3D survey was processed by Geco-Prakla at Geco-Prakla's Perth and Gatwick (U.K.) processing centres in 1995. Table 3.3 shows the processing sequence applied on these data. The data were acquired and processed as 114 x 50 fold 3D lines with additional 67 x 100 fold 3D vessel lines. Two strike lines (V2L95-019 and V2L95-43) shown in figures1.1a and 1.1b are selected from this survey and reprocessed.

Table 3.2. Summary of acquisition parameters of the 2D and the 3D seismic profiles

Data acquisition	**2D Caulerpa-1992**	**3D Laminaria-1995**
Source	Liton sleeve Gun	Bolt Gun
Volume	2250 cubic inches	3328 cubic inches
No. of guns	24	Not known
Pressure	2000 psi	2000 psi
Streamer length	4000 m	3800 m
No. of Channels	240	304
Spacing	13.3	12.5
Streamer tow depth	7 m	8 m

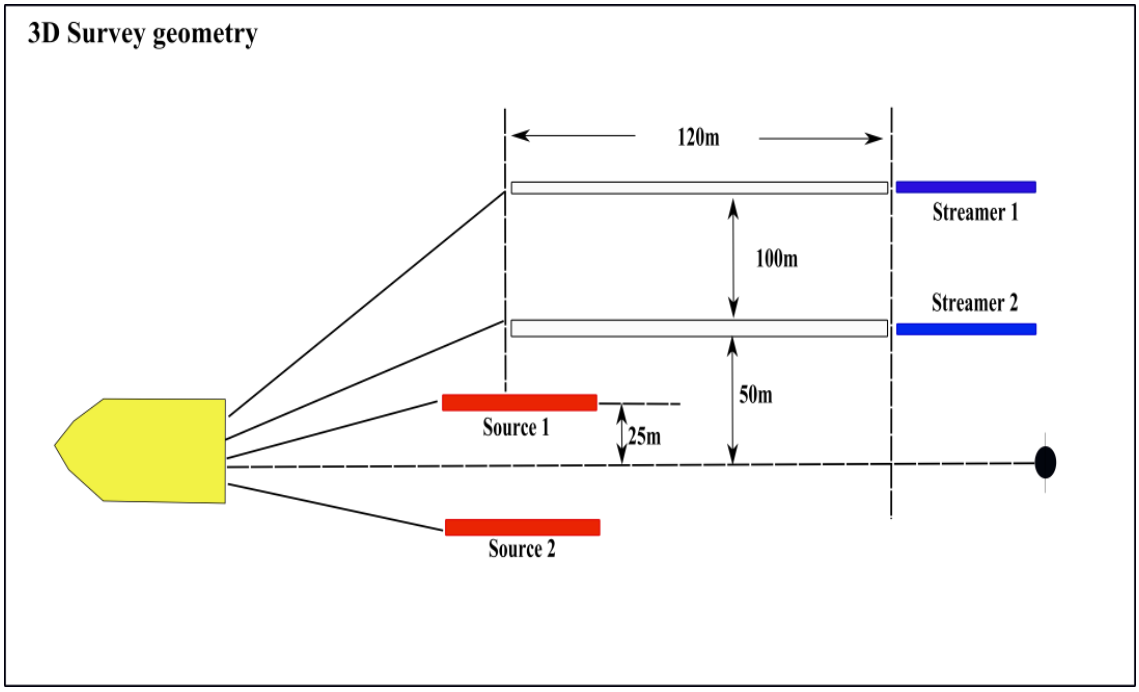

Figure 3. 3. Seismic acquisition configuration of the 2D pre-stack data along lines 2L95-019 and 2L95-43.

Table 3.3. Summary of the seismic processing on the 1995 Laminaria 3D seismic data by the Geco-Parkla

3D processing sequence
FK filtering in the shot domain
Deterministic zero phasing
3D dip move out (DMO)
Velocity analysis
Multiple suppression
One pass 3D time migration.

3.3 Methodology

3.3.1 Seismic processing

Seismic processing includes attenuation of the noise, enhancing the signal and migrating seismic events to their actual location in space. The results of seismic data processing depend on the technique used in processing and the data acquisition parameters (Yilmaz, 2001; Bacon et al., 2003). In general, the principal steps to achieve the desired result includes: 1) deconvolution; 2) stacking; and 3) migration. These can be viewed as working on the seismic data in the three domains of time, offset and common mid-point respectively (Figure. 3.4) (Yilmaz, 2001).

Reprocessing for the 2D and 3D seismic data is applied (Figure 3.5) to investigate variations in the seismic amplitude anomalies at the seabed due to different processing workflows (Figure 3.1 b). The seismic data are processed using Globe Claritas V6.2.11 software. As near as possible a similar sequence of processing is applied along the selected 2D and 3D profiles (figures 3.1a and 3.1b).

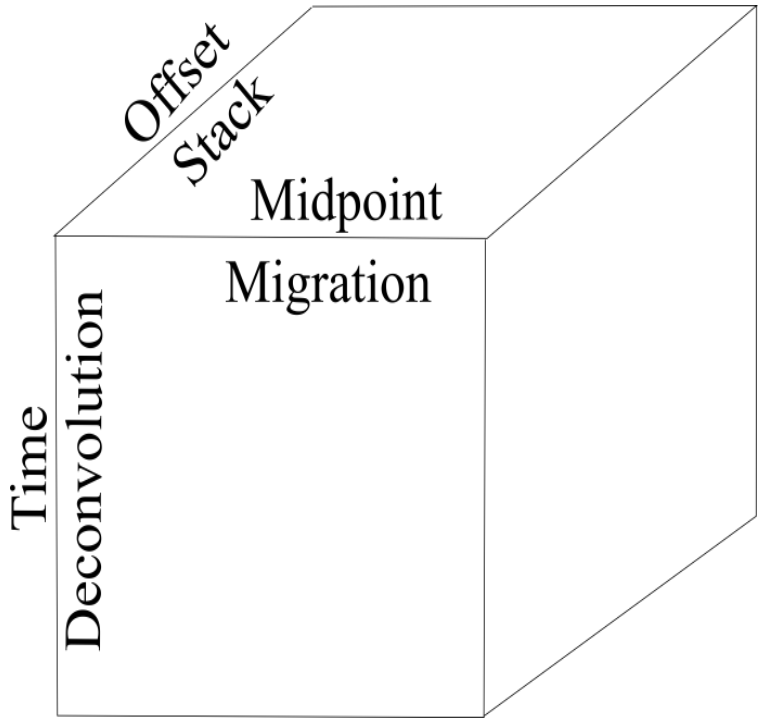

Figure 3.4 The main seismic process includes 1) deconvolution; 2) stacking; and 3) migration. Seismic data volume representing the main processing sequence (modified from Yilmaz et al., 2001).

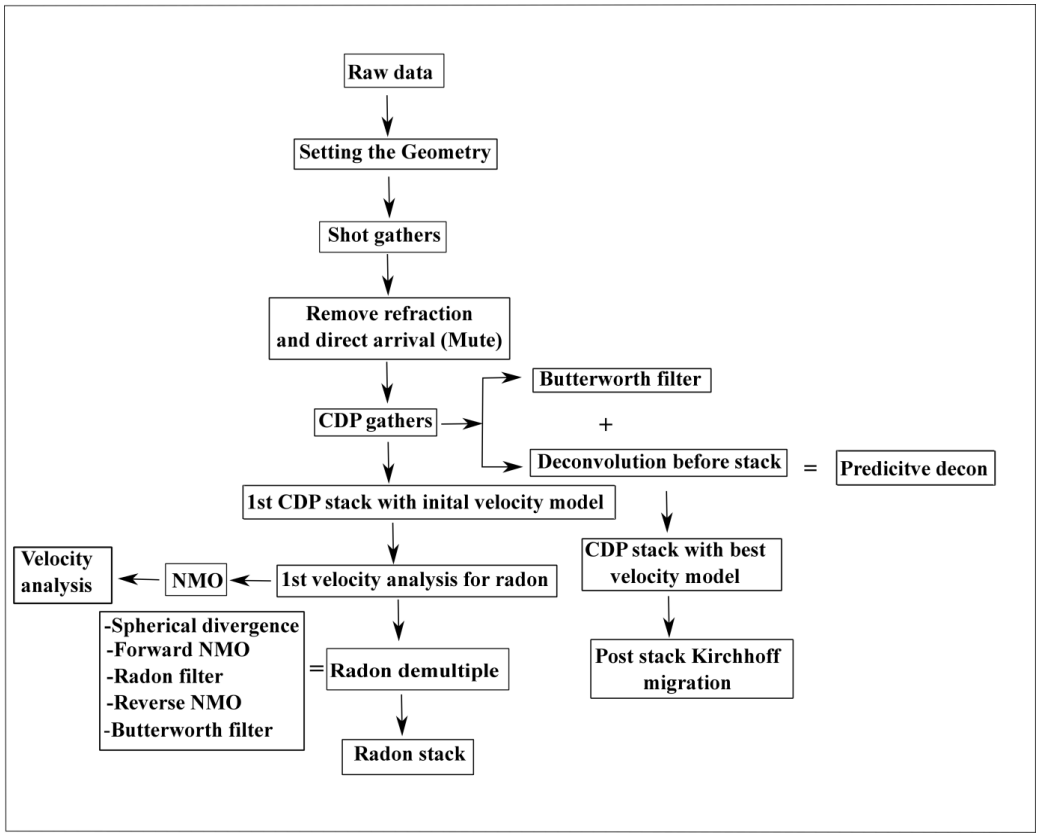

Figure 3. 5. Workflow of re-processing the 2D and 3D pre-stack seismic data.

3.3.1.1 Noise attenuation and front mute application

The first step in seismic processing is to set up the geometry of the seismic data. The geometry for the 2D profiles is set up based on the parameters as in Figure 3.2 and for the 3D profiles as in Figure 3.3. The next step is the removal of the noise that are caused by the refraction arrivals , as shown in Figure 3.6, by applying the front mute function and keeping the reflection energy. The amplitude above the front mute is set to zero amplitude with a 100 ms taper (figures 3.7a and 3.7b). Then the shot gathers are transformed into the CMP gathers to produce the first CMP stack section (Figure 3.7 c) using the first simple velocity model. This helps in identifying the quality of the seismic data and the problems that need to be removed from the seismic data.

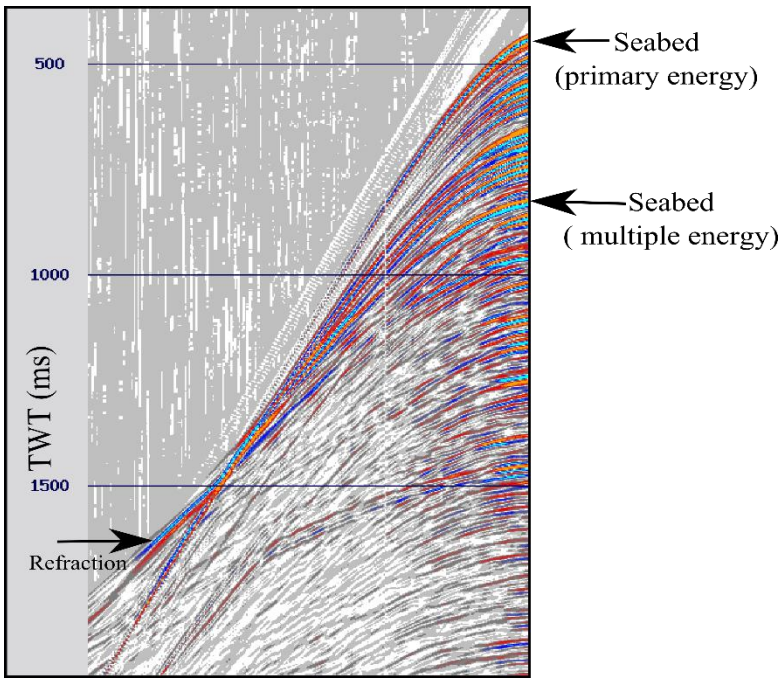

Figure 3.6. Shot gather from Line 3329 from the 2D seismic data showing the refraction energy, the seabed primary and multiple reflections.

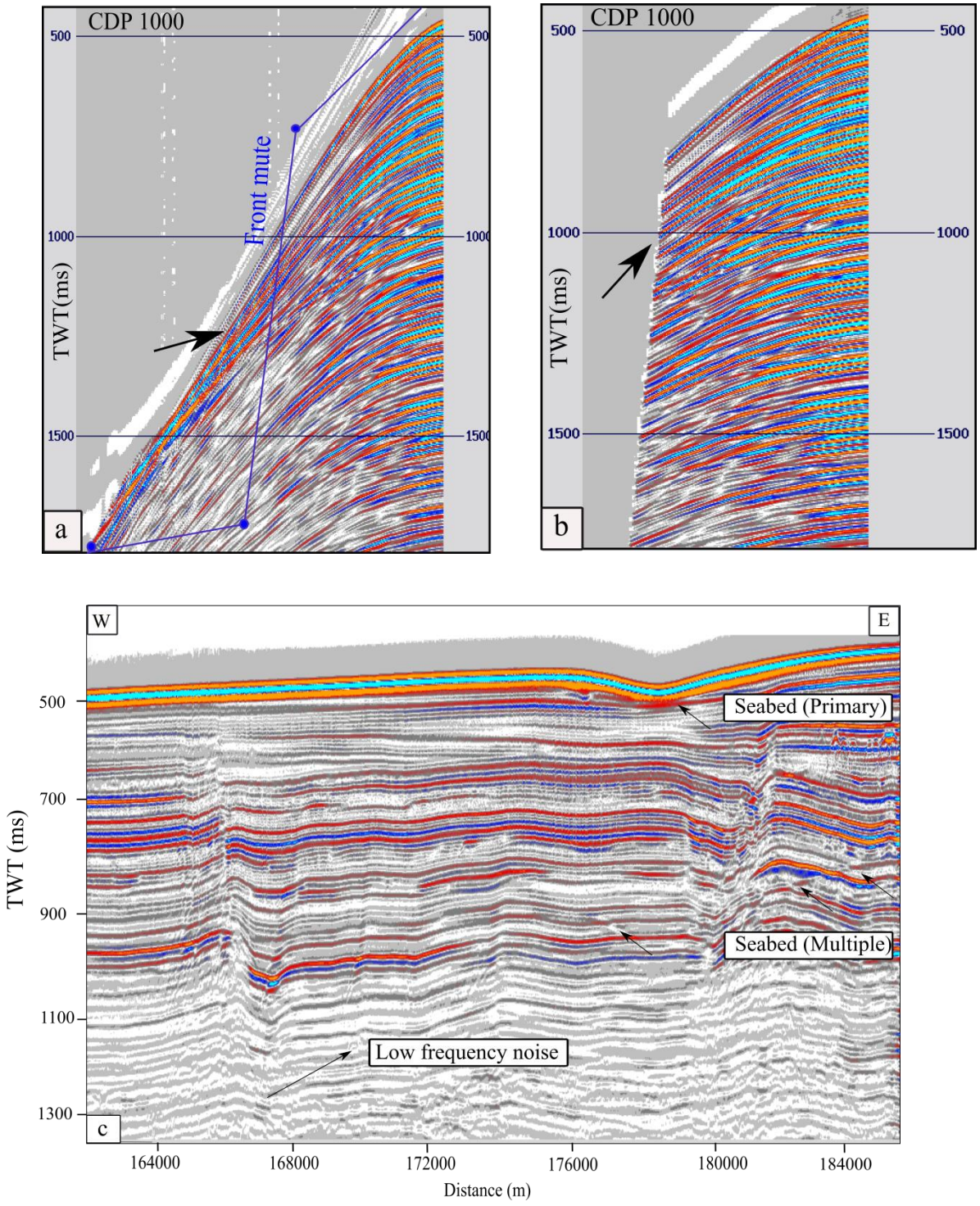

Figure 3.7. CDP gather from Line-19 from the 3D seismic data. **(a)** Before muting. **(b)** After muting. Note that the amplitude above the front mute is removed by multiplication with zero **(c)** First stack section using the first simple velocity model.

3.3.1.2 Velocity analysis and normal moveout (NMO) correction

Velocity analysis is a process to determine the velocity model that will be used in the NMO correction. The NMO correction followed by the stacking of the traces within each CMP gather suppresses unwanted noise from the seismic data, e.g. “multiple” reflections, and enhances the “primary” reflections. Multiples are the delayed reflections that arrive later than the causative primary reflections due to reflection at the free-surface (Bacon et al., 2003). This noise is suppressed by flattening the primary reflections in the CMP gathers (figures 3.8a, 3.8b and 3.8c) that are then used to produce the optimum stack section. The improvement in the signal-to-noise ratio (approximately proportional to root N where N is the fold of cover) helps distinguish the significant features at the subsurface (Muirhead and Datt, 1976).

The velocity analysis includes the velocity semblance map, CMP gathers and initial stack section. The building of a velocity model is done by picking velocities that best flatten the hyperbolic primary reflections (figures 3.8a, 3.8b and 3.8c). In this study, velocities are picked at every 25 CMPs to get an accurate velocity model. After determining the first velocity model a second CMP stack section is generated.

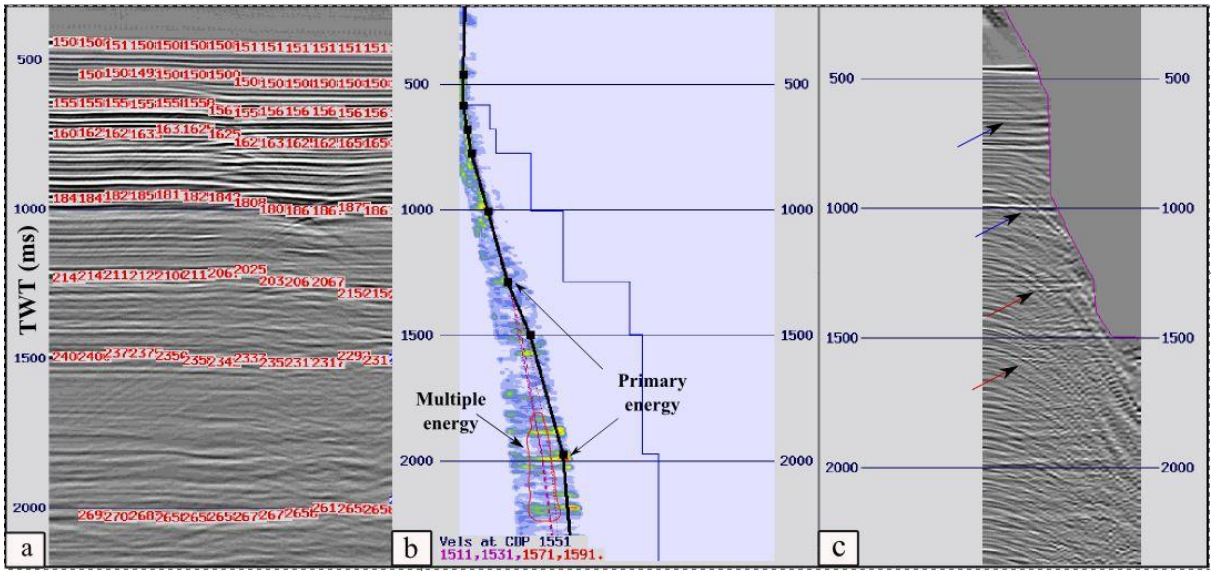

Figure 3. 8. The three windows used for velocity analysis along Line-3328 from the 2D seismic data. **(a)** The CDP stack section showing the picked velocities. **(b)** The velocity semblance map. **(c)**The CDP gather after picking the velocities, note the primary events are now flat with increasing offset (blue arrows) whereas the multiple energy still retains a curvature (red arrows) and therefore is suppressed during the stacking process.

3.1.1.3 Spherical divergence correction

The strength of the seismic waves is affected by many factors as they propagate through the earth; these factors include spherical divergence which causes the amplitude to decay due to the spreading of the wavefront as it travels away from the source (Yilmaz, 2001). As the purpose of this study is to quantify the amplitude anomalies at the seabed, spherical divergence is therefore applied to compensate for the amplitude loss for the different propagation distances to the seabed.

3.3.1.4 Radon transform multiple removals

After applying the first pass of the velocity model, primary reflections are flattened, but not the multiples. However, as shown by the blue arrows in Figure 3.9 a, the multiples have strong amplitudes that are at least as strong as the primaries (red arrows). Therefore, to get a more robust velocity model, a Radon demultiple process is applied to suppress the unwanted multiple events. In the processing package used in this project, Claritas®, this process is called "PRT". It works by separating the input gathers into three components: wanted signal, unwanted noise and unmodelled data. The first step is to select the limits of the moveout range to be modelled; the intention is to include both the required primaries and unwanted multiple noise in the model but excluding the uncorrelated background noise. The Radon transform converts the data into intercept/moveout space such that the primaries and multiples map to different areas. This modelled data are then split into signal and noise (multiples) by applying a mute to suppress the unwanted multiple energy (Foster and Mosher, 1992) (figures 3.9a, 3.9b, 3.9c and 3.9d).

In the process applied here there were two extra steps introduced. For the 2D data, the CMP gathers were not ordered with a regular number of traces in each CMP gather due to variations in ship speed during acquisition; this coupled with low fold meant that the far offset arrivals could be spatially aliased. Therefore, super gathers were formed by combining two CMP gathers prior to the Radon demultiple (Figure 3.10). The other step was, rather than muting the multiples in radon space, the primaries were suppressed so the inverse Radon transform comprised the multiple wave field, which was then subtracted from the original gather. This is found to be more robust and less prone to produce processing artefacts (Sheriff and Geldart, 1995; Yilmaz, 2001).

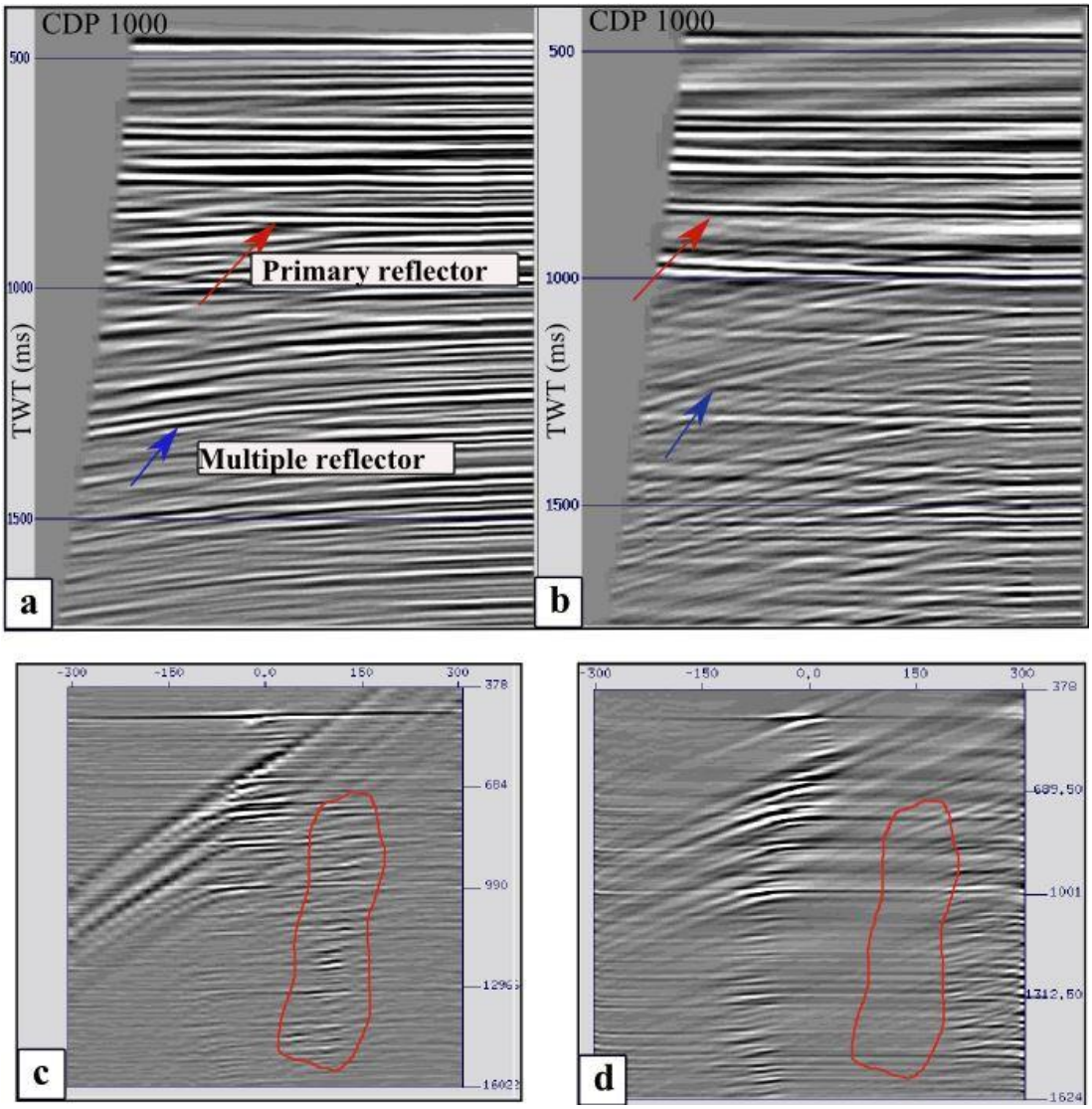

Figure 3.9. Example of Radon demultiple along line-19 from the 3D seismic data. **(a)** CDP gather before applying Radon; **(b)** CDP gather after applying Radon. **(c)** Radon mute model showing the multiple energy highlighted in red. **(d)** Radon mute model showing how multiple energies are supressed as highlighted in red. The primaries were suppressed so the inverse Radon transform comprised the multiple wave fields, which was then subtracted from the original gather.

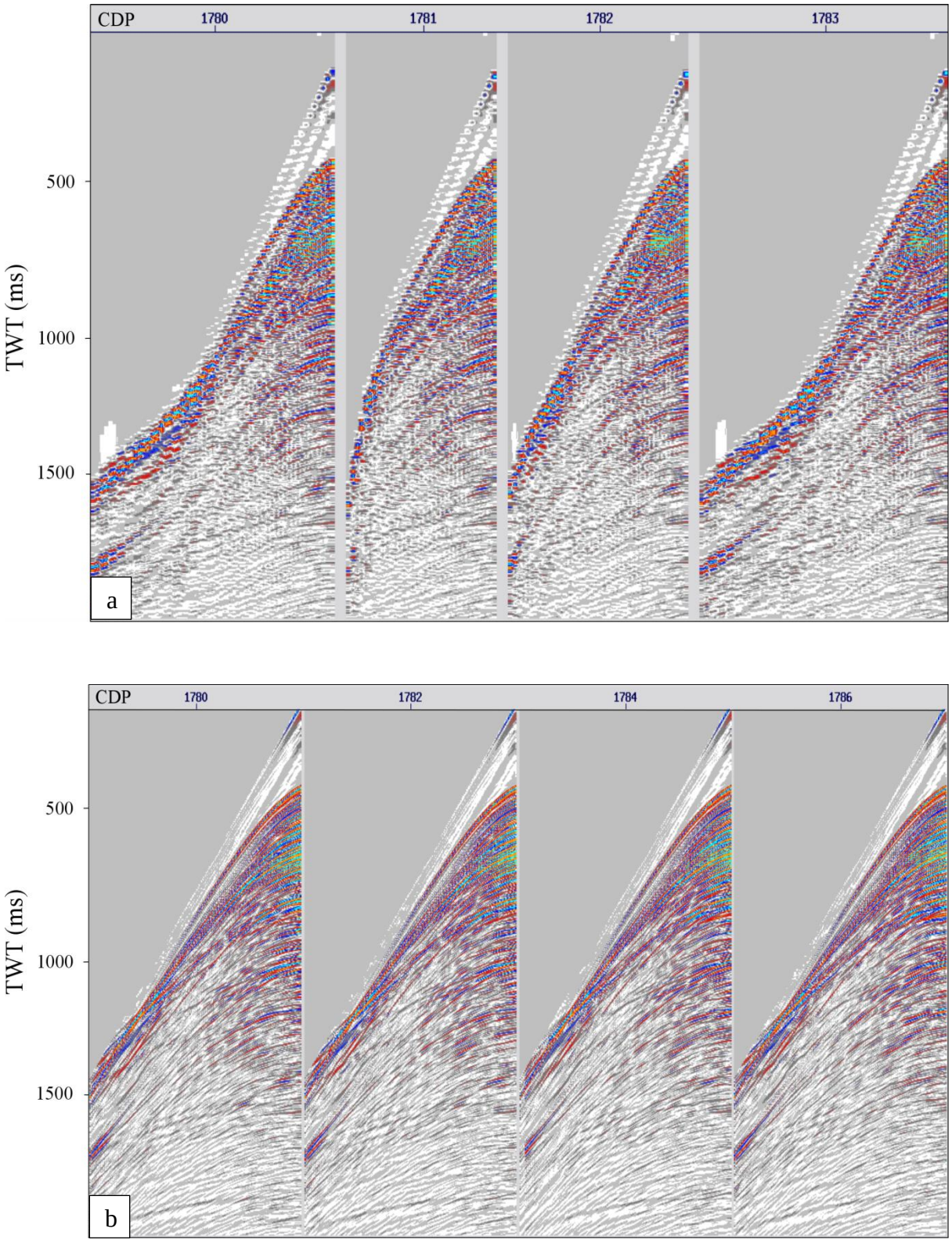

Figure 3.10. CDP gathers from Line- 3330 from the 2D seismic data. **(a)** Unordered CMP gathers. **(b)** Ordered CDP gathers. Note that in the supergather process, two CMP gathers are combined.

3.3.1.5 Frequency filters

To get a better resolution for the seismic data, two filters are applied on the 2D and 3D pre-stack data. The following sections explain the principle of each filter.

3.3.1.5.1 Butterworth bandpass filter

The Butterworth filter is a frequency filter that is used to suppress unwanted noise outside the bandwidth of the seismic signal by defining the frequencies that allowed to pass through this filter (Yilmaz, 2001). Therefore, prior to the Radon demultiple job, this filter was applied to suppress the low frequency sea noise and the high frequency noise. The Butterworth filter used here is set so that the corner frequencies are 20, 40, 80, 120 Hz, which correspond to filter amplitudes of 0.05, 0.95, 0.95, 0.05 and the phase of the filter was set to be zero.

3.3.1.5.2 Deconvolution (inverse filter)

In seismic exploration, the seismic wavelet produced by the source travels through different stratigraphic strata which act as a band-pass filter for seismic waves until they reach the receiver. Higher frequencies are preferentially attenuated (Yilmaz, 2001), so with increasing travel time the signal becomes dominated by lower frequencies which tend to be contained in the bubble pulse coda of the source wavelet (Hobbs and Snyder, 1992). Deconvolution helps to improve the resolution of the seismic data by compressing the seismic wavelet towards a spike by whitening the frequency spectrum and hence improves the resolution. Also, it recovers the higher frequencies, attenuates short-period multiples and generates a zero-phase wavelet that is easier for interpretation (Yilmaz, 2001). There are two types of deconvolution: **1)** deterministic deconvolution, when the effects to be removed are known; **2)** statistical deconvolution, which needs to derive the wavelet properties form the data itself

(Sheriff and Geldart, 1995; Yilmaz, 2001). As for the data processed here the source wavelet was not measured for either survey, so deconvolution was limited to the latter option.

There are two types of statistical deconvolution:

a) ***Spiking Deconvolution****:* this filter tries to compress the seismic wavelet into a spike shape to represent the reflectivity of the subsurface. This filter sometimes gives an unstable result which is related to the stability and bandwidth of the source wavelet. So this type of deconvolution filter was not used.

a) ***Predictive Deconvolution****:* this filter is used to remove periodic parts of seismic traces such as short-period multiples and bubble pulse coda from the source. There are two parameters that need to be set: the filter length, which should be two or three times the main period in the data; the gap length, which is typically set to the 'second zero-crossing of the autocorrelation function' this ensures that the bubble pulse and short-period multiples are suppressed (Yilmaz, 2001) (Figure 3.11). Importantly, the autocorrelation function needs to be long enough to ensure that the geology is not filtered and is typically set to ten times the filter length, so a window of 1000 ms is used in this study.

As part of the workflow different filter gaps, lengths and autocorrelation design windows were tested to get an optimum decovolution filter that best improves the resolution of the seismic data. Then, the same deconvolution filter was applied along all the seismic lines.

After the pre-stack processing described above, the CMP gathers were NMO-corrected with the picked velocity model, muted to remove distorted arrivals and refractions at the longer offsets, then stacked.

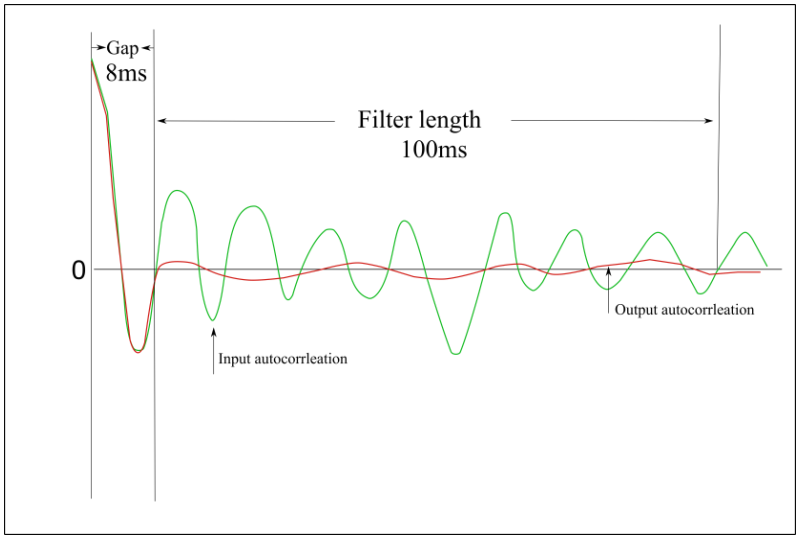

Figure 3.11. Example of a wavelet showing the settings of the gap and the filter length used in the deconvolution filter.

3.3.1.6 Kirchhoff migration

The stacked CMP section will contain reflected data from different locations which might not be positioned in their actual locations (Sheriff and Geldart, 1995). Kirchhoff migration is a post-stack process that moves the dipping events to their correct spatial location subject to a given velocity model. The Kirchhoff migration is based on the Huygens principle; this migration is achieved by repositioning each hyperbola to its origin (Simm and Bacon, 2014).

Kirchhoff migration is sensitive to the input velocity model, and an accurate velocity model is required for this process. After applying migration, the faults and dipping layers should be relocated to their actual location and overall clarity of the final image is improved (figures 3.12a and 3.12b).

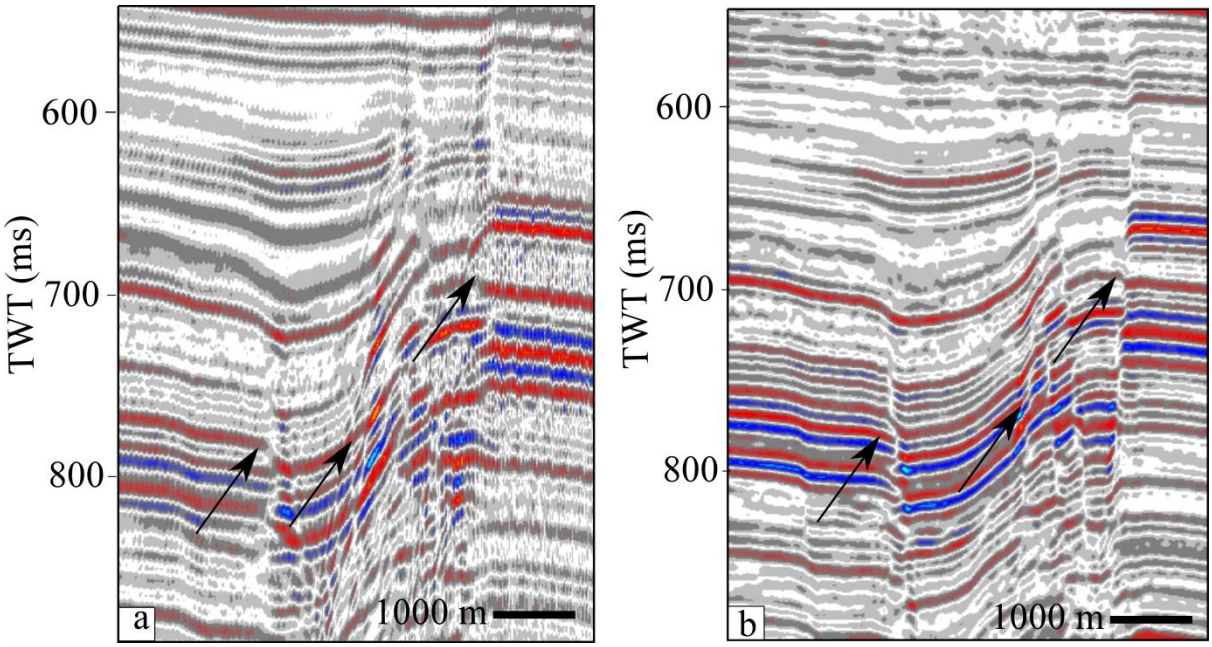

Figure 3.12. Example of Kirchhoff migration along Line-3330 from the 2D seismic data. **(a)** Partial stack section before applying Kirchhoff migration. **(b)** Partial stack section after applying Kirchhoff migration. Note the sharpness of the faults compared with the faults before applying the Kirchhoff migration as shown by arrows.

3.4 Results

The main purpose of this study is to examine how robust or certain the seabed amplitude anomalies are that occur in the southern part of the study area (Figure 3.1b). Five seismic lines from both 2D and 3D surveys (Figure 3.1a) were re-processed using the same processing steps shown in Figure 3.5. The final images were displayed to compare the seismic amplitude anomalies from these lines with the corresponding 3D sections extracted from the 1995 Laminaria 3D volume described in Chapter 2.

3.4.1 The effect of seismic processing on the final stack image

3.4.1.1 The sensitivity of the Radon demultiple with the velocity model

The Radon demultiple is based on a number of parameters that need to be provided by the user. These parameters include defining the minimum and maximum moveout parabolic limits that need to be modelled, the noise region and the NMO correction. Ideally the Radon filter suppresses the multiples and leaves the primary reflection as shown in Figure 3.9. However, the Radon filter is sensitive to the specified parameters and an initial stack section for Line-19 shows that the seabed reflector within the CDP range between 800 and 1000 has a dim area. On investigating this apparent amplitude anomaly was found to have been caused by an error in picking slightly higher velocities at the seabed (1538 and 1525 m/s instead of 1519 m/s) (figures 3.13a and 3.13b). Once the velocity model is corrected and the Radon filter re-run the amplitude anomaly disappears as shown in figures 3.13c and 3.13d.

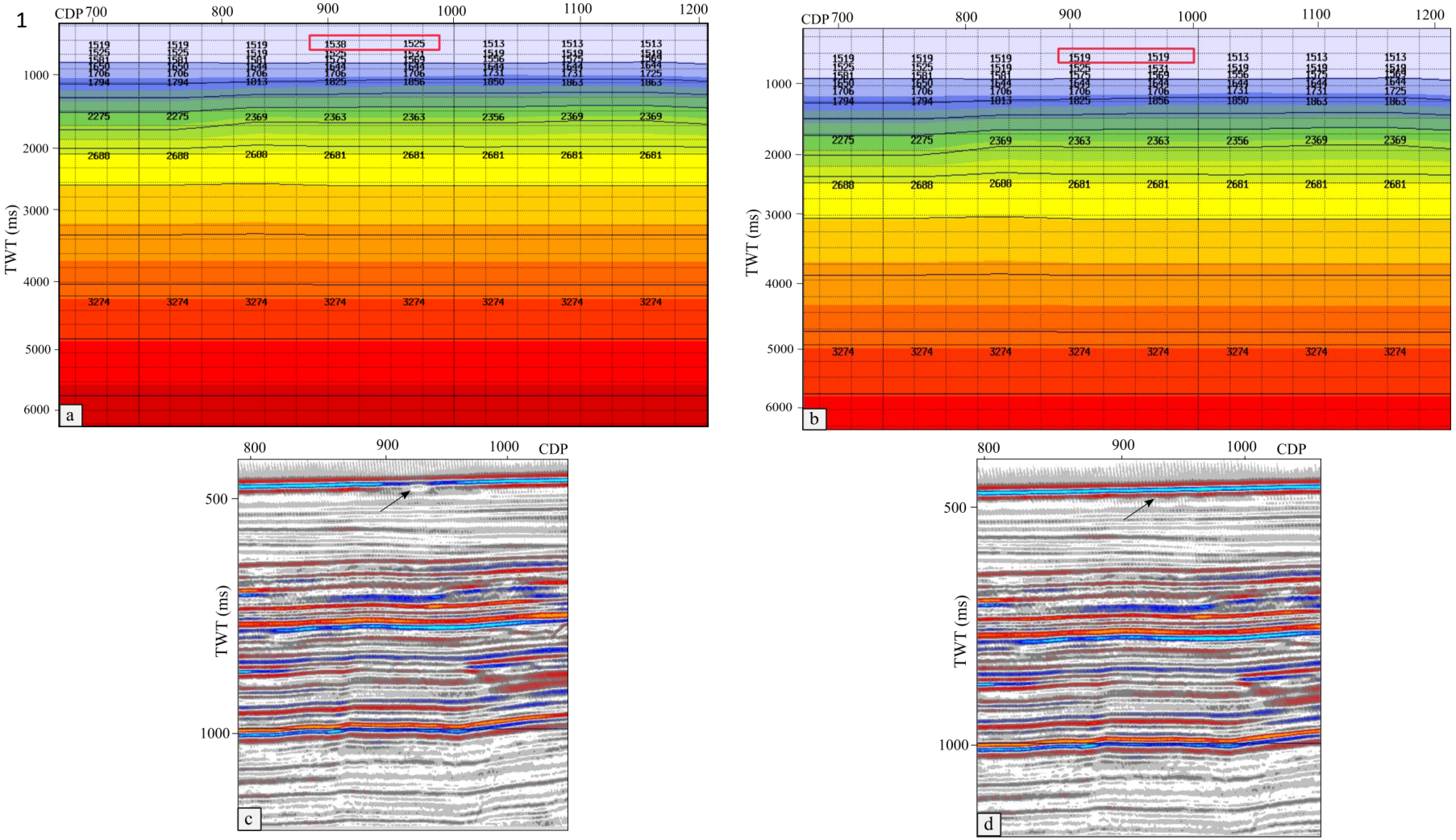

Figure 3.13. Velocity model along Line-19 from the 3D seismic data **(a)** Velocity model with incorrect velocity at the seabed. **(b)** Velocity model with correct velocity at the seabed. **(c)** Partial stack section along Line-19 with incorrect velocity model. **(d)** Partial stack section along Line-19 with correct velocity model. Note that the seabed reflector within CDPs between 800 and 1000 has a dim area in Figure 3.14c that is caused by an error in picking high velocities at the seabed; this dim amplitude is enhanced after correcting the velocity model within these CDPs as shown by arrow in Figure 3.13d.

3.4.1.2 The effect of Radon on the appearance of the amplitude anomalies

The Radon demultiple was applied to suppress the multiple energy in the seismic data. However, the amplitude anomalies at the seabed above Fault F10 (Figure 3.14a) are less obvious on the final image compared with the original 2D section extracted from the 3D volume, as shown by arrows 1 and 2 (figures 3.14a and 3.14b). In fact, the final stack section along Line-3328 shows that the amplitude anomaly along Fault F10 becomes dimmer in the footwall contrary to what was observed in the 3D volume data.

3.4.1.3. The sensitivity of the amplitude anomalies with the deconvolution filter

Predictive deconvolution is applied along all the seismic lines. Three ranges for the gap lengths (8,4, 16 ms)are tested with a filter length of 100 ms, Figures 3.15b, 3.15c and 3.15d along Line-19 to produce the best filter that shows similar amplitude anomalies at the seabed shown in Figure 3.15a. The deconvolution filter with a gap length of 8 ms was chosen as the one with the most similar results for the amplitude anomaly at the seabed. Figure 3.16 show how this deconvolution filter has improved the resolution of the seismic data by compressing the seismic wavelet and attenuating the reverberation shown in the autocorrelation panels. Then this filter is applied along all the seismic lines (43, 3328, 3329 and 3330) (Figure 3.1). The results after the inclusion of the deconvolution filter along Line-3328 show the amplitude anomaly associated with Fault F10, as shown by arrows 1 and 2 in Figure 3.17, compared with the original 2D seismic section (3D seismic volume) in Figure 3.14a and 3.14b.

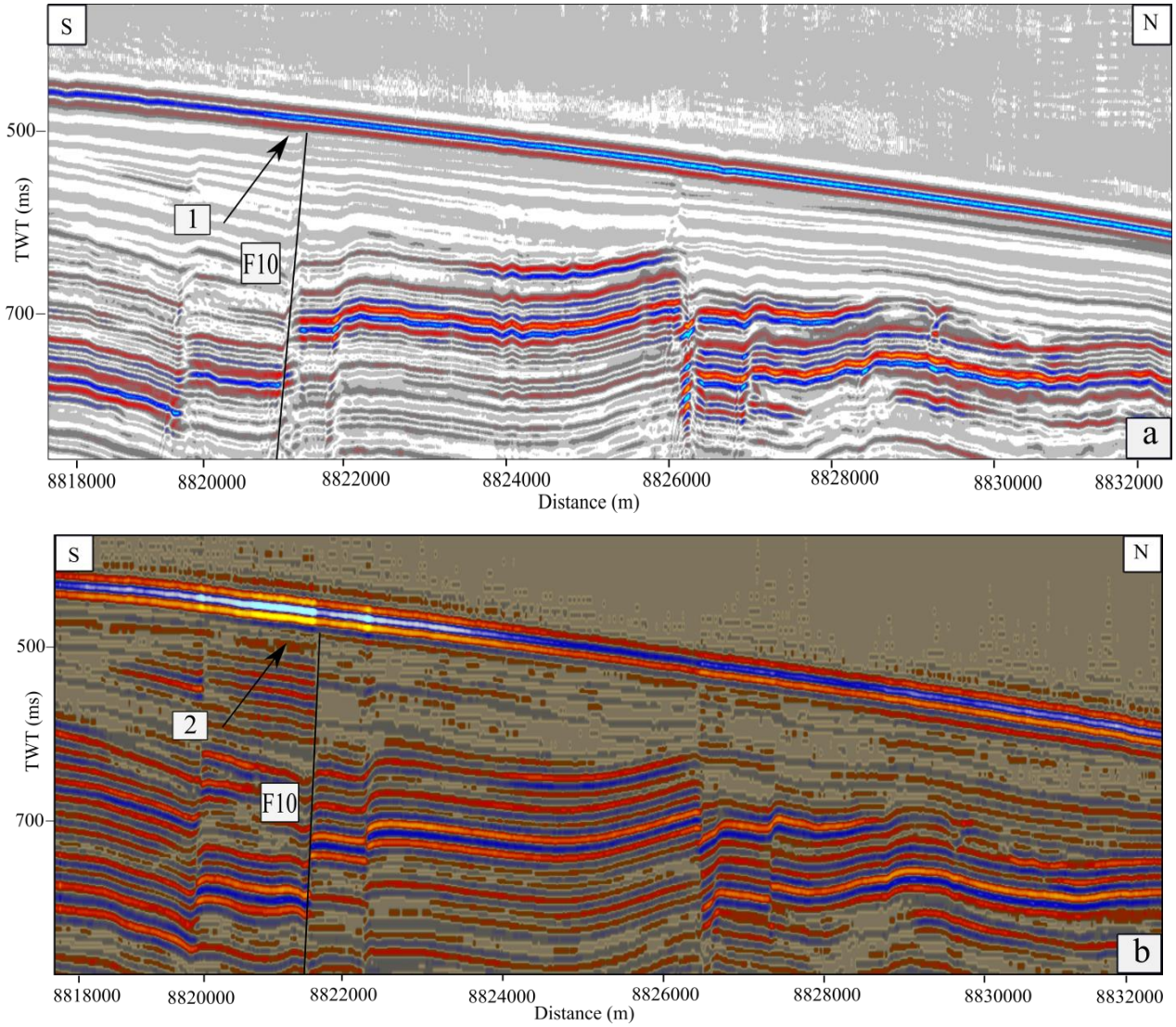

Figure 3.14. Result of radon filter. **(a)** Stack section along Line-3328 with the Radon filter. **(b)** Stack section from the original 3D seismic volume. Note that the amplitude anomaly along Fault F10 is weak and not obvious such as the associated anomaly along this fault in the original 3D seismic section.

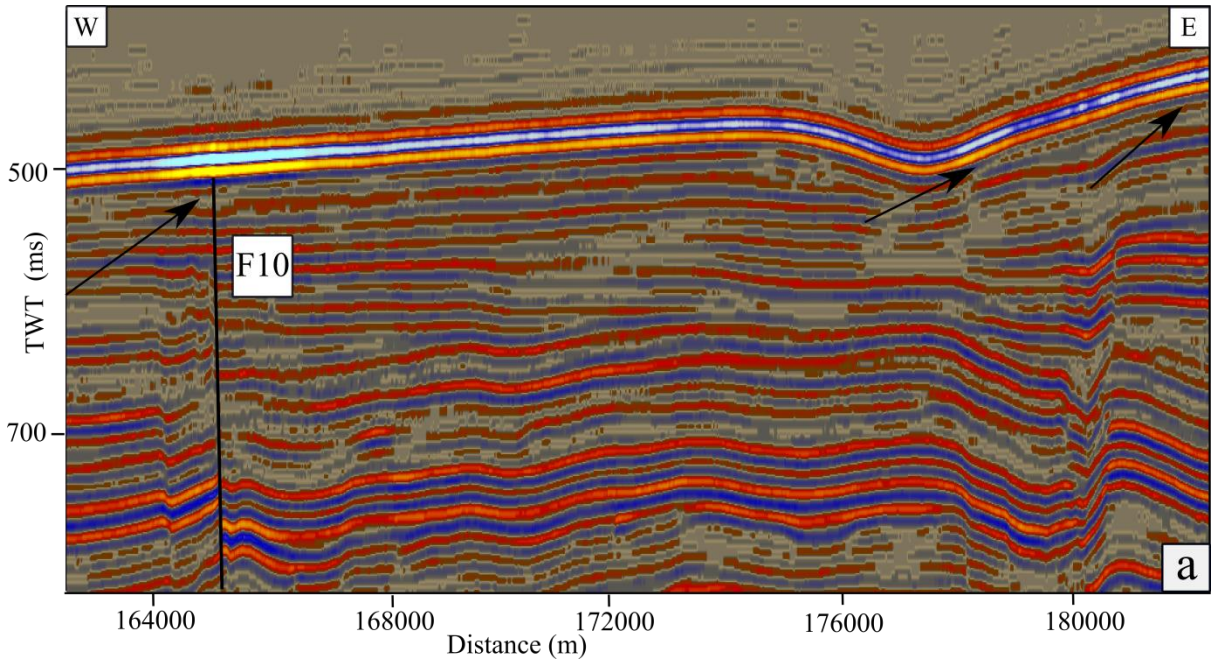
W
E
500
700
TWT (ms)
F10
a
164000
168000
172000
176000
180000
Distance (m)

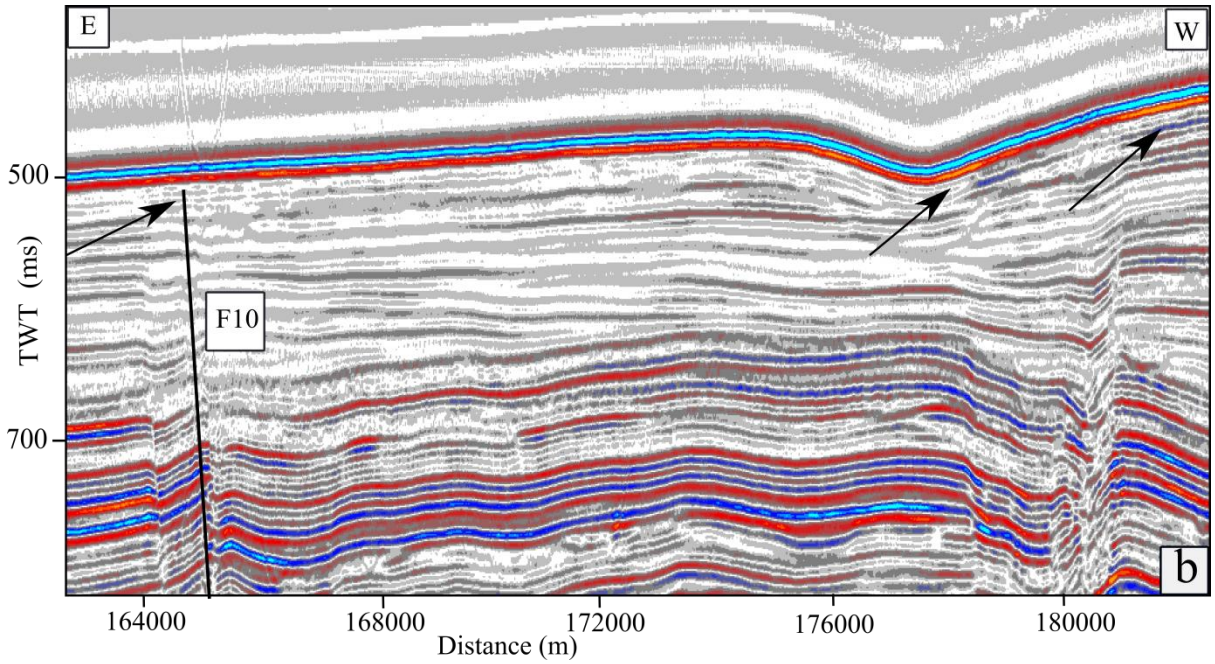
E
W
500
700
TWT (ms)
F10
b
164000
168000
172000
176000
180000
Distance (m)

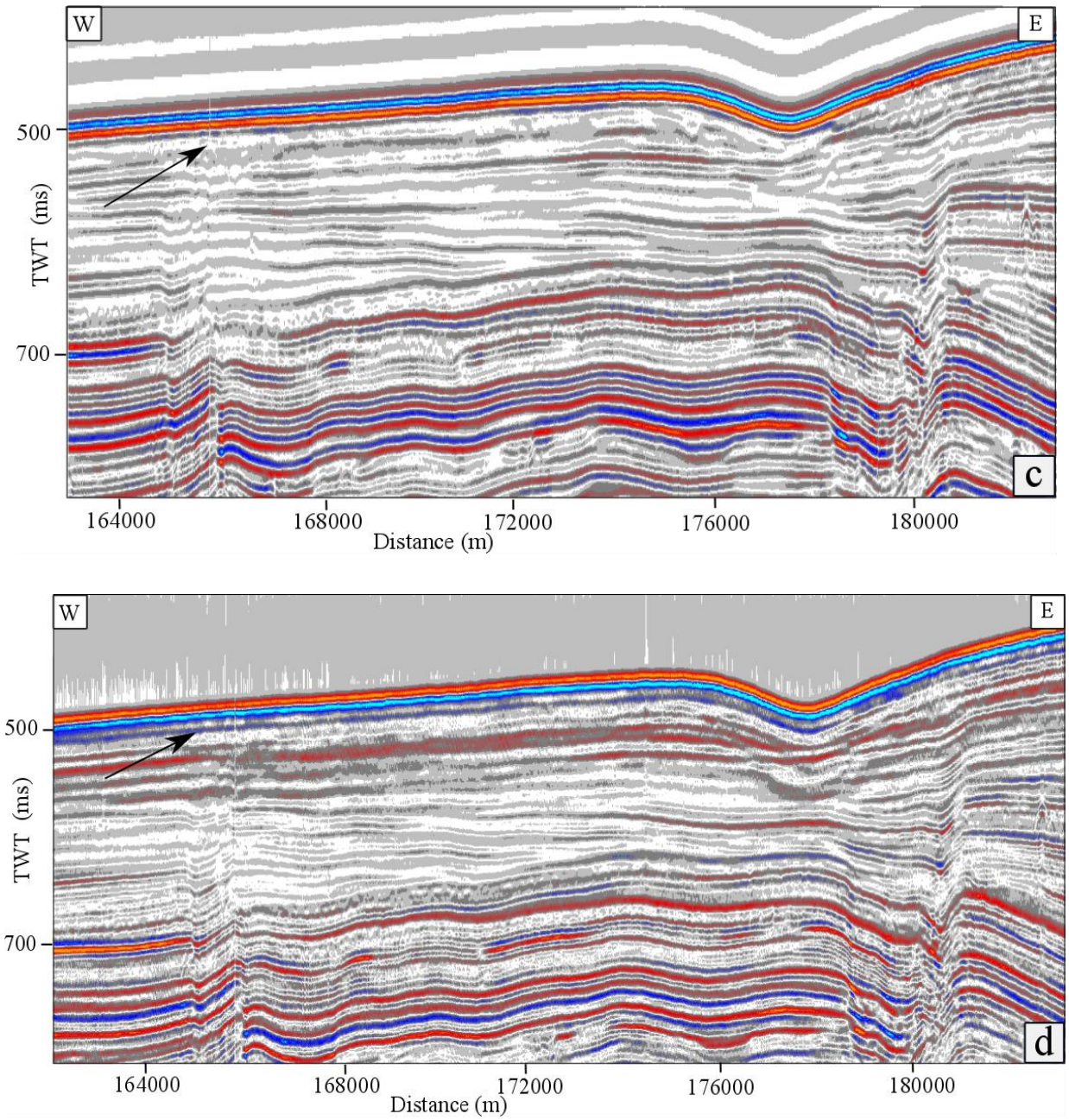

Figure 3.15. Results of testing the deconvolution filter along Line-19. **(a)** 2D seismic section from the original 3D seismic volume. **(b)** Line-19 with a deconvolution filter of filter length 100ms and gap length 8ms. **(c)** Line-19 with a deconvolution filter of filter length 100ms and gap length 4ms. **(d)** Line-19 with a deconvolution filter of filter length 100ms and gap length 16ms. Note that the deconvolution filter of filter length 100ms and gap length 8ms show similar results as shown by arrows for the amplitude anomaly at the seabed as shown in the original 3D seismic volume.

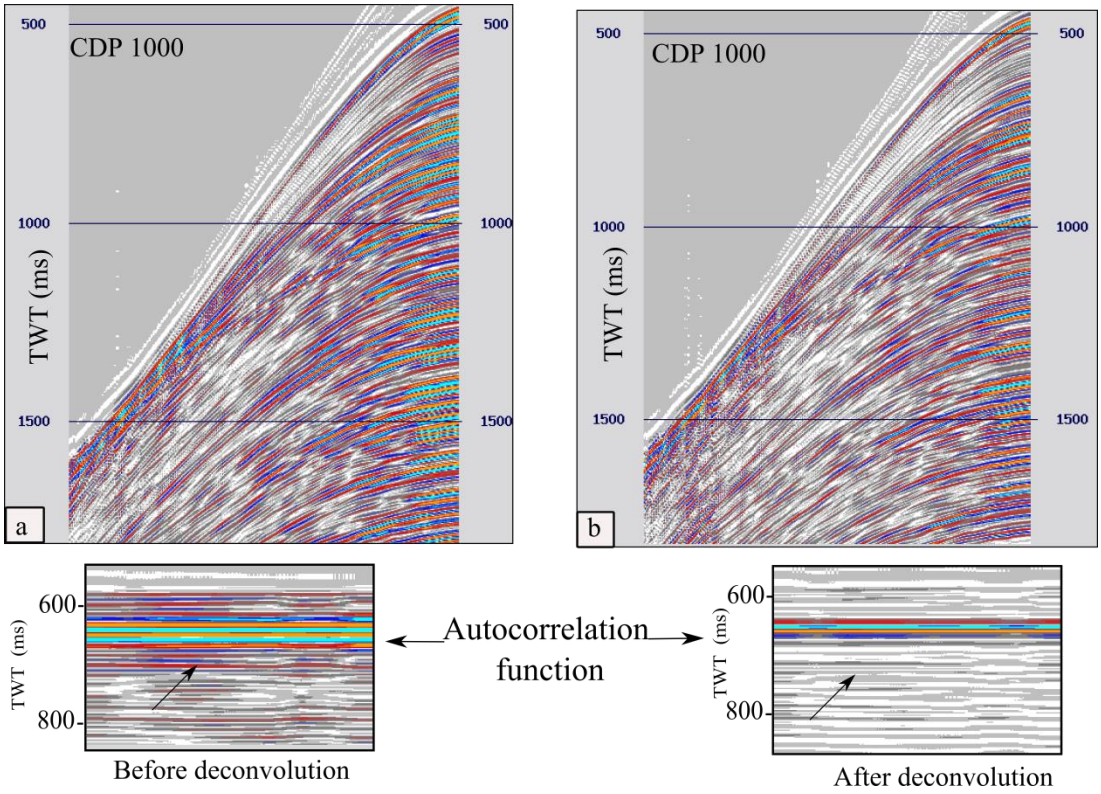

Figure 3.16. CDP gather from Line-19. **(a)** Before applying deconvolution. **(b)** After applying deconvolution. Note that this filter has improved the resolution of the seismic data by compressing the seismic wavelet and attenuating the low frequencies.

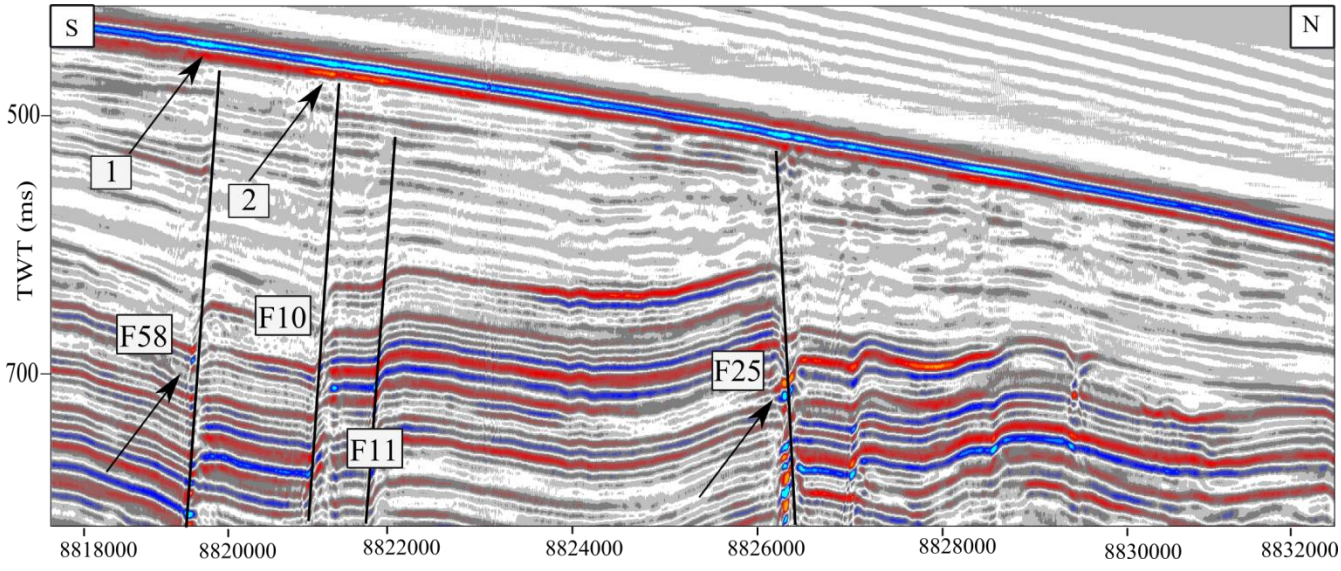

Figure 3.17. Result of the deconvolution with filter length of 8ms and gap length of 100ms along Line 3328. Note how the filter has improved or promoted the appearance of the amplitude anomalies at the seabed as shown by arrows 1 and 2 compared to the final stack with radon filter in Figure 3.14a.

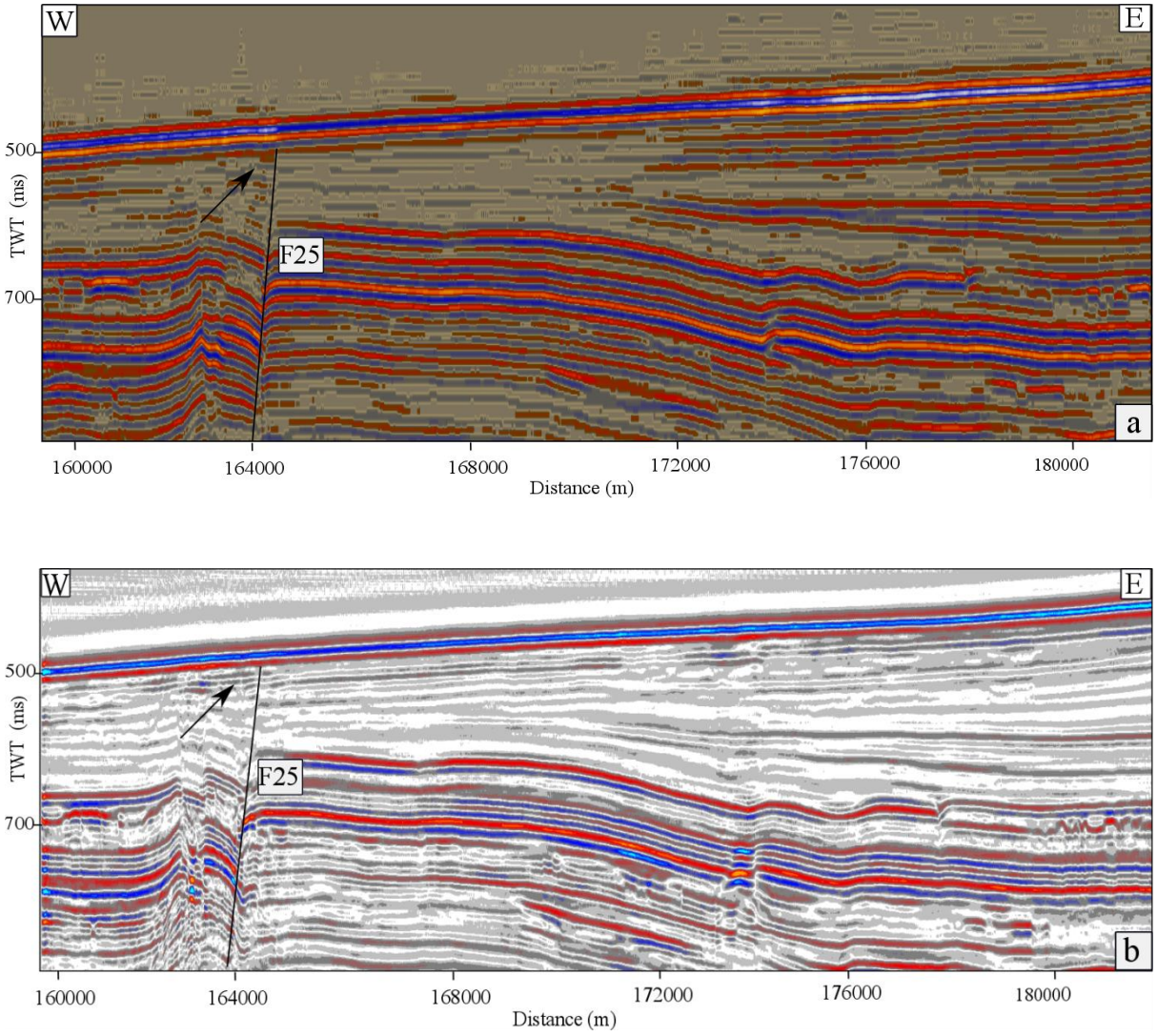

Figure 3.18. (a) The original 2D seismic section from the 3D seismic volume. **(b)** Final seismic stack section of Line-43 with the deconvolution of gap length 8ms and filter length 100ms.

Also, the deconvolution filter along Line-43 from the 3D pre-stack data in the northern part of the study area (Figure 3.18b) shows results of weaker seabed anomalies similar to those of the final stack section compared to the equivalent section from the original 3D seismic volume in Figure 3.18a.

3.4.2 Post-stack migration (Kirchhoff migration)

The final step in the seismic processing is the Kirchhoff migration which re-positions the primary reflections to their original positions and removes the effect of the dip on the final stack sections (figures 3.19a, 3.19b, 3.19c and 3.19d). The post-stack Kirchhoff migration provides an improved image for the final stack seismic sections; in particular, it enhanced the sharpness of the faults and produced a better image compared with the faults along the original 2D seismic stacked sections extracted from the original 3D seismic volume, as shown by arrows 1, 2 and 3 in figures 3.19a, 3.19b, 3.19c and 3.19d. More important is that Kirchhoff migration does not alter the amplitude anomalies mapped at the seabed.

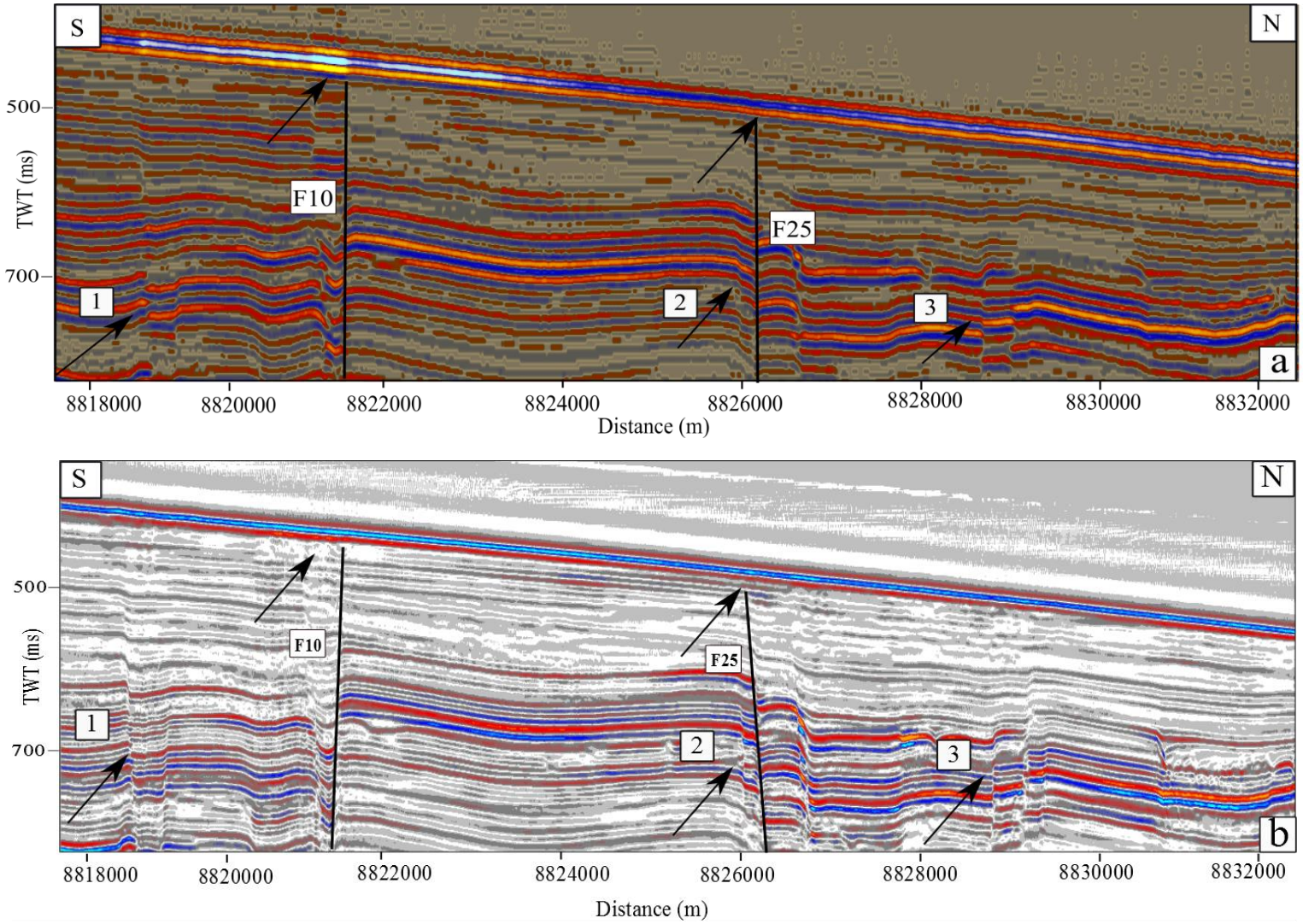
S
N
500
700
TWT (ms)
F10
F25
1
2
3
a
8818000
8820000
8822000
8824000
8826000
8828000
8830000
8832000
Distance (m)
S
N
500
700
TWT (ms)
F10
F25
1
2
3
b
8818000
8820000
8822000
8824000
8826000
8828000
8830000
8832000
Distance (m)

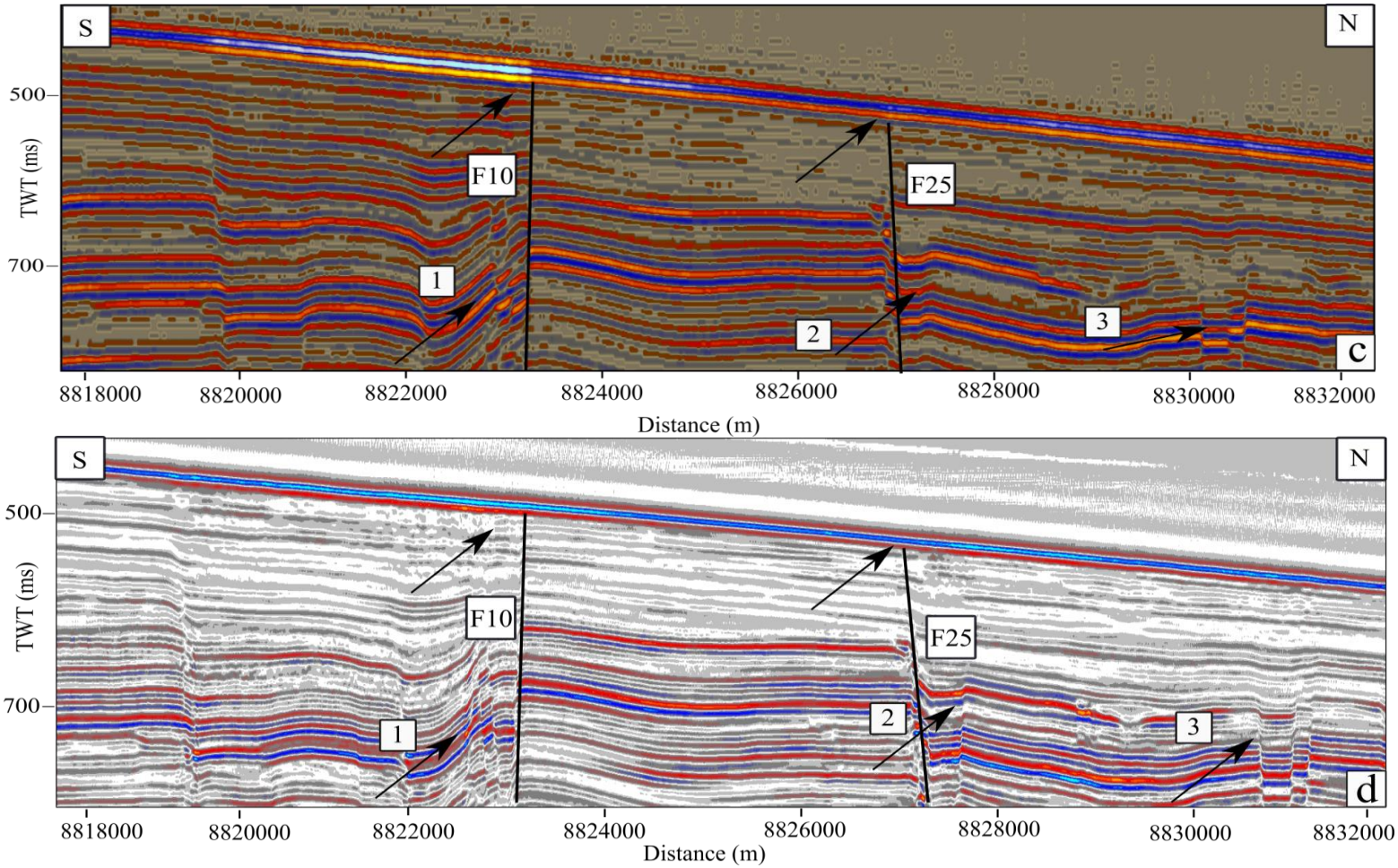

Figure 3.19. **(a)** The original 2D seismic stack section (from the 3D volume) along Line-3329 from the 2D seismic data. **(b)** The result of the post-stack Kirchhoff migration along the 2D–Line-3329. **(c)** The original 2D seismic stack section (from the 3D volume) along Line-3330 from the 2D seismic data. **(d)** The result of the post-stack Kirchhoff migration along the 2D–Line-3330. Arrows 1, 2 and 3 shown in 19a, 19b, 19c and 19d show the differences in the sharpness of the faults along the two sections.

3.5 Discussion

3.5.1 The sensitivity of the Radon demultiple and the deconvolution in the final stack seismic sections

In this study, the Radon filter was applied, and it managed to suppress the multiples; however, it did not produce the same anomaly at the seabed, in particular above Fault F10. The Radon filter is sensitive to many parameters that could affect the final result and, as demonstrated above, in particular to the input velocity model. There is a risk that the amplitude anomalies observed on the 3D data volumes used in Chapter 2 and in the Langhi et al. (2010) study are an artefact of poor velocity picking for the multiple suppression processing. However, it is considered to be unlikely as careful quality control on the velocity model would reveal the cause, and the correction is simple.

To avoid any effects from the Radon demultiple filter, frequency filtering was tested without application of the Radon. This was possible as the target was the seabed reflection event which was clear of the first multiple event.

3.5.2 Effects of frequency filters on the seismic anomalies at the seabed from different data sets in the Laminaria High

The processing results of the 2D and the 3D pre-stack data confirm the amplitude anomalies shown in the 3D seismic volume (Figure 3.1b). The effect of the thin bed could also be considered along the seabed reflector. As explained in the introduction section that amplitude anomalies could also result from the tuning effect of varying bed thickness (Widess, 1973) and that the ability of thin layers respond is frequency dependent. Hence, these anomalies might be created by the effect of thin layer and fluids content.

It is noted that the seabed anomaly in particular above Fault F10 along the processed lines (19, 3328, 3329 and 3330) is weaker compared with the same anomaly associated with Fault F10 along the original 3D seismic volume. These different results could be related to the manipulation of the frequency spectrum through the deconvolution and Butterworth bandpass filter. Also, this is probably due to the limitations of the simplified processing workflow used here as the objective was to understand the influences of processing rather than to reproduce the same result. Tests showed that the perception of the amplitude anomalies could be changed by varying the filter parameters of the filters. For this reason, it is concluded that there is a possibility that the anomalies along the processed data in this chapter and the interpreted 3D data in Chapter 2 could be related to the different parameters used in processing these data sets. However, given that using a basic processing workflow it was possible to produce sections which showed strong similarities with the 3D volume gives confidence that the anomalies are robust.

Furthermore, the discussion above may explain the reason for the different distributions of amplitude anomalies at the seabed in this study and in Langhi et al.'s (2010) study. This is because Langhi's study used merged seismic data that consisted of three data sets acquired at different times. Hence, there may have been some manipulations applied when merging the data to match the frequency content of the combined data which may have altered the relative amplitude anomalies.

3.6 Conclusion

- The most important outcome from this chapter is the issue of using processed data without the knowledge of the background processing sequence for the data. For this reason the veracity of processing of any seismic data needs to be questioned, and should not be taken for granted especially if different surveys produce conflicting interpretations.
- This study shows that it is possible to produce amplitude anomalies that are similar to those shown in the 3D data in Chapter 2 by applying basic processing sequences that include just the deconvolution and Butterworth filters which are both forms of manipulation of the frequency spectrum.
- It is concluded that the amplitude anomalies mapped in Chapter 2 are reliable and caused by localised changes in the subsurface.
- It is concluded that the sensitivity of amplitude anomalies to the frequency content which could explain the apparent difference between mine and Langhi's et al (2010) interpretation.

Chapter 4: Petroleum migration modelling in the Laminaria High: influence of critically stressed faults on hydrocarbon migration and leakage

4.1 Introduction

Amplitude anomalies appear on the seabed in the Laminaria High and are associated with major faults in the southern part of the survey area (Figure 4.1) (Chapter 2). These anomalies are interpreted as authigenic carbonate cementation developed in response to hydrocarbon leakage along major faults in the study area and the nearby areas (Hovland et al., 1994., O'Brien et al., 1999; O'Brien and Wood, 1995; Langhi et al., 2010). The aim of this chapter is to undertake hydrocarbon migration modelling in order to investigate the impact of faults and host-rock lithologies on hydrocarbon seepage at the present-day sea floor.

Drilling in the Laminaria High area discovered many underfilled or breached hydrocarbon traps. The majority of the 67% unsuccessful exploration wells in the study area failed due to trap breaching. (De Ruig et al., 2000). Previous studies suggest that the state of stress resolved on trap bounding faults has influenced trap integrity (Castillo et al., 2000). Reservoir stress studies in the Timor Sea (Castillo et al., 1998) and the North Sea (Wiprut and Zoback, 2000) suggested that fault geometry, the principal stress direction and magnitude, and pore pressure play an important role in trap integrity along the reservoir-bounding faults. Shuster et al. (1998) suggested that hydrocarbon leakage in the islands of Kai and Tanimbar in the Timor Sea occurs along critically stressed faults due to the change in the stress field, which mainly results from the oblique collision between the Australian and Eurasian plates and the subsequent fluid leakage.

Mildren et al. (1994) and Castillo et al. (1998) argued that the orientation of the fault planes relative to the Late Miocene-Recent stress field in the Timor Sea in the Zone of Cooperation (ZOCA) is controlling the sealing potential of fault-bounded traps.

Cooper et al. (1998) suggested that the dilational fault tip propagation of the Jurassic and Late Tertiary faults during Tertiary extension is responsible for hydrocarbon leakage. King et al. (1994) argued that stress interaction between adjacent faults would influence fault activity, such that a slip on one fault can increase or inhibit a slip on another. This observation has important implications for fault activity, and this, in turn, might induce a given fault to becoming open, allowing fluid migration or leakage.

Hydrocarbon accumulation occurs when the resistive force (capillary entry pressure) equals or exceeds the driving force (buoyancy pressure) along the carrier bed (Schowalter, 1979). Migration modelling in sedimentary basins is not straightforward due to the uncertainties in the heterogeneities of lithofacies and their petrophysical properties (Luo et al., 2015; Carruthers, 2003). Studies of petroleum migration have covered the understanding of many aspects of migration (Carruthers, 2003) and leakage including the reasons for dry wells around the world. For example, Corradi et al. (2009) applied a 3D lithofacies model in West Africa in a marine basin to address the issue of a dry well located in a petroleum system with a particularly productive source rock. Migration models showed that hydrocarbons were deviated laterally due to the existence of a seal layer, which prevented hydrocarbons from flowing through the carrier beds. Also, petroleum modelling can help in identifying the more likely hydrocarbon pathways in the subsurface, in particular areas that are affected by hydrocarbon leakage.

Abbassi et al. (2015) used a three-dimensional (3D) migration model, based on the interpreted faults and horizons from the Laminaria High and adjacent Nancar Trough. The faults were separated into syn- and post-rift sets, which were assumed to be either “open” or “closed” with respect to hydrocarbon migration (Abbassi et al., 2015, their Table 3). This approach was used to predict the locations of filled and breached traps

across the Laminaria High. However, the paper provides little information on how the "open" and "closed" faults were implemented in the simulations. More fundamentally, the limitations in processing time meant that Abbassi et al.'s (2015) 3D models were entirely deterministic. The study described in the present chapter differs from Abbassi et al.'s approach in two important aspects. First, it models hydrocarbon migration in two dimensions (2D), along vertical cross-sections. 2D methods require less computational time and therefore permit a stochastic approach, based on multiple realisations. A stochastic approach is preferable because it allows the uncertainties in the input parameter ranges to be evaluated (see section 4.3.2.2.4). Second, this study uses a more geologically driven approach to assigning fault properties. In particular, it tests the hypothesis that critically stressed faults (or fault segments) are more likely to permit fluid migration (see section 4.6.2.1 and 4.6.2.2).

Here, I use Permedia® software to model hydrocarbon migration and seepage. The detailed methodology is described in ***section 4.6.2*** but, briefly, the models are based on depth-converted seismic reflection profiles that constrain the large (deca- to kilometre) scale geometry of the faults and reflectors from the seabed down to the reservoir/source rock interval. The profiles are converted to raster images, and individual pixels are assigned a capillary entry pressure according to the host rock lithology (calibrated using well-log data) and whether the pixel lies along a critically-stressed fault plane (estimated based on the locations and orientations of mapped fault planes and the *in-situ* pore-pressure and stress gradients, e.g. Morris et al. 1996). Migration is simulated by evaluating the relative magnitudes of driving (e.g. the buoyancy force of fluids) and resisting (e.g. the capillary entry pressure) forces at each pixel at every timestep. A limitation of this approach – and that of Abbassi et al. (2015) – is that migration modelling is based on the present-day fault and horizon geometries.

Therefore, the models are designed to provide insights into the controls on hydrocarbon seepage at the present-day, but provide no direct information about the development of hardgrounds preserved on more deeply-buried, "palaeo-seabed" horizons (e.g. Horizon H9, Chapter 2). A second limitation relates to the analysis and identification of critically-stressed fault planes. It is important to emphasise that there is no single, deterministic value of slip (or dilation) tendency (Morris et al. 1996) above which a fault is critically stressed. Rather, I evaluate the slip and dilation tendencies on multiple faults and then rank these according to magnitude. The underlying assumption is that faults with larger slip and/or dilation tendencies are more likely to act as fluid conduits that those with smaller slip and dilation tendencies. Finally, the models presented here simulate secondary migration from the source rock intervals; leakage and re-migration from the Laminaria Formation reservoirs are implicit.

The objectives of this study are to perform migration modelling to **(a)** investigate the role of the stress regime on fault flow properties; **(b)** constrain the circumstances of when faults act as conduits, compared to flows through the background stratigraphic section; and **(c)** assess how migration modelling and percolation can inform our understanding of seepage in the area of interest. In this study, it is hypothesised that hydrocarbon leakage at the seabed is associated with the critically stressed faults. To address these objectives, this study: **1)** examines the role of the critically stressed faults on fluid migration; **2)** models the possible fluid migration pathways and investigates the formation of the amplitude anomalies at the present-day seabed; and **3)** investigates the effect of the heterogeneity of the lithology (the entry pressure values) along fault traces.

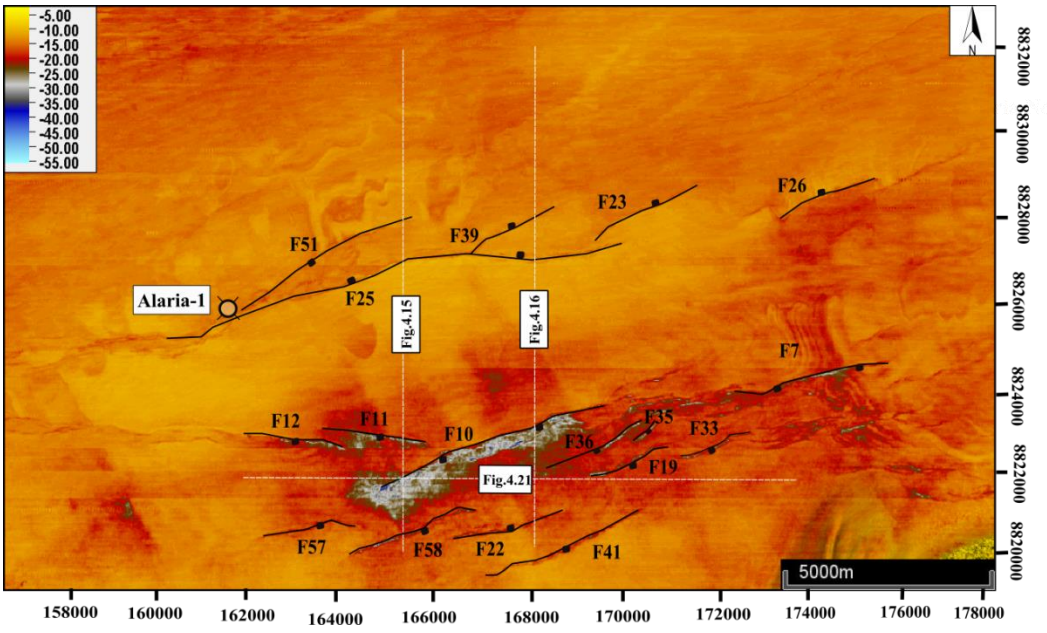

Figure 4.1. Original amplitude map of the seabed showing the location of the seismic sections in the N-S and E-W direction that are used in the migration modelling. Note that the main Fault F10 is associated with the amplitude anomaly at the seabed with no evidence of these anomalies along Fault F25 in the northern part of the study area. Cross lines no. are 2525 and 2275 and the inline no. is 2375.

4.2 Geological setting

This study is focused on the Laminaria High in the northern part of the Bonaparte Basin; it is located near the edge of the Timor Trough, bordered by the Nancar and Cartier troughs to the south and the Flamingo Syncline to the south-east (Smith et al., 1996) (Figure 4.2a).

The structural trend of the Laminaria High is orientated E-W, and the direction of the present-day maximum horizontal stress (SH max) is NNE-SSW, sub-perpendicular to the regional fault strike (De Ruig et al., 2000) (Figure 4.2a). For the purposes of our study, the key structures that accommodated Mesozoic to Neogene extension on the Laminaria High are: 1) a set of ENE-WSW striking, Jurassic-Cretaceous horst and graben structures; and 2) a set of mainly ENE-WSW striking, Neogene normal faults

that initiated above the reactivated Mesozoic structures (Gartell et al., 2006) (Figure 4.2a). A deeper set of E-W striking, Permian horsts underlay the area (Langhi et al., 2008), but are too deep to be imaged within our 3D seismic volume, and are not considered further here.

4.3 Lithostratigraphic and petroleum elements

The Lower to Middle Jurassic are represented by the Plover Formation. This formation comprises very thick, sand-dominated, fluvial and deltaic sediments that reflect the deltaic and shelf marine environment which represents the pre- or early rift sequence (Smith et al., 1996; de Ruig et al., 2000) (Figure 4.2b). This sequence is considered to be the gas and oil source rock at a depth of approximately 3500 m and is 114 m in thickness. The Plover source rock contains heterogeneous type II/III kerogen (Abbassi et al., 2015).

The Middle to Upper Jurassic sequence on the Laminaria High is the most important section that controls the hydrocarbon accumulation (Smith et al., 1996) (Figure 4.2b). The reservoir section lies within the Callovian to Lowermost Oxfordian Laminaria Formation. This formation consists of massive sandstone with minor interbedded claystone. During the Upper Jurassic to Lower Cretaceous, the Laminaria Formation was conformably overlain and sealed by the Frigate shale formation within the Oxfordian–Kimmeridgian succession. The Frigate shale consists of a thick section of shale interbedded with minor silty sandstone (Smith et al., 1996) and is overlain by the open marine shales of Flamingo (Tithonian-Berriasian) and Echuca Shoals (Valanginian-Barremian) formations (Figure 2b). These formations reflect the deepening of the depositional environment, which coincides with a rise in the relative sea level. They represent the seal section as a thick Mesozoic sequence of shale and silty claystone (Wittham et al., 1996). The Frigate and Flamingo formations are

considered to be potential source rocks in addition to the Lower Cretaceous Echuca Shoals formation (Abbassi et al., 2015) (Figure 4.2b).

The Lower to Upper Cretaceous is represented by the Bathurst Island Group (Figure 4.2b). At the top of this group, the lithology changes from dominantly clastic sequences into a carbonate-dominated sequence represented by the Johnson, Hibernia, Prion and Cartier formations (Palaeocene to Oligocene). The Miocene to Pleistocene Oliver and Barracouta formations include calcarenite and calcilutite, which are the shallowest sedimentary strata within the study area, and represent an extensive cover of prograding shelf carbonate deposits (Wittham et al., 1996) (Figure 4.2b).

The Australian Plate converged with the Indonesian arc in the Tertiary and resulted in rapid heating of the source rocks. This collision is considered to be the major contributing factor in generating hydrocarbons (Smith et al., 1996). The initial hydrocarbon charge of oil and gas occurred during the Late Jurassic-Early Cretaceous, followed by the main phase of oil charge in the Middle to Late Eocene. The late phase of oil and gas charge is suggested to have occurred from the Miocene onward (de Ruig et al., 2000)

Hydrocarbons are trapped within the structural traps that consist of east-west trending tilted normal faults or horst blocks which formed during the Upper Jurassic rifting (Whittam et al., 1996). Secondary reverse structures associated with the main east-west faults are suggested to act as secondary hydrocarbon traps and/or migration barriers (Langhi and Borel, 2008).

In 1994, ten wells were drilled in the permit area AC/P8, covering the area of Laminaria High at the northern edge of the Bonaparte Basin (Figure 4.2a). However, no new oil fields were found; rather, anticipated traps were found to be breached and

drained. Most of the drilled wells show evidence of residual oil (De Ruig et al., 2000; Abbassi et al., 2015), and evidence of hydrocarbon leakage is seen in this area. This was confirmed by petrophysical and geochemical analyses of core samples in the nearby areas (e.g the Vulcan sub-basin and the Yampi Shelf) (O'Brien and woods, 2005; Rollet et al., 2006).

Fault activity and reactivation are suggested to have played a key role in hydrocarbon leakage in the study area. De Ruig et al. (2000) argued that during reactivation, the Jurassic faults were linked with the Miocene-Pliocene faults and hydrocarbon leakage occurred at those points where the critically stressed parts of the Jurassic faults linked with the Tertiary faults.

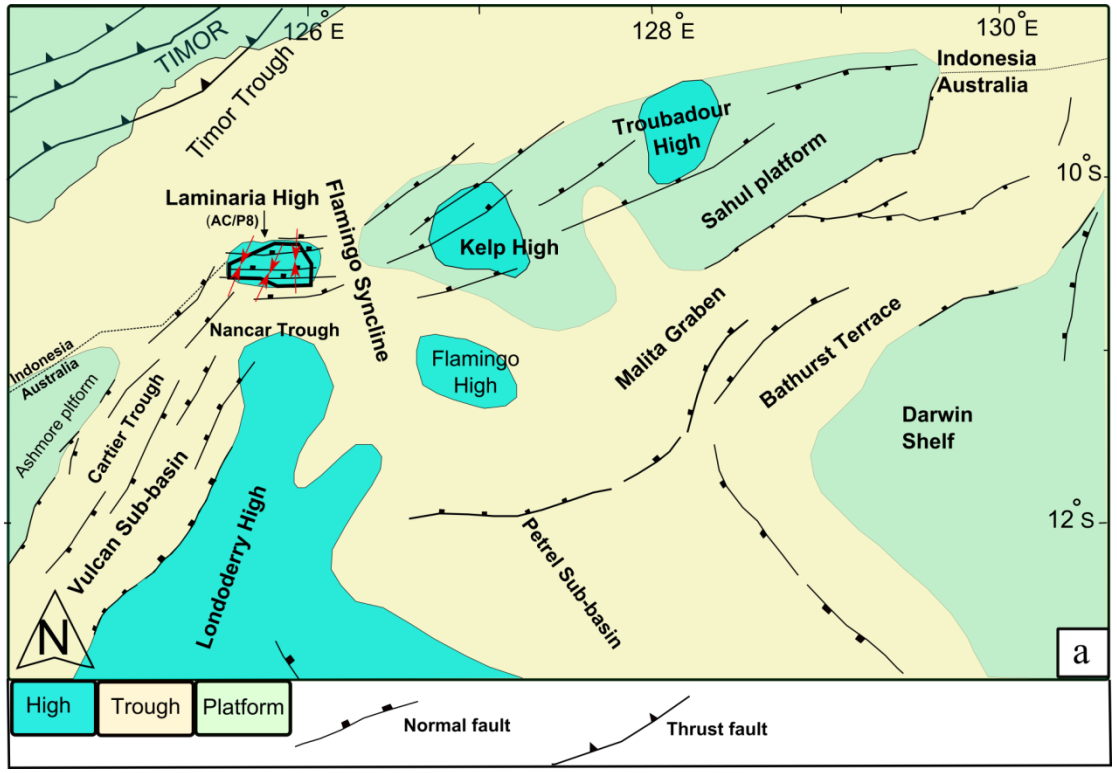

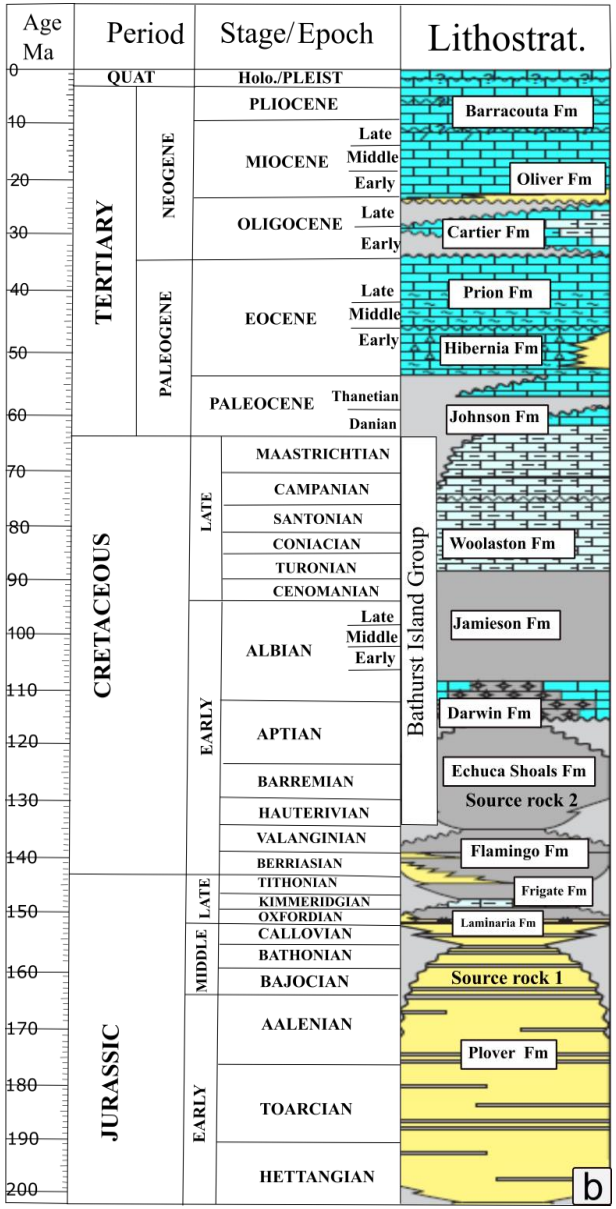

Figure 4.2. (a) Geological setting and Jurassic structure regional map of northwestern Bonaparte Basin modified from Long and Imber (2012). Note the study area is highlighted in the black box and the red arrows show the stress direction in the Laminaria High (after Castillo et al., 2000), **(b)** Generalised stratigraphic column for the Laminaria High.

4.4 Mechanisms of secondary hydrocarbon migration

Primary hydrocarbon migration is the movement of hydrocarbons from the source rock, while the further movement of hydrocarbons into more permeable layers along the carrier bed is secondary migration (Schowalter, 1979) (Figure 4.3).

The main driving force for secondary hydrocarbon migration in the subsurface is the bouyancy force (Pw), it occures due the density differences between the hydrocarbons and the surrounding pore water (Carruthers and Ringrose, 1998). The buoyancy force will increase with increasing the density differences for a length of hydrocarbon column (Equation 4.1) (Tissot and Welte, 1978):

$$P_w=(\rho_w-\rho_p)gh \qquad (4.1)$$

Where P_w is the buoyancy force, ρw is the density of water (kg/m^3), ρp is the density of petroleum, *g* is the acceleration due to gravity in m/s^2, and *h* is the height of the oil column in m.

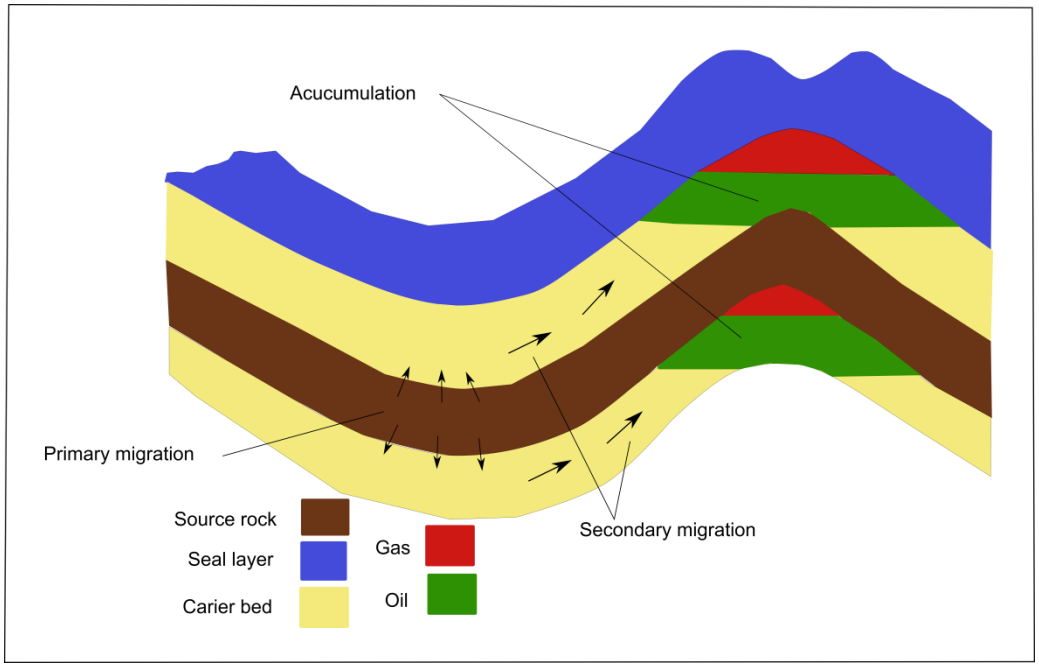

Figure 4.3. Primary and secondary petroleum migration processes (modified from Tissot and Welte, 1984)

When hydrocarbons start to migrate from one rock pore to another pore, there will be a resisting force against hydrocarbon migration which is the capillary pressure (Pc). It is the minimum pressure required to push the hydrocarbon through the pore of the rock and displace the water. The magnitude of this force, is known as the capillary entry pressure (CEP). This pressure is calculated as (Equation 4.2) (Downey, 1984; Vavra et al., 1992):

$$Pc = \frac{2\Upsilon\cos\theta}{R} \qquad (4.2)$$

Where Pc is the CEP in Pascal (N/m^2), Υ is the interfacial tension (N/m), Θ is the contact angle between the fluid boundary and the rock, and R is the radius of the pore throat (Figure 4.4).

To allow hydrocarbon migration, the buoyancy force (Pw) of a column should exceed the capillary entry pressure (Pc) of the rock (i.e. Pw > Pc) (Vavra et al., 1992).

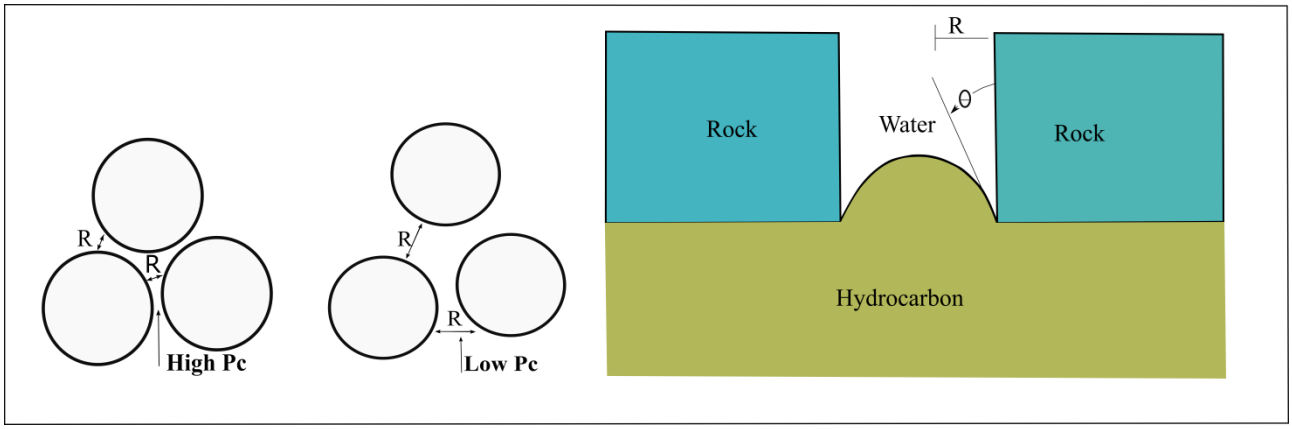

Figure 4.4. Parameters controlling the capillary displacement pressure (modified from Downey, 1984), Note the capillary entry pressure increase when the throat radius of the largest connected pores decreases and vice versa.

4.4.1 The behaviour of hydrocarbons during secondary migration

Secondary hydrocarbon migration starts as a result of a very low charge rate from the source rock. The low charge rate limits dispersion of hydrocarbons, which migrate as thin strings through the carrier beds (Schowalter, 1979). This means that the volume of oil-bearing rock is less than the water-bearing rock. Hydrocarbon accumulation occurs at or under layers of higher capillary pressure for the lithologies (seal layers), and then the thin strings of hydrocarbons will thicken as the buoyancy pressure increases and hydrocarbon accumulation continues below the seal layer; eventually the buoyancy force will overcome the capillary pressure of the seal layer and breaching will occur and then branches of oil strings will develop (Carruthers and Ringrose, 1998 and Carruthers, 2003). The process of breaching and migration will continue until it reaches another seal layer that has higher capillary pressure than the buoyancy force of the hydrocarbons, which prevents hydrocarbon migration from reaching the surface (Carruthers and Ringrose, 1998; Carruthers, 2003).

4.5 Fault transmissivity and the role of slip and dilation tendency on hydrocarbon migration and leakage

Faults have potentially two roles in controlling fluid flow in sedimentary basins. They can behave as seals (low permeability barriers and high capillary pressure) or as pathways (high permeability and low capillary pressure) (Knipe, 1993).

The dominant control of a fault seal in this study is to increase the capillary entry pressure (Pc) of the barrier rock along, or across the fault plane. Faults can act as seals under different circumstances (Weber et al., 1978 and Yielding et al, 1997) (Figure 4.5):

1) “Juxtaposition”, when a sand reservoir is juxtaposed aginst a low permeability sequence (e.g. shale);

2) “Clay smear”, when the clay or the shale penetrates the fault plane, in a way that increases the entry pressure along the fault plane;

3) “Cataclastic”, which results from the sand grain crushing that produces a fault gouge of finer grained material; hence it creates a higher capillary pressure along the fault;

4) “Diagenesis”, when the fault plane becomes partially or completely impermeable due to preferential cementation, which creates a hydrostatic seal.

In all cases, the impact is to reduce the pore-throat radii along or across the fault plane, thus increasing the capillary entry pressure. Fault seals can fail by capillary leakage when the buoyancy pressure of hydrocarbons exceeds or equals the capillary entry pressure (CEP) of the carrier bed or the fault surface (Jones et al., 2000).

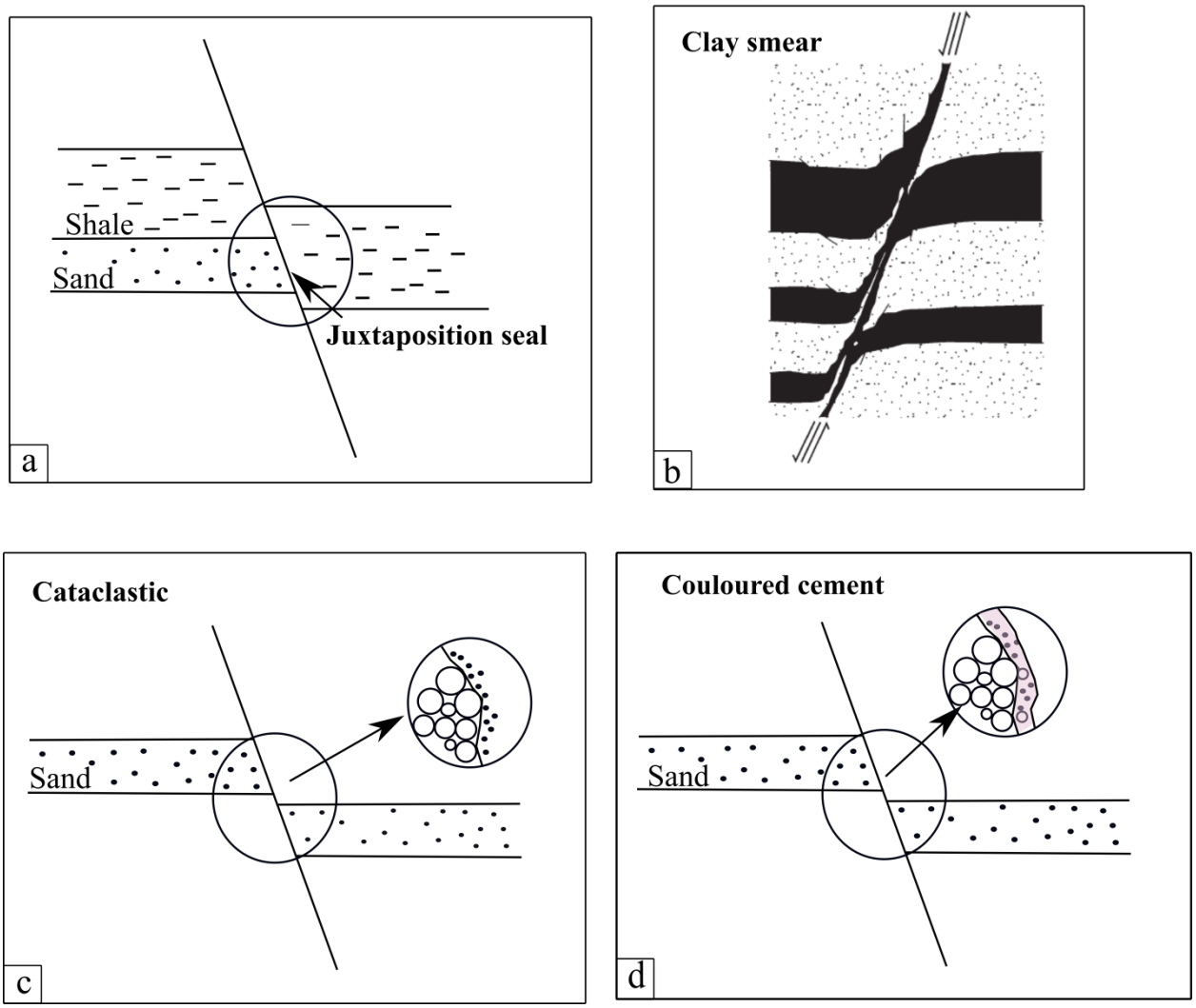

Figure 4.5. Schematic of fault seal conditions. **(a)** Juxtaposition, when a sand reservoir is juxtaposed aginst a low permeability sequence (e.g. shale). **(b)** Clay smear, when the clay or the shale penetrates the fault plane, in a way that increases the entry pressure along the fault plane (from Yielding et al., 1997). **(c)** Cataclastic, which results from the sand grain crushing that produces a fault gouge of finer grained material; hence it creates a higher capillary pressure along the fault. **(d)** Diagenesis, when the fault plane becomes partially or completely impermeable due to preferential cementation, which creates a hydrostatic seal.

On the other hand, faults can be conductive pathways for fluid flow. Townend and Zoback (2000) argue that critically stressed faults maintain high crustal permeabilities and hydrostatic fluid pressures over timescales of 10–1000 yr. They suggest that brecciation with slip along critically stressed faults (i.e. faults that are in a state of incipient failure) counters the mechanism of fault sealing. Brecciation will tend to disrupt clay smears and lead to dilatancy. Hence, resulting in incremental failure of faults and maintaining high permeability (Townend and Zoback, 2000).

The likelihood of faults to slip can be estimated given knowledge of the stress field and orientation of the fault surface. Slip along faults is likely to occur when the shear stress (τ) exceeds or is equal to the frictional resistance (F), which is proportional to the normal stress (σ_n) along the fault surface. Therefore, the fault surface will slip based on its cohesive strength and the coefficient of friction (μ) (Morris et al., 1996).

$$F \leqslant \tau = \mu \ \sigma_n \tag{4.3}$$

Slip-tendency (T_s) analysis is used for assessing the relative risk of fault slip and leakage. It is a type of stress attribute that can be mapped at any fault surface (Morris et al., 1996). This attribute is a function of the ratio of normal to shear stress on the fault surface:

$$T_s = \tau / \sigma_n \tag{4.4}$$

Slip tendency ratios vary from 0-1; the higher the number, the more likely the fault will slip on a cohesionless surface (Morris et al., 1996). Barton et al. (1995) showed that faults would be conductive pathways for fluid flow when they are critically stressed, i.e. when the ratio of shear to normal stress acting on the fault surface is

between ~ 0.5-1. In contrast, non-critically stressed faults are less likely to be hydraulically conductive.

Another stress attribute that is used for slip assessment is the dilation tendency (T_d), which is a function of the ratio of the differential stresses (Figure 4. 6):

$$T_d = (\sigma_1 - \sigma_n)/ (\sigma_1 - \sigma_3) \quad (4.5)$$

where σ_1 is the maximum principal stress, σ_3 is the minimum principal stress.

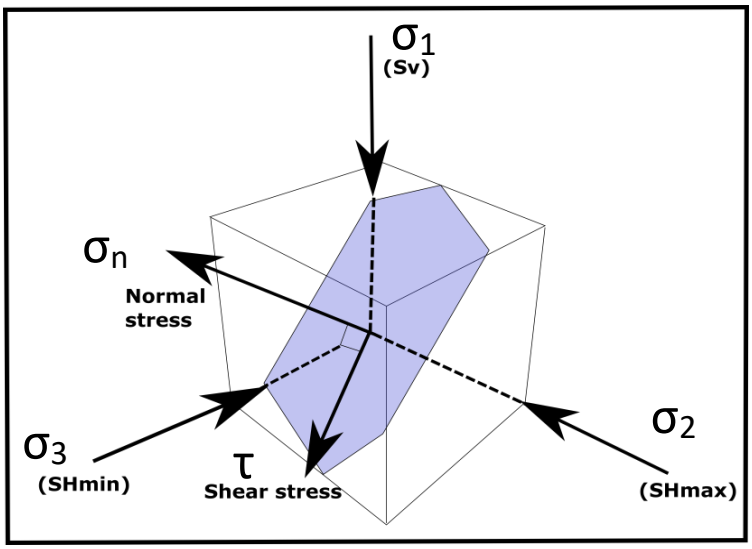

Figure 4.6. Normal stress σ_n, and shear stress τ on an arbitrary surface. The stress field is defined by three principal stress components σ_1, σ_2 and σ_3.

The dilation tendency indicates which fault orientation is more likely to be open and to allow fluids to migrate through the fault surface. The dilation tendency varies from 0-1; the higher the value, the more likely the fault will dilate, and fluids transmit through this fault (Morris et al., 1996).

However, assigning any fault as being sealing or non-sealing is not simple, due to the combination of variations in the throw and the lithology results in heterogeneous fault surfaces. Hence, a single fault may act as a seal over some parts of its surface and leak over others (Weber et al., 1978 and Yielding et al., 1997).

4.6 Data and methodology

4.6.1 Data

In this study, we use 2D seismic crossline and inline sections extracted from depth-converted 3D volumes provided by Geoscience Australia (Chapter 2). Depth conversion is performed using check-shot data and interval velocities from well Alaria-1. The time-depth curve is shown in Appendix_3A. Also, the well Alaria-1 completion report is used to extract the lithological and stratigraphic information of the study area. For the purposes of this study, the 2D seismic sections crosscutting the amplitude anomalies that exist in the southern part of the seabed are chosen (Figure 4.1).

4.6.2 Methodology

In this section, two methods are explained and their results presented. First, critical stress analysis (slip and dilation analyses) along 3D fault planes is applied using Trap Tester® to evaluate the stress behaviour along faults. Second, migration models are produced using Permedia® to assess how migration modelling and percolation can inform our understanding of hydrocarbon seepage along the seabed in the area of interest. The results from the stress analysis are used to estimate the capillary entry pressures for fault traces along the seismic sections (Section 4.6.2.2.2).

Note: for all migration models, the term “CEP” is used for the input capillary entry pressures.

4.6.2.1 Critical stress analysis

Determining the relationship between faults and the in-situ state of stress provides a means for assessing the relative risk of fault slip and hydrocarbon leakage. The study area is characterised by a strike-slip stress regime where the principal stresses are S_{Hmax} (maximum horizontal stress), > S_V (vertical stress) and >S_{Hmin} (minimum horizontal stress), and the orientation of S_{Hmax} is N015E (Castillo et al., 2000). Slip and dilation tendency attributes are calculated and mapped along interpreted fault planes within the area of interest using the in-situ stress data shown in Table 4.1. To test the sensitivity of stress field to the input stress gradient, the stress gradient was varied by ±0.0004 MPa/m to envelope the stress gradient from Castillo et al's. (2000) study. Also, the stress direction of the stress gradient is varied by ±6 (Castillo et al., 2000). The stress field is generated using the minimum horizontal stress (S_{Hmin}), maximum horizontal stress (S_{Hmax}), vertical stress values (S_V), stress direction and pore pressure (PP) that are estimated from Castillo et al. (2000). This stress field calculates the slip and dilation tendency attributes along each fault, which is then mapped along fault surfaces.

Table 4.1. **(a)** Principal stress field parameters from Castillo et al. (2000) varied by ±0.0004 MPa/m in order to calculate the slip and dilation tendencies. **(b)** The stress direction for the study area from Castillo et al. (2000) varied by ±6°.

a	Stress gradient(MPa/m) ±0.0004 (Castillo et al., 2000)
S_{Hmin}	0.0144 (Castillo et al. 2000)
	0.0148
	0.0140
S_{Hmax}	0.0267 (Castillo et al. 2000)
	0.0263
	0.0271
S_V	0.0236 (Castillo et al. 2000)
	0.0232
	0.024
Pore pressure(PP)	0.01

b	Stress direction (Azimuth) ±6 degrees		
SHmin	105°(Castillo et al.,2000)	99°	111°
SHmax	15°(Castillo et al .,2000)	9°	21°
SV	N/A	N/A	N/A

4.6.2.2 Migration modelling

4.6.2.2.1 Principal workflow using Permedia®

In this study, Permedia® software (Halliburton) is used to model the petroleum migration (Carruthers and Neufeld, 2008) along a selected 2D seismic sections in the N-S and E-W directions. It is based on generating a mesh from the imported 2D seismic amplitude image and consists of a large number of grid cells (Figure 4.7a,b and c). Each cell appears as a separate colour representing a flow identification domain (FID), where each colour is assigned a single petrophysical property, in my case the capillary entry pressure (CEP), defined as the pressure that is required to allow

migration of the non-wetting phase (oil or gas) into the wetting phase (water). Flow occurs when the accumulated hydrocarbons can invade an adjacent grid cell with a lower CEP. The migration modelling is done in time steps of 0.5 million years and to start the migration, the temperature in each source rock cell is increased by 2° C timestep^{-1} until hydrocarbons are expelled from the source rock. Generation continues until the source rock reaches the maximum present-day temperature as shown in Table 3, which is calculated from the geothermal gradient. Modelling of petroleum migration is made through a series of steps which set up the input data for each model. These steps include: **(a)** interpreting the lithology from the seismic section and well information; **(b)** assigning CEP values for each lithology; and **(c)** defining the source rock location and properties. Models are run using the static migration module, which includes the volume properties (or petrophysical properties), source rock properties, and pressure–volume–temperature (PVT) data for hydrocarbons. A summary of these steps is shown in Figure 4.8.

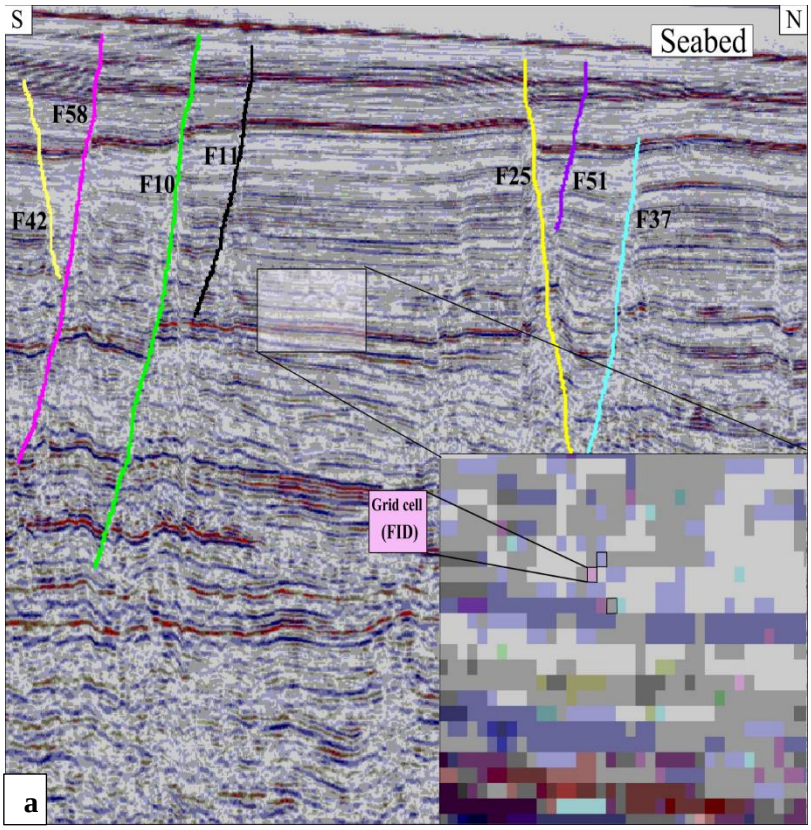

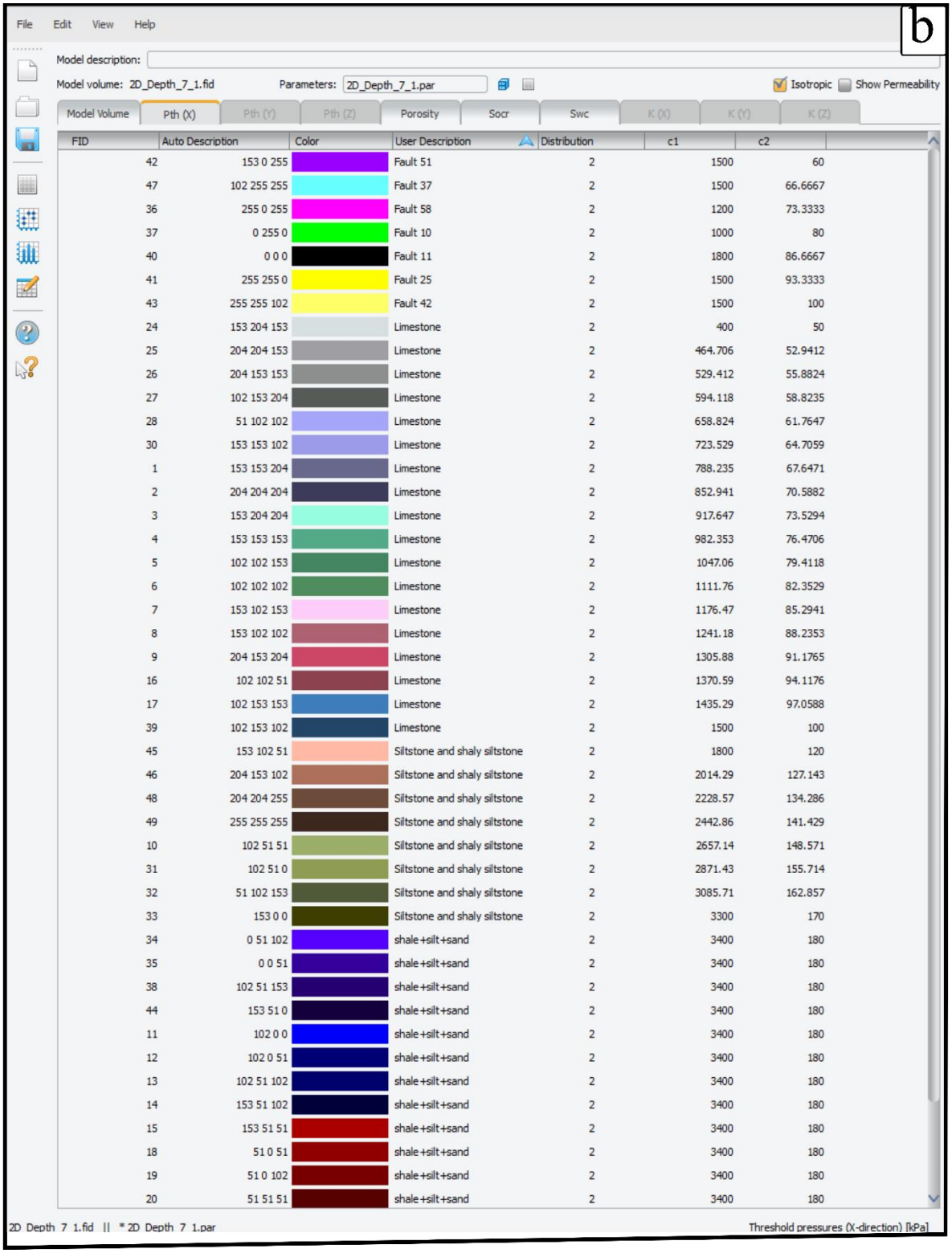

FID	Auto Description	Color	User Description	Distribution	c1	c2
42	153 0 255		Fault 51	2	1500	60
47	102 255 255		Fault 37	2	1500	66.6667
36	255 0 255		Fault 58	2	1200	73.3333
37	0 255 0		Fault 10	2	1000	80
40	0 0 0		Fault 11	2	1800	86.6667
41	255 255 0		Fault 25	2	1500	93.3333
43	255 255 102		Fault 42	2	1500	100
24	153 204 153		Limestone	2	400	50
25	204 204 153		Limestone	2	464.706	52.9412
26	204 153 153		Limestone	2	529.412	55.8824
27	102 153 204		Limestone	2	594.118	58.8235
28	51 102 102		Limestone	2	658.824	61.7647
30	153 153 102		Limestone	2	723.529	64.7059
1	153 153 204		Limestone	2	788.235	67.6471
2	204 204 204		Limestone	2	852.941	70.5882
3	153 204 204		Limestone	2	917.647	73.5294
4	153 153 153		Limestone	2	982.353	76.4706
5	102 102 153		Limestone	2	1047.06	79.4118
6	102 102 102		Limestone	2	1111.76	82.3529
7	153 102 153		Limestone	2	1176.47	85.2941
8	153 102 102		Limestone	2	1241.18	88.2353
9	204 153 204		Limestone	2	1305.88	91.1765
16	102 102 51		Limestone	2	1370.59	94.1176
17	102 153 153		Limestone	2	1435.29	97.0588
39	102 153 102		Limestone	2	1500	100
45	153 102 51		Siltstone and shaly siltstone	2	1800	120
46	204 153 102		Siltstone and shaly siltstone	2	2014.29	127.143
48	204 204 255		Siltstone and shaly siltstone	2	2228.57	134.286
49	255 255 255		Siltstone and shaly siltstone	2	2442.86	141.429
10	102 51 51		Siltstone and shaly siltstone	2	2657.14	148.571
31	102 51 0		Siltstone and shaly siltstone	2	2871.43	155.714
32	51 102 153		Siltstone and shaly siltstone	2	3085.71	162.857
33	153 0 0		Siltstone and shaly siltstone	2	3300	170
34	0 51 102		shale+silt+sand	2	3400	180
35	0 0 51		shale+silt+sand	2	3400	180
38	102 51 153		shale+silt+sand	2	3400	180
44	153 51 0		shale+silt+sand	2	3400	180
11	102 0 0		shale+silt+sand	2	3400	180
12	102 0 51		shale+silt+sand	2	3400	180
13	102 51 102		shale+silt+sand	2	3400	180
14	153 51 102		shale+silt+sand	2	3400	180
15	153 51 51		shale+silt+sand	2	3400	180
18	51 0 51		shale+silt+sand	2	3400	180
19	51 0 102		shale+silt+sand	2	3400	180
20	51 51 51		shale+silt+sand	2	3400	180

Figure 4.7. **a.** 2D seismic section (A-A`) with a zoom into this section showing a mesh that has a large number of grid cells. Each cell appears as a separate colour representing a flow identification domain (FID); each colour was assigned as a single petrophysical property (CEP) in the volume editor. **b.** Extract of the volume editor parameter from Permedia showing the input CEP values and distribution assigned to lithologies and colour scales representing assigned lithofacies in normal distribution (see section 4.6.2.2.4 in text) for the first scenario along section A-A`) .

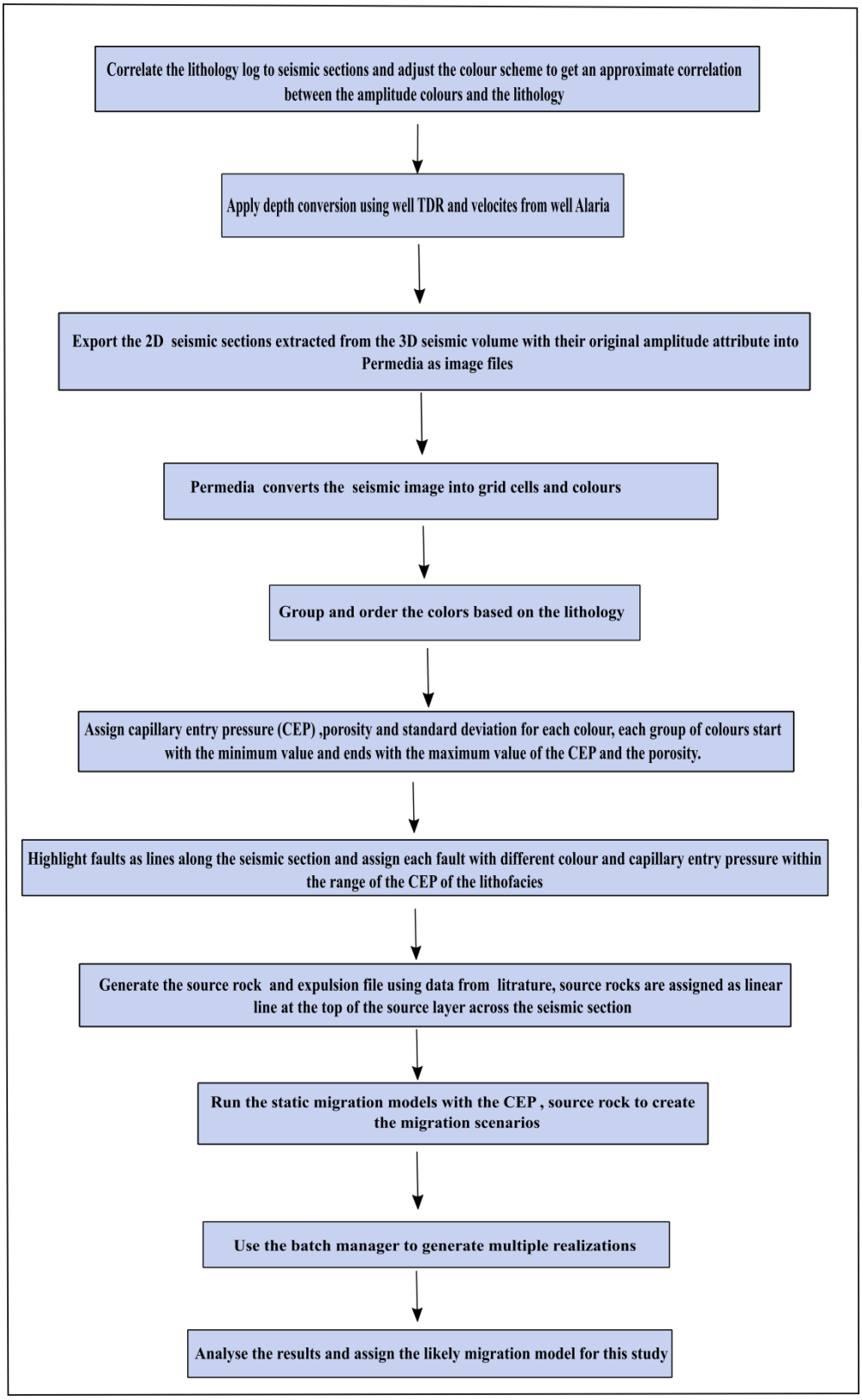

Figure 4.8. Summary of workflow adopted in the methodology used to build the migration models.

4.6.2.2.2 Correlation between the capillary entry pressures (CEP) and the corresponding lithologies

The main petrophysical parameter in the modelling is the capillary entry pressure (CEP) values that are assigned to each grid cell of the 2D seismic image.

The lithologies at the Laminaria High are divided into a clastic-dominant sequence from the Lower Jurassic (Plover Formation) to the Middle Cretaceous (Jamieson Formation), and then a carbonate-dominant sequence from the Upper Cretaceous (Woolaston Formation) up to the Quaternary (Barracouta Formation). There are two critical factors that we need to set in our models: **(a)** the CEP values for the lithologies in the study area; and **(b)** the relationship between the seismic colours and lithologies.

The threshold pressure varied based on the different lithofacies and the distribution of the capillary entry pressures in the model. In seismic interpretation, the identification of major features is related to the amplitude of the seismic reflection, in particular the low and high amplitude indicators. For example, interfaces between clay sequences and sand sequences may result in high reflective amplitudes known as “bright spots” (Brown, 2014). Ukekwe et al. (2012) estimate the lithofacies types based on the relationship between the velocity and the density. Based on this relationship, the dense lithofacies (e.g. claystone) have high capillary entry pressure, and the less dense lithofacies (e.g. sandstone) have low capillary entry pressure. However, the heterogeneity of the carbonate limestone lithofacies due to diagenesis leads to high complexity in its petrophysical properties and causes some difficulties in assigning the capillary entry pressure in the models used to predict fluid flow/migration (Cullen, 2017). Also, for this study, there was not much information regarding CEP values for the carbonate rocks.

Therefore, a subjective approach to assign the CEP values was adopted as follows:

***1) interpretation of the limestone type*:** The carbonate sequence is provided in the Alaria-1 well report; the limestone is grouped into three types: a) calcilutite consisting of both silt- and clay-size particles, less than 0.062 mm in diameter; b) calcisiltite consisting of detrital silt-size particles, 0.062 to 0.002 mm; and c) calcarenites (the carbonate equivalent of sandstone) consisting of detrital sand-size particles, 0.0625 to 2 mm in diameter. The detailed definition of the limestone in the carbonate sequence enables us to assign the CEP for the carbonate lithofacies based on their grain size. In general the finer grains have higher capillary entry pressure and the coarser grains have lower capillary entry pressur. Also, these values were correlated with the CEP values in Cullen's (2017) study. The CEP values for the clastic lithofacies were taken from studies by Schlomer and Krooss (1997), Schowalter (1979), Ukekwe et al. (2012).

2) the choice of colour scale along the seismic image: These are calibrated based on the lithofacies described well Alaria-1 in the report. The lithology colours and the assigned CEP values used in this study are summarised in Table 4.2 and Figure 4.9.

The secondary hydrocarbon modelling is performed through a faulted sedimentary sequence. Faults are assigned in the model as lines along the fault traces using different colours from the background lithology (FID colours) of the seismic section (Figure 9). The results from the stress analysis are used to estimate the capillary threshold pressure values for the grid cells along each fault line that intersects the 2D seismic sections (e.g. Ts $\geq$ 0.4 corresponds to CEP $\leq$ 1500 and Ts $\leq$ 0.3 corresponds to CEP $\geq$ 1800). The CEP values along each fault line were given values within the range of CEP values of the background lithologies of the seismic section (Tables 4.2, 4.4 and 4.5).

Table 4.2. Capillary entry pressures assigned to the lithofacies in all models and the chromatic colour scales showing representing assigned lithofacies with their corresponding sources

	Lithology	*CEP in Oil/Water (KPa)-Min*	*CEP in Oil/Water (KPa)-Max*	*CEP Sd.(% of CEP) (min)*	*CEP Sd.(% of CEP) (max)*	*Source of CEP data*
High	***Alternate bedding of limestone(Calcilutite), shale, silt, and sand*** 	***3400***	***3400***	***180***	***180***	***Schlomer & Krooss (1997) and Ukekwe et al., (2012)***
Middle	***Siltstone and shaly siltstone*** 	***1800***	***3300***	***120***	***170***	***(Newcastle University Caprock group) and Ukekwe et al., (2012)***
Low	***Alternate bedding of limestone (Calcisiltite and Calcarenite), calcareous clay and sand*** 	***400***	***1500***	***50***	***100***	***Schowalter(1979)*** ***Schlomer and Kroos (1997)*** ***and Cullen ,(2017)***

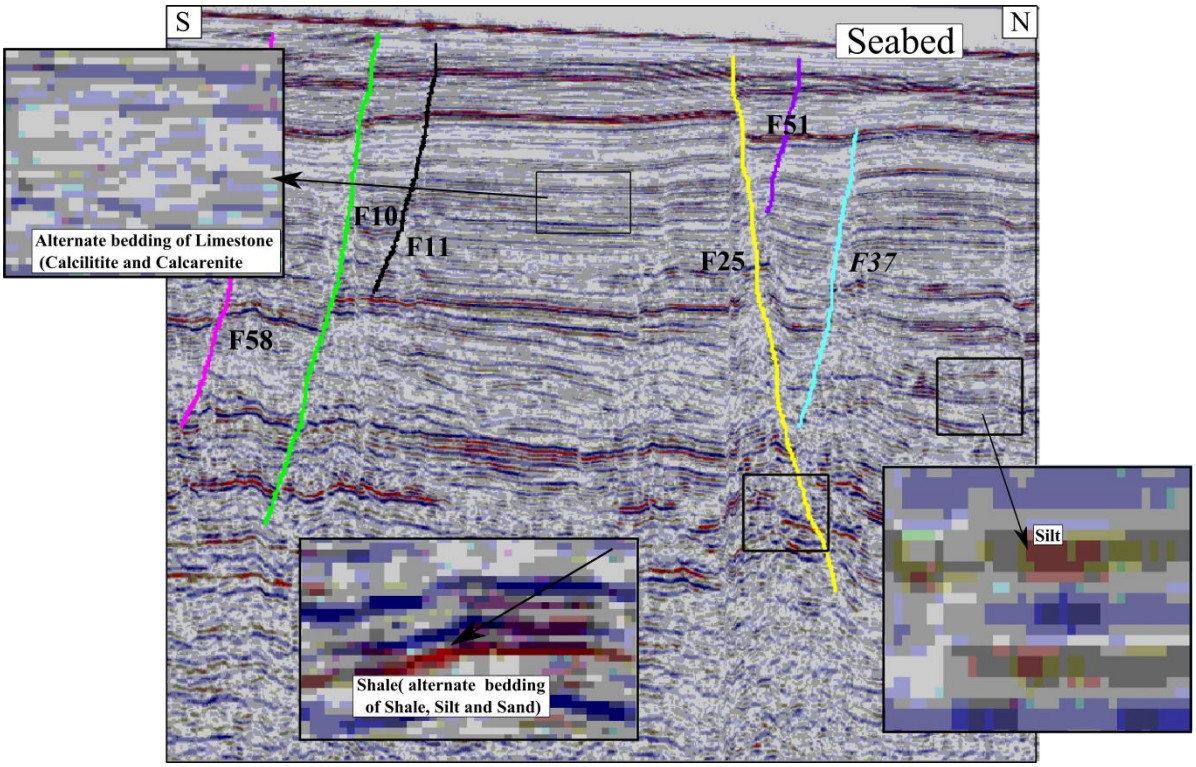

Figure 4.9. Heterogeneous lithofacies represented as seismic colours identified by zooming into the cross section. Note that the lithology along the seismic section is separated into three groups of lithofacies and CEP values as shown in Table 4.2.

4.6.2.2.3 Source rocks' location, properties and other inputs for the models

Two source rocks are considered in the model: the Plover and Echuca Shoals shale formations within the Middle Jurassic–Lower Cretaceous sequences (Abbassi et al., 2015) (Figure 4.2 b). The location and the depth of these source rocks are estimated from the Alaria-1 well report. In Permedia™, the source rocks were modelled as lines, and each of them followed a single reflector that reflected the top of the source rocks that expelled hydrocarbons into the layers above. The source rock file includes the petrophysical properties (i.e. capillary entry pressure) and the expulsion properties which describe the movement of hydrocarbons from the source rock to the carrier bed. It consists of a combination of parameters called the kinetic components data that includes the total organic carbon (TOC) that enables the rock to generate hydrocarbons, and the hydrogen index (HI), which indicates the organic richness and petroleum of the source rock; the Kerogen type and the maximum present-day temperature are shown in Table 4.3.

Water density was set to 1020 kg/m^3 for all the models. A single value for the density is used because the modelling in Permedia® does not include depth-dependent gradients of density based on the geothermal gradient. The temperature of the seabed surface is set to 5℃ for all models. The pressure-volume-temperature (PVT) data for the generated hydrocarbons is taken from the sample (PVT) data provided in Permedia®, this data includes the fluid densities, bubble points, interfacial tension, phase and dew point as a function of temperature and pressure.

Table 4.3. Source rock properties and kinetic components data used as input parameters for the petroleum models. Data obtained from well reports, Abbassi et al. (2015) and Permedia 5000.12. Note that the GOR, oil and gas densities change with pressure and temperature at each time step in the model.

Source rock	Kerogen type	TOC (%)	HI	Maximum temperature	Total GOR (from PVT data)	Oil density Kg/m3 (from PVT data)	Gas density Kg/m^3 (from PVT data)
Echuca Shoals Fm.	**II/III**	**2.5**	**300**	**130-150 ℃**	**887**	**809**	**112**
Plover Fm.	**II/III**	**3.5**	**350**				

4.6.2.2.4 Multiple realisations and the probability distribution of the capillary entry pressure (CEP)

Modelling in Permedia uses a discrete colour system to set the CEP, which produces a discrete capillary scale rather than a continuous one. Therefore, to generate a probability distribution function for the CEP scale, a standard deviation is applied to the CEP values for each grid cell. When the model is run, each grid cell has a standard probability distribution along the assigned CEP. So the CEP ranges along the lithology will be continuous along the colour range. This will produce multiple models with different outcomes, due to the slight differences in the output CEP within each grid cell. Therefore, a normal distribution was used to produce a continuous distribution for the CEP values, and also to allow the colour of each lithology to overlap. Each parameter was associated with two coefficients (c1 and c2) (Figure 4.10) in that the mean CEP for each colour was entered in c1, and a standard deviation entered in c2 as shown in Table 4.2. Based on this distribution, Permedia will produce thousands of combinations of the same model and assign each of them a value, which is called a "seed". This seed allows the use of the same model multiple times with variable inputs. This is the concept of "stochastic modelling", in that Permedia picks a CEP value for

each grid cell from the assigned CEP distribution parameters and creates a single realisation of each parameter. These multiple realisations are then combined and risked along a range of probable scenarios to get a probability model by running a risk analysis model (i.e. probability that petroleum migrated into a given cell). This analysis will help to quantify the uncertainties in the produced models and to identify the most likely hydrocarbon migration routes at any point in the model.

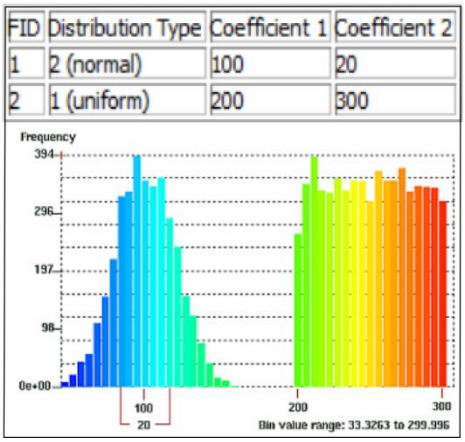

Figure 4.10. Types of threshold pressure distributions. In the normal distribution, c1 is the mean CEP and c2 is the standard deviation; in the uniform distribution, c1 is the minimum CEP and c2 is the maximum CEP. In this study a normal distribution for the CEP's values is used.

4.6.2.2.5 Migration Scenarios

The main purpose of migration modelling is to understand the circumstances under which migration will preferentially occur along faults. The outcomes from the different migration models were compared with the actual hydrocarbon distribution, which includes evidence of hydrocarbon leakage at the seabed. The hypothesis tested is that hydrocarbon leakage is associated with the critically stressed faults (Figure 4.1) to understand why there is apparent difference in ongoing leakage between the southern and northern areas covered by this study. Two models were run with two scenarios along each seismic section in the N-S direction using different parameters

in each model. Also, another two models were run with different scenarios along section A-A` (Figure 4.1).

To provide some cross-line control, one migration model is run along another section in the E-W direction and its results compared with the N-S cross line models (Figure 4.1).

Finally, risk or probability analysis was applied to each scenario to get an analysis of how often the grid cells show fluid migration through the entire realisation. This analysis will test the uncertainties in model assumptions, in particular the entry pressure values along the faults and the lithofacies sequence. Four scenarios are proposed in this study:

- ***Scenario 1*:** the purpose of this scenario is to examine how critically stressed faults influence hydrocarbon leakage. Two models of fluid migration were run, testing two possibilities for the entry pressure along the faults. In **model 1**, the CEP value along the main fault F10 is suggested to be less than the main fault F25; while in **model 2**, faults F10 and F25 have the same CEP value (Table 4.4 and section 4.6.2.2.2).

- ***Scenario 2:*** the purpose of this scenario is to examine the effect of the heterogeneity of fault properties on hydrocarbon migration and leakage. It is assumed that the lithology along each fault line is not uniform; hence, the entry pressure values along these faults are variable. We suggest that the lithology along faults is more compacted with depth; hence higher entry pressure values are assigned along the deeper fault lines. To demonstrate this assumption, fault lines that extend to greater depths are separated into upper and lower parts with two

different colours. Two groups of CEP along each fault trace were chosen; in **model 1** the CEP values were grouped near the lower range of the CEP of the lithofacies as shown in Table 4.5, while in **model 2** the CEP values were grouped near the middle range as shown in Table 4.5. This approach was applied to test the possible range of CEP along faults that are more likely to produce these migration scenarios.

- **Scenario 3:** this scenario will test the possibility that Fault F10 is less stressed than Fault F25. Therefore, high CEP is assigned along Fault F10. The reason for testing this scenario is to investigate how this will affect hydrocarbon migration to the seabed.

- **Scenario 4:** this scenario will test the possibility that both faults F10 and F25 are not stressed. Therefore, high CEP is assigned along these faults. This is to test how plausible this assumption is and what impact it has on hydrocarbon migration from source rocks to the seabed.

Note: Both of the above scenarios (3 and 4) were only applied along section A-A`.

Table 4.4. Capillary entry pressure data assigned to the each fault line in models one and two for scenario 1. Note that these values were ranged within the original CEP values of the background lithologies in Table 4.2

Scenario 1 (section A-A`)		
Model 1		Model 2
Fault no.	CEP (kPa)	CEP (kPa)
F10	1000	1000
F11	1800	1800
F25	1500	1000
F37	1500	1500
F42	1500	1500
F51	1500	1500
F58	1200	1200

Scenario 1 (section B-B`)		
Model 1		Model 2
Fault no.	CEP (kPa)	CEP (kPa)
F10	1000	1000
F22	1200	1200
F25	1800	1000
F36	1000	1000
F39	1200	1200
F44	1200	1200

Table 4.5. Capillary entry pressure data assigned to each fault line in models one and two for scenario 2. Note that these values ranged within the original CEP values of the background lithologies in Table 4.2

Scenario 2 (section A-A`)		
Model 1 (Low CEP)		Model 2 (Middle CEP)
Fault no.	CEP (kPa)	CEP (kPa)
F10(upper part)	900	1800
F10(lower part)	1200	2000
F11	1800	2200
F25 (upper part)	1200	2200
F25 (lower part)	1500	2400
F37	900	2000
F42	900	2000
F51	900	2000
F58 (upper part)	900	1800
F58 (lower part)	1100	2000

Scenario 2 (section B-B`)		
Model 1 (Low CEP)		Model 2 (Middle CEP)
Fault no.	CEP(kPa)	CEP (kPa)
F10(upper part)	900	1800
F10(lower part)	1200	2000
F22	1000	1800
F25 (upper part)	1200	2200
F25 (lower part)	1500	2400
F39	1000	2000
F36	1000	2000
F44(upper part)	1000	2000
F44 (lower part)	1500	2200

4.7 Results

4.7.1 Analaysing critically stressed faults

Two groups of dipping faults are included in this analysis and are active at the seabed and some of them are associated with amplitude anomalies at the seabed (e.g. faults F10, F11, F36 and F58). The first group includes faults F10, F11, F36, F44, F51 and F58 dipping to the southwest direction, and the second group includes faults F22, F39 and F25 dipping to the northeast direction. Slip and dilation-tendency analysis are performed along these faults using the mean stress values of Castillo et al. (2000). A 3D fault model in the area of interest is shown in figures 4.11a, 4.11b and 4.11c.

The slip tendency (Ts) along faults in the southern part of the survey area is variable. Fault F10 shows vertical bands of increased slip tendency, in particular at the linkage points between fault surfaces as assigned by arrows in figures 4.11a and 4.11b (i.e. the linkage between faults F10, F11 and F22; the Ts is ≥ 0.5 at these points). The minimum Ts along Fault F10 is ≤ 0.3 and the maximum is ≥ 0.5. The east end of Fault F58 has a low T_S of ≤ 0.2 and then the Ts increases slightly (Ts = 0.4-0.5) towards the NW. Note that in Figure 4.1, Fault F58 is associated with small amplitude anomalies at the seabed. Ts along Fault F22 is variable and ranged between 0.3 to the west and 0.4-0.5 at the linkage point between faults F22 and F36, as shown by the arrow in Figure 4.11a. Fault 11 has the lowest Ts of ≤ 0.3 and fault F36 shows a Ts of ≥ 0.3-0.4. Both of these faults are associated with amplitude anomalies at the seabed (Figure 4.1).

Faults at the northern part show a different distribution of the Ts value. The slip tendency at the east end of Fault F25 has a Ts of ≤ 0.2, while the west end of this fault has a Ts of ≥ 0.4, in particular at the linkage point between faults F25 and F51, as shown by the arrow in Figure 4.11a. Fault F51 has a Ts range from 0.3-0.5. Faults F39 and F44 have a Ts of ≥ 0.4, and the Ts increases at the linkage point between F25 and F44. Figure 4.1 shows that the faults F25, F39 and F51 are not associated with amplitude anomalies at the seabed.

The dilation tendency (Td) in Figure 4.11b shows that the main fault F10 is more likely to be open than fault F25. The Td along fault F10 has a minimum Td of 0.3 and a maximum Td of ≥ 0.5. Fault F25 has a maximum Td of 0.5 at the NW, and the Td decreases towards the SE.

Another two stress fields, varying by ±0.0004MPa/m of the mean stress gradient of Castillo et al. (2000), are used as shown in Table 4.1 and figures 4.12 and 4.13 to test the sensitivity of the slip and dilation tendencies to the input stress values. Figures 4.13a, 4.13b and 4.13c show similar results and not much difference in the slip-tendency attribute: **(a)** Fault F10 has minimum Ts = 0.125 and maximum Ts = 0.65; Fault F25: minimum Ts = 0.125 and maximum Ts = 0.55; **(b)** Fault F10 has minimum Ts = 0.13 and maximum Ts = 0.65; Fault F25: minimum Ts = 0.125 and maximum Ts = 0.55; (c) Fault F10 has minimum Ts = 0.125 and maximum Ts = 0.625; Fault F25: minimum Ts = 0.125 and maximum Ts = 0.55.

The sensitivity was also tested regarding the S_{Hmax}, S_{Hmin} and Sv strike direction of ±6° from the main stress direction of Castillo et al. (2000) (figures 4.14a and 4.14b). Again, the results from these plots also show no significant differences amongst them. The following section will explain the principal workflow for hydrocarbon migration and test if these results are consistent with hydrocarbon migration pathways along

these faults and with the existence of the high amplitude anomalies at the present day seabed (Figure 4.1).

Figure 4.11. 3D model of the Laminaria High fault system with fault surfaces coloured based on **(a)** the slip tendency; **(b)** the dilation tendency; **(c)** zoom in of slip tendency attribute mapped along Faults F10 and F25. These faults were used in the petroleum modelling. Location of these faults is marked Figure 4.1. Note two dip-sections (A-A` and B-B`) and one strike section (C-C`) that are used in migration modelling.

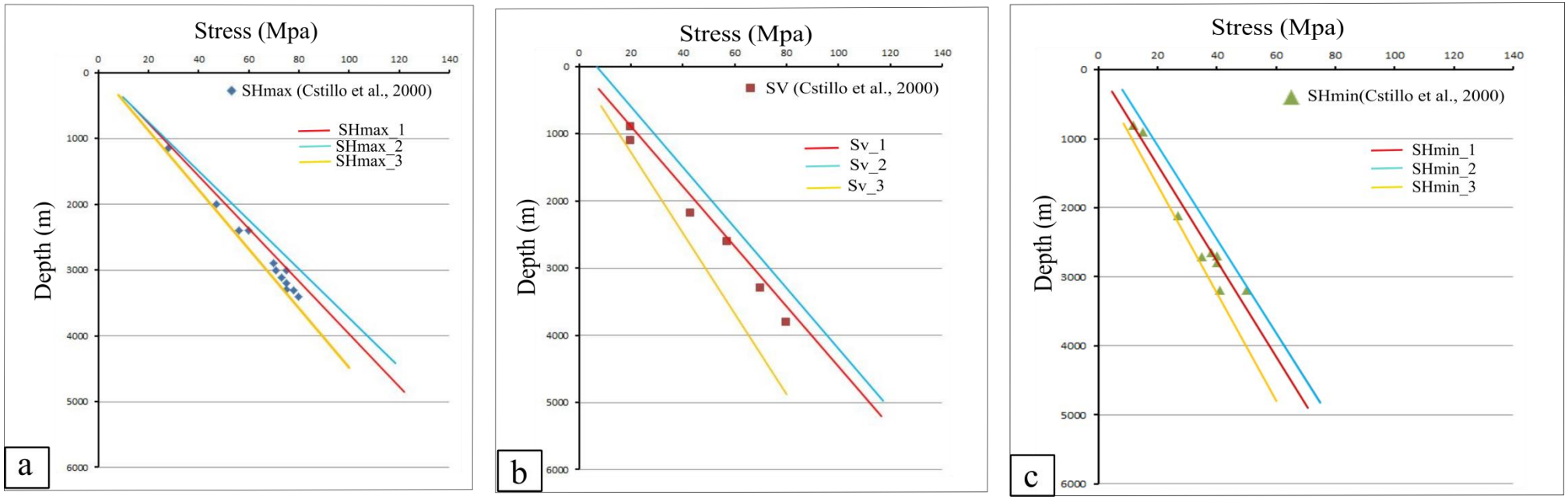

Figure 4.12. Calculated stress state resolved on faults. **(a)** S_{Hmax} **(b)** S_V **(c)** S_{Hmin} varied by ±0.0004 from the original stress value used in Castillo et al.'s study (2000), as shown in Table 1. Note: **1** is the average principal stress values from Castillo et al. (2000); **2** is the stress values varying by +0.0004 of the average stress; **3** is the stress values varying by -0.0004 of the average stress.

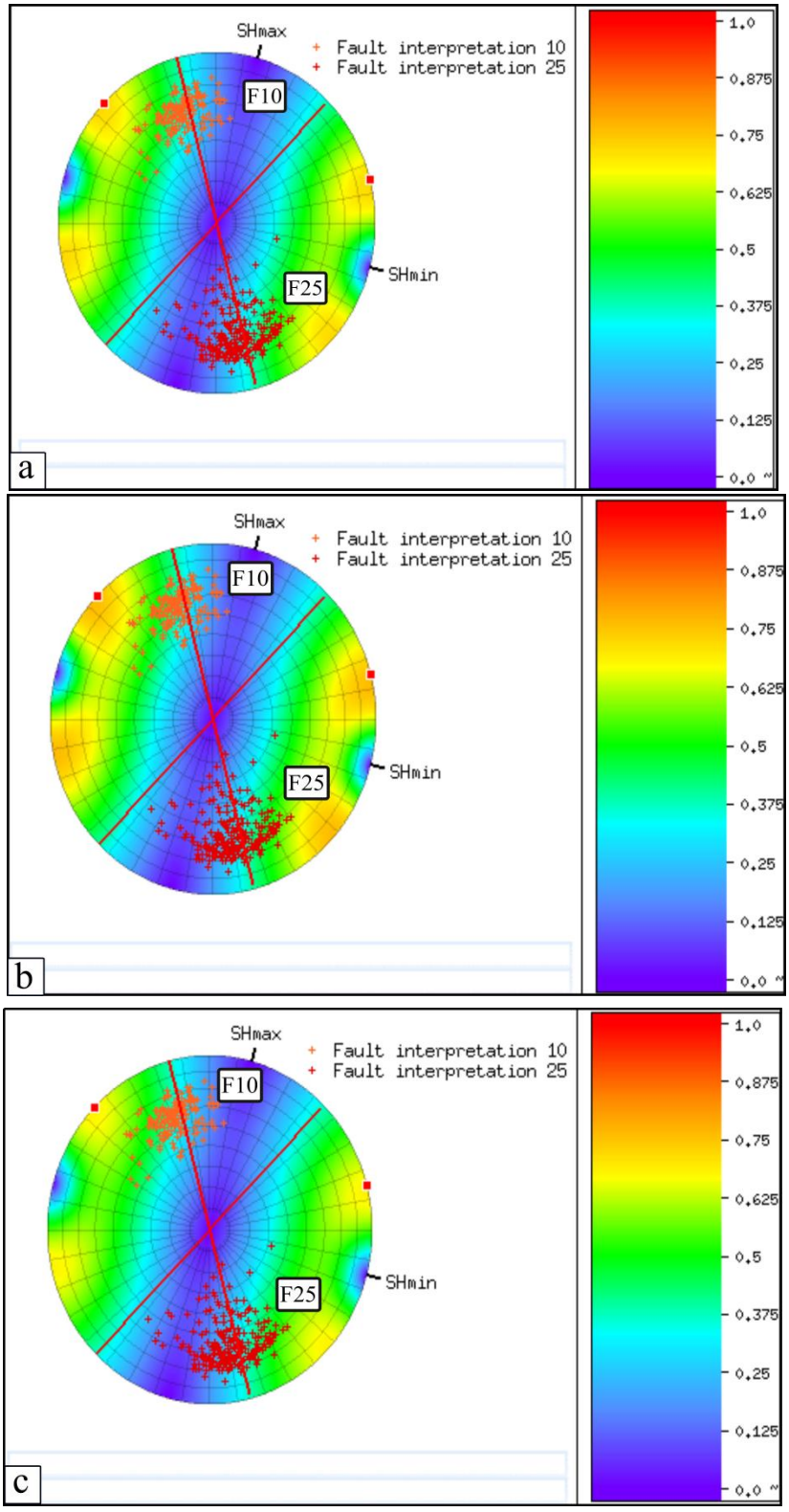

Figure 4.13. Slip tendency stereograph for Faults F10 and F25. Each cross on the stereograph represents the fault pole along each fault plane with their corresponding azimuth, dip and the slip tendency. Results are displayed along the three stereograph projections coloured according to the slip tendency attribute **(a)** Fault F10: minimum Ts = 0.125 and maximum Ts = 0.65; Fault F25: minimum Ts = 0.125 and maximum Ts = 0.55; **(b)** Fault F10: minimum Ts = 0.13 and maximum Ts = 0.65; Fault F25: minimum Ts = 0.125 and maximum Ts = 0.55; **(c)** Fault F10: minimum Ts = 0.125 and maximum Ts = 0.625; Fault F25: minimum Ts = 0.125 and maximum Ts = 0.55.

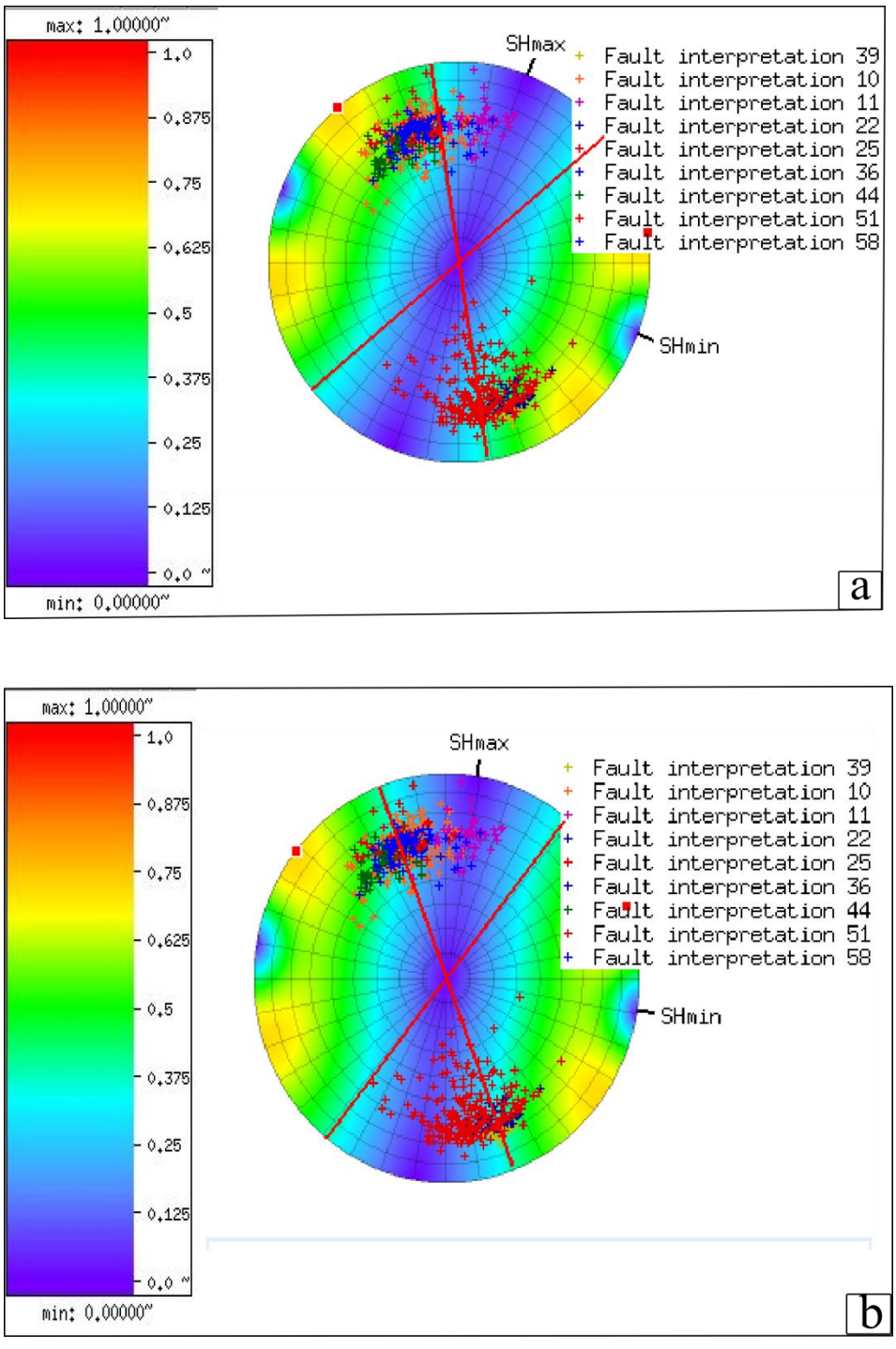

Figure 4.14. Slip tendency stereographs measured along fault surfaces used in the stress analysis **(a)** Stress direction21°; **(b)** Stress direction (9°). Crosses are fault poles plotted on this stereograph.

4.7.2 Migration modelling results

4.7.2.1 Migration modelling along seismic section A-A`

Once hydrocarbons are expelled from the source rock, the buoyancy force increases until it exceeds the capillary entry pressure (CEP) of the carrier layers. In general, the migration models show vertical hydrocarbon migration along faults coupled with lateral migration below the seal layers and between faults. Fluids migrate along faults with two patterns of flow based on the CEP values along the faults: 1) focused – fluids migrate as a linear pattern along faults; 2) diffused – fluids are guided by faults.

- Scenario 1*: *The effect of critical stress faults on fluid migration

1. Model 1

In this model (Figure 4.15a), hydrocarbons were expelled from throughout the source rock vertically until it produced enough hydrocarbons with enough buoyancy that exceeds the CEP of the carrier bed. Hydrocarbons then migrated throughout Fault F10 more easily than Fault F25 due to the lower CEP assigned along Fault F10. This focuses flow along Fault F10, whereas on Fault F25 the flow is more diffuse. It is noted that Fault F25 is guiding hydrocarbon migration from the source rock up to the seabed due to the dip of the seabed reflector at the footwall of Fault F10. Hydrocarbons migrate along faults F25 and F51; this migration coupled with lateral migration between faults F25, F52, F37 and F10 is shown by arrows in Figure 4.15a. Lateral migration occurs between faults F10 and F58 at ca. 750 m, then fluids leak from Fault F10 to the surface. Migration has stopped due to higher CEP at approximately 600 m and 800 m within the Oliver and Barracouta formations such that hydrocarbons are trapped below the two bright reflectors, as shown by arrows in Figure 4.15a.

2. Model 2

In this model (Figure 4.15b), the same migration routes from the source rocks occur as in model 1. Hydrocarbons mainly migrate along faults F10 and F25 due to their low CEP, which are thus favourable pathways for migration. This has the result of focusing hydrocarbon flow along faults F10 and F25 up to the seabed. Hydrocarbons are hardly migrating along faults F37, F42 and F58 due to the assumption that faults F10 and F25 are more critically stressed than the other faults. Hydrocarbons exit laterally from Fault F10 towards faults F11 and F25, then hydrocarbons are trapped under the seal layer at ca. 600 m below mean sea level, as shown by the arrow in Figure 4.15b. However, hydrocarbons continue to migrate vertically along faults F10 and F25, creating two hydrocarbon accumulations in the southern and northern parts of the seabed. Lateral migration occurs between faults F11 and F10 at ca. 800 m, and fluid leaks from F11 and F58 to the seabed.

Risk analysis is then applied, which is a combination of multiple models from each scenario that have different outputs due to the probability distribution that is applied (section 4.6.2.2.4). This analysis quantifies the uncertainty in assigning the CEP values for the lithology and along fault lines, giving migration routes for hydrocarbons for the present day and showing how often hydrocarbons occur in grid cells of the seismic section. Figure 4.15c shows the final risk analysis model of the multiple realisations from models 1 and 2; green indicates the more likely migration routes in all models, while yellow indicates that only 50% of the models show hydrocarbons along these routes. This analysis suggests that hydrocarbons migrate along both faults F10 and F25. However, this model shows that hydrocarbons start to migrate along Fault F25 at depth ca. 1750 m, while along Fault F10, hydrocarbon starts to migrate at ca.2500. This suggest that Fault F25 is less likely to be conduit pathway for hydrocarbon

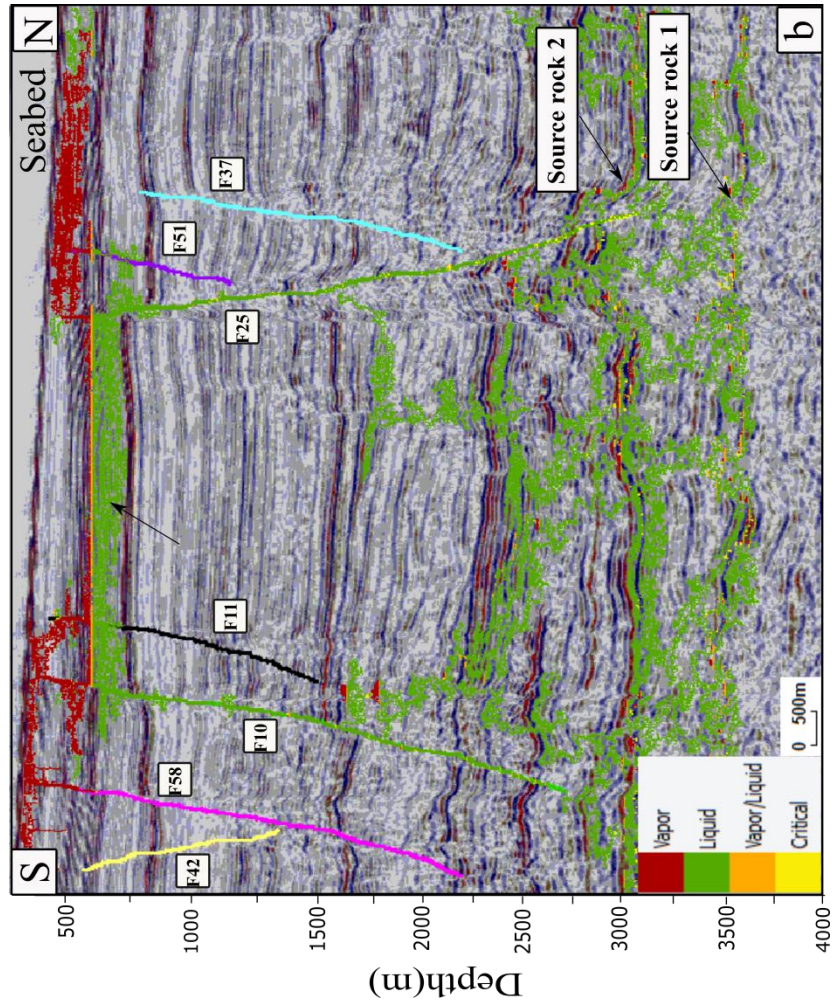
b
Seabed
N
S
Source rock 2
Source rock 1
F37
F51
F25
F11
F10
F58
F42
Vapor
Liquid
Vapor/Liquid
Critical
0 500m
Depth(m)
500
1000
1500
2000
2500
3000
3500
4000

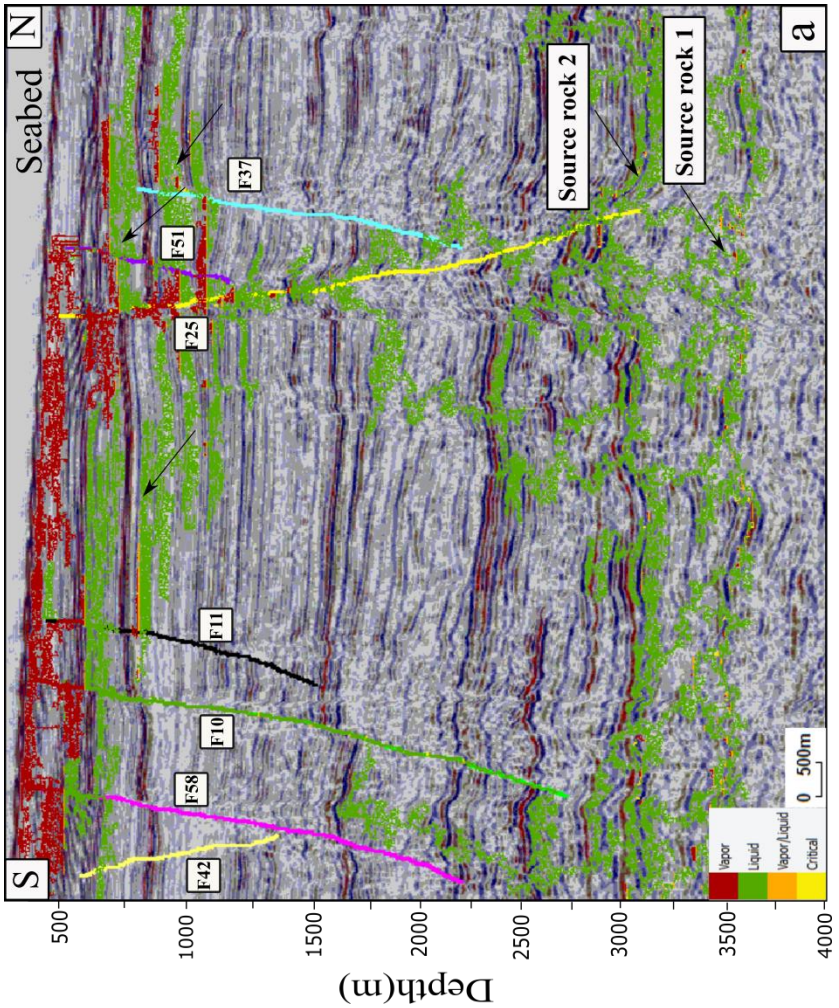
a
Seabed
N
S
Source rock 2
Source rock 1
F37
F51
F25
F11
F10
F58
F42
Vapor
Liquid
Vapor/Liquid
Critical
0 500m
Depth(m)
500
1000
1500
2000
2500
3000
3500
4000

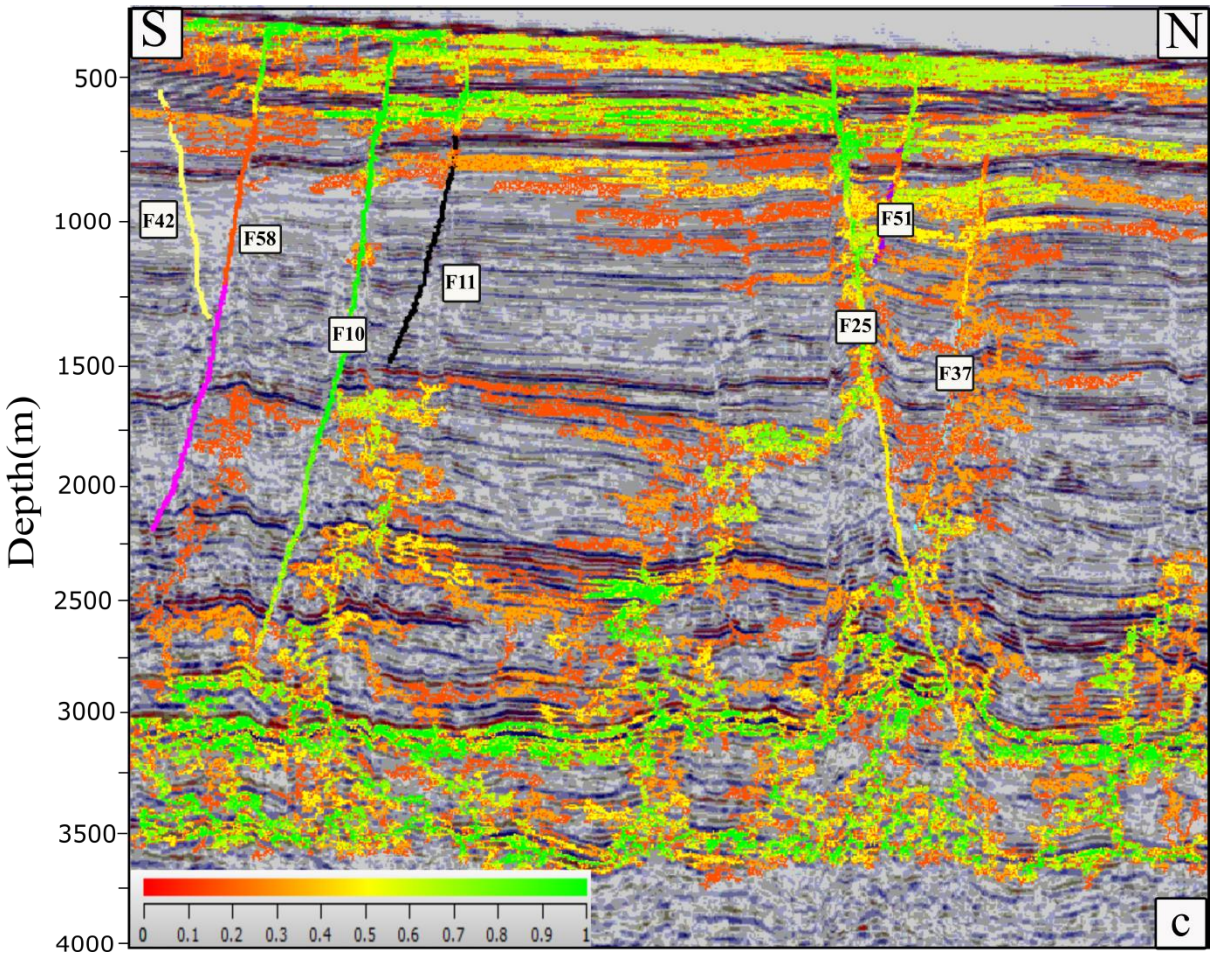

Figure 4.15. Results of the migration model along section A-A` (scenario 1). **(a)** Model 1: it is assumed that Fault 10 is more stressed (low CEP along the fault line) than Fault 25 (high CEP along the fault); this focuses flow along the fault plane of Fault F10, whereas on F25 the flow is more diffuse. **(b)** Model 2: it is assumed that faults F10 and F25 have the same CEP; in this case fluid flows are more focused along faults F10 and F25. **(c)** A risk analysis model showing the results from multiple realisations along the two models and the more likely pathways for fluids to migrate along these two models. Note that the green colour shows that in all models hydrocarbon migration occurs through these pathways; the yellow colour shows that 50-60% of models show hydrocarbon migration through the seismic section; and the light to dark orange colours show that only a few models (40-0%) show hydrocarbon migration through the seismic section.

Scenario 2: The effect of heterogeneity of the lithology along fault traces

In both models, it is assumed that the main fault F10 is more critically stressed than Fault F25.

1. Model 1

In this model (Figure 4.16a) hydrocarbons were expelled from throughout the source rock vertically until it produced enough hydrocarbons with enough buoyancy forces that exceeded the CEP of the carrier bed, then vertical migration from the source rock starts at depth of ca. 2250 as shown by arrow 1 in Figure 4.16a. Variable CEPs along faults are assigned within the lower range of the background lithologies as shown in Table 4.5. It is noted that fluids flowing along faults F10 and F25 are more diffuse in the deeper parts of faults F10 and F25 and guide vertical fluid migration. Then fluids migrate vertically along faults F10, F25 and F37, coupled with lateral migration between faults F25, F51 and F37, and show similar hydrocarbon accumulation below the key reflectors in model 1 of scenario 1, as shown by arrow 2. Along faults F10 and F25 from a depth of approximately 1650 m below the mean sea level, the buoyancy force of the hydrocarbons attempts to overcome the CEP of the lithofacies along these faults, producing fault-bounding traps as shown by arrows 3 and 4 in Figure 4.16a.

2. Model 2

Hydrocarbons were expelled from throughout the source rock vertically until it produced enough hydrocarbons with enough buoyancy that exceeded the CEP of the carrier bed (Figure 4.16b). Vertical migration starts as shown by arrow 1, following the lithology and the dip of the carrier bed. Variable CEPs along faults are assigned near the middle range of the background lithologies as shown in Table 4.5. Fluid start to migrate throughout Fault F10 at ca. 2250m below the sea level. While the fluids flowing along faults F25, F37 and F51 are diffuse. It is noted that lateral migrations

between faults F10, F25 and F11 have invaded more cells and it is easier for the hydrocarbons to flow towards F11, rather than to leak through F25. Based on this observation, we suggest that the buoyancy forces for hydrocarbons are lower than the CEP of the lithofacies along Fault F25. Hydrocarbons continue to migrate upwards guided by fault F25 but discontinue before reaching the seabed. At the northern part of the seismic section, it is noted that migration along faults F51 and F37 are also guiding hydrocarbon migration but ceases before reaching the seabed. This suggests that hydrocarbons encounter a barrier bed with higher CEP lithofacies, which produced hydrocarbon accumulation below the key reflectors at ca. 600 m and 800 m, as shown by arrows 2 and 3 in Figure 4.16b.

To evaluate these two models, a risk analysis is run that gives the probability model from the multiple realisations of the input models (Figure 4.16c). This model shows that the most likely pathways for fluid migration are associated with faults F10, F11, F25 and F58. It suggests that fluid flow is more focused towards the southern part of the section, which is then considered as a high-risk area for hydrocarbon leakage to the seabed.

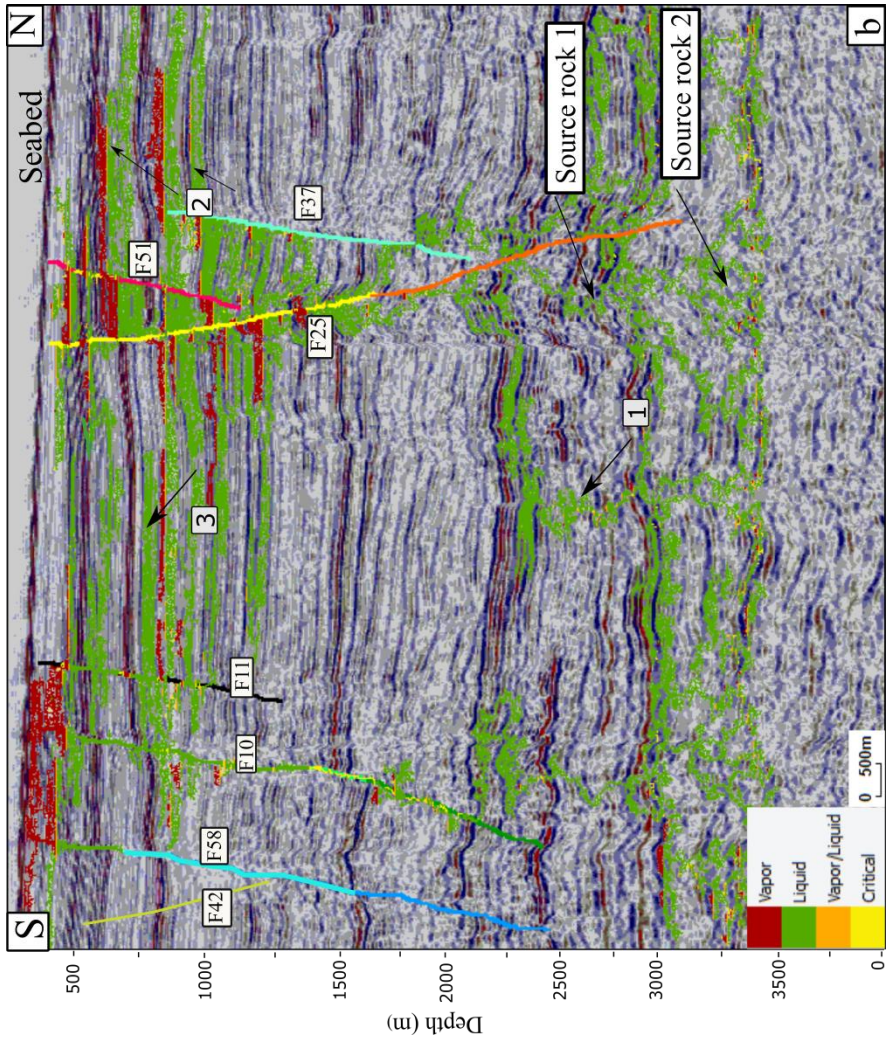
b
N
S
Seabed
Source rock 1
Source rock 2
F51
F37
F25
F11
F10
F58
F42
1
2
3
Vapor
Liquid
Vapor/Liquid
Critical
0 500m
Depth (m)
500
1000
1500
2000
2500
3000
3500
0

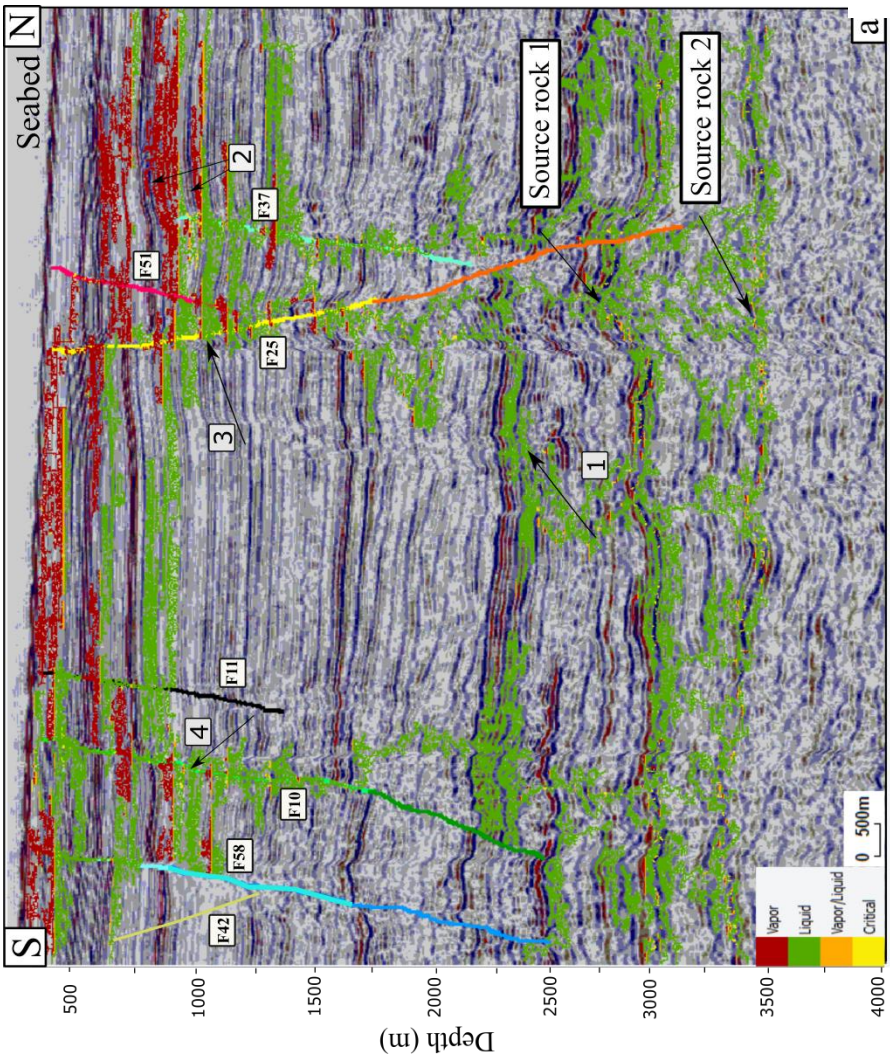
a
N
S
Seabed
Source rock 1
Source rock 2
F51
F37
F25
F11
F10
F58
F42
1
2
3
4
Vapor
Liquid
Vapor/Liquid
Critical
0 500m
Depth (m)
500
1000
1500
2000
2500
3000
3500
4000

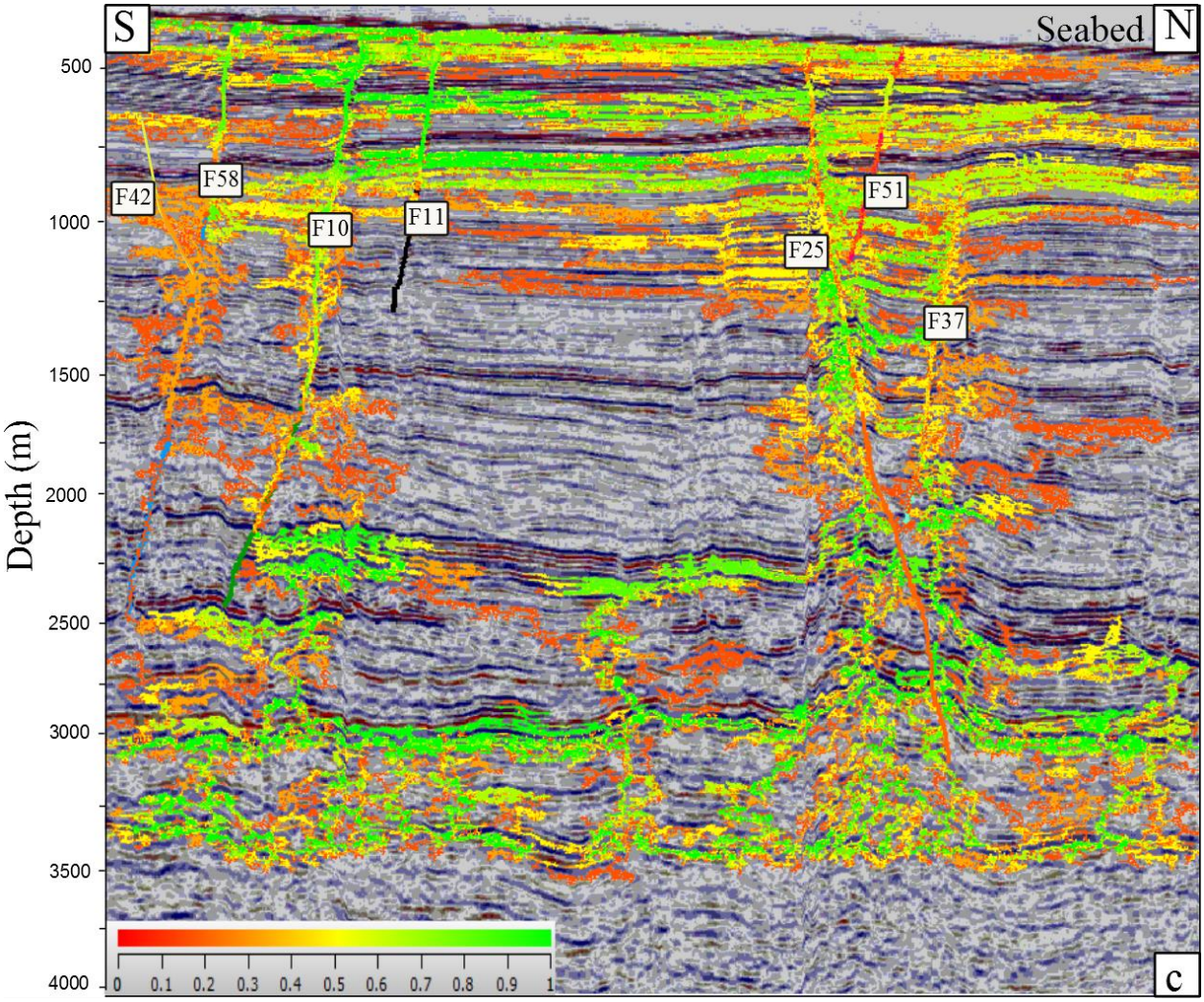

Figure 4.16. Results of the migration model along section A-A` (scenario 2). **(a)** In model 1, I assign the CEPs along faults within the lower range of the background CEPs. **(b)** In model 2, I assign the CEPs along faults within the middle range of the background CEPs. **(c)** A risk analysis model showing the results from multiple realisations along the two models and the more likely pathways for fluid to migrate along these two models. Note that the green colour shows that in all models hydrocarbon migration occurs through these pathways; the yellow colour shows that 50-60% of the models show hydrocarbon migration through the seismic section; and the light to dark orange colours show that only a few models (40-0%) show hydrocarbon migration through the seismic section.

4.7.2.2 Hydrocarbon migration along seismic section B-B`

- Scenario 1 – The effect of critically stressed faults on fluid migration

Models are run along this section (figures 4.17a and 4.17b) using the same assumption and methodology applied to section A-A`.

1. Model 1

In this model (Figure 4.17a) hydrocarbons were expelled from throughout the source rock vertically until it produced enough hydrocarbons with enough buoyancy that exceeded the CEP of the carrier bed. Vertical migration started at ca. 3000 m from the Echuca Shoal Formation and hydrocarbons mainly migrated towards fault F10 due to the dip of the beds. In this model, it is assumed that Fault F10 is more critically stressed than Fault F25. Based on that, hydrocarbons are more likely to migrate along Fault F10, reaching the seabed to the south. However, hydrocarbon migration is still guided by faults F25 and F44, as shown by arrows 1 and 2 in Figure 4.17a. Hydrocarbons migrate laterally between faults F25, F39 and F44, and then are trapped, producing an accumulation below the key reflectors at ca. 600 m and 800 m within the Barracouta and Oliver formations. Lateral migration occurs between F10 and fault F25, but it noted that migration is stopped below the key reflectors at ca. 600 m and 800 m within the Barracouta and Oliver formations, as shown by arrows 3 and 4 in Figure 4.17a, and there are no fluids reaching the seabed in the northern part. Hydrocarbons also migrate laterally between faults F10 and F36 in the south of the seismic section, as shown by arrow 5 in Figure 4.17a, and then fluids migrate vertically up to the seabed. Lateral migration occurs between faults F36 and F22, and then Fault F22 acts as a barrier for fluid migration from 900 m to 1250 m, then the upper part of this fault allow some hydrocarbon to migrate up to the seabed in the south of the seismic section (Figure 4.17a).

2. Model 2

In this model (Figure 4.17b), hydrocarbons were expelled from throughout the source rock vertically until it produced enough hydrocarbons with enough buoyancy that exceeded the CEP of the carrier bed, then vertical migration started at ca. 3000 m along Fault F10, guided by the dip of the beds above the source horizon, as shown by arrow 1 in Figure 4.17b. Fluids migrate along F10 more easily than along F25, although a similar CEP is assigned along these faults. Also, fluids migrate vertically from the source rock guided by faults F25 and F44, as shown by arrows 2 and 3 in Figure 4.17b.

Vertical migration along Fault F10 is coupled with lateral migration between faults F10 and F36, and migration stops at ca. 900 m within the Oliver Formation, as shown by arrow 4 in Figure 4.17b; Fault F10 then acts as a preferential pathway for fluids to migrate to the seabed. Lateral migration also occurs between faults F10 and F25, as shown by arrows 5 and 6, and hydrocarbons are trapped at ca. 600 m and 800 m within the Barracouta and Oliver formations. Lateral migration occurs between faults F39 and F44 at ca. 700-750 m in the northern part of this section; fluids are then leaking from the upper part Fault F44 to the seabed in the northern part of the seabed.

Risk analysis models indicate the uncertainty of the input parameters of these models (Figure 4.17c). About 70-80% of the models show hydrocarbons migrating along faults F10 and some parts of Fault F36 allow hydrocarbon migration at ca.900-1100m (green colour) and hydrocarbon is leaking from Fault F10 to the seabed. A few models (30-40%) show possible migration routes along Fault F25 and hydrocarbon are not migrating along Fault 39. It is noted that less than 10% of the models show accumulations at the northern end of the seabed. This model show that the stress analysis (Figure 4.11a) is consistent with these results, in particular for fluid flow

along the main fault F25, as this section crosses this fault plane where the slip tendency is < 0.2. Also, it is noted that the dip of the beds above the source horizon is guiding the lateral migration to the south and not many hydrocarbons migrate towards faults F25 and F44 in the deeper section.

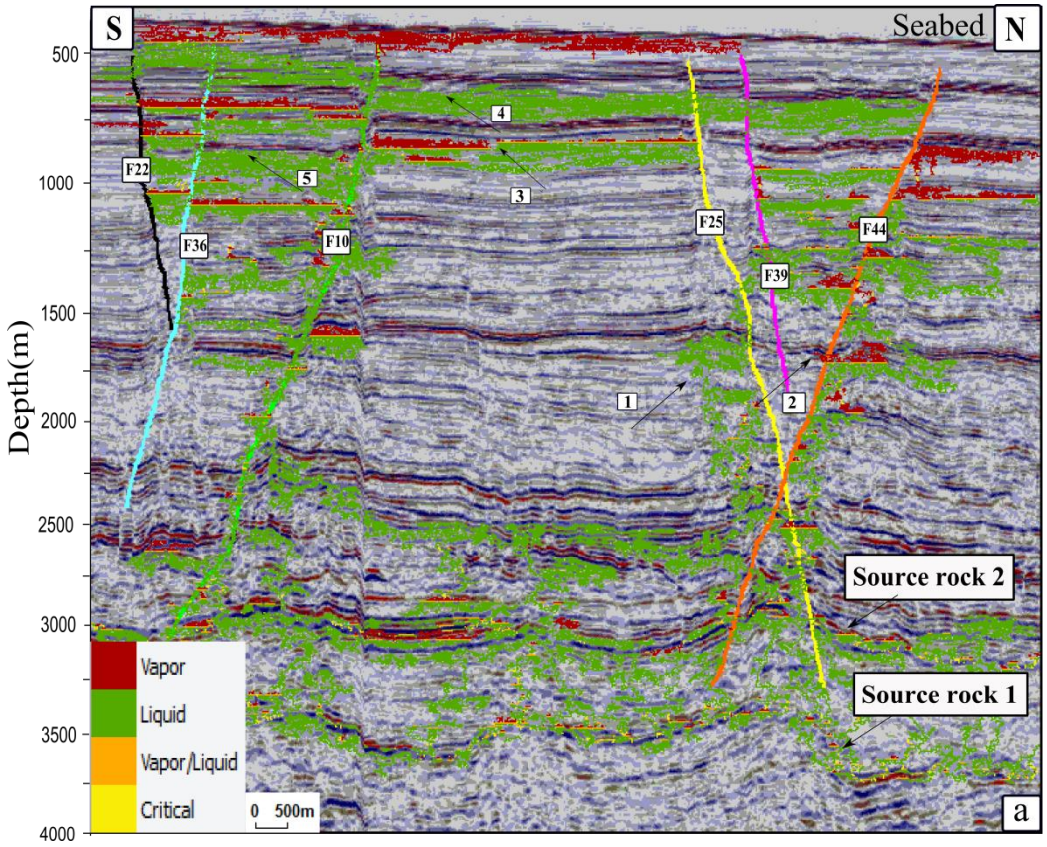
S
Seabed
N
Depth(m)
500
1000
1500
2000
2500
3000
3500
4000
F22
F36
F10
F25
F39
F44
1
2
3
4
5
Source rock 2
Source rock 1
Vapor
Liquid
Vapor/Liquid
Critical
0 500m
a

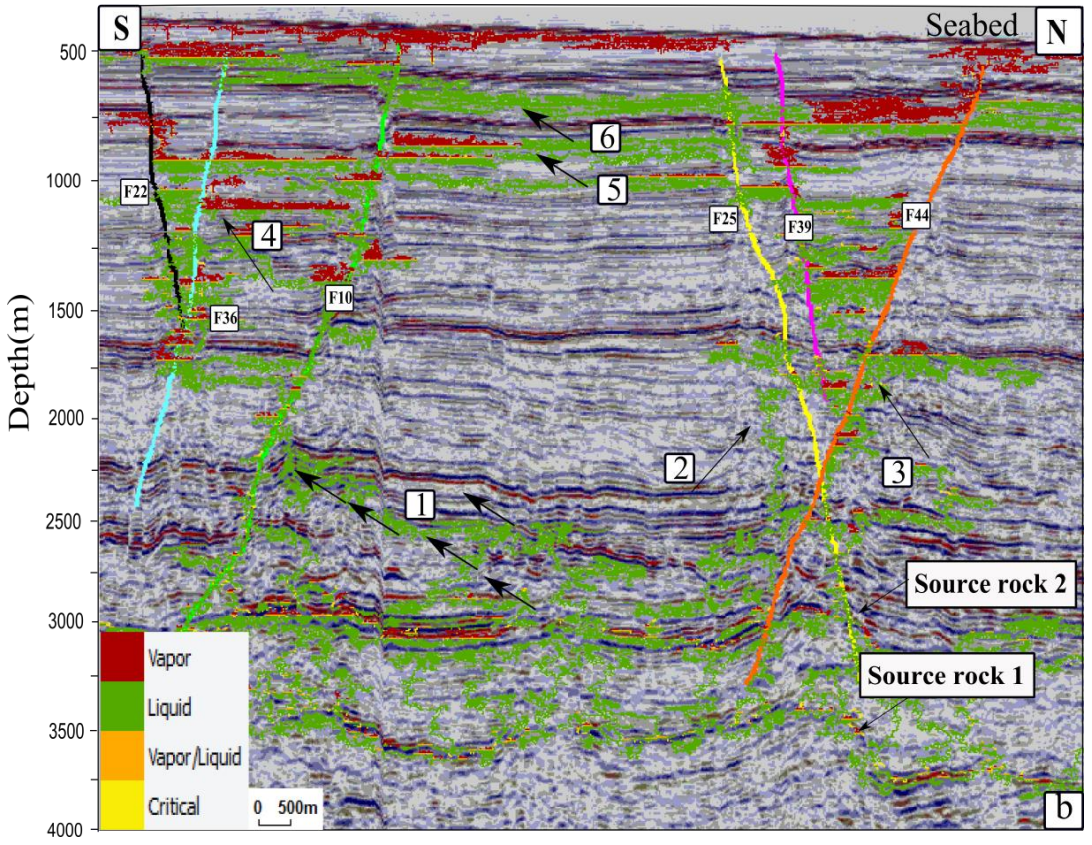
S
Seabed
N
Depth(m)
500
1000
1500
2000
2500
3000
3500
4000
F22
F36
F10
F25
F39
F44
1
2
3
4
5
6
Source rock 2
Source rock 1
Vapor
Liquid
Vapor/Liquid
Critical
0 500m
b

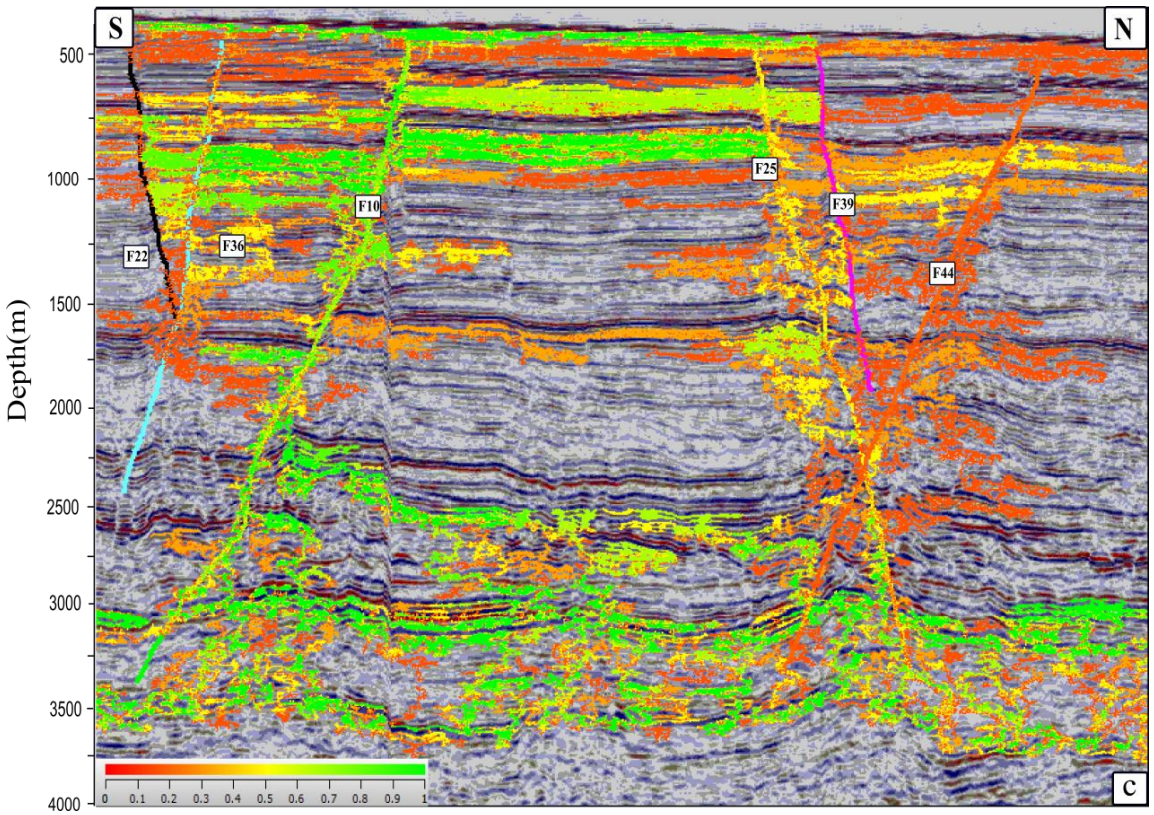

Figure 4.17. Results of the migration model along section B-B` (scenario 1). **(a)** In model 1, I assumed that Fault 10 is more stressed (low CEP along the fault line) than Fault 25 (high CEP along the fault). **(b)** In model 2, I assumed that faults F10 and F25 have the same CEP; in this case fluid flows are more focused along faults F10 and F25. **(c)** A risk analysis model showing the results from multiple realisations along the two models and the more possible pathways for fluid to migrate along these two models. Note that the green colour shows that in all models hydrocarbon migration occurs through these pathways; the yellow colour shows that 50-60% of the models show hydrocarbon migration through the seismic section; and the light to dark orange colours show that only a few models (40-0%) show hydrocarbon migration through the seismic section.

- Scenario 2: The effect of heterogeneity of the lithology along fault traces

In this scenario, I run two models, and I apply the same methods that I applied in section A-A` of scenario 2 regarding the entry pressure values along faults and the role of the critical stress faults.

1. Model 1

In this model (Figure 4.18a) hydrocarbons were expelled from throughout the source rock vertically until it produced enough hydrocarbons with enough buoyancy that exceeded the CEP of the carrier bed and allowed fluids to migrate upward through the carrier bed. It is obvious that the dip of the layers above the source rock is guiding migration towards Fault F10, as shown by arrows 1 in Figure 4.18a. Hydrocarbon migration starts along faults F10, F25 and F44 at ca. 3000 m, with lateral migration occuring between faults F10 and F25 starting at ca. 900m, as shown by arrow 2 in Figure 4.18a, producing hydrocarbon accumulationss below the key reflectors at ca. 600 m and 800m; fluids then continue to leak along faults F10 and F25 upwards to the seabed. It is noted that the lower part of Fault F44 is guiding hydrocarbon migration and then fluid migrate throughout this fault up to the seabed and this migration is copuled with lateral migration between faults F44 and F39 as shown by arrow 3 . Fault F39 is guiding hydrocarbon migratio rather than allowing fluid to migrate through this fault. The vertical migration along Fault F10 is coupled with lateral migration towards Fault F36 at ca. 900-1000m as shown by arrow 4. It is noted that little hydrocarbon is migrating through Fault F36 and then hydrocarbons are leaking through Fault F22 at ca.600m reaching the seabed in the south of the seismic section as shown by arrow 5 in Figure 4.18a.

2. Model 2

In this model (Figure 4.18b) hydrocarbons were expelled from throughout the source rock vertically until it produced enough hydrocarbons with enough buoyancy that exceeded the CEP of the carrier bed. Hydrocarbon migration at ca.3000m is guided by faults F10 and F44, while hydrocarbon along Fault F25 is hardly migrate as shown by arrow 1. Lateral migration occurs between faults F10, and F36, starting at ca. 1750 m, as shown by arrow 2 in Figure 4.18b. Lateral migration occurs between faults F36 and Fault F22, and Fault F22 is acting as a barrier for hydrocarbon migration shown by arrows 3 and then allow hydrocarbon migration to the seabed as shown by arrow 4. Also, lateral migration occurs between faults F10, F25, F39 and F44, and fluids are trapped by the two key reflectors at ca. 600 m-800 m below the sea level, as shown by arrows 5, and 6 in Figure 4.18b.

The risk analysis results (Figure 4.18c) from multiple models suggest the most probable routes (green colour) for migration are along F10, F36 and F25. Hydrocarbon flow along F25 is diffuse and is more focused along F10. A few models (10-20%) show hydrocarbon accumulation in the northern part of the seismic section and less hydrocarbons migrate along Fault 44.

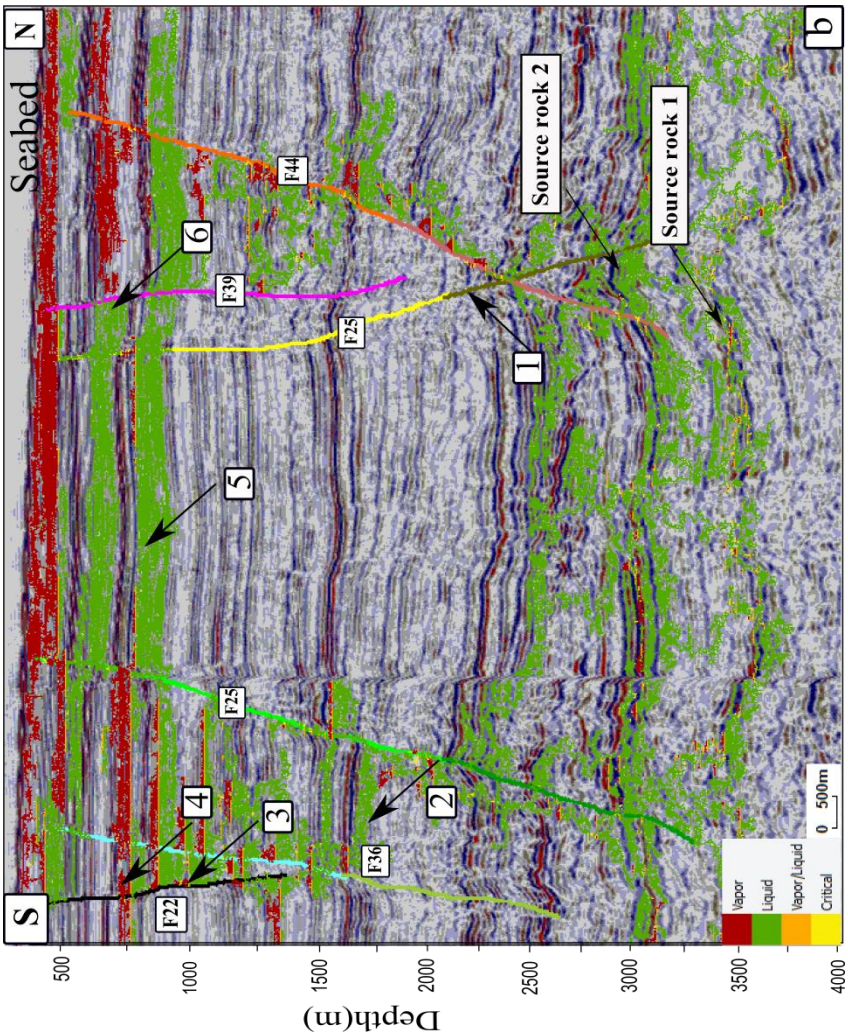
Seabed
N
S
b
Source rock 2
Source rock 1
F44
F39
F25
F36
F22
1
2
3
4
5
6
Vapor
Liquid
Vapor/Liquid
Critical
0 500m
Depth(m)
500
1000
1500
2000
2500
3000
3500
4000

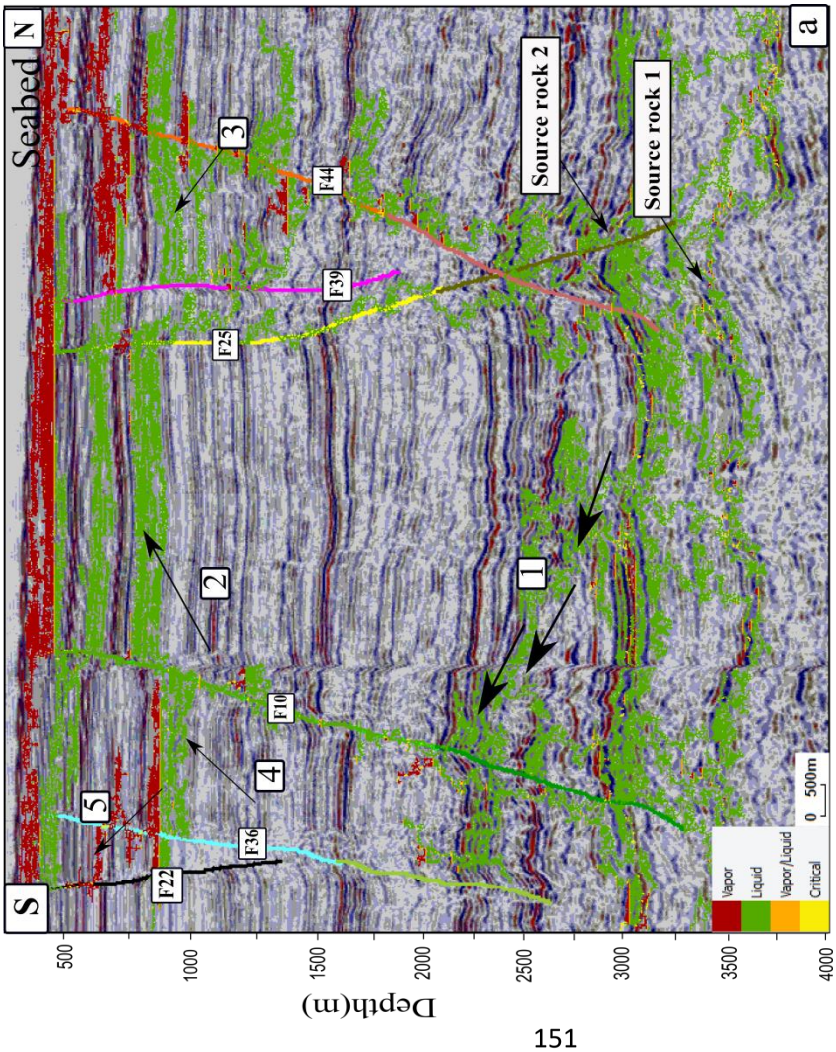
Seabed
N
S
a
Source rock 2
Source rock 1
F44
F39
F25
F10
F36
F22
1
2
3
4
5
Vapor
Liquid
Vapor/Liquid
Critical
0 500m
Depth(m)
500
1000
1500
2000
2500
3000
3500
4000

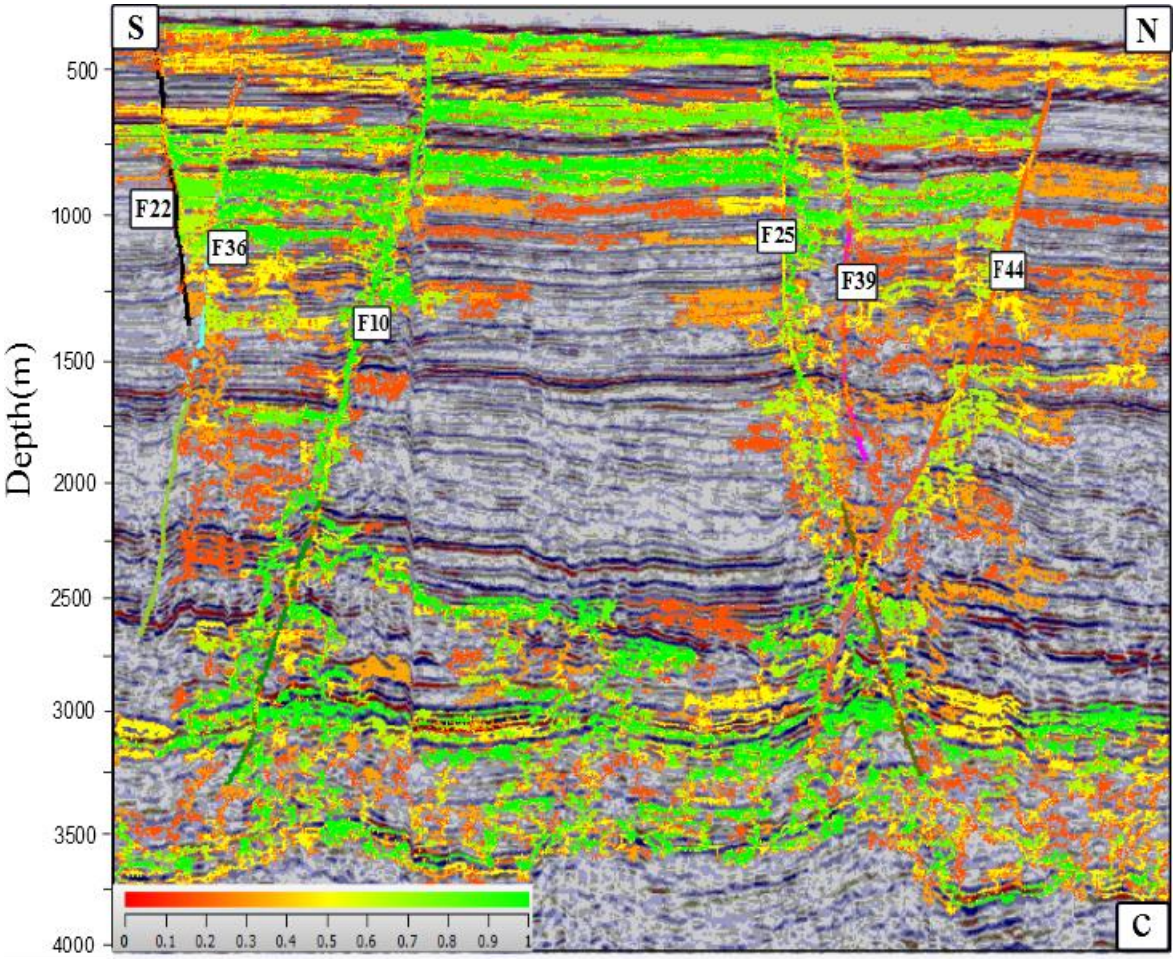

Figure 4.18. Results of migration along the seismic section B-B`. **(a)** Migration model 1 from the first scenario. **(b)** Migration model 1 from the second scenario. **(c)** The final risk analysis from multiple models. The colour scheme shows the fraction of realisations in which hydrocarbons migrate through the cell. Note that the green colour shows that in all models hydrocarbon migration occurs through these pathways; the yellow colour shows that 50-60% of the models show hydrocarbon migration through the seismic section; and the light to dark orange colours show that only a few models (40-0%) show hydrocarbon migration through the seismic section.

4.7.2.3 Additional migration models

Another two models were run along section A-A` to examine the role of other possibilities (section 4.6.2.2.5) for fault properties in fluid migration. These two possibilities are:

- ***Scenario 3: Fault F10 is less stressed than Fault F25***

In this model (Figure 4.19) a CEP value of 3000 kPa is assigned along Fault F10 and 1200 kPa along Fault F25. Hydrocarbons were expelled from the source rock and started to migrate along the source bed until the buoyancy force reached or exceeded the CEPs of the carrier bed. Vertical migration from the source rocks to the overlying beds occurs at ca. 2700 m below sea level (Figure 4.19). It is noted that fluids mainly migrate and are focused along Fault F25 but coupled with lateral migration with Fault 10 at ca. 1100 m below sea level, as shown by arrow 1 in Figure 4.19. Fault F37 is guiding hydrocarbon migration coupled with lateral migration towards fault F25, which results in a trap bounded by a fault as shown by arrow 2 in Figure 4.19. Fault F10 in this model is acting as a barrier fault plane that guides the vertical migration starting at ca. 2000 m below sea level, and then this migration is coupled with lateral migration towards Fault F25 below the key reflectors at ca 600 m and 850 m below sea level. Then, fluids leak from Fault F25, reaching the seabed to the south guided by the dip of the seabed. There is no migration along faults F58 and F42. However, it is noted that hydrocarbons escaped to the south side of the model at ca. 2500 m below sea level, as shown by arrow 3 in Figure 4.19.

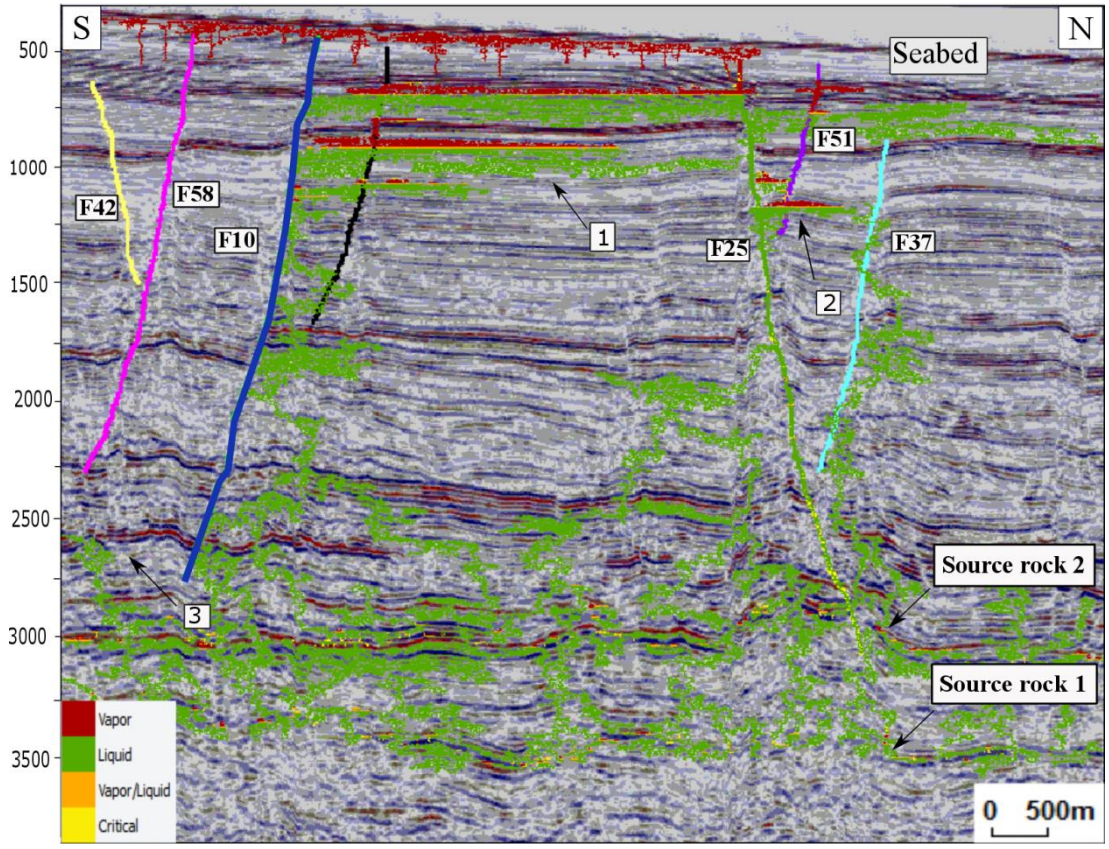

Figure 4.19. Results of the migration model along section A-A`. This model assumes that Fault F10 is less stressed than Fault F25.

- ***Scenario 4: Faults F10 and F25 have high CEP***

In this model (Figure 4.20), a CEP value of 3000 kPa is assigned along faults F10 and F25, and the CEPs along the rest of the faults were kept the same as assigned in ***model 1*** for ***scenario 1*** along section A-A`. Migration in this model shows the same routes of fluid migration from the source rocks as in scenario 3. However, it is noted that the vertical migration of fluids is guided by faults F10 and F25, but they also act as barriers for lateral fluid migration. Also, there is vertical migration from the source rock starting at ca. 2750 m below sea level, which is guided by Fault F37, and shows that hydrocarbons are escaping north out of the model at ca. 1250 m below sea level, as shown by arrow 1 in Figure 4.20. Furthermore, it is noted that there is lateral migration

between faults F10 and F25 starting at ca. 1700 m. Hydrocarbons are then trapped by a barrier bed at ca. 800 m below sea level below the strong reflector, as shown by arrow 2 that is assigned as an interbedded layer of shale/silt/sand and no hydrocarbons migrate to the surface.

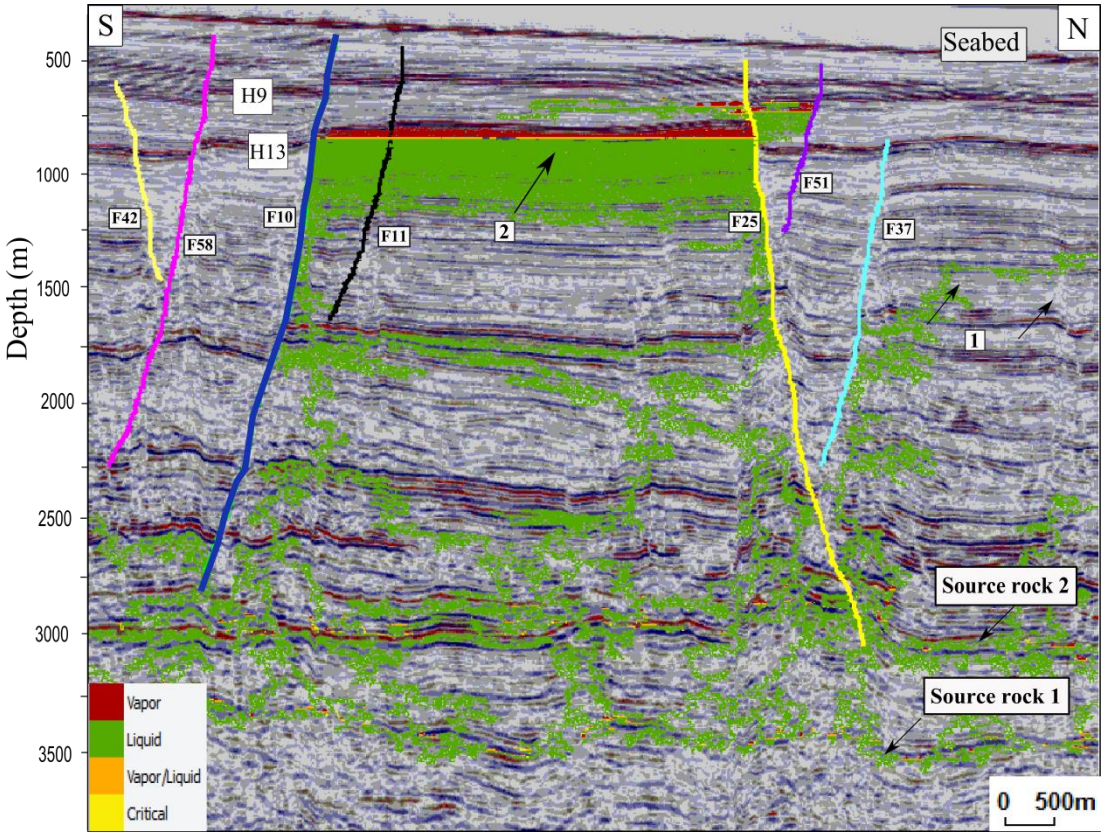

Figure 4.20. Results of migration model along section (A-A`). This model assumed that Faults F10 and Fault F25 has high CEP's or act as closed faults. Note that Faults F10 and F25 are guiding fluid migration from source rock and then hydrocarbon are trapped by a high CEP barrier bed.

4.7.2.4 Hydrocarbon migration along seismic section C-C` in the E-W direction

Migration modelling (Figure 4.21) is performed along the in-line seismic section in the E-W direction to compare migration pathways with the N-S direction. This line is chosen as it cross cuts the amplitude anomaly along Fault F10 and intersects the cross lines A-A` and B-B`, which help to provide some cross line control. One scenario is

tested along this line assuming that Fault F10 is stressed.

In this model, the CEPs along faults F10 and F24 are the same, with a value of 1000 kPa. Hydrocarbons are expelled from the source rocks until they generate enough hydrocarbons that have enough buoyancy forces to overcome the CEP of the overlying layers (Figure 4.21). It is noted that hydrocarbon migration is directed by the dipping strata as shown by arrows 1 and 2 in Figure 4.21, and then fluids invade the overlying beds and migration starts and is guided by Fault F10. It noted that Fault F24 is acting as a barrier for hydrocarbon migration at ca. 1100 m, as shown by arrow 3 in Figure 4.22. Lateral migration occurs from Fault F10 to the west at ca. 1100 m and fluids are again trapped by the same key reflectors as in previous models (e.g. model 1, section A-A`). Lateral migration occurs again between faults F10 and F24 at ca. 500 m, with fluids migrating along Fault F10 to the surface to the east and west of the section. Note that hydrocarbon migration has stopped to the east of the seismic section at ca. 1400 m, as shown by arrow 4 in Figure 4.21. This observation suggest that hydrocarbon migration is encountering a high CEP layer that is difficult to invade. It is noted that the migration system in the E-W direction is similar to that in the N-S sections, regarding the role of the dipping strata in guiding fluid migration. However, hydrocarbon migration along Fault F10 is more guided by this fault, rather than focussed along Fault F10.

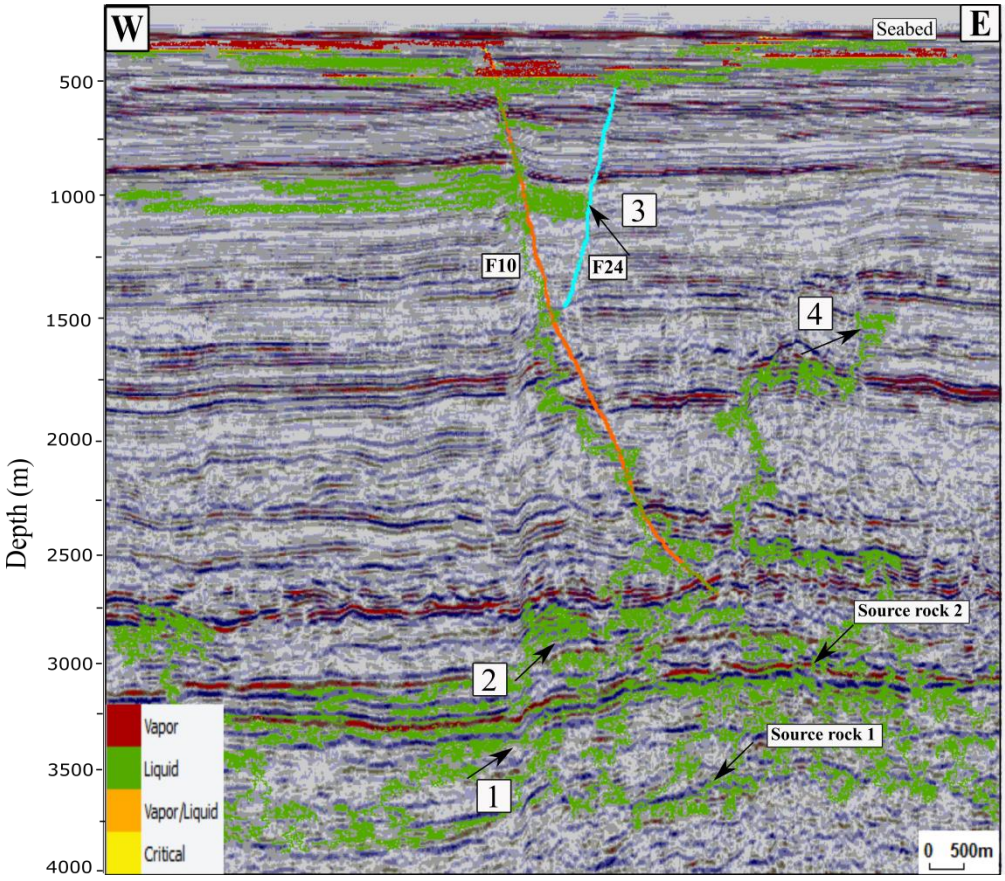

Figure 4.21. Migration model along section C-C` showing how fluids migrate from the source rock and then migrate vertically along F10 to the southern part of the seismic section, in addition to the lateral migration to the north without reaching the surface. Note how the dipping of the bedding at the source rock level is guiding the fluid flow.

4.8 Discussion

Migration modelling has been run along two seismic sections in the N-S direction and one section in the E-W direction that cross the amplitude anomalies which are mainly associated with Fault F10 in the southern part of the seabed (i.e. the area where hydrocarbon leakage is observed) (Figure 4.1). The key aim of these models is to evaluate the circumstances which result in preferential leakage to the seafloor (Figure 4.1) and to investigate the role of faults in controlling hydrocarbon migration. A better understanding of the hydrocarbon system will contribute to reducing the exploration risk for the Laminaria High.

In all models, hydrocarbons are expelled from the source rock and start to migrate laterally within the source layers until the buoyancy force of the hydrocarbons exceeds the CEP of the background lithologies. Then hydrocarbon migration is guided by faults and by the dipping of the carrier beds.

To further the understanding of the different circumstances for fluid migration, this study has explored the parameters under which certain faults are likely to be the principal leakage conduits, given the stress regime, CEP of faults versus the background lithologies, and variability of CEP along faults. Two scenarios were applied to each seismic section (A-A` and B-B`), in addition to another two scenarios along section A-A`, to examine the role of critically stressed faults on hydrocarbon migration and the heterogeneity of lithology along fault traces.

4.8.1 Stress analysis

This study focused on the role of the main faults F10 and F25 in hydrocarbon migration. Evidence of hydrocarbon leakage on the seabed (Figure 4.1) Castillo et al. (2000) stated that the E-W bounding faults in the Laminaria High are not critically stressed and therefore, are capable of preserving hydrocarbon columns. However, in this study, the stress analysis results showed that Fault F10 is possibly more critically stressed in terms of slip and dilation tendency than Fault F25. This suggests that Fault F10 is more likely to slip and leak, which is consistent with the amplitude anomaly being associated with Fault F10 in the southern part of the study area.

The stress analysis showed that the linkage between two fault planes has resulted in increasing the slip and the dilation tendency on one fault and decreasing them on the other, as shown in Figures 4.11a and 4.11b. This could be related to the local change in fault orientation in zones of linkage (Ligtenberg, 2005).

The stress analysis was applied assuming a homogeneous (no spatial variation) and static (no change with time) regional stress field. However, the Laminaria High is located at the edge of Timor Island, which is considered as a tectonically active area. In the beginning of the Late Miocene (at about 3-5 Ma) to the present day, the Timor Sea has transformed into a collisional setting due to the oblique convergence between the Australian and Eurasian plates and is seismically active as supported by earthquakes. Some of these have a significant magnitude such as the M 6.3 Cockatoo Earthquake in 1997 (Castillo et al., 2000). Cowie (1998) stated that a seismic rupture of a fault results in stress perturbations and induces stress changes on neighbouring faults, which will delay or advance the occurrence of future earthquakes, so that the stress fields can change rapidly with time.

Sibson et al. (1975) suggest that stress varies temporally, and that before any seismic failure, faults that are located around the area of a pending earthquake will dilate due to an increase in the tectonic shear stress. This causes a reduction in fluid pressure in the dilation zone, and a considerable amount of fluid can migrate through these open cracks. As the fluids fill these fractures, if they cannot escape then the pressure will rise rapidly, causing the frictional resistance to decrease. This scenario follows an accepted model for triggering earthquakes (Sibson et al., 1975). From the above discussion it is concluded that due to the changes in the stress field in the study area it is possible that some faults were open at some time and allowed fluid migration to reach the seabed; however, the stress could vary along these faults, either during the seismic cycle or due to Coulomb stress transfer processes, which makes it less likely to see evidence of hydrocarbon leakage (amplitude anomalies) at the seabed in the northern part of the study area.

4.8.2. The role of critically stressed faults and the choices of the CEP in fluid migration

Stress analysis results are used to estimate the CEP values along fault traces that intersect seismic sections (A-A` and B-B`) (Figures 4.1). The results suggest that migration pathways show different routes based on the assigned CEP values along faults and the dipping of the carrier beds. The role of the faults is summarised below.

a. Faults act as linear pathways for vertical migration

Assigning low CEP along faults (i.e. CEP within the lower range of the lithofacies) in Table 4.2 allows linear and focused migration for hydrocarbons from the source rock towards the surface (e.g. Figure 4.15a, Fault F10, and 4.15b, faults F10 and F25). The implication is that hydrocarbon migration is more focused along these faults and allows migration towards the surface. Also, it shows that migration mainly starts from the source rocks towards faults F10 and F25, as shown in models 1 and 2 of scenario 1 (figures 4.15a and 4.15b).

b. Faults act as a general guide for vertical migrations

In other cases, when the CEPs along faults are assigned within the middle (e.g. Figure 4.16b, Fault F25, and Figure 4.17a, Fault F44) and the higher CEP ranges of the lithofacies (e.g. Figure 4.19, Fault F10), faults act as barriers. In these models, faults guide the direction of migration from the source rock to the surface but are not the conduits. For example, when a high CEP is assigned along Fault F10, and a low CEP is assigned along Fault F25, the migration pathways show that hydrocarbon migration is guided by Fault F10 and fluids still reach the seabed, as shown in Figure 4.19. Also, it is noted that the dipping of the strata along the seismic section has a principal role

in delivering the hydrocarbons towards the faults, which then promote the migration to the surface (figures 4.16 and 4.18).

c. Faults act as barriers and thus allow hydrocarbon accumulation

Faults may also act as barriers to lateral migration. For example, in figures 4.18a and 4.18b, lateral migration occurs between faults F36 and F22. The stress analysis shows that Fault F22 has a slip tendency of 0.4 to 0.5 at the east end tip where the seismic section intersects this fault, which suggests the possibility of this fault to slip. However, some parts of Fault F22 are acting as a barrier, leading to hydrocarbon accumulation between faults F36 and F22 (figure 4. 18), and other parts of this fault allow lateral migration of hydrocarbons through Fault F22. This result could be related to the heterogeneity of the CEP for the lithofacies within the fault zone (Fault F22), which makes the fault act as a barrier at some point and conduit during migration (Smith,1966).

4.8.3 The effect of heterogeneity along the fault on fluid migration

The heterogeneity along faults was tested by assuming that faults became more compacted with depth so that the CEP increased along the deeper parts of the faults. Two ranges of CEP (within the lower and middle ranges of the CEP of the lithofacies) were tested in scenario 2. The results from scenario 2 along sections A-A` and B-B` suggest similar conclusions to scenario 1, in that faults are acting as barriers for hydrocarbon migration when assigning high CEPs along the fault traces. The upper parts of Fault F10 in Figure 4.17b act as a linear pathway for focused migration, while Fault F25 acts as a general guide for migration due to Fault F25 having been assigned a higher CEP than Fault F10, based on the stress analysis along Fault F25. However, the extent to which it is possible to assign the absolute CEP values along faults in this study is questionable, and a further fault seal analysis is required (Bretan et al., 2003).

4.8.4 Migration modelling outcomes

The tested scenarios presented show how hydrocarbon migration is mainly influenced by fault properties, the distribution of the CEP along faults versus the CEP of background lithofacies. It shows that migration could also occur in the absence of slip, depending on the CEP within the fault zone, which in this study depends on the background lithofacies (Bretan et al., 2003). Furthermore, the dip of the strata along the seismic section has a key role in directing fluids from the source rocks to the surface, as shown in Figure 4.18b. The probability distribution for the petrophysical properties assigned along each model and the risk analysis models helped to quantify the uncertainty in the model results and identify the most probable hydrocarbon accumulation. The risk analysis shows that the southern part of the seismic section is considered as a risk area for hydrocarbon leakage along Fault F10. However, as discussed in section 4.8.1, the stress field could be temporally modified; hence, hydrocarbon migration and leakage along faults could change with time. For example, Figure 4.19 shows that there is a possibility of hydrocarbon leakage to the surface along Fault F25, although there is no evidence of amplitude anomalies on the seabed (Figure 1). This result is consistent with the fact that the stress field is temporally modified with time along fault planes (Sibson et al., 1975) and could act as barriers or conduits based on the stress regime.

4.8.5 Estimation of CEP along faults using shale gouge ratio

In the current study, the impact of faults on migration was investigated by assigning a range of CEP to pixels along the interpreted fault planes. This simple approach can be justified by the aim, which was to investigate the first-order influence of faulting on leakage in this area. However, standard practice within the hydrocarbon industry assumes that the clay content within the fault zone is the main control on whether a

fault acts as a lateral seal. Therefore, estimation of clay ratio is crucial to predict the capillary pressure when conducting more detailed fluid migration studies (Knipe et al., 1998). Bretan et al. (2003) used the shale gouge ratio (SGR) to estimate the fault zone capillary entry pressure (FZP) in order to estimate hydrocarbon column heights. The SGR is calculated at a given point on a fault surface by this equation (Yielding et al., 1997):

$$SGR = \frac{(\mathrm{Vsh}\Delta \mathrm{Z})}{\mathrm{t}} * 100\% \quad (4.6)$$

Where Vsh is the volume of shale, ΔZ is the bed thickness and t is the throw.

Their study calculates the capillary entry pressure within the fault zone by the equation:

$$\mathrm{FZP(bar)}=10^{(\mathbf{SGR/27-C})} \quad (4.7)$$

C is variable with depth, when the burial depth is less than 3.5km, C is 0.5; the burial depth between 3.0 and 3.5km, C is 0.25; the burial depth exceeds 3.5km, C is 0 (Bretan et al., 2003).

I used this approach to compute the shale gouge attribute along the studied fault surfaces, using the volume of shale ($\boldsymbol{V_{shale}}$) adjacent to the fault. The $\boldsymbol{V_{shale}}$ property was derived from gamma log. The shale gouge attribute was then mapped along faults that are associated with the amplitude anomalies at the seabed (e.g., F10, F11 and F58) and values of shale gouge ratio were extracted as shown in Table 4.6. The capillary entry pressure was then calculated at the intersection points for these faults using the Eq.4.7 and shown in Table 4.6 and Figure 4.22.

The magnitude of the CEP along faults (e.g. Fault F10) used in the current modelling differ from those calculated using Bretan et al's (2003) method, for example, Fault F10 in model one along section A-A` in section 4.4.2.1.1 has a CEP value of 1000 kPa along the entire length of this fault, however, the calculated CEP suggest that the upper parts of this fault are heterogeneous and have CEP values of 995 kPa at depth 463.51 m and 3905 kPa at depth 507.67 m.

It was aimed to use the 3D fault surface along with their shale gouge ratio to run migration models using the 3D seismic volume. However, there was an issue with Permedia in positioning fault planes within the 3D seismic volume which make it difficult to run these models. Also, the gamma logs only cover data at depths from 450m to 850m which means that there are no calculated SGR along the entire length of the fault. Furthermore, the Bretan et al. (2003) method is based on data derived from clastic reservoir sequences; it is not clear how it relates to carbonates, such as those encountered in the Plio-Pleistociene of the Laminaria High. Hence, an alternative methodology was used in this study as explained in section 4.6.2 and the CEP values along faults were ranged based on the stress analysis results as explained in section 4.6.2.2.2.

Table 4.6. Shale gouge ratio and CEP values calculated by Eq. 4.7 at the intersection points of faults F10, F11and F58 with the seismic cross line no. 2525.

Fault no.	**Shale gouge ratio**	**CEP (KPa)**	**Depth(m)**
F10	26.37	995	463.51
F10	42.18	3905	507.67
F11	29.59	1300	450.54
F11	39.81	3100	503.27
F58	41.13	3565	702.57
F58	32.17	1636	812.10

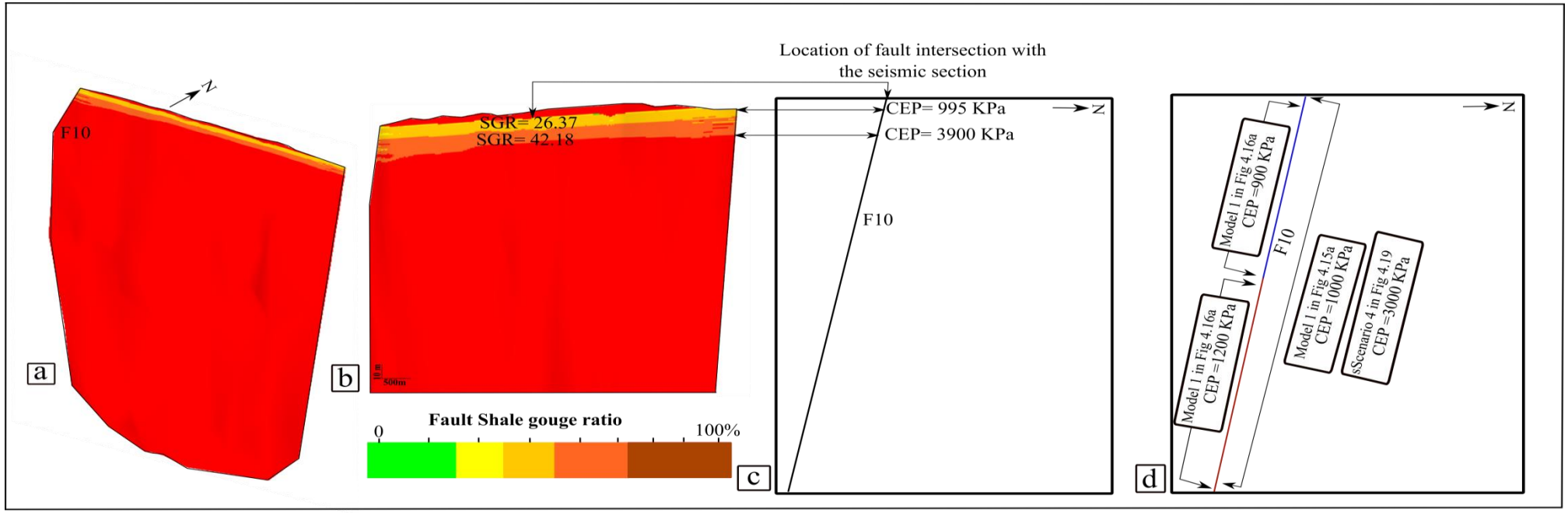

Figure 4.22. Example of shale gouge attribute. **(a)** Shale gouge ratio mapped along the 3D display of fault F10; **(b)** Zoom in along Fault F10 showing the SGR values at the intersection point with the seismic section. **(c)** Schematic of seismic section A-A` along Fault F10 showing values of CEP calculated using Bretan et al's (2003) method at the intersection point of Fault F10 and the seismic section. **(d)** Schematic of seismic section A-A` along Fault F10 showing values of CEP ranged based on the stress analysis.

4.9 Limitations of the models and main assumptions

Many assumptions were made when setting the inputs for the migration models and there are certain limitations in the results due to these assumptions.

The capillary entry pressure (CEP) for the clastic lithofacies were assigned based on the studies of Schlomer and Krooss (1979), Schowalter (1979), Ukekwe et al. (2012). For the carbonate sequence, I assign the capillary entry pressure based on the grain size in the definition of rock type (limestone) from the geological interpretation in the well report, in addition, to the CEP values from (Cullen, 2017). It would be better to apply the seismic inversion technique to estimate the lithologies directly from the seismic data (Veeken et al., 2009). These techniques will give more confidence in the relationship between the seismic colours (amplitude) and the CEP values for the lithofacies. For future work, it should also be possible to explore the implications of assigning different CEPs to lithologies on migration pathways from those used in this study.

The capillary entry pressures (CEP) for a particular lithofacies should increase with depth as a result of decreasing the pore size and increasing the stress with depth. Therefore, at the bottom of the model, the lithofacies should have higher CEPs from those at the top of the model. Permedia does not consider the effect of rock compaction with depth. For example, the red and blue colours on the seismic section are assigned as interbedded layers of shale, silt and sandstone within the Echua Shoal, Flamingo, Frigate and Plover formations and were assigned a CEP of 3400 kPa. However, the same colours appear within the shallow subsurface along the seismic reflectors, hence assigning the same CEP values causes these layers to act as a barrier for vertical hydrocarbon migration. For example, all models show two bright key reflectors within the Barracouta and Oliver formations at ca. 600 and 800 m below sea level (e.g. figures

4.16 and 4.20). However, these formations are mainly limestone (65%) with interbedded layers of shale and sandstone, so are probably not seals or barriers for vertical hydrocarbon migration. For this reason the results from scenario 4 cannot be accepted and the condition that was applied does not give a realistic result.

Furthermore, in all models, it is noted that there is a large hydrocarbon accumulation below the seabed reflector, which has the same red and blue colours associated with high CEP values. However, the CEP at this level should be lower than 3400 kPa so the fluid would escape easily through the seabed. To resolve this issue, it would be better to exclude the seabed surface from the seismic section to avoid this accumulation near the surface. For example, Figure 4.23 shows the onset of hydrocarbons reaching the seabed when the model was stopped as soon as the hydrocarbons reached the seabed; after that point hydrocarbons should escape through the seabed and no accumulation should occur below the seabed.

The shale gouge ratio mapped along fault planes was supposed to be used in the migration models to calibrate CEP in the Permedia model. However, there was an issue with Permedia in positioning fault planes within the cross sections. Therefore, due to time limits, this method was not included in this study.

The pressure-volume-temperature (PVT) will affect the density of the hydrocarbons, which in turn will influence the buoyancy forces. In this study, the sample PVT data from Permedia was used as there is no available PVT data for the hydrocarbons in the study area. It was not possible to edit the PVT file in Permedia to test the sensitivity of the migration pathways to different values for these data. However, Permedia allows assigning the source rock properties and kinetic components for hydrocarbons, as shown in Table 3 from Abbassi et al. (2015), which allow realistic results to be produced for the models.

Depth-converted seismic sections are used in the migration models. Depth conversion might affect the pattern of fluid migration along the seismic section due to the slight changes in the geometry of the structures.

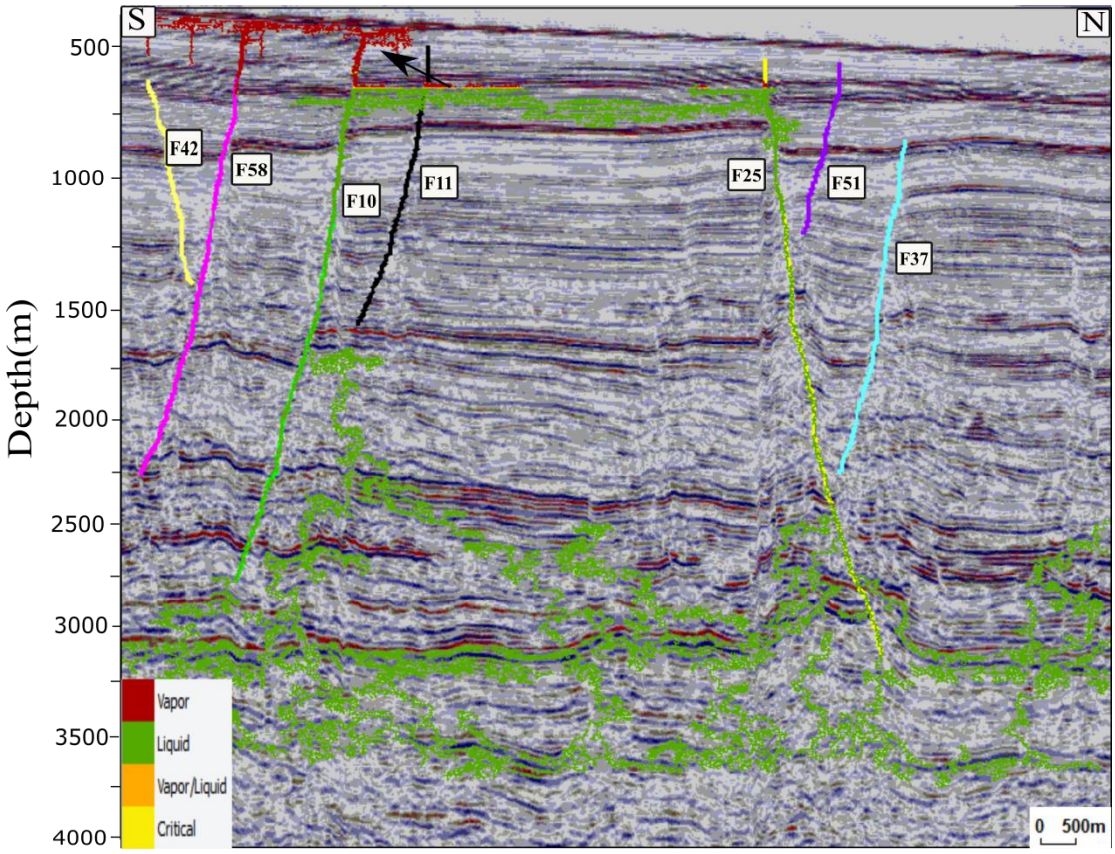

Figure 4.23. Migration results that show the first petroleum that reach the surface from model 2 of scenario 1 along section A-A`. Note that Fault F10 is leaking prior to Fault F 25.

4. 10 Conclusion

- The stress analysis shows that Fault F10 is relatively more stressed than Fault F25, and the preferential migration results along Fault F10 are consistent with the stress analysis. However, although Fault F25 leaks hydrocarbons to the surface in some models, no evidence of hydrocarbon leakage at the seabed suggests that the stress field is not static in the study area.
- The migration results show that fluid migration in the study area is not only controlled by faults, but they have a principal role in directing fluids from the source rock to the surface. However, leakage and migration could also occur in the absence of the slip and depending on the CEP within the fault zone, which in this study depends on the background lithofacies.
- The dip of strata in all models is guiding hydrocarbon migration from the source rock to the surface. In addition, the dip of the seabed to the south is considered as the main reason for directing fluid towards the south.
- Different distributions of the CEPs along the faults have a significant impact on fluid flow in that faults could act as 1) linear pathways for focussed migration, this is mainly when a low CEP is assigned along the fault line; 2) a general guide for migration when a high CEP is assigned along the fault; 3) a conduit for hydrocarbon migration at some point and a barrier at another point of the fault surface based on the distribution of the lithofacies within the fault zone.

Chapter 5: Summary, discussion, and future work

The aims of this chapter are: (1) to provide a summary of the main results presented in Chapter 2, 3 and 4; (2) to synthesise and integrate these findings; and (3) to discuss the wider implications of this study and potential future work.

2D and 3D seismic data sets have been used to analyse the evidence of hydrocarbon leakage at the seabed and the shallow subsurface. In this study, I have integrated analyses of seismic amplitudes and other attributes with structural interpretation to investigate: 1) the relationship between the amplitude anomalies at the interpreted key horizons and the structural control on fluid migration; 2) the influence of seismic processing and acquisition on seismic interpretation; and 3) the impact of critically stressed faults on fluid migration.

Many authors studied amplitude anomalies or fluid-escape features – but very few authors attempt to understand the geophysical processing steps that underlie their datasets. However, this thesis has integrated the geophysical processing study (using pre-stack seismic data) with the geological interpretation/modelling which could considered to be the key importance of this study.

5.1 Structurally-controlled, authigenic carbonate cementation

In Chapter 2 the distribution of amplitude anomalies at the seabed and in the shallow subsurface was analysed using 3D seismic reflection data to investigate the relationships between the amplitude anomalies, the present-day structure, and active faults that intersected the palaeo-seabed at different times during the deposition of the syn-faulting, Pliocene-Pleistocene succession. Results of this study confirmed that the amplitude anomaly at the seabed is located on the up-dip side of the fault trace, and is elongated parallel to the two-way time (TWT) structural contours on the seabed. These observations are consistent with the anomalies having developed in response to structurally-controlled fluid seepage along, and up-dip migration away from the fault trace. Other amplitude anomalies were mapped on horizons beneath the sea-floor. Anomalies at the oldest syn-faulting reflector, whilst located adjacent to fault traces, are discordant to the local TWT structural contours (Figure 5.1). These observations are also consistent with structurally-controlled fluid seepage and cementation whilst the reflector was at the (palaeo-) seafloor; however the resulting hardgrounds were subsequently buried and deformed during ongoing sedimentation and fault growth/linkage. The result from this chapter confirms Langhi's et al. (2010) study of the structural control of subsurface structures on the distribution of amplitude anomalies at the seabed. Furthermore, this study demonstrates the role of small-scale faults on fluid migration. Gartrell et al. (2006) suggested that breached or partially-breached hydrocarbon traps at reservoir level (Laminaria Formation) are the result of where the reservoir is cut, or is bounded by vertically continuous, long-lived faults that link the reservoir with discharge sites at the seabed. However, in this thesis (Chapter 2), there is no clear relationship between the occurrences of anomalies and the magnitude of throw, or the duration of activity, along the Cenozoic faults. A conceptual diagram is proposed (Figure 5.2) to explain the fault – related fluid flow and authigenic carbonate growth in relation to fluid flow.

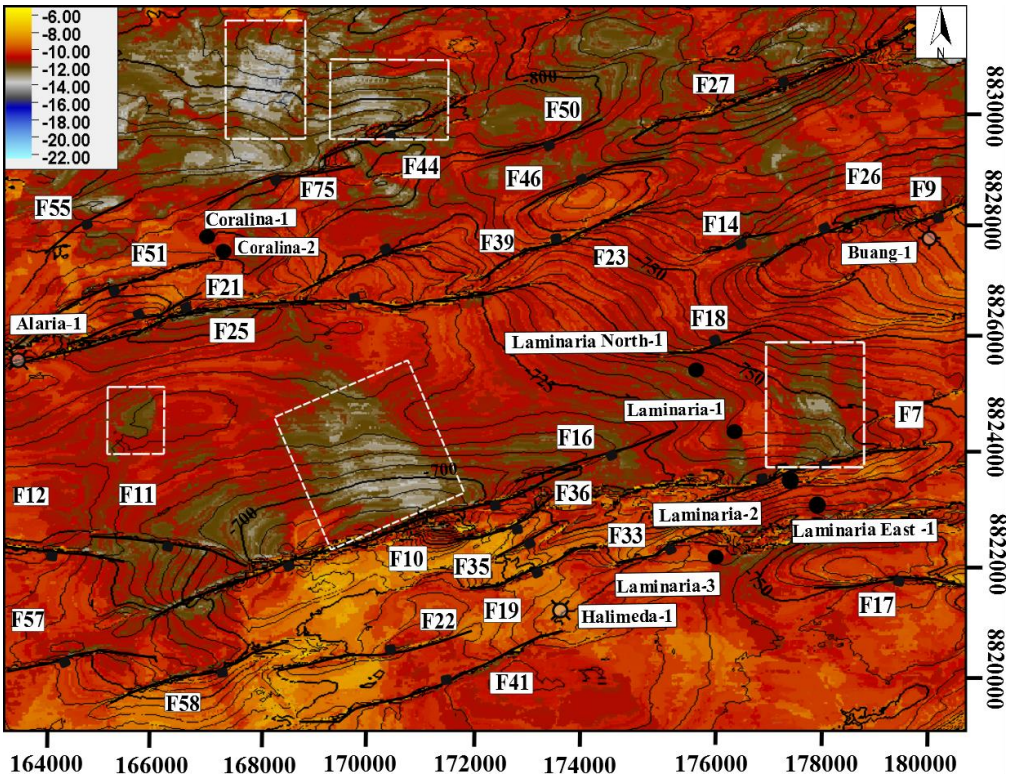

Figure 5.1. Amplitude map for H9, overlain by the two-way time structural contours for this horizon. The map shows high negative amplitude anomalies along faults F10, F11, F12 and F7 in the southern part of the study area, and along faults F44 and F75 in the northern part. The white boxes indicate places were the strike of the TWT contour lines are discordant to the trends of the amplitude anomalies.

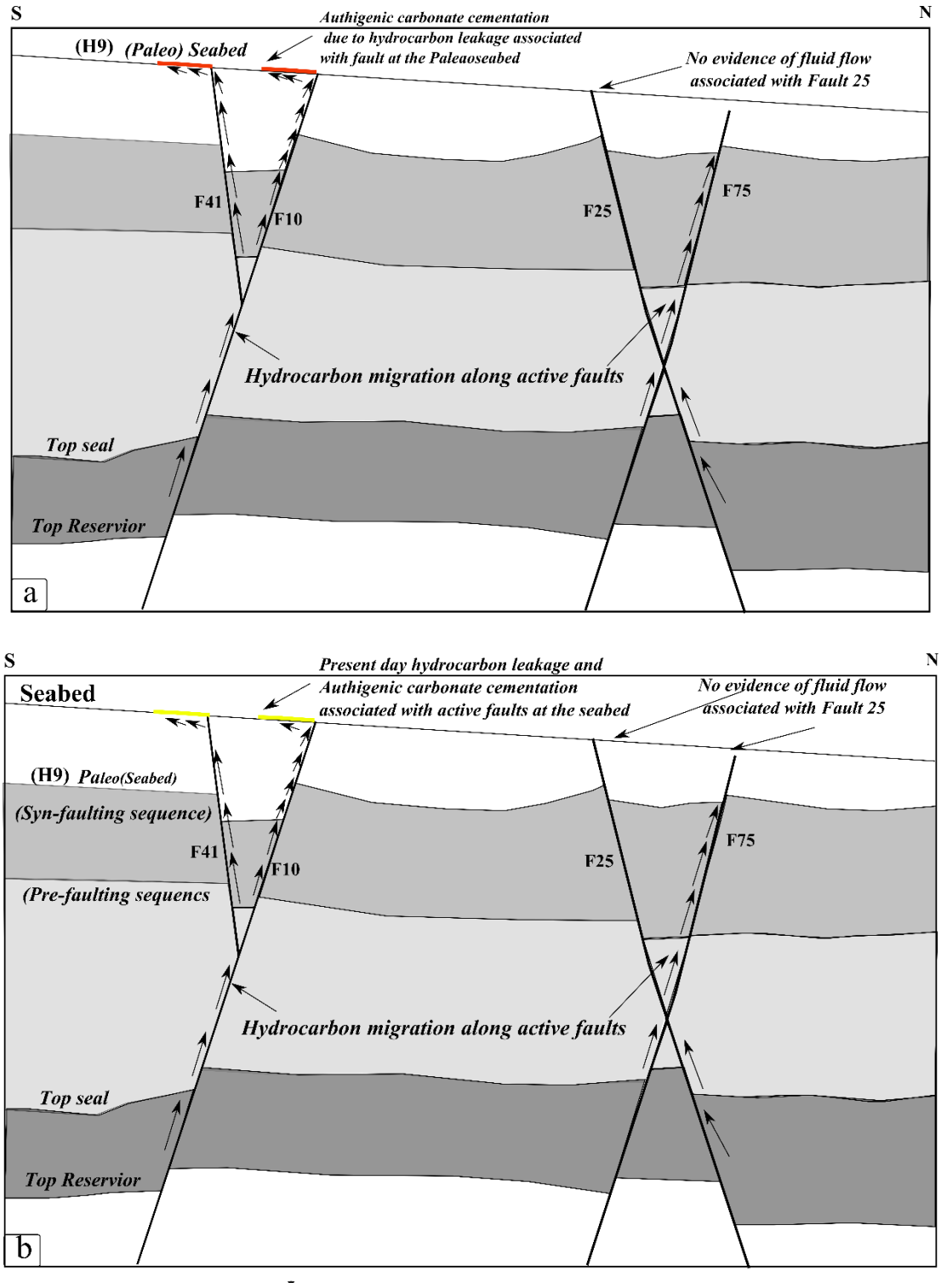

Figure 5.2. Conceptual diagram explain the fault –related fluid flow and authigenic carbonate growth in relation to fluid flow. **a**. Paleo-Seabed (H9), black arrows show hydrocarbon migration pathways along active faults and show the production of authigenic carbonate cementation. **b.** Present day seabed showing hydrocarbon leakage and the production of autigenic cementation associated with active faults.

5.2 The veracity of amplitude anomalies at the seabed

Reprocessing of 2D (1992, Caulerpa) and 3D (1995, Laminaria) pre-stack seismic data were applied to examine the veracity of amplitude anomalies at the seabed (Chapter 3). It is hypothesised that the amplitude anomalies at the seabed in the 3D seismic volume (Chapter 2) are sensitive to the processing sequence applied to the pre-stack seismic data. This study showed that by applying simple but similar processing steps to that applied to the 3D seismic volume; it is possible to produce similar amplitude anomalies at the seabed. However, it was noted that amplitude anomalies at the seabed are sensitive to the velocity model; in particular, when applying radon demultiple to suppress the multiple energy in the seismic data. The result of reprocessing these data suggested that the different result of mapping the seabed reflector in this study and Langhi's et al. (2010) study could result from the different processing parameters applied to each data set (Figure 5.3). Since Langhi et al's (2010) study merged and used three seismic datasets that were acquired at different times (1995, 1999, and 2000), it could be that these merged data were subjected to different processing to adjust the frequency of these data, and to remove acquisition differences between the three data sets. As concluded in this study, amplitude anomalies at the seabed are frequency dependent so any manipulation in the frequency filters could affect these amplitude anomalies (Brown, 2011).

There is not a 'unique' way to process seismic data. What gives an optimum result in one part may enhance noise in another, leading to the risk of false interpretation. For this reason, it is possible to overlook subtle features in the seismic data (Marfurt and Alves, 2015).

5.3 Effects of survey date on the seismic anomalies at the seabed from different data sets in the Laminaria High

Reprocessing of the 2D (1992, Caulerpa) that covered the Laminaria High showed similar but not identical amplitude anomalies compared with the original 3D seismic volume (1995), and it is proposed that these difference could be related to the processing applied on each data set. Another possibility is that there may have been continuous, or distinct episodes of seepage and authigenic carbonate cementation occurring between 1992 and 1995. In other words, there may be a *geological* explanation for the differences between the Caulerpa and Laminaria datasets.

The differences in the time of acquiring the two survey shots in this study could suggest that regional tectonic activity in the wider study area could modify the stress field in the study area, which then will change the stress conditions

The Laminaria High is located at the edge of at the edge of Timor Sea, which is a tectonically active area as discussed in Chapter 4 (section 4.8.1) In the beginning of the Late Miocene (at about 3-5 Ma) to the present day, the Timor Sea has transformed into a collisional setting due to the oblique convergence between the Australian and Eurasian plates and is seismically active as shown by earthquakes (Figure 5.4a). Some of these have a significant magnitude, such as the M 6.3 Cockatoo in West Australia in 1994 and the M6.4 in the Banda Sea in north-west Australia in 1997 (Castillo et al.,1998, 2000) (Figures 5.5a and 5.5b).

Geoffrey et al. (1999) and Stein, (1999) stated that earthquakes are known to redistribute the stresses in the rock volumes surrounding active faults. Simpson and Reasenberg (1994) argued that post earthquake fluid flow will increase the effective coefficient of friction which

cause long term increase in the static stress changes; hence will change fluid flow behaviour and their seismic evidences associated with seismically active faults. It is therefore possible that modification of the stress field following one or more earthquakes in the vicinity of the Laminaria High triggered, or facilitated fluid seepage and authigenic carbonate cementation between 1992 and 1995.

These changes in stress will result in changing the pressure and temperature which might result in potential changing in amplitude anomalies caused by fluid flow. Changes in pressure are directly related to changes in stress without the need for any significant fluid movement. Batzle and Wang, (1992) argued that seismic properties of pore fluids (e.g. density and velocity) could vary under different condition of pressure and temperature. For example, oil viscosity will increase with decreasing temperature and increasing pressure and molecular weight. Agersborg et al. (2006) simulate the seismic reflection response in fluid-fill fracture reservoir in terms of pore fluid pressure changes. This study showed that the seismic response could be changed due to opening or closing fractures due to changes in pore fluid pressure. However, the main reason for the differences in the amplitude anomalies at the seabed between the reprocessed profiles from the 2D survey acquired in 1992 and 2D profiles extracted from the 3D survey acquired in 1995, still needs further understanding and research in terms of the time scale between the two survey and how possible the above discussion could be applied in this study.

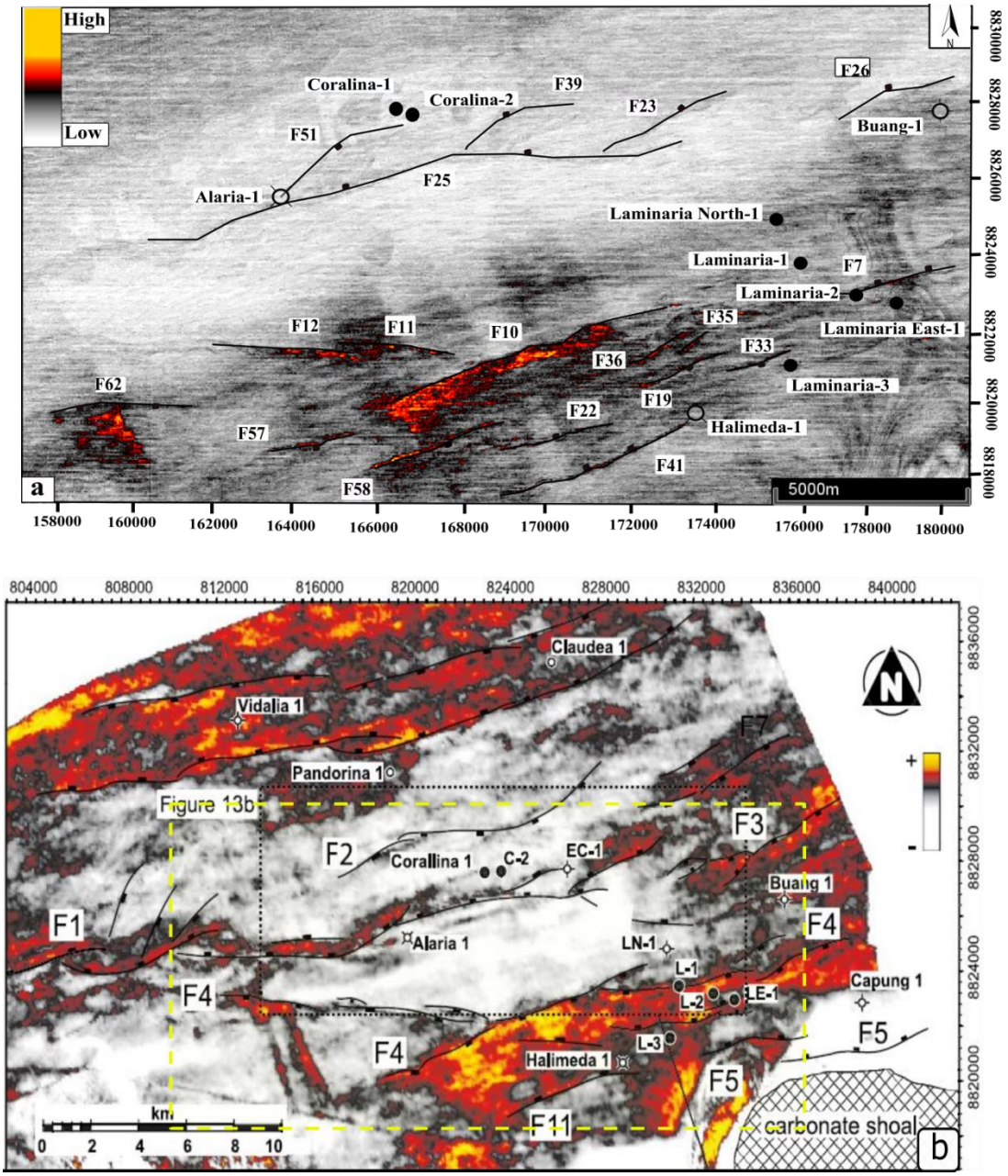

Figure 5.3 Spectral decomposition map at 30 Hz frequency extracted from the seabed showing the fault traces and well locations. SD anomalies, indicated by the hot colours, are associated with the major faults in the southern part of the study area. **(b)** Spectral decomposition map at 30 Hz for the seabed (from Langhi et al. (2010) authorised by the AAPG Journal). This map shows a different distribution of SD anomalies compared to **(a)**. The yellow dashed box is the area covered by Figure 2.6a. Note the difference in x axis coordinates, Langhi et al. (2010) used a different Universal Transverse Mercator (UTM) projection, also note the fault numbering schemes are different between the two plots.

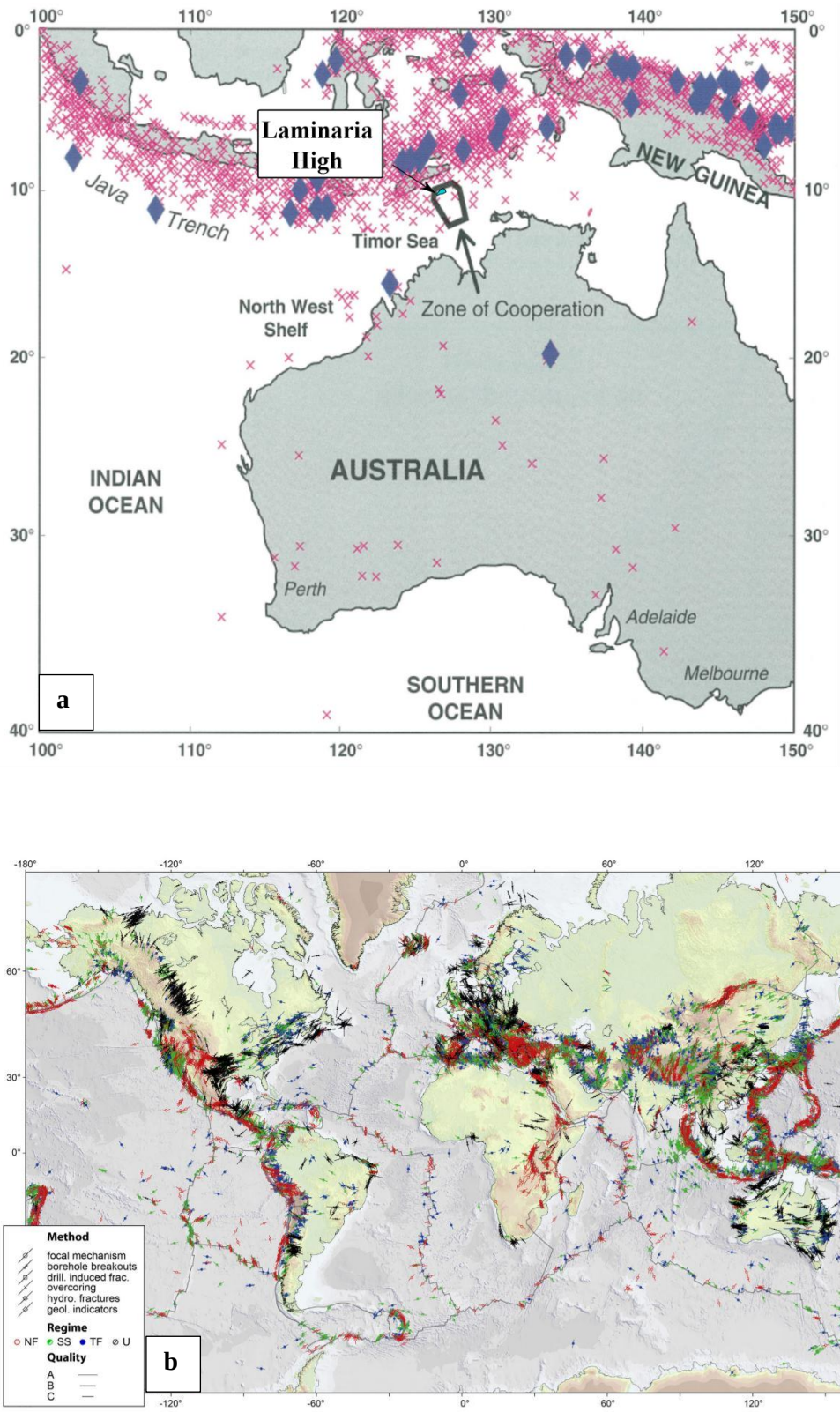

Figure 5.4. a. Earthquakes record along the Australian-Indonesian collision zone from 1979 t0 1997. Crosses are earthquakes with M > 4.5 and diamonds are earthquakes with M > 6.5 (from Castillo et al., 1998). Note that the Laminaria High is located within this active area. b. world stress map based on the WSM databse released in 2008. Lines shows the maximum horizontal stress $S_{H;}$ red is for normal faults, green for strike-slip faults, black for unknown fault regime (from Heidbach et al, 2010).

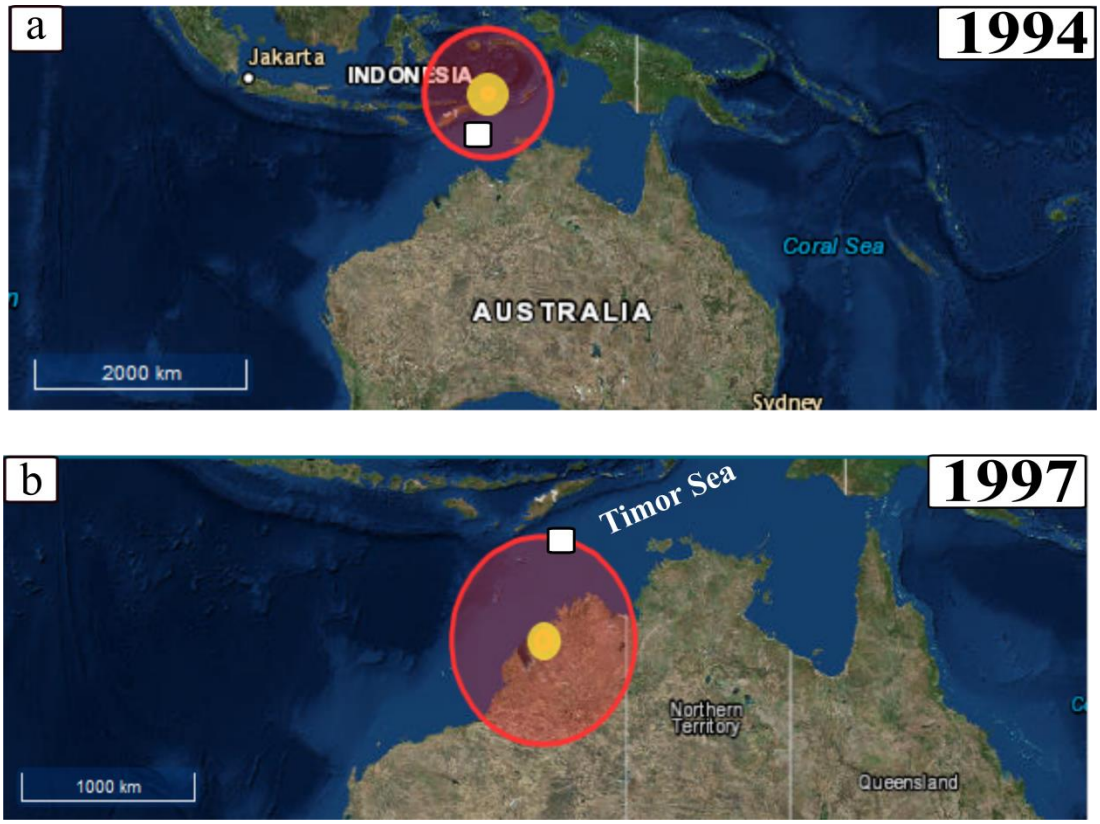

Figure 5.5. Earthquakes near the Laminaria High. **(a)** M 6.3 in the Banda Sea. **(b)** M 6.3 Cockatoo in west Australia. The white box is the location of the study area.

5.4 Critically-stressed faults and fluid migration

Chapter 4 tested the hypothesis that hydrocarbon leakage at the present-day seabed is associated with stressed faults. Analysis of the slip and dilation tendencies showed that parts of some fault surfaces within the study area are critically stressed (e.g., Fault F10) and that these are associated with amplitude anomalies at the seabed. On the other hand, some faults are not stressed (e.g., Fault F11) but are also associated with amplitude anomalies at the seabed. The stress boundary conditions in this study (Chapter 4) were applied assuming a homogeneous (no spatial variation) and static (no change with time) regional stress field. However, the Laminaria High is located at the edge of Timor Trench, which is a tectonically

active area. The collision of the Australian plate margin is a complex and ongoing process. Therefore, the stress field could be changing over time (Gartrell and Lisk, 2005). Also, the orientation and magnitude of the stress field have been changed since the onset of hydrocarbon leakage (Mildern et al., 1994; Castillo et al., 2000; de Ruig et al, 2000). Therefore, a fault that acts as a seal under the current stress field may have been a conduit for fluid migration in an earlier period. Similarly, any change in the stress field could make a fault seal (de Ruig et al., 2000). Gartrell and Lisk (2005) suggested that hydrocarbon leakage associated with fault reactivation in the Skua field in the Vulcan sub-basin is associated with the paleostress regime rather than the present day stress field. The above supports my result of the stress analysis being inconsistent with hydrocarbon leakage associated with some of the active faults at the seabed.

Migration models assigned one and/or two capillary entry pressure (CEP) values along faults of interest identified on the seismic section based on the stress analysis results. Fisher et al. (2001) assumed that fault zone properties are homogeneous along the entire length of the fault. However, Bretan et al. (2003) showed that fluid migration is mainly controlled by the heterogeneity within the fault zones which depend on the pore size of the pore throats in fault zones and the interfacial tension of oil to water at reservoir conditions. The Bretan et al. (2003) study calibrated the shale gouge ratio to estimate the capillary entry pressure of fault zone; a more objective, repeatable approach could have been applied in this study by using shale gouge ratio (SGR) mapped on fault surface to estimate the capillary entry pressure along each point that intersects the seismic sections, as discussed in Chapter 4. However, due to the limitation in migration modelling as discussed in Chapter 4 and the limited availability of the gamma log data that only covers depths from 450 to 850m.. Therefore, in the current study, the impact of faults on migration was investigated by assigning a range of CEP to pixels along the interpreted fault planes. This simple approach

can be justified as the aim was to investigate the first-order influence of faulting on leakage in this area. As anticipated, hydrocarbon migration is mainly controlled by the capillary entry pressures of the lithofacies within the fault zone. In addition, I found that the dip of the sediment layers also influences hydrocarbon leakage from the subsurface to the seabed. However, the relationship between fault seal analysis (e.g. slip and dilation analyses) and fluid migration is complex and still uncertain. It depends on the throw variation, lithology and pore pressure, hence, the fault could act as a seal at some point of this fault and as a conduit for fluid migration at another point (Yielding et al., 1997).

5.5 Implications of this study

The findings of this research should be of broad interest those studying hydrocarbon migration and leakage in a range of normally-faulted petroleum basins (e.g., North Sea; the Gulf of Mexico and the Timor Sea). Understanding the mechanism of hydrocarbon leakage together with fault seal analysis is essential to interpret the geophysical evidence of fluid migration in many basins.

The relationship between the TWT structural maps and seismic amplitude maps could compensate to some degree for the lack of geochemical analysis and core samples in other studies. In particular, correlate the subsurface structures with evidence of hydrocarbon accumulation from the seismic data could show how consistent are the seismic evidences of hydrocarbons with the structural highs.

In this study, TWT maps were interpreted from the 3D time migrated seismic data, but preferably seismic depth images should be used. This is because the slight changes in the geometry of the structures, in particular, when correlating the subsurface structures with hydrocarbon accumulation which might show some different distribution of fluid flow. However, this requires choosing the optimum velocity model.

Integrating 2D or 3D seismic migrated data with their pre-stack seismic data will increase the confidence of seismic interpretation. Inaccurate seismic processing could enhance some artefacts in the seismic data which might be interpreted as a subtle feature in the subsurface (Brown, 2005). Therefore, this study suggests that any study based on 2D or 3D seismic interpretation; in particular, using seismic attributes should consider the background of processing these data.

The result of migration modelling could add the potential to understand the impact of fault properties on fluid migration. A similar methodology could be tested elsewhere in basins, and further migration modelling could be applied by integrating SGR attribute along fault surfaces using 3D seismic data. The use of 3D seismic data will help to show migration pathways in both the dip and strike direction. Also, using the SGR attribute mapped along fault surfaces calibrated with the capillary entry pressure (Bretan et al., 2003), reduces the uncertainties raised in Chapter 4.

5.5 Future work

A range of strategies could be planned to further test the methods and quantify the limitations of this study. A range of strategies could be planned to further test the methods and quantify the limitations of this study. For example, applying geochemical, isotopic (e.g. carbon and oxygen isotopic) and mineralogical analyses for core samples taken from the seabed in the study area will help to determine the origin of the carbon within these cemented areas at the seabed and the shallow horizons (O'Brien and Woods., 1995).

It would be of interest to focus a study on amplitude variation with offset (AVO) using seismic pre-stack data to identify the origin of amplitude anomalies at the seabed and the subsurface horizons (Montazari, 2013). In this study, initial AVO analysis was applied on the 2D (1992) pre-stack time migrated seismic data using Claritas® (appendix_4A) to

identify the AVO classification for the amplitude anomalies at Horizon H9 in Chapter 2. However, further AVO analysis is required to perform fluid substitution (Foster et al., 2010) which needs more log data (e.g. density log) to create synthetic seismogram and compare the AVO behaviour in the modelling software with the AVO results from the raw pre-stack seismic data in Claritas®.

Similarly, it would be beneficial to carry out seismic inversion technique (Veeken et al., 2009) to convert the seismic amplitude to physical rock properties as it will add further confidence in particular, in assigning the CEP values for the background lithology in migration modelling.

Also, the use of high-resolution seismic data as it reduces some of the uncertainty and is useful for further investigation of seismic anomalies in the shallow subsurface. It would be very interesting to compare the released survey I have from Geosciences Australia used in Chapter 2 with the high-resolution data acquired by Woodside Petroleum as part of their platform site survey data to investigate the most recent growth history on the shallow faults (Woodside well-seabed survey data). Detailed analysis of faults in the shallow subsurface using the high resolution seismic data will provide further generic understanding about the distribution, timing and rates of movement on these potential shallow geohazards. Also, these data allow the interpretation of more horizons in the shallow subsurface that could support the paleoseabed analysis in Chapter 2. Furthermore, it would be useful to extract amplitude maps along the shallow horizons for further investigation of any significant seismic evidence of hydrocarbon migration/ leakage. As it might be possible to recognise some pockmarks or small scale fluid flow features from these data.

References

Abbassi, S., Primio, R., Horsfield, B., Edward, D., Volk, H., Anka, Z., George, S., 2015. On the filling and leakage of petroleum from traps in the Laminaria High region of the northern Bonaparte Basin, Australia. *Marine and Petroleum Geology*.59, pp.91–113. https://doi:S0264817214002554.

Aplin, AC.,Larter, SR., 2005. Fluid flow, pore pressure, wettability and leakage in mudstone cap rocks. In: Evaluating Fault and Cap Rock Seal (eds Boult P, Kaldi J), American Association of Petroleum Geologists Hedberg Series, v.2, pp.1–12.

Ashcroft, W. 2011. A Petroleum Geologist's Guide to Seismic Reflection. Wiley-Blackwell, Oxford.

Agersborg, R.,M. Jakobsen, B. O. Ruud, and T. A. Johannsen, 2007, Effects of pore fluid pressure on the seismic response of a fractured carbonate reservoir: Studia Geophysica et Geodaetica, **51**, no. 1, 89–118.

Andresen, K.J., Huuse, M., Clausen, O.R., 2008. Morphology and distribution of Oligoceneand Miocene pockmarks in the Danish North Sea — implications for bottom current activity and fluid migration. Basin Research 20, 445–466.

Andresen, K.J., Huuse, M., 2011. 'Bulls-eye' pockmarks and polygonal faulting in the Lower Congo Basin: relative timing and implications for fluid expulsion during shallow burial. *Marine Geology*, v. 279, pp. 111-127.

Arntsen, B., Wensaas, L., Loseth, H., and Hermanrud, C. 2007. Seismic modelling of gas chimneys. *Geophysics*, v. 72, no. 5, pp. 251-259.

Arts, R., and Vandeweijer, V. 2011. The challenges of monitoring CO2 storage: *Leading Edge* (Tulsa, OK), v. 30, pp. 1026-1033. https:// doi: 10.1190/1.3640526.

Aydin , A.,2000. Fractures, faults, and hydrocarbon entrapment, migration, and flow. *Marine and Petroleum Geology*, v.17, pp.797– 814.

Bacon, M., Simm, R., and Redshaw, T. 2003. 3-D Seismic Interpretation. Cambridge University Press, Cambridge.

Barton, C.A., Zoback, M.D. and Moos, D., 1995. Fluid flow along potentially active faults in crystalline rock. *Geology*, v. 23, pp.683-686.

Baillie, P., Powell, C.M.A., Li, Z., Ryall, A., 1994. The tectonic framework of Western Australia's Neoproterozoic to Recent sedimentary basins. In: Purcell, P.G., Purcell, R.R. (Eds.), The Sedimentary Basins of Western Australia, Proceedings of the Petroleum Exploration Society of Australia Symposium. Perth, Western Australia, pp. 45-62.

Bailey, W., Shannon, P,M., Walsh, J.J., Unnithan, V., 2003. The spatial distributions of faults and deep sea carbonate mounds in the Porcupine Basin, offshore Ireland. *Marine and Petroleum Geology*, v. 20, pp. 509-522.

Barnes, O.R., and Goldberg, E.D. 1976. Methane production and consumption in anoxic marine sediments. *Geology*, v. 4, no. 5, pp. 297-300.

Benjamin, U.K., and Huuse, M.,2017. Seafloor and buried mounds on the western slope of the Niger Delta. *Marine and Petroleum Geology*, v. 83, pp. 158-173.

Betzler, C., Lindhorst, S., Hübscher, C., Lüdmann ,T., Fürstenau ,J., Reijmer ,J.,2011.Giant pockmarks in a carbonate platform (Maldives, Indian Ocean). *Marine Geology*, v.289, pp.1-16.

Bretan, P., Yielding, G., Jones, H., 2003. Using calibrated shale gougeratio to estimate hydrocarboncolumn heights. *AAPG BULLTIN*, v, 87, no. 3, pp. 397-413.

Bretan, P, 2016. Trap Analysis: an automated approach for deriving column height predictions in fault-bounded traps. *Petroleum Geoscience.https://* doi:10.1144/10.44.petgeo2016-022.

Blumenberg, M., Walliser, E., Taviani, M., Seifert, R., and Reitner, J. 2015. Authigenic carbonate formation and its impact on the biomarker inventory at hydrocarbon seeps: A case study from the Holocene Black Sea and the Plio-Pleistocene Northern Apennines (Italy). *Marine and Petroleum Geology*, v. 66, pp. 532-541.

Brown, A.R., 2005. Pitfalls in 3D seismic interpretation. *The Leading Edge*, v.24, pp.716-717.

Brown, A.R. 2011. Interpretation of Three-Dimensional Seismic Data, seventh edition, AAPG, Memoir 42, SEG Investigations in Geophysics, no. 9, Tulsa, Oklahoma, USA.

Byerlee, J.D., 1978. Friction of rocks: Pure and Applied Geophysics, v. 116, pp.615–626.

Carruthers, D. and Ringrose, P., 1998. Geological Society, London, Special Publications Secondary oil migration: oil-rock contact volumes, flow behaviour and rates. *Geol. Soc. Lond. Spec. Publ.*, 144, pp.205-220.https:// doi:10.1144/GSL.SP.1998.144.01.16.

Carruthers, D.J., 2003. Modeling of Secondary Petroleum Migration Using Invasion Percolation Techniques. *In*: DÜPPENBECKER, S. & MARZI, R. (eds) *Multidimensional basin modeling, AAPG/Datapages Discovery Series*, v. **7**, pp.21-37.

Carruthers, D. and Neufeld, C., 2008. Method and System for Modelling Petroleum Migration. *United States Patent Application Publication,* US 2008/0262809 A1.

Cartwright, J., and Huuse, H. 2005. 3D seismic technology: the geological 'Hubble'. *Basin Research*, v. 17, no. 1, pp. 1-20.https://doi: 10.1111/j.1365-2117.2005.00252.x.

Cartwright, J.,2007. The impact of 3D seismic data on the understanding of compaction, fluid flow and diagenesis in sedimentary basins. *Journal of the Geological Society*,v.164, pp.881-893.

Cartwright J, Santamarina C., 2015. Seismic characteristics of fluid escape pipes in sedimentary basins: implications for pipe genesis. Marine Petroleum Geology , v.65, pp.126–140. https://doi:10.1016/j.marpetgeo.2015.03.023

Castillo D, Hillis RR, Asquith K, Fischer M.,1998. State of stress in the Timor Sea area, based on deep wellbore observations and frictional failure criteria: application to fault-trap integrity. In: Purcell PG, Purcell RR, editors.The Sedimentary basins of western Australia 2: Proceedings of Petroleum Exploration Society of Australia Symposium,Perth, WA. pp. 325–41.

Castillo, D.A, Bishop, D.J., Donaldson, I., de Ruig, M., Trupp, M. and Shuster, M.W., 2000. Trap integrity in the Laminaria High-Nancar Trough region, Timor Sea: Prediction of fault seal failure using well-constrained stress tensors and fault surfaces interpreted from 3D seismic. *AAPPEA Journal*, v. 40, pp.151-173.

Charlton, T.R., Barber, A.J., and Barkham, S.T. 1991. The structural evolution of the Timor collision complex, eastern Indonesia. *Journal of Structural Geology*, v. 13, pp. 489–500.

Chen, Q., and Sidney, S., 1997. Seismic attribute technology for reservoir forecasting and monitoring: *The Leading Edge*, v.16, pp.445– 456.

Chenrai, P and Huuse, M.,2017. Pockmark formation by pore water expulsion during rapid progradation in the offshore Taranaki Basin, New Zealand. *Marine and Petroleum Geology,* v. 82, pp. 399-413.

Childs, C., Easton, S.J., Vendeville, B.C., Jackson, M.P.A., Lin, S.T.,Walsh, J.J., Watterson, J., 1993. Kinematic analysis of faults in aphysical model of growth faulting above a viscous salt analogue.*Tectonophysics,*v. 228, pp. 313–329.

Childs, C. Nicol, A., Walsh, J., Watterson, J., 2003. The growth and propagation of synsedimentary faults. J*ournal of Structural Geology*, v.25, pp.633–648

Corradi, A., P. Ruffo, A. Corrao, and C. Visentin, 2009, 3D hydrocarbon migration by percolation technique in an alternative sand-shale environment described by a seismic facies classification volume: *Marine and Petroleum Geology*, v.26, pp.495–503. https:// doi: 10.1016/j.marpetgeo.2009.01
.002.

Cowley, R., O'Brien, G.W., 2000. Identification and interpretation of leaking hydrocarbons using seismic data: a comparative montage of examples from the major fields in Australia's north west shelf and Gippsland Basin. *Aust. Pet. Prod. Explor. Assoc. J,* v.40, pp.121-150

Cooper, G.T., Barnes, C.R., Bourne J.D. and Channon, G.J. (1998) Hydrocarbon leakage on the North West Shelf, Australia: New information from the integration ofairborne laser fluorosensor (ALF) and structural data. In Purcell, P.G and R.R. (eds). The Sedimentary Basins of Western Australia 2. Procedings Western Australian Basins Symposium, Perth, pp. 255-272

Cowie, P.A., 1998. A healing-reloading feedback control on the growth rate of seismogenic faults. *Journal of Structural Geology*, v. 20, pp.1075-1087.

Cullen, E.E, 2017. Petroleum Migration Modelling of the Offshore Northern Mauritania Basin, Block C-19. Department of Earth Sciences, Durham University, MSci Earth Science (Geology).

Davies, R., Yang, J., Hobbs, R., and Li, A. 2014. Probable patterns of gas flow and hydrate accretion at the base of the hydrate stability zone. *Geology*, v. 42, pp.1055-1058. https://doi.org/10.1130/G36047.1

Dimitrov, L., and Woodside, J.,2003. Deep sea pockmark environments in the eastern Mediterranean. Marine Geology, v.195, pp.263-276.

De Ruig, M.J., Trupp, M., Bishop, D.J., Kuek,D., Castillo, D.A., 2000. Fault architecture and the mechanics of fault reactivation in the Nancar Trough/Laminaria area of the Timor Sea. *APPEA Journal*, pp.174–193.

Dyt, C.P., Langhi, L., Bailey, W.P., 2012. Automating conceptual models to easily assess trap integrity and oil preservation risks associated with fault reactivation. *Mar. Pet. Geol*,v.30, pp, 81-97.

Downey, M. W., 1984, Evaluating seals for hydrocarbon accumulations: *AAPG Bulletin*, v. 68, pp. 1752–1763.

England, W., Mackenzie, A., Mann, D. & Quigley, T., 1987. The Movement and Entrapment of Petroleum Fluids in the Subsurface. *Journal of the Geological Society*,144, pp. 327-347.

Feng, D., Chen, D., and Peckmann, J. 2009. Rare earth elements in seep carbonates as tracers of variable redox conditions at ancient hydrocarbon seeps. *Terra Nova*, v. 21, pp. 49-56. https:// doi: 10.1111/j.1365-3121.2008.00855.x.

Ferrill, D.A., Wittmeyer, G., Sims, D., Colton, S., Armstrong, A. and Moriss, A.P., 1999. Stressed rock strains groundwater at Yucca Mountain, Nevada. *GSA Today*,

pp.1-7.

Foster, D.J. and Mosher, C.C., 1992. Suppression of multiple reflections using the Radon transform. *Geophysics*, v, 57, pp.386–395.

Foster, D. J., Keys, R.G., Lane, F.D., 2010. Interpretation of AVO anomalies. *Geophysics*, v. 75, pp.3-13.

Gartrell, A., Zhang, Y., Lisk, M., Dewhurst, D., 2003. Enhanced hydrocarbon leakage at fault intersections: an example from the Timor Sea, Northwest Shelf, Australia. *Journal of Geochemical Exploration.*, v.78-79, pp. 361-365.

Gartrell, A., Zhang, Y., Lisk, M. & Dewhurst, D., 2004. Fault intersections as critical hydrocarbon leakage zones: integrated field study and numerical modelling of an example from the Timor Sea, Australia. Mar. Petrol. Geol., v. 21, pp.1165-1179.

Gartrell, A., W. R. Bailey, and M. Brincat, 2005, Strain localisation and trap geometry as key controls on hydrocarbon preservationin the Laminaria High area: *APPEA Journal.*, v. 45, p. 477–492

Gartrell, A., Bailey, W.R. & Brincat, M., 2006. A new model for assessing trap integrity and oil preservation risks associated with postrift fault reactivation in the Timor Sea. *AAPG Bulletin*., v.90, pp.1921–1944.

Geoffry, C.P.K., Stein, R., Lin, J.,1994. Static stress changes and the triggering of earthquakes. *Bulletin of the Seismological Society of America.*, v.84, pp.935-953.

George, S.C., Lisk, M., and Eadington, P.T. 2004. Fluid inclusion evidence for an early, marine-sourced oil charge prior to gas-condensate migration, Bayu-1, Timor Sea, Australia. *Marine and Petroleum Geology.*, v. 21, pp. 1107-1128.

Geoscience Australia, 2018. http://www.ga.gov.au/data-pubs, Accessed 05-06-2018.

Heggland, R., 1998., Gas seepage as an indicator of deeper prospective reservoirs. A study based on exploration 3D seismic data. *Marine and Petroleum Geology.*, v. 15, pp. 1-9.

Heggland, R. 2005. Using gas chimneys in seal integrity analysis: A discussion based on case histories. In P. Boult and J. Kaldi, (eds) Evaluating fault and cap rock seals: *AAPG Hedberg Series.*, pp. 237-245.

Heidbach, O., M. Tingay, A. Barth, J. Reinecker, D. Kurfeß, and B. Müller,2008, The World Stress Map database release 2008, accessed at http://dcapp3-14.gfz-potsdam.de/pub/stress_maps/stress_maps.html.

Hillis, R. R., Sandiford, M., Reynolds, S. D. & Quigley, M. C. 2008. Present-day stresses, seismicityand Neogene-to-Recent tectonics of Australia's'passive' margins: intraplate deformation controlledby plate boundary forces. In: Johnson, H., Dore´ ,A. G., Gatliff, R. W., Holdsworth, R., Lundin,E. R. & Ritchie, J. D. (eds) The Nature and Originof Compression in Passive Margins. GeologicalSociety, London, Special Publications, 306, 71–90.

Hobbs, R., and Snyder, D., 1992. Marine seismic sources used for deep seismic reflection profiling. *First break* ., v. 10, pp 417-426.

Hovland, M. 1984. Gas-induced erosion features in the North Sea. *Earth Surface Processes and Landforms.*, v. 9, pp. 209-228.

Hovland, M., Talbot, M.R., Qvale, H., Olaussen, S., and Aasberg, L. 1987a. Methane-

related carbonate cements in pockmarks of the North Sea. *Journal of Sedimentary Petrology.*, v. 57, pp. 881-892.

Hovland, M.,1987b. The formation of pockmarks and their potential influence on offshore construction. *Quarterly Journal of Engineering Geology and Hydrogeology*, pp.13-22. https:// doi 10.1144/GSL.QJEG.1989.022.02.04.

Hovland, M., Judd, A.G., 1988. Seabed Pockmarks and Seepages: Impact on Geology, Biology and the Marine Environment. Graham and Trotman, London, p. 293.

Hovland, M. 1990. Do carbonate reefs form due to fluid seepage? *Terra Nova*, v. 2, pp. 8-18.

Hovland, M., Croker, P.F., and Martin, M. 1994. Fault-associated seabed mounds (carbonate knolls?) off western Ireland and north-west Australia. *Marine and Petroleum Geology.*, v. 11, pp. 232-246.

Hovland, M., Gardner, J.V., and Judd, A.G. 2002a. The significance of pockmarks to understanding fluid flow processes and geohazards. *Geofluids*, v. 2, pp. 127-136.

Hovland, M. 2002b. On the self-sealing nature of marine seeps. *Continental Shelf Research.*, v. 22, pp. 2387-2394.

Howarth, V., and Alves, T.M. 2016. Fluid flow through carbonate platforms as evidence for deep-seated reservoirs in Northwest Australia. *Marine Geology.*, v. 380, pp. 17-43.

Jones, R.M. et al., 2000. Integrated hydrocarbon seal evaluation in the Penola Trough, Otway Basin. *APPEA Journal.*, v. 40, no. 1, pp.194-2.

Judd, A.G., and Hovland, M. 1992. The evidence of shallow gas in marine sediments. *Continental Shelf Research.*, v. 12, pp. 1081–1095.

Judd, A. G., 2005, Gas emissions from mud volcanoes: Significance to global climate change, in G. Martinelli and B. Panahi, eds., Mud volcanoes, geodynamics and seismicity: Proceedings of the North Atlantic Treaty Organization (NATO) Advanced Research Workshop on Mud Volcanism, Geodynamics and Seismicity, Baku, Azerbaijan, May 2003: NATO Science Series: IV: Earth and Environmental Sciences., v. 51.

Judd, A.G., and Hovland, M., 2007. Seabed Fluid Flow: the Impact of Geology, Biology and the Marine Environment. *Cambridge University Press.*

Kallweit, R.S, and Wood, L. C., 1982. The limits of resolution of zero-phase wavlets. *Geophysics.*, v.47,pp. 1035-1046.

Keep, M., Clough, M., and Langhi, L. 2002. Neogene tectonic and structural evolution of the Timor Sea region, NW Australia. In M. Keep and S. Moss, (eds) The sedimentary basins of Western Australia: *Proceedings of Petroleum Exploration Society of Australia Symposium*., 3, pp. 341–353.

Kearey, P., Brooks, M., and Hill, I. 2002. An Introduction to Geophysical Exploration, third edition. Blackwell Science, Oxford.

King, G.C.P., Stein, R.S. and Lin Jian, 1994. Static stress changes and the triggering of earthquakes. *Bulletin of Seismological Society of America.*, v. 84, pp.935-953.

Knipe, R.J., 1993. The influence of fault zone processes and diagenesis on fluid flow, *in* A.D. Horbury and A.G. Robinson (eds), Diagenesis and basin development: AAPG Studies in Geology., v.36, pp.135–154.

Knipe, R. J., G. Jones, and Q. J. Fisher, 1998. Faulting, fault sealing and fluid flow in hydrocarbon reservoirs: An introduction, in G. Jones, Q. J. Fisher, and R. J. Knipe,

eds., Faulting, fault sealing and fluid flow in hydrocarbon reservoirs: *Geological Society (London) Special Publication.*,v. 147, p. vii–xxi.

Langhi, L. and Borel, G.D., 2008. Reverse structures in accommodation zone and early compartmentalization of extensional system, Laminaria High (NW shelf, Australia). *Marine and Petroleum Geology*.,v. 25, pp.791-803.

Langhi, L., Zhang, Y., Gartrell, A., Underschultz, J., Dewhurst, D.,2010. Evaluating hydrocarbon trap integrity during fault reactivation using geomechanical three dimensional modelling :An example from the Timor Sea, Australia. *AAPG BULLETN v.*94, pp.567-591. https://doi:10.1306/10130909046.

Langhi, L., Ciftci, N.B., and Borel, G.D. 2011. Impact of lithospheric flexure on the evolution of shallow faults in the Timor foreland system. *Marine Geology*., v. 284, pp. 40-54.

Lavering, I and Jones, A., 2002. Carbonate Shoals And Hydrocarbons In The Western Timor Sea. Geoscience Australia, PESA *News.*, no.55.

Lisk, M., Brincat, M.P., Eadington, P.J., and O'brien, G.W. 1998. Hydrocarbon charge in the Vulcan Sub-basin. In: Purcell, P.G. and Purcell, R.R. (eds) The sedimentary basins of Western Australia 2: *Proceedings of the West Australian Basins Symposium, Perth*, pp. 287–303.

Ligtenberg, J.H.,2003. Sealing quality analysis of fault and formations by means of seismic attributes and neural networks. *Extended Abstracts at EAGE Fault and Top Seals Conference*,8-11 September,Montpellier.

Ligtenberg, J.H. 2005. Detection of fluid migration pathways in seismic data: implications for fault seal analysis. *Basin Research.*, v. 17, pp. 141-153.

Lindsey, J. P., 1989. The Fresnel zone and its interpretive significance.*The Leading Edge*, v. 8, pp. 33–39.

Long, J.J., Imber, J., 2010. Geometrically coherent continuous deformation in the volume surrounding a seismically imaged normal fault-array. *Journal of Structural Geology.*, v.32, pp.222-234.

Long, J.J., Imber, J., 2012. Strain compatibility and fault linkage in relay zones on normal faults.*Journal of structural Geology.,v.*36, pp.16-26.

LØseth, H., Gading, M., Wensaas., L., 2009. Hydrocarbon leakage interpreted on seismic data. Marine and Petroleum Geology,v.26, pp. 1304-1319.

Luo, Y., Higgs, W.G., Kowalik, W.S., 1996. Edge detection and stratigraphic analysis using 3D seismic data. *SEG 1996 Expanded Abstracts,* pp.324–327.

Luo, X., Hu, Z., Xiao, Z., Zhang, B., Yang, W., Zhao, H., Zhao, F., Lei, Y. and Zhang, L., 2015. Effect of carrier bed hetrogeneity on hydrocarbon migration. *Marine and Petroleum Geology*, v. 68, pp.120-131.

Manzocchi, T., Childs, C., Walsh, J.J., 2010. Faults and fault properties in hydrocarbon flow models. Geofluids 10, 94–113, http://dx.doi.org/10.1111/j.1468-8123.2010.00283.x

Marfurt, Kurt J., and Tiago M. Alves. 2015. “Pitfalls and Limitations in Seismic Attribute Interpretation of Tectonic Features.” *Interpretation,* v, 3, pp,SB5-SB15, doi/10.1190/INT-2014-0122.1.

Meldahl, P., Heggland, R., Bril, B., and de Groot, P. 2001. Identifying faults and gas chimneys using multi-attributes and neural networks. *The Leading Edge*, pp. 474-482.

Milkov, A. V., 2000. Worldwide distribution of submarine mud volcanoes and associated gas hydrates. *Marine Geology,* v. 167,pp. 29–42.

Mildren, S.D., Hillis, R.R., Fett, T., and Robinson, P.H. 1994. Contemporary Stresses in the Timor Sea: Implications for Fault-trap Integrity. In: Purcell, P.G. and Purcell, R.R. (eds) The sedimentary basins of Western Australia: Proceedings of the Petroleum Exploration Society of Australia, Perth, pp. 291–300.

Morris, A., Ferrill, D.A. and Henderson, D.B., 1996. Slip tendency analysis and fault reactivation. *Geology*,v. 24, pp.275-278.

Montazeri,M., 2013. Reprocessing of 2D Reflection Seismic Marine Data and Investigation into the AVO behavior of Cambrian Sandstones, Southern Baltic Sea, Sweden. Independent thesis Advanced level (degree of Master), Uppsala University, Disciplinary Domain of Science and Technology, Earth Sciences, Department of Earth Sciences, Geophysics.

Moray, A.J. 1988. Regional Geology of the Offshore Bonaparte Basin. In: Purcell, P.G. and Purcell, R.R. (eds) The North West Shelf, Australia, PESA Symposium, Perth, pp, 287–309.

Moss, J.L., Cartwright, J., 2010. 3D seismic expression of km-scale fluid escape chimneys from offshore Namibia. *Basin Research* , v. 22, pp.481-501.

Muirhead, K. J., and R. Datt., 1976. The N-th root process applied to seismic array data. *Geophys. J. R. Astron. Soc*, v. 47, pp.197–210.

Newton, R.S., Cunningham, R.C., and Schubert, C.E. 1980. Mud volcanoes and pockmarks: Seafloor engineering hazards or geological curiosities? In: Paper 3729, Offshore Technology Conference, Houston, TX, May 1980.

O'Brien, G.W., and Woods, E.P., 1995. Hydrocarbon-related diagenetic zones (HRDZs) in the Vulcan Sub-basin, Timor Sea: recognition and exploration implications. *APEA Journal*, v. 35, pp. 220–52.

O'Brien, G. W., M. Lisk, I. R. Duddy, J. Hamilton, P. Woods, andR. Cowley, 1999, Plate convergence, foreland developmentand fault reactivation: Primary controls on brine migration,thermal histories and trap breach in the Timor Sea, Australia: Marine and Petroleum Geology, v. 16, p. 533– 560.

O'Brien, G.W., Glenn, K., Lawrence, G., Williams, A., Webster, M., Burns, S., Cowley, R., 2002b. Influence of hydrocarbon migration and seepage on benthic communities in the Timor Sea, Australia. *APPEA Journal* , v. 42 ,pp. 225–240.

Othman, A.A.A., Fathy, M., Maher, A., 2016. Use of spectral decomposition technique for delineation of channels at Solar gas discovery, offshore West Nile Delta, Egypt. *Egyptian Journal of Petroleum*, v. 25, pp. 45–51. https://doi.org/10.1016/j.ejpe.2015.03.005

Partyka, G., J. Gridley, J., Lopez, 1999, Interpretational applications of spectral decomposition in reservoir characterization: The Leading Edge., v.18, pp.353– 354. https://doi:10.1190/1.1438295.

Paull, C.K., Hecker, B., Commeau, R., Freeman-Lynde, R.P., Neumann, C., Corso, W.P., Golubic**,** S., Hook, J.E., Sikes, E., and Curray, J. 1984. Biological Communities at the Florida Escarpment Resemble Hydrothermal Vent Taxa. *Science*, v. 226, pp. 965-967.

Powell, T.G. 2004. Australia's hydrocarbon provinces – Where will future production come from? *The APPEA Journal*, v. 44, pp. 729-740.

Puryear, C.I, and Castagna, J.P.,2008. Layer-thickness determination and stratigraphic interpretation using spectral inversion: Theory and application. *Geophysics*, v.73, pp.37-48.

Robert, H.H., Carney,R.S., 1997. Evidence of episodic fluid, gas, and sediment venting on the northern Gulf of Mexico continental slope. *Economic Geology*, v. 92, pp. 863-879.

Roberts, H.H., Feng, D., 2013. Carbonate precipitation at Gulf of Mexico hydrocarbon seeps: an overview. In: Abrams, M., Aminzadeh, F., Berge, T., Connolly, D., O'Brien, G. (Eds.), Hydrocarbon Seepage: From Source to Surface. *SEG/AAPG Special Publication*, pp. 43–61.

Rollet, N. Logan, G.A., Kennrad, J.M., O'Brien., Jones, A.T., Sexton., 2006. Characterisationand correlation of active hydrocarbon seepage using geophysical data sets: An example from the tropical, carbonate Yampi Shelf, Northwest Australia. Marine and Petroleum Geology,v. 23 pp.145–164. https:// doi: S0264817205001273.

Schroot, B.M., Klaver, G.T., and Schüttenhelm, R.T.E. 2005. Surface and subsurface expressions of gas seepage to the seabed — examples from the Southern North Sea. v. 22, pp. 499–515.

Schlomer, S. and Kross, B.M., 1997. Experimental characterization of the hydrocarbon sealing efficieny of caprocks. *Marine and Petroleum Geology*, v.14, pp.565-580.

Schowalter, T.T., 1979. Mechanics of secondary hydrocarbon migration and entrapment. *AAPG Bulletin*, v.63, pp.723-760.

Sheriff, R.E.,1975. Factors affecting seismic amplitudes, *Geophys. Pros*., v,23, pp.125-138.

Sheriff, R.E., and Gildert, L.P. 1995. Exploration Seismology, second edition, Cambridge University Press, Cambridge.

Shuster, M.W., Eaton, S., Wakefield, L.L. and Kloosterman, H.J., 1998. Neogene tectonics, greater Timor Sea, offshore Australia: Implications for trap risk. *APPEA Journal (Australian Petroleum Production and Exploration Association)*, v. 38, pp.351-379.

Sibson, R.H., Moore, J. MeM. and Rankin, A.H., 1975. Seismic pumping - a hydrothermal fluid transport mechanism. *JI Geol. Soc. Lond.*, v. 131, pp.653-659.

Sills, G.C., Wheeler, S.J., 1992. The significance of gas for offshore operations. *Continental Shelf. Research*, v.12, pp.1239-1250.

Simm, R., Bacon, M., 2014. Seismic Amplitude: An Interpreter's Handbook. Cambridge University Press.

Simpson, R. W. and P. A. Reasenberg (1994). Earthquake-induced static stress changes on central California faults, in *The Loma Prieta, California, earthquake of October 17, 1989—techtonic processes and models*, R. W. Simpson (Editor), *U.S. Geol. Surv.Profess. Pap. 1550-F.*

Smith, G.C., Tilbury, L.A., Chatfield.A, Senycia, and P,Thompson, N.,1996. Laminaria - A new Timor Sea discovery: *Australian Petroleum Production and Exploration Association Journal*, v. 36, pp.12-28.

Smith, D. A.,1966.Theoretical considerations of sealing and non-sealing faults". *Bull, Am, Ass. Petr, Geol.*, v.50, pp. 363-374.

Steeples, D.W., Miller, R.D., 1988. Avoiding pitfalls in shallow seismic reflection surveys. *Geophysics*, v. 63 , pp. 1213-1224.

Stein, R.S.,1999. The role of stress transfer in earthquake occurrence. *Nature*,v.402, pp.605-609.

Stewart, S.A., Davies, R.J., 2006. Structure and emplacement of mud volcano systems in the South Caspian Basin. AAPG Bulletin,v. 90 , pp. 771–786

Tissot, B.P. and Welte, D.H., 1984. Petroleum Formation and Occurrence (2nd Edition), Springer, Berlin, p.699.

Townend, J., Zoback, M.D., 2000. How faulting keeps the crust strong. Geology, v. 28, pp.399-402.

Ukekwe, C. C. 2012. Modelling secondary hydrocarbon migration in continental margins:Influence of mass transport and sediment heterogeneity on seal capacities and migration pathways. Masters Thesis, Newcastle University.

Van Tuyl, J., Alves, T.M., Cherns, L. 2018. Pinnacle features at the base of isolated carbonate buildups marking point sources of fluid offshore Northwest Australia, doi.org /10.1130/B31838.1.

Vavra, C.L., Kaldi, J.G. and Sneider, R.M., 1992. Geological application of capillary

pressure: A review. *The American Association of Petroleum Geologists Bulletin*, v. 76, pp.840-850.

Veeken, P.C.H., Priezzhev, I.I., Shamaryan, L.E., Shteyn, Y.I., Barkov, A.Y. and Ampliov, Y.P., 2009. Nonlinear multitrace genetic inversion applied on seismic data across the Shtokman field, offshore northern Russia. *Geophysics*, v. 74, pp.49-59.

Weber, K. J., G. Mandl, W. F. Pilaar, F. Lehner, and R. G. Precious,1978. The role of faults in hydrocarbon migration and trapping in Nigerian growth fault structures: *Offshore Technology Conference 10, paper OTC* 3356, p. 2643–2653.

White, R. 1977. Seismic bright spots in the Gulf of Oman. *Earth and Planetary Science Letters*, v. 37, pp. 29-37.

Whittam, C.B., Norvick, M.S., Mclntyre, C.L., 1996. Mezozoic and Cainozoic tectonstratigraphy of Western ZOCA and adjacent areas. *AAPEA (Australian Petroleum Production and Exp.lorationAssociationJournal*,v.36,pp209-231.

Widess, M. B.,1973. How thin is a thin bed. Geophysics, v.38, pp. 1176 – 1180.

Wiprut, D. and Zoback, M.D., 2002. Fault reactivation, leakage potential, and hydrocarbon column heights in the northern North Sea. *NPE Special Publication*, v.11, pp.203-219.

Woodside Offshore Petroleum Pty Ltd. Alarari-1 well completion report, interpretive data, February 1998.

Whibley, M., and Jacobson, T. 1990. Exploration in the Northern Bonaparte Basin, Timor Sea – WA-199-P. *APEA Journal*, v. 30, pp. 7–25.

Yielding, G., Freeman, B. and Needham, 1997. Quantitative fault seal prediction. *The*

American Association of Petroleum Geologists, v. 81, pp.897-917.

Yielding, G., Bretan, P., Freeman, B., 2010. Fault seal calibration: a brief review. Geological Society, London, Special Publications, v.347, pp. 243–255. http://dx.doi.org/10.1144/SP347.14.

Yilmaz, OZ. (2001). Seismic data analysis: processing, inversion, and interpretation of seismic data. Investigations in geophysics, 2nd edition, Volume I. Tulsa, OK, Society of Exploration Geophysicists.

Appendices

Appendix_1A: TWT seismic horizons that were used in chapter 2 to constrain the throw distributions along active faults in Chapter 2. Note that Fault traces are drawn approximately for reference purposes.

Appendix_1B: Variance and edge detection attribute mapped along Horizons H9 and H10 in Chapter 2

Appendix_1C: Throw-contoured strike projection maps of faults F11, F12 and F22, showing the intersections of each mapped horizon in the footwall and hanging wall of each fault. The black dotted line indicates the boundary between the pre- and syn-faulting sequences.

Appendix_2A: Radon demultiple applied along the seismic lines 43, 3329 and 3330 in Chapter 3.

Appendix_2B: Butterworth filter applied along the seismic Line 19 from the 3D seismic data with frequencies of 2-4-80-160 in Chapter 3.

Appendix_3A: Time-Depth curve used in depth conversion for the 3D seismic data used in Chapter 4.

Appendix_3B: Slip tendency stereograph for Faults F10, F11, F22, F25, F36, F39, F44, F51.

Appendix_ 3C: Gamma log and the corresponding sonic log used to extract the Vshale and the SGR attributes.

Appendix_4A: Initial AVO analysis from the raw seismic data.

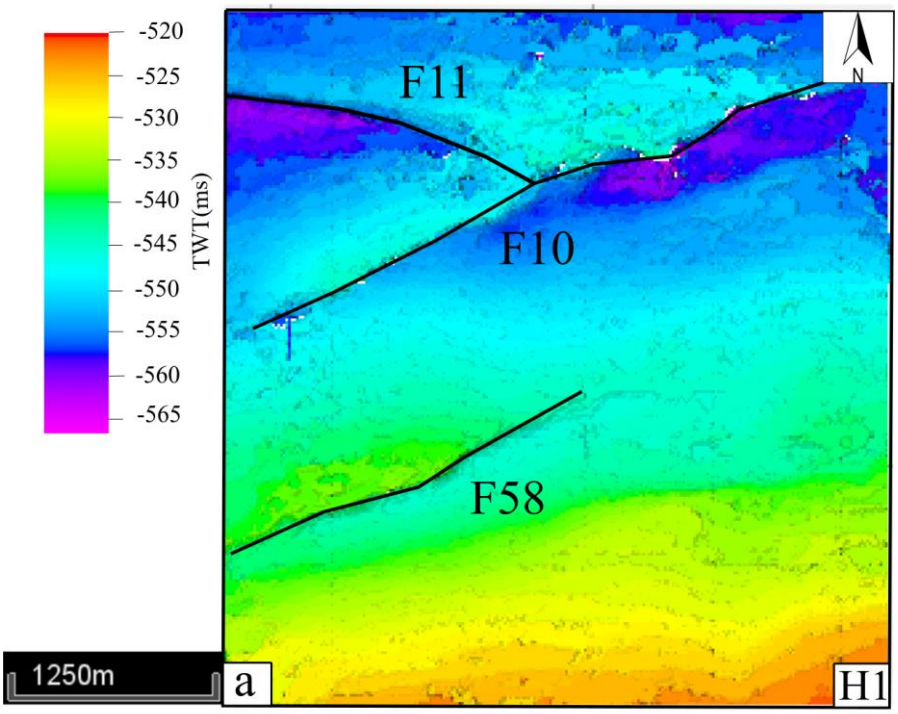
-520
-525
-530
-535
-540
-545
-550
-555
-560
-565
TWT(ms)
F11
F10
F58
N
1250m
a
H1

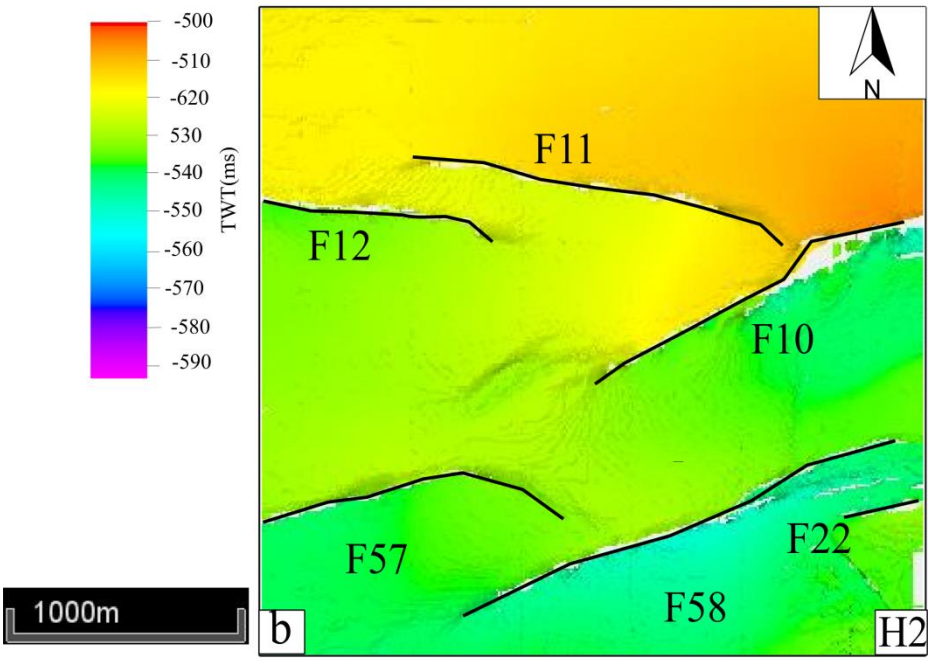
-500
-510
-620
530
-540
-550
-560
-570
-580
-590
TWT(ms)
F11
F12
F10
F57
F22
F58
N
1000m
b
H2

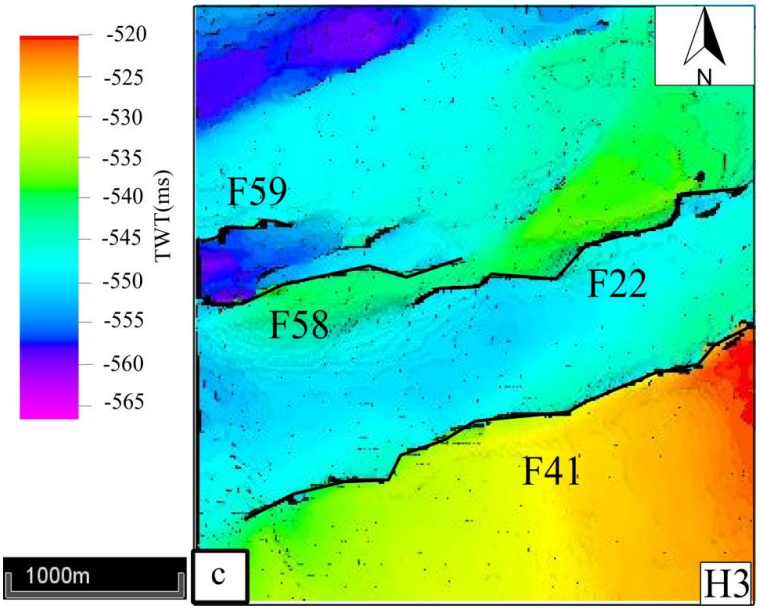
-520
-525
-530
-535
-540
-545
-550
-555
-560
-565
TWT(ms)
N
F59
F58
F22
F41
1000m
c
H3

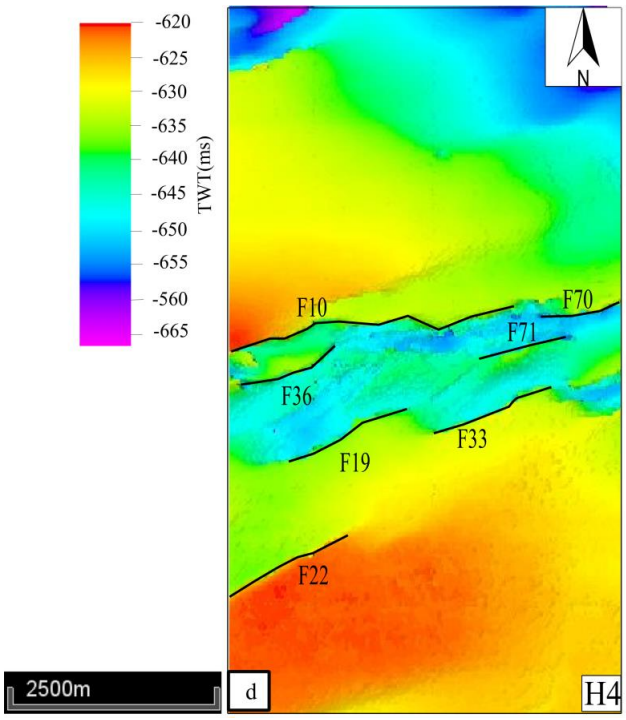
-620
-625
-630
-635
-640
-645
-650
-655
-560
-665
TWT(ms)
N
F10
F70
F71
F36
F33
F19
F22
2500m
d
H4

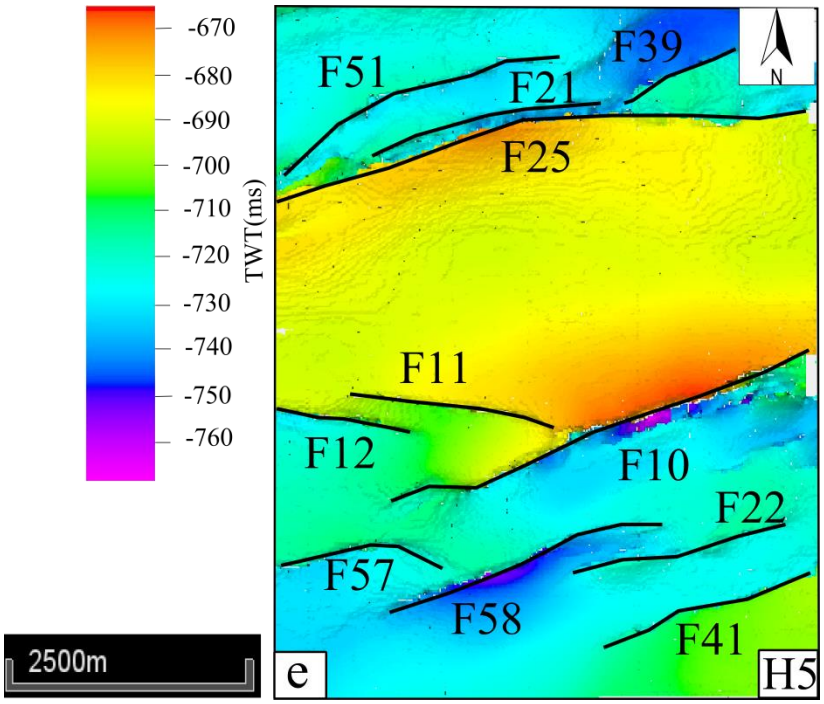
-670
-680
-690
-700
-710
-720
-730
-740
-750
-760
TWT(ms)
F51
F21
F39
F25
F11
F12
F10
F22
F57
F58
F41
N
2500m
e
H5

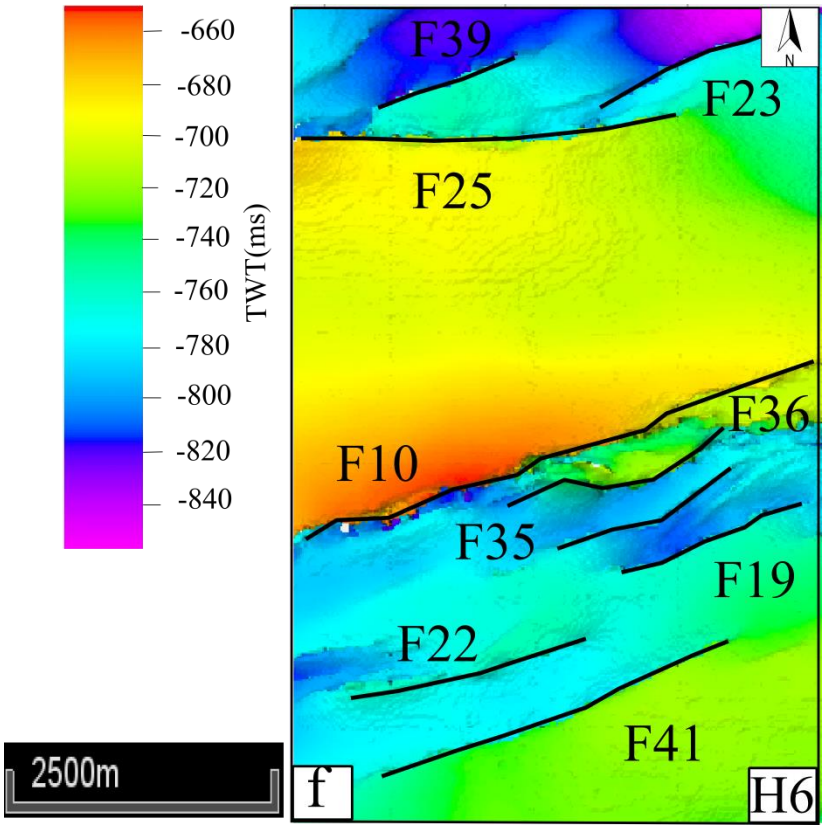
-660
-680
-700
-720
-740
-760
-780
-800
-820
-840
TWT(ms)
F39
F23
F25
F36
F10
F35
F19
F22
F41
N
2500m
f
H6

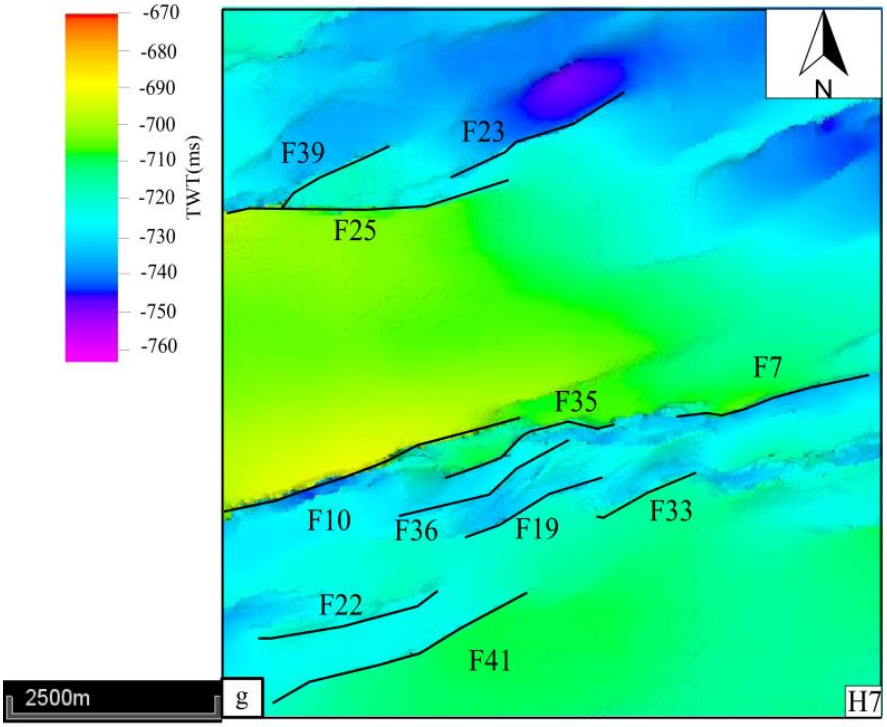
-670
-680
-690
-700
-710
-720
-730
-740
-750
-760
TWT(ms)
N
F39
F23
F25
F7
F35
F10
F36
F19
F33
F22
F41
2500m
g
H7

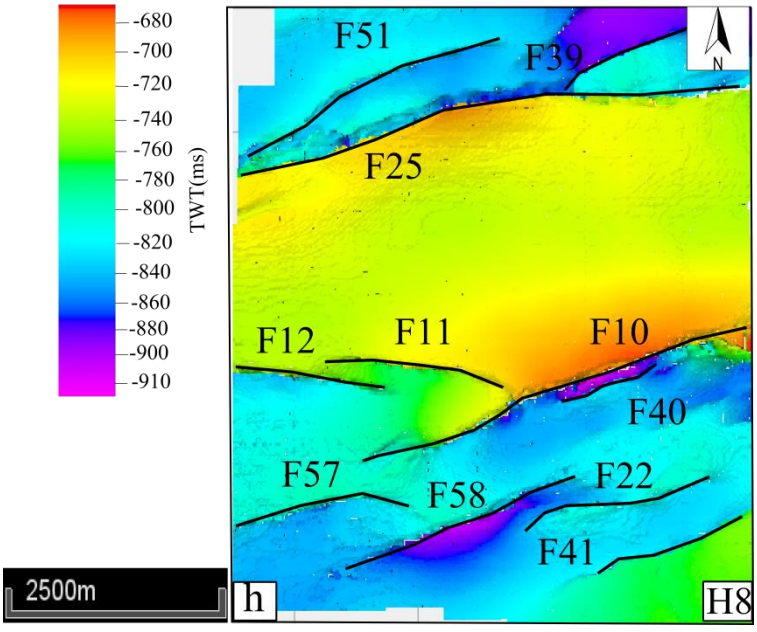
-680
-700
-720
-740
-760
-780
-800
-820
-840
-860
-880
-900
-910
TWT(ms)
N
F51
F39
F25
F12
F11
F10
F40
F57
F58
F22
F41
2500m
h
H8

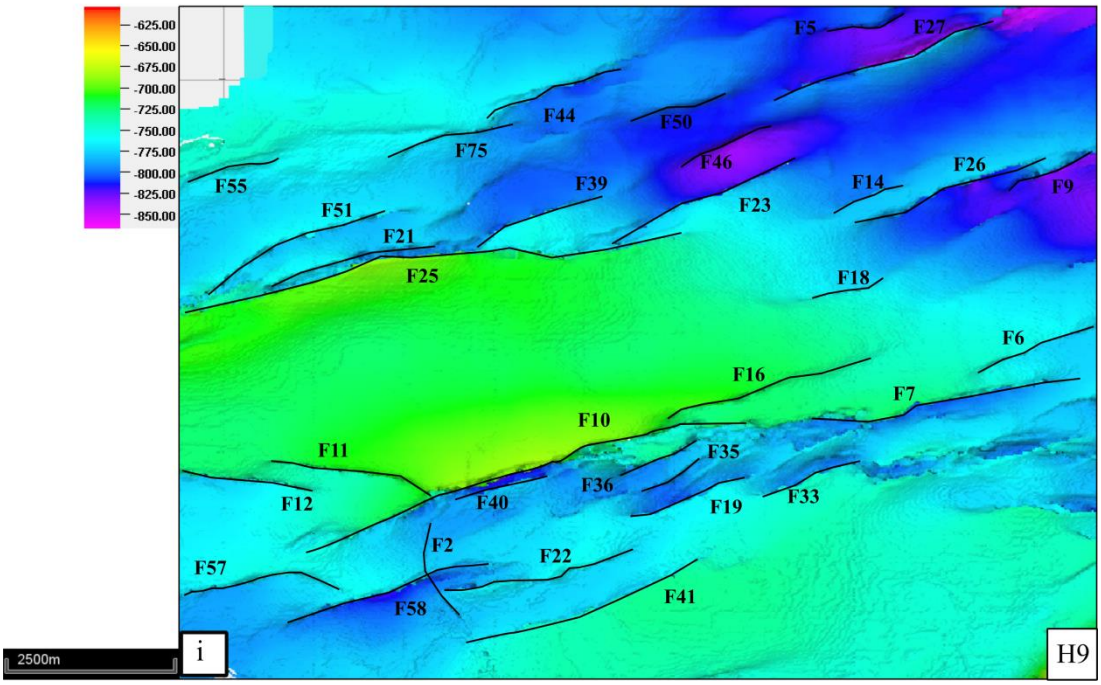
-625.00
-650.00
-675.00
-700.00
-725.00
-750.00
-775.00
-800.00
-825.00
-850.00
F5
F27
F44
F50
F75
F46
F55
F39
F14
F26
F9
F51
F23
F21
F25
F18
F6
F16
F7
F10
F11
F35
F36
F12
F40
F19
F33
F2
F22
F57
F41
F58
2500m
i
H9

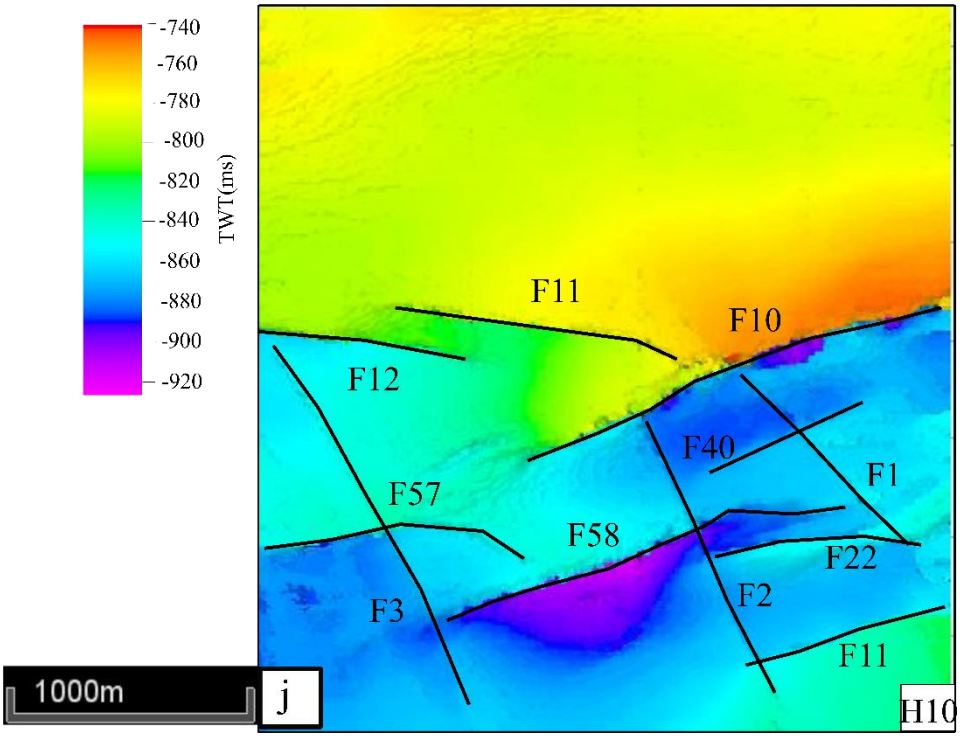
-740
-760
-780
-800
-820
-840
-860
-880
-900
-920
TWT(ms)
F11
F10
F12
F40
F1
F57
F58
F22
F3
F2
F11
1000m
j
H10

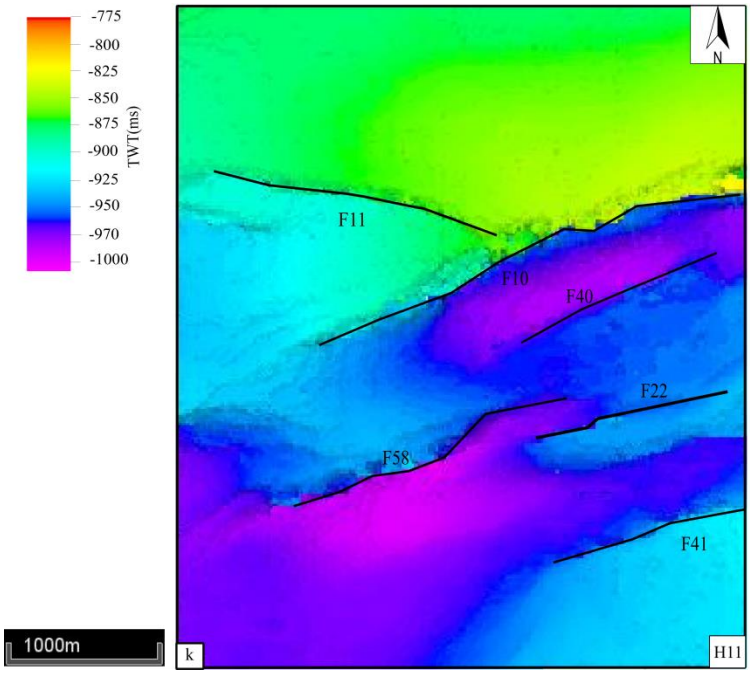
-775
-800
-825
-850
-875
-900
-925
-950
-970
-1000
TWT(ms)
N
F11
F10
F40
F22
F58
F41
1000m
k
H11

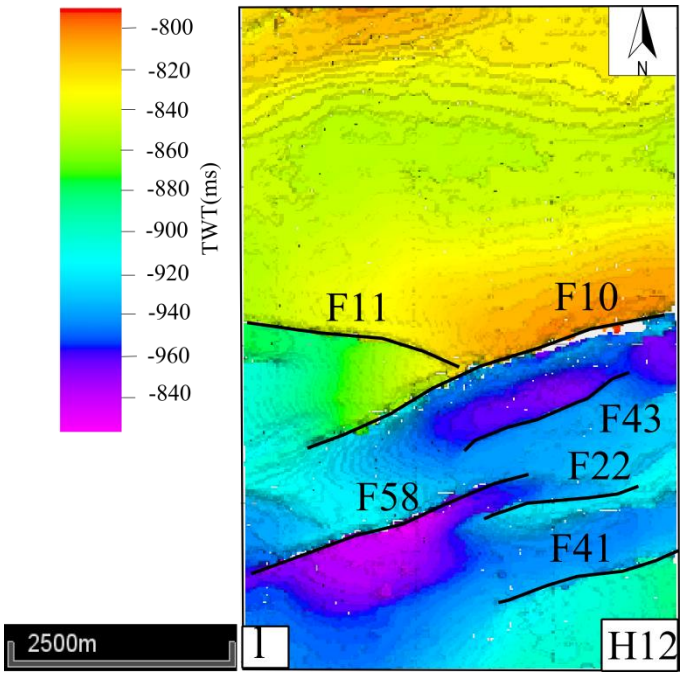
-800
-820
-840
-860
-880
-900
-920
-940
-960
-840
TWT(ms)
N
F11
F10
F43
F22
F58
F41
2500m
I
H12

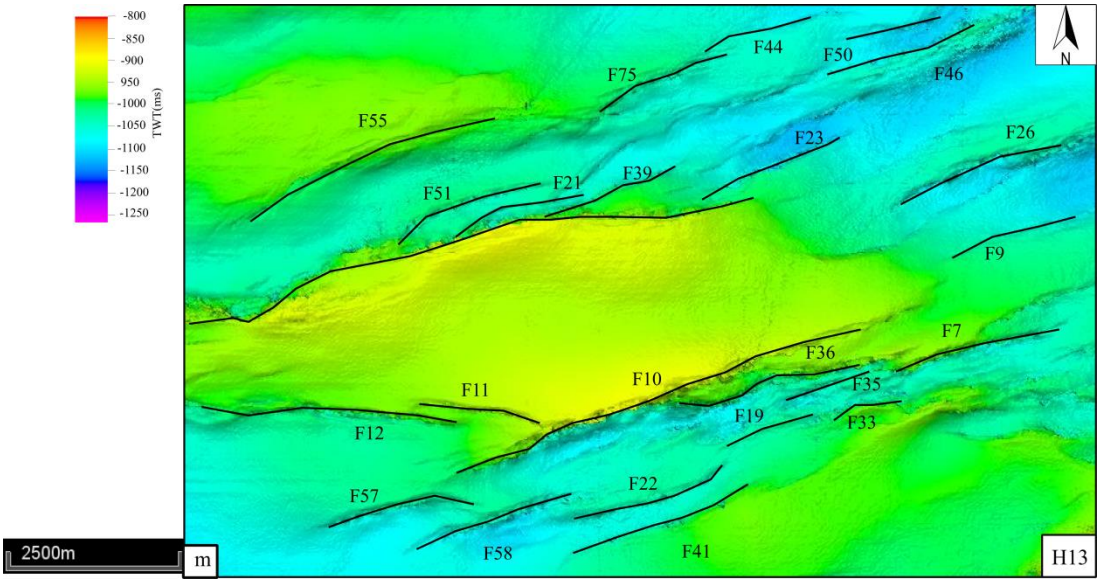

Figure 1A TWT seismic horizons that were used in chapter 2 to constrain the throw distributions along active faults in Chapter 2. Note that Fault traces are drawn approximately for reference purposes.

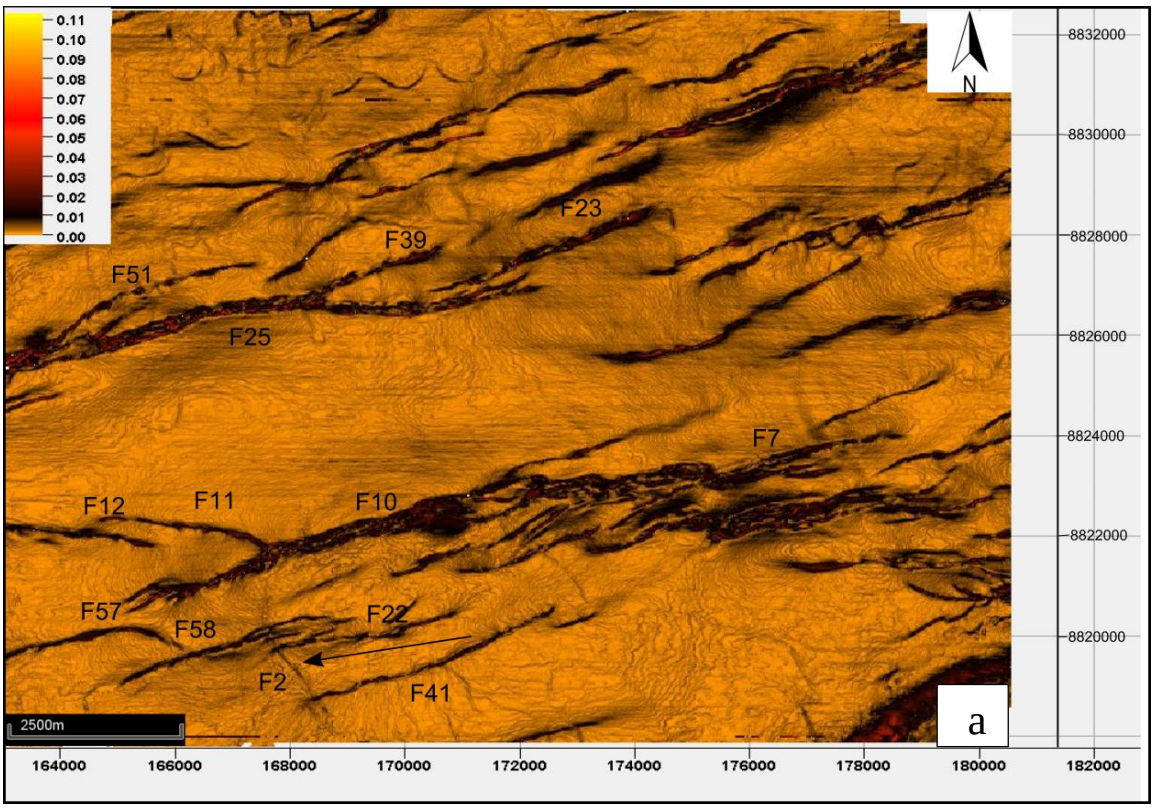

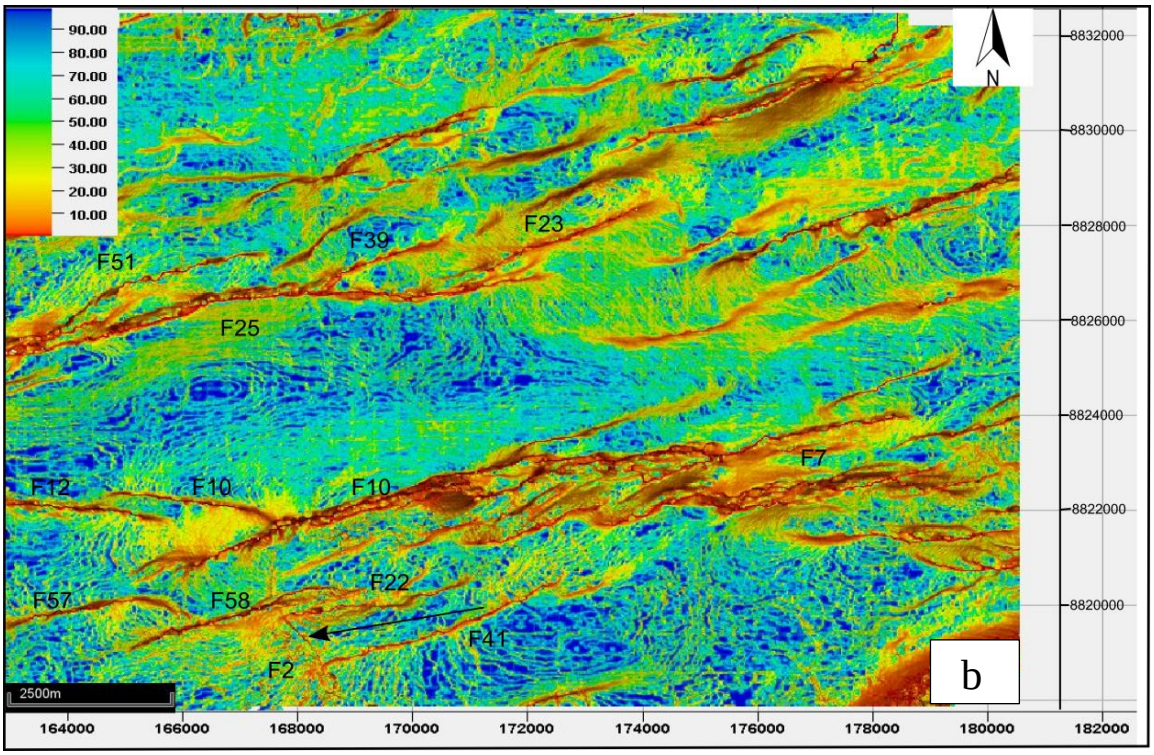

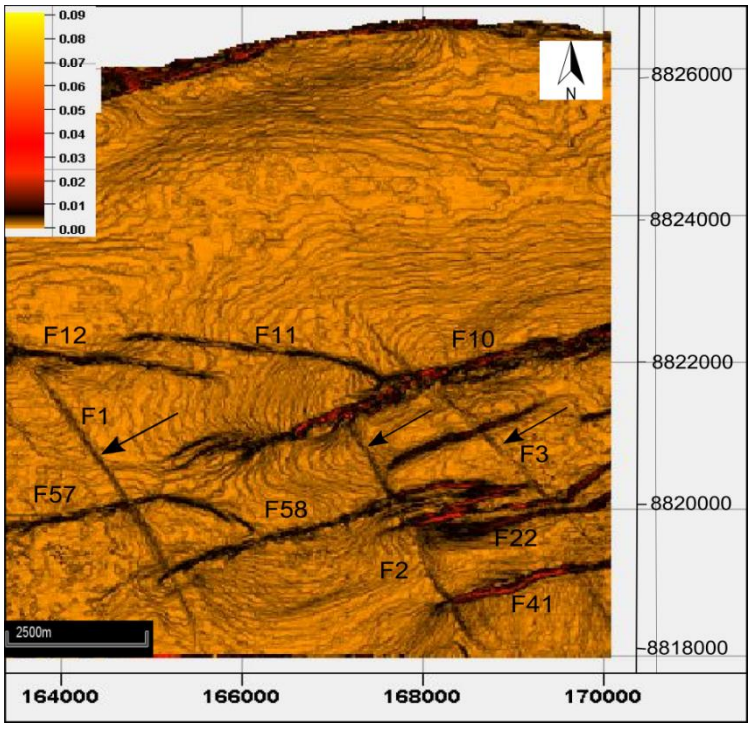

Figure.1B. (a) Variance attribute mapped along Horizon H9 (b) Edge detection attribute mapped along Horizon H9. (c) Variance attribute mapped along Horizon H10.

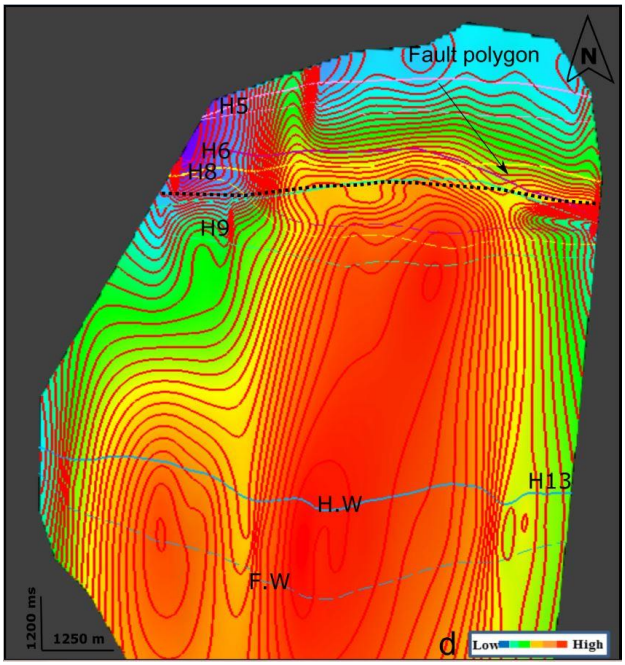

Figure. 1C. Throw-contoured strike projection maps of fault F41, showing the intersections of each mapped horizon in the footwall and hanging wall of each fault. The black dotted line indicates the boundary between the pre- and syn-faulting sequences. Note that H9 is located approximately within this boundary were the contour lines change from sub-vertical to sub-horizontal.

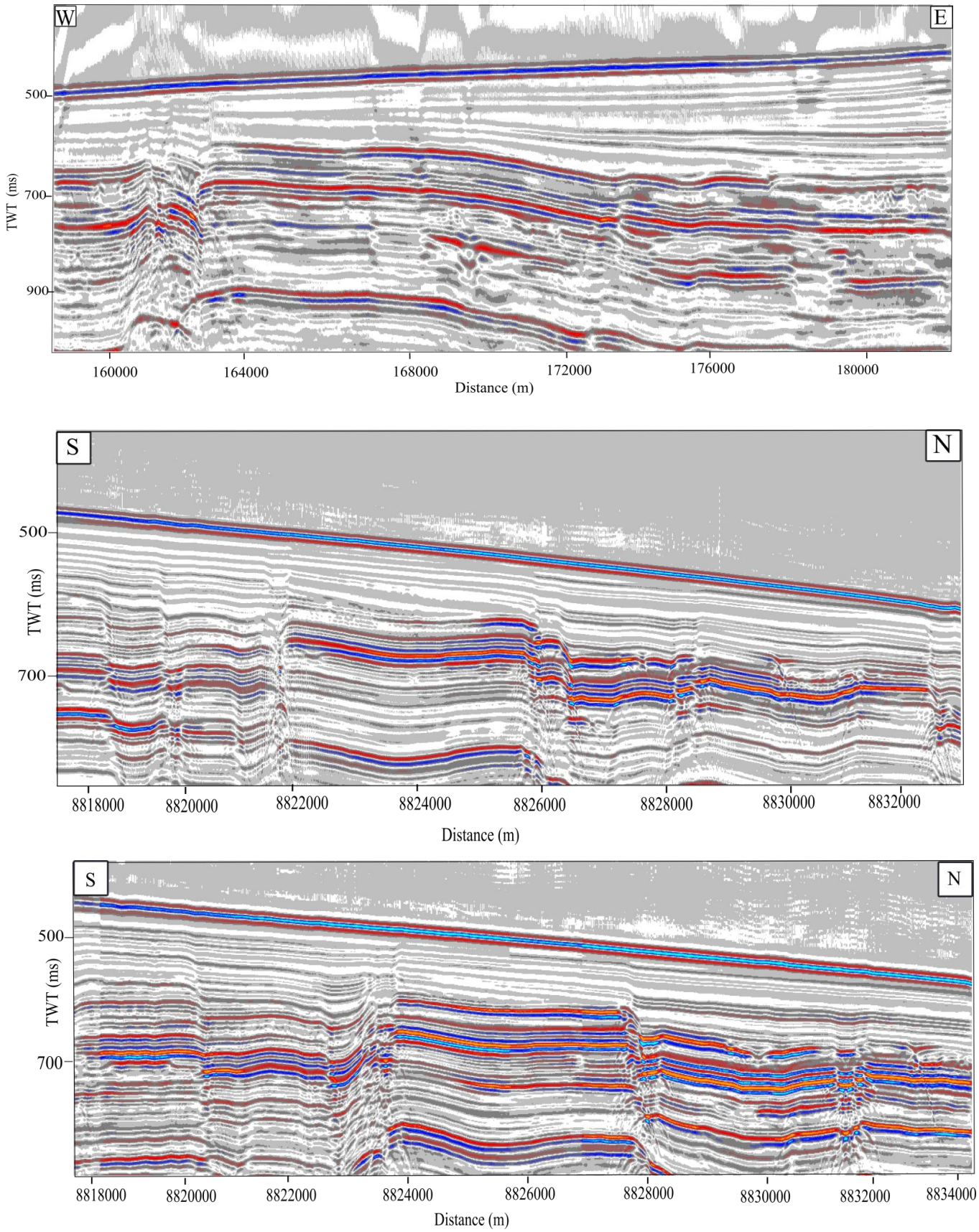

Figure 2A. Radon demultiple applied along the sismic lines 43, 3329 and 3330. Note that the radon demultiple produce different amplitude distribution at the seabed compared with the original 3D seismic volume in Chapter 3 in figures 3.18a , 3.19a and 3.19c.

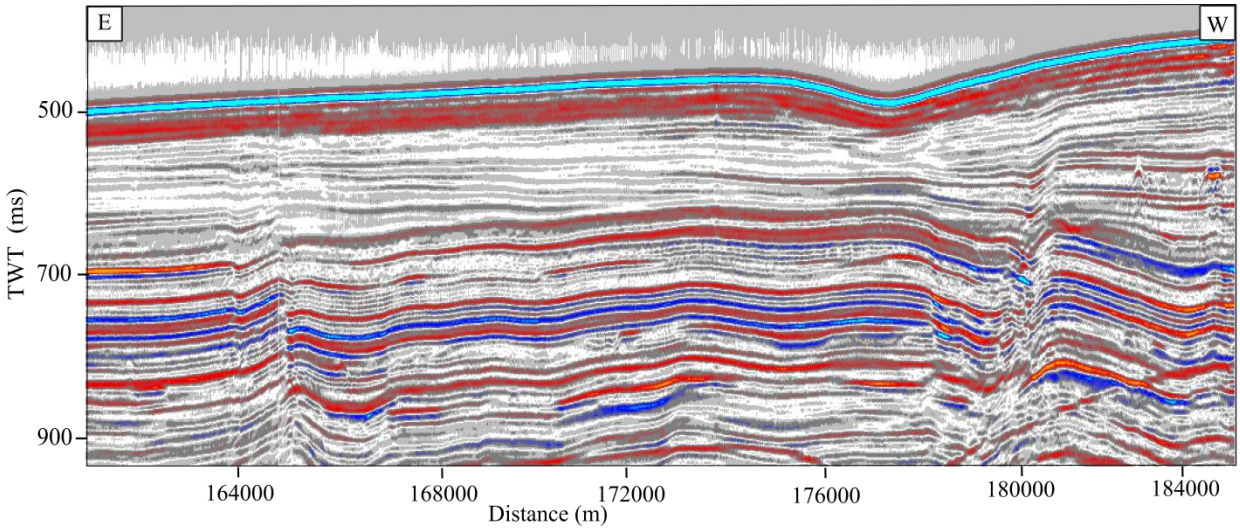

Figure 2B. Butterworth filter applied along the seismic Line 19 from the 3D seismic data with frequencies of 2-4-80-160.

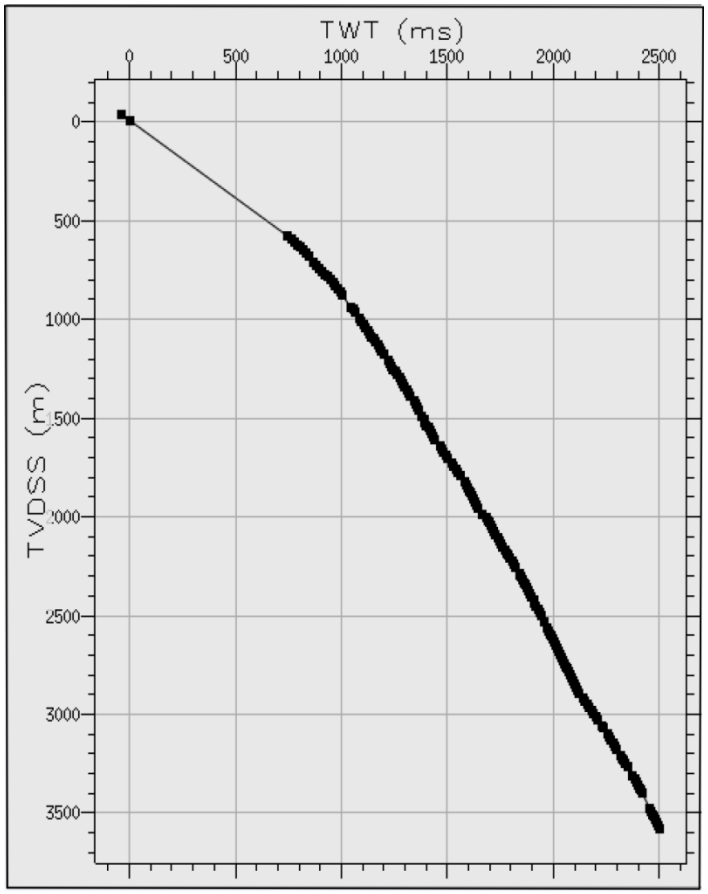

Figure 3A. Time-Depth curve used in depth conversion for the 3D seismic data used in Chapter 4

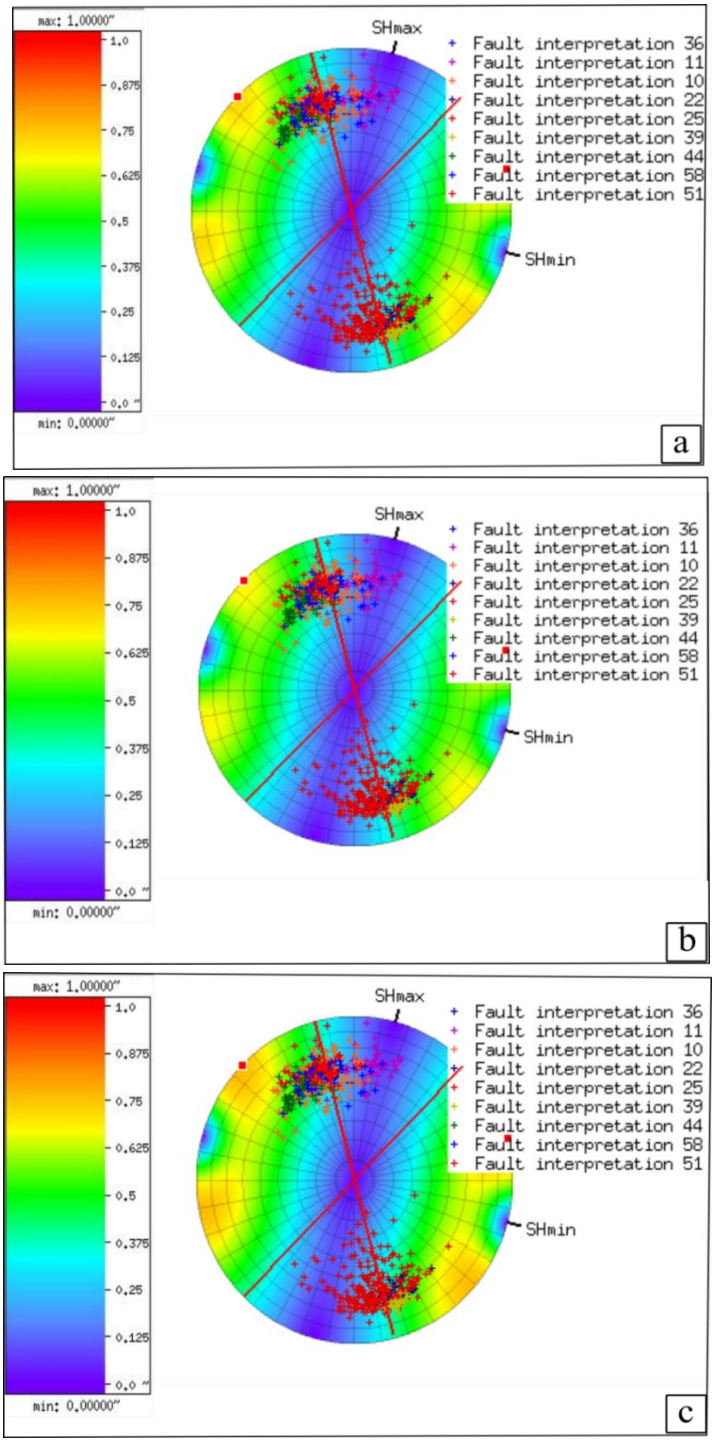

Figure 3B. Slip tendency stereograph for Faults F10, F11, F22, F25, F36, F39, F44, and F51 . (a) Slip tendency using the average stress value from Catillo et al.(2000). (b) Slip tendency extracted from the stress value varied by -0.0004Ma/m. (c)) Slip tendency extracted from the stress value varied by +0.0004.Each cross on the stereograph represents the fault pole along each fault plane with their corresponding azimuth, dip and the slip tendency. Results are displayed along the three stereograph projections coloured according to the slip tendency attribute.

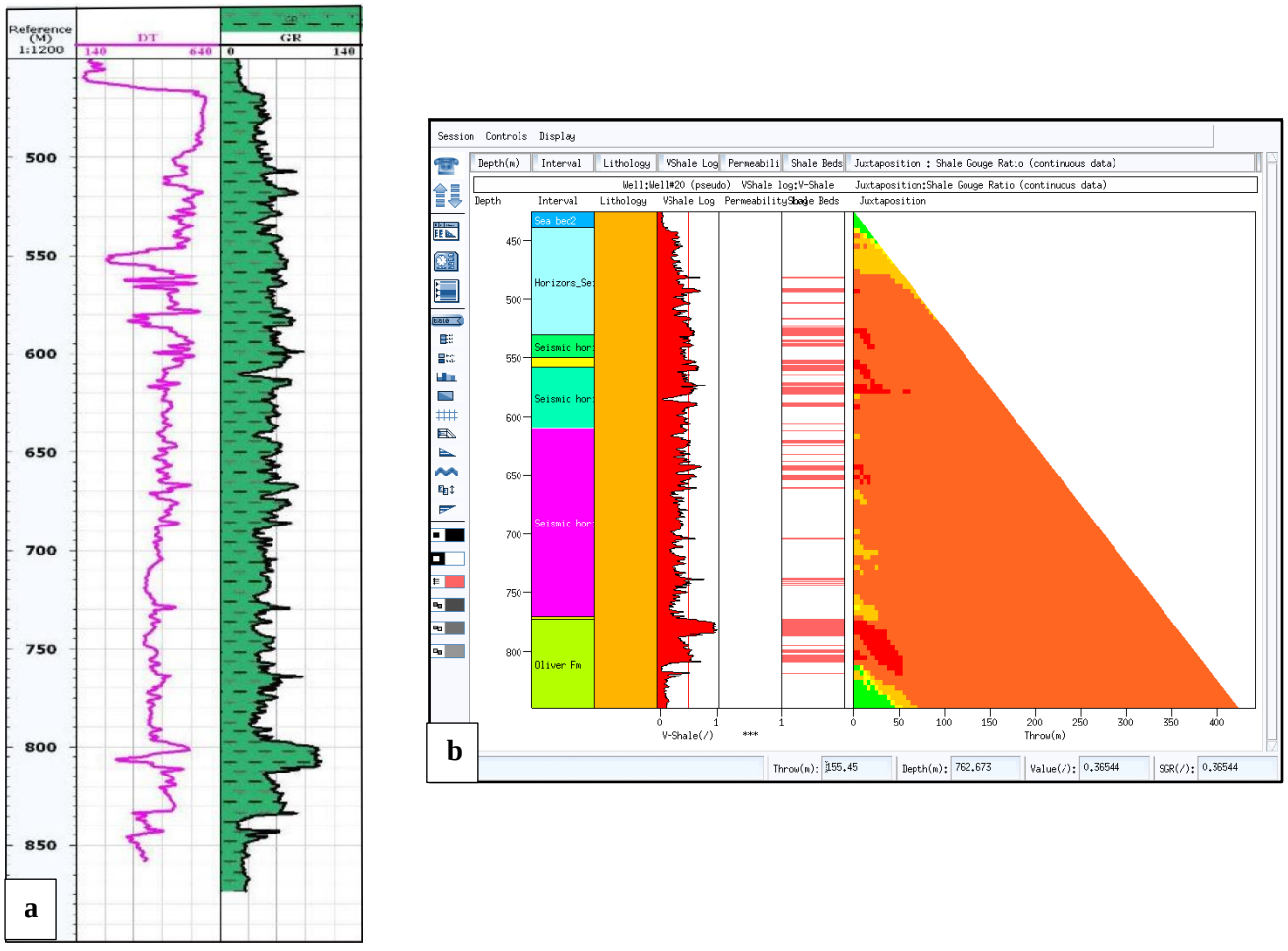

Figure 3C . **a.** Gamma log and the corresponding sonic log used to extract the Vshale and the SGR attributes. **b.** The shale gouge triangle and Vshale log used calculate the SGR attribute.

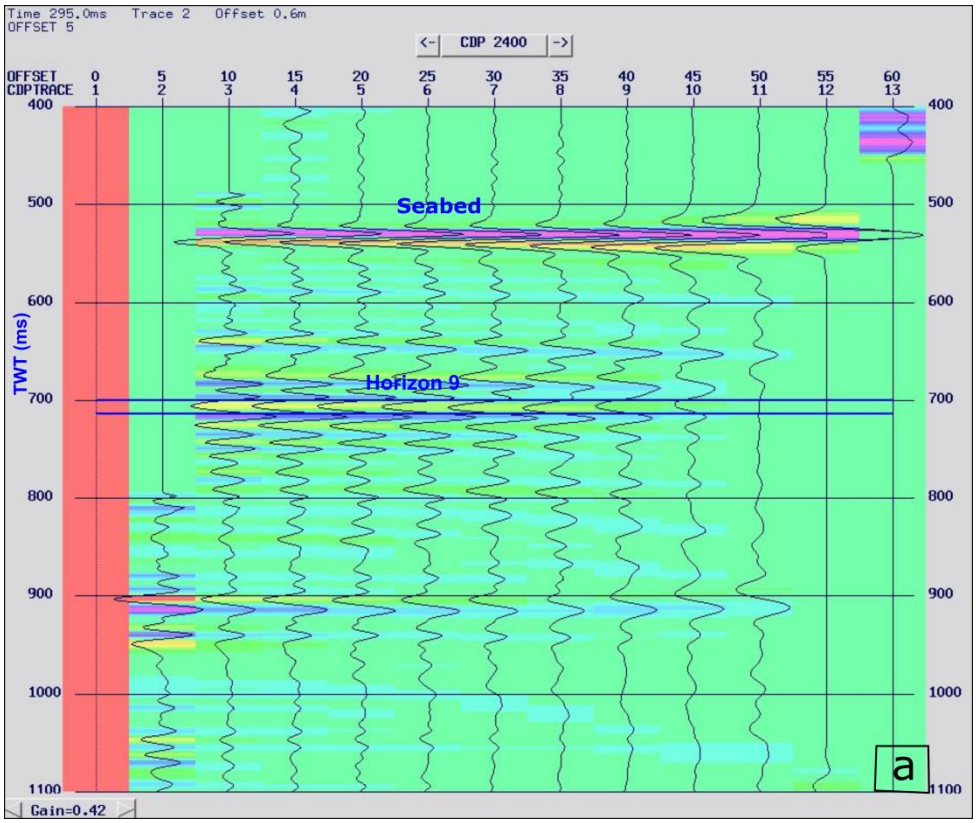

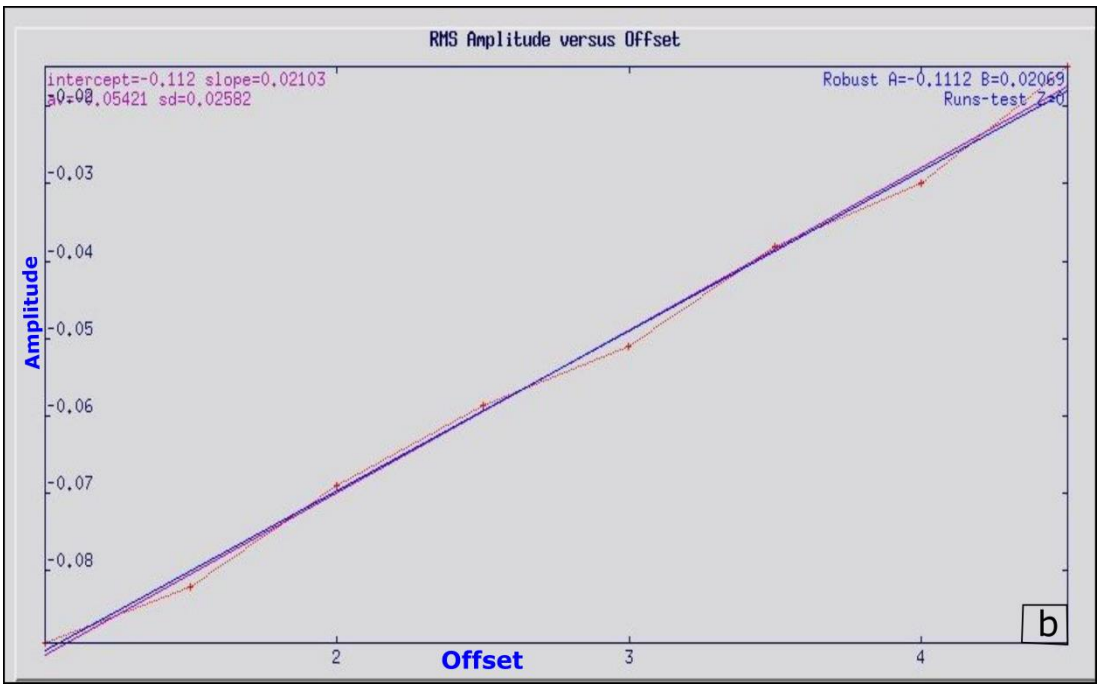

Figure 4A. AVO analysis from the raw seismic data. (a) Angle CDP gathers (2400) from Line 3328 showing the target Horizon 9 and the seabed. (b) cross plot of the intercept (A) reflection coefficient and the gradient (B). Note that the AVO cross plot shows AVO class 4 (negative intercept decreasing with offset).